

CHARACTERIZATION OF INTERFACIAL ENERGY OF THIN FILMS  
THROUGH CURRENT INDUCED DIFFUSIVE INTERFACIAL VOIDING

A Dissertation

Submitted to the Faculty

of

Purdue University

by

Yuvraj Singh

In Partial Fulfillment of the

Requirements for the Degree

of

Doctor of Philosophy

August 2019

Purdue University

West Lafayette, Indiana

**THE PURDUE UNIVERSITY GRADUATE SCHOOL**  
**STATEMENT OF DISSERTATION APPROVAL**

Dr. Ganesh Subbarayan, Chair

School of Mechanical Engineering

Dr. Muhammad A. Alam

School of Electrical and Computer Engineering

Dr. Mysore Dayananda

School of Materials Engineering

Dr. Charles M. Krousgrill

School of Mechanical Engineering

**Approved by:**

Dr. Jay P. Gore

Head of the School Graduate Program

## ACKNOWLEDGMENTS

I have a lot of people to thank for their help and support over the entire course of my time at Purdue. Any dedication I write may not do enough justice but, I would like to begin by thanking Prof. Subbarayan for being a supportive mentor and giving me the opportunity to pursue a higher degree. Without his encouragement and faith in my abilities this would not be possible. I would also like to thank Prof. Alam, Prof. Dayananda and Prof. Krousgrill for serving on my committee.

Given the length of time I have been associated with our research group, the list of friends and labmates is long. I would like to begin by thanking my group of labmates that have graduated. Dennis, Abhishek, Subramanya, Kritika, Nikhil, Simranjit, Chaitra, Kaushik, Hung-Yun, Tao and Anirudh have all played a huge role in the way I navigated through graduate school. I enjoyed some of our light hearted banter and discussions in the office. From the present group of labmates, I would like to thank Travis for being a good friend and for finding me a roof to call home this last year. I'd like to thank Sudarshan for spending endless days and nights working with me at the cleanroom this past year and for being a good friend. I thank Pavan and Anirudh for their help with the theory part of my thesis and words of encouragement. Colin for his help with making the test equipment while, listening to me talk about the importance of a good surface finish. I would also like to thank Chun-Pei, Yaxiong, David, Maryam, Sukshitha and Huanyu for teaching me new things. It is safe to say, without these group of friends, life would have been a little dull at work.

I feel blessed to have the kind of emotional support I have had along the way. Away from work, I had great roommates and friends that livened up my life. I thank Anand, Shrikant and Agni for being there through thick and thin. Any dedication I write would be incomplete without mentioning the most important people in my life. My parents, brother, sister and Becky have all earned this degree as much as I have.

Their patience and love has been the only thing that kept me going when I saw no hope.

Finally, I would like to thank *Waheguru* for his blessings and all the opportunities he has afforded me.



## TABLE OF CONTENTS

	Page
LIST OF TABLES . . . . .	viii
LIST OF FIGURES . . . . .	ix
ABSTRACT . . . . .	xv
1. INTRODUCTION . . . . .	1
1.1 Motivation . . . . .	1
1.2 Research Objective . . . . .	3
1.3 Thesis Outline . . . . .	5
2. BACKGROUND: ELECTROMIGRATION . . . . .	8
2.1 Review of Electromigration . . . . .	8
2.1.1 Effect of Microstructure . . . . .	11
2.1.2 Geometric Effects on Electromigration . . . . .	14
2.1.3 Electromigration Lifetimes . . . . .	17
3. TEST STRUCTURE DESIGN AND MATERIAL SELECTION . . . . .	20
3.1 Background: Electromigration Test Structures . . . . .	20
3.2 In-situ Electromigration Testing . . . . .	22
3.3 Material Selection . . . . .	27
3.3.1 Diffusion Barrier Layer . . . . .	28
3.3.2 Capping Layer . . . . .	31
3.4 Geometry . . . . .	34
3.4.1 Conductor - Copper . . . . .	35
3.4.2 Diffusion Barrier Layer/Capping Layer . . . . .	37
3.5 Finite Element Modeling . . . . .	39
3.5.1 2-D Model . . . . .	39
3.5.2 3-D Model . . . . .	43
4. FABRICATION PROCESS . . . . .	47
4.1 Process Details . . . . .	47
4.1.1 Lithography . . . . .	47
4.1.2 Deposition . . . . .	51
4.1.3 Etching . . . . .	53
4.1.4 Miscellaneous . . . . .	54
4.2 Fabrication . . . . .	54
4.3 Fabrication Challenges . . . . .	68

	Page
5. TEST SETUP AND EXPERIMENTAL PLAN . . . . .	72
5.1 Development of Test Setup . . . . .	72
5.1.1 Tracking Voids and Failures . . . . .	72
5.1.2 Resistance Measurements . . . . .	73
5.1.3 Temperature Control . . . . .	74
5.2 Design of Test Apparatus . . . . .	75
5.2.1 Design Requirements . . . . .	75
5.2.2 Final Design . . . . .	76
5.3 Preliminary Measurements . . . . .	82
5.4 Test Plan and Procedure . . . . .	84
6. EXPERIMENTAL RESULTS . . . . .	88
6.1 Resistance Measurement . . . . .	88
6.1.1 Joule Heating . . . . .	91
6.2 Morphology of Interface . . . . .	95
6.2.1 Cathode End . . . . .	95
6.2.2 Anode End . . . . .	100
6.2.3 Surface Texture . . . . .	102
6.3 Measurements of Void Length . . . . .	103
6.4 Velocity of Interface . . . . .	105
6.5 Width Variation . . . . .	105
6.5.1 Temperature Variation . . . . .	108
6.5.2 Current Density Variation . . . . .	110
7. A CONTINUUM MODEL FOR ELECTROMIGRATION . . . . .	113
7.1 Overview . . . . .	113
7.2 Derivation of Balance Laws at the Interface . . . . .	113
7.2.1 Interface Transport Theorem . . . . .	114
7.2.2 Balance Laws at the Interface . . . . .	115
7.3 Conditions for Phase Growth . . . . .	119
7.4 Statistical Growth Condition . . . . .	121
7.4.1 Application to Small Deformation Diffusive Void Growth . . . . .	122
8. EXTRACTION AND VALIDATION OF INTERFACIAL ADHESION EN- ERGY . . . . .	124
8.1 Activation Energy . . . . .	124
8.2 Extraction of Interfacial Adhesion . . . . .	130
8.3 Validation of Extracted Interfacial Adhesion . . . . .	135
9. VALIDATION OF FRACTURE TOUGHNESS: SUPER LAYER TEST . . . . .	140
9.1 Overview . . . . .	140
9.2 Super Layer Test . . . . .	140
9.2.1 Super Layer Test Specimen Fabrication . . . . .	142
9.2.2 Results: Super Layer Test . . . . .	145

	Page
10. CONCLUSIONS AND FUTURE WORK . . . . .	147
10.1 Summary of Work . . . . .	147
10.2 Implications of the study . . . . .	148
10.3 Future Work . . . . .	149
REFERENCES . . . . .	150
A. INSTABILITY AT BONDED HETEROGENEOUS FILM INTERFACE .	160
A.1 Motivation . . . . .	160
A.2 Scope of the Present Study . . . . .	163
A.3 Finite Element Simulation of Peeling Failure in Heterogeneous Films	165
A.4 Semi-Analytical Solution for Peeling Failure of Heterogeneous Film .	168
A.4.1 Analytical Solution for Adhesion Portion . . . . .	169
A.4.2 Semi-Analytical Solution for Adhesion-Free Portion . . . . .	176
A.5 Results and Discussion . . . . .	183
A.5.1 Discussion on Peel Force Variation . . . . .	183
A.5.2 Discussion on Energy Variation . . . . .	187
A.5.3 Impact of Cohesive Parameters . . . . .	191
A.6 Summary . . . . .	193
VITA . . . . .	196

## LIST OF TABLES

Table	Page
3.1 TiN Properties. . . . .	41
3.2 Cu Properties. . . . .	41
4.1 Spin Coat Recipe Details. . . . .	55
4.2 Process steps for AZ1518 . . . . .	60
4.3 Process steps for AZ1518 . . . . .	61
4.4 Process steps for TiN etch recipe . . . . .	63
4.5 Process steps for PR dry etch recipe . . . . .	63
4.6 Passivation process recipe for SiN <sub>x</sub> . . . . .	65
5.1 Table of resistivity measured at room temperature. . . . .	82
5.2 Test Structure Variation . . . . .	86
5.3 Test plan: Current density variation . . . . .	86
5.4 Test plan: Temperature variation . . . . .	87
8.1 Summary of structures and methods used in copper electromigration tests. . . . .	126
8.1 Continued. . . . .	127
8.2 Summary of copper electromigration test results. . . . .	128
8.2 Continued. . . . .	129
8.3 Activation energies calculated in this study . . . . .	130
8.4 Fit results for variation in current density . . . . .	134
A.1 Boundary conditions at the different points for Case 4. . . . .	173

## LIST OF FIGURES

Figure	Page
1.1 Examples of thin film debond (a) Telephone cord buckling in thin film [9] (b) Micrographs of failure in Al thin films on a flexible substrate under externally applied tension [13] (c) SEM micrograph of failure in a copper damascene line after electromigration [18]. . . . .	2
1.2 (a) Schematic of the line-via-line structure [23] (b) SEM micrographs of a moving metal edge in a conductive line subject to electromigration [23]. . .	4
1.3 Void growth rate as a function of interfacial debond energy [23]. . . . .	4
2.1 Schematic of diffusion paths for atoms in a micro volume [40]. . . . .	12
2.2 Median Time to Failure for Aluminum interconnects with varying mi- crostructures [41]. . . . .	13
2.3 Void nucleation and growth sites in a line-via-line structure where grain boundaries span the width of the interconnect [42]. . . . .	14
2.4 Schematic depicting the cross-section of the structure used by Blech. . . .	15
3.1 Void formation in line-via-line structure imaged post testing [57]. . . . .	21
3.2 A line-via-line schematic for a test structure with two layers of metallization.	21
3.3 Details of (a) Test structure used in the study (b) In-situ test setup for SEM observations (c) Post failure FIB cross-section indicating void growth in line-via-line structures [57]. . . . .	23
3.4 Details of (a) Test structure (b) Post failure FIB cross-section indicating void growth in line-via-line structure as a function of time [59]. . . . .	24
3.5 Details of (a) Test structure used by Lee <i>et al.</i> (b) Edge displacement captured by SEM during electromigration experiments [60]. . . . .	25
3.6 Details of (a) Top view of the EM structure used by Kirimura <i>et al.</i> (b) Cross-section view of the EM structure [62]. . . . .	26
3.7 (a) Void evolution observed in the EM structure (b) Void drift velocity for different cap materials observed during In-situ experiments by Vanstreels <i>et al.</i> [63]. . . . .	26

Figure	Page
3.8 XRD spectra for $Cu/TiN/SiO_2/Si$ samples; (a) as-deposited and after annealing in $N_2$ for 1 hour at (b) 500° C, (c) 600° C (d) 700° C and (e) 800° C [67]. . . . .	30
3.9 AES depth profiles for $Cu/TiN/SiO_2/Si$ samples; (a) as-deposited and after annealing in $N_2$ for 1 hour at (b) 500° C, (c) 700° C (d) 800° C [67].	31
3.10 The diffusion coefficients of copper in different barriers (TiN, TaN, and TiZrN) in the temperature range of 600 – 900° C [66]. . . . .	32
3.11 Variation of resistivity ratio ( $\rho(T)/\rho(0)$ ) with temperature for different TiN films, where normalizing factor $\rho(0)$ is taken as residual resistivity [68].	33
3.12 Schematic of configurations for capping layers [72]. . . . .	34
3.13 Trends in maximum current densities and targeted current densities for Cu interconnects [72]. . . . .	35
3.14 Schematic of the 2-D model along with the mesh used for this numerical study. . . . .	40
3.15 Pictorial representation of the boundary conditions used in this study. . . .	40
3.16 Current density distribution in the structure at the cathode end of the Cu line. . . . .	42
3.17 Temperature rise at the cathode end due to an applied current. . . . .	42
3.18 Maximum temperature rise as a function of the current density in Cu. . . .	43
3.19 Top view of the mesh used for the two cases with varying base layer widths.	44
3.20 Top view of the current density distribution for a Cu line with a narrow TiN base layer. . . . .	44
3.21 Top view of the current density distribution for a Cu line with a wide TiN base layer . . . . .	45
3.22 Plot of the normalized current density along the top and bottom edge of the Cu line for (a) Narrow base layer (10 $\mu m$ ) (b) Wide base layer (40 $\mu m$ ).	46
4.1 Schematic of sidewall profile for negative tone and positive tone resist. . .	48
4.2 Schematics of the fabrication process for electromigration test structures. .	56
4.3 Mask to define the pattern for the Cu lines. . . . .	57
4.4 Optical image of the exposed and developed region on the substrate. . . .	58
4.5 Cu lines on TiN post lift off. . . . .	59
4.6 Mask used to define the area where Ta is to be deposited. . . . .	60

Figure	Page
4.7 Mask for TiN dry etch. . . . .	62
4.8 Top view of substrate after the PR development for TiN etch mask. . . . .	62
4.9 Top view of substrate after TiN etch. . . . .	64
4.10 Top view of substrate TiN etch with a Ta diffusion barrier layer. . . . .	65
4.11 Mask for passivation wet etch. . . . .	66
4.12 Final structure cross-section schematics for the three test specimens. . . . .	67
4.13 Stitch error in mask write during E beam lithography leading to poor mask definition. . . . .	68
4.14 Tear in the thin film observed after lift-off. . . . .	69
4.15 Crack formation in PR due to high temperature exposure during Ta deposition. . . . .	70
4.16 Hardened top surface of the PR mask for TiN etching. . . . .	71
5.1 Circuit for a 4-wire resistance measurement setup [79]. . . . .	74
5.2 Schematic of test setup control and feedback loop. . . . .	76
5.3 CAD image for the designs of the test setup (a) Top view of the CAD model with the aluminum plate with the stages and probe holder (b) Isometric view of CAD model with the aluminum plate with the stages and probe holder. . . . .	78
5.4 (a)Test setup for ex-situ experiments under an optical microscope (b) Test specimen holder with the ceramic heater and needle probes. . . . .	79
5.5 Test Setup in the SEM chamber for in-situ experiments. . . . .	80
5.6 Image of the front diagram GUI in Labview. . . . .	81
5.7 Variation in resistance for two TiN structures (deposited at different times) as a function of temperature. . . . .	83
5.8 Process flow used for the electromigration tests. . . . .	85
5.9 Diffusivities for surface, grain boundary and lattice diffusion of Cu and Al [81]. . . . .	85
6.1 Resistance change observed for test structures subject to varying temperatures at a fixed current density $j = 3 \times 10^6$ A/cm <sup>2</sup> (a) Test structures with SiN capping layer (b) Test structures with Ta diffusion barrier layer (c) Test structures with TiN diffusion barrier layer. . . . .	89
6.1 Continued. . . . .	90

Figure	Page
6.2 Resistance change observed for devices subject to varying current stressing conditions at a fixed test temperature $T = 275\text{ }^{\circ}\text{C}$ (a) Test structure with Ta diffusion barrier layer (b) Test structure with $\text{SiN}_x$ capping layer. . . .	92
6.3 Joule heating failure observed in the base layer with Ti (15nm) and Ta (5nm) (a) Optical image of failure location (b) Resistance change observed during testing. . . . .	94
6.4 Joule heating failure observed in Al. . . . .	95
6.5 SEM images of the cathode end of test specimens after testing at $T = 275\text{ }^{\circ}\text{C}$ and $j = 3 \times 10^6\text{ A/cm}^2$ (a) Test Structure with TiN diffusion barrier layer (b) Test Structure with $\text{SiN}_x$ capping layer (c) Test Structure with Ta diffusion barrier layer. . . . .	97
6.5 Continued. . . . .	98
6.6 SEM images of the cathode end of test specimens after testing at $T = 200\text{ }^{\circ}\text{C}$ and $j = 3 \times 10^6\text{ A/cm}^2$ (a) Test Structure with TiN diffusion barrier layer (b) Test Structure with $\text{SiN}_x$ capping layer (c) Test Structure with Ta diffusion barrier layer. . . . .	98
6.6 Continued. . . . .	99
6.7 SEM images of the anode end of test specimens after testing at $T = 275\text{ }^{\circ}\text{C}$ and $j = 3 \times 10^6\text{ A/cm}^2$ (a) Test Structure with TiN diffusion barrier layer (b) Test Structure with $\text{SiN}_x$ capping layer (c) Test Structure with Ta diffusion barrier layer. . . . .	100
6.7 Continued. . . . .	101
6.8 EDS spectra of the hillock formation on the anode end of the line. . . . .	102
6.9 Surface texture of a blank Cu film before anneal. . . . .	103
6.10 Optical images of void length recorded for $10\text{ }\mu\text{m}$ wide Cu lines. . . . .	104
6.11 Measurement made in Image J for one of the test structures after an interval of testing. . . . .	105
6.12 Record of the length of voids as a function of varying test temperatures and fixed current density $3 \times 10^6\text{ A/cm}^2$ for different test structures (a) Test temperature $T = 200\text{ }^{\circ}\text{C}$ (b) Test temperature $T = 230\text{ }^{\circ}\text{C}$ (c) Test temperature $T = 250\text{ }^{\circ}\text{C}$ (d) Test temperature $T = 275\text{ }^{\circ}\text{C}$ . . . . .	106
6.12 Continued. . . . .	107
6.13 Interface motion in Cu lines of varying widths. . . . .	109



Figure	Page
6.14 Velocity recorded for different test structures at $j = 3 \times 10^6$ A/cm <sup>2</sup> and varying temperatures (a) Test structure with Ta diffusion barrier layer (b) Test structure with TiN diffusion barrier layer (c) Test structure with SiN capping layer. . . . .	109
6.14 Continued. . . . .	110
6.15 Velocity recorded for different test structures at $T = 275^\circ\text{C}$ and varying current densities (a) Test structure with Ta diffusion barrier layer (b) Test structure with SiN capping barrier layer. . . . .	112
7.1 Control volume (interface pillbox) with generalized field and fluxes. . . .	114
7.2 Schematic showing the definition of the normals to the interface and to the boundary of the interface subregion $\Gamma_s$ . . . . .	115
8.1 Log-linear fit to velocity data for different test structure at fixed current density $j = 3 \times 10^6$ A/cm <sup>2</sup> and varying temperatures (a) Test structure with Ta diffusion barrier layer (b) Test structure with SiN <sub>x</sub> capping layer (c) Test structure with TiN diffusion barrier layer . . . . .	131
8.1 Continued . . . . .	132
8.2 Plot of current density variation test data for the Ta and SiN diffusion/cap layer structures. . . . .	133
8.3 (a) Sandwich specimen test schematic [112] for a four point bend test, (b) Schematic of the cross-section of a sandwich specimen test structure [114].	136
8.4 Results for steady state energy release rate obtained through four point bend tests on sandwich specimen tests by Lane et al. [23]. . . . .	138
8.5 Results for steady state energy release rate obtained through four point bend tests on sandwich specimen tests. [114] . . . . .	138
8.6 (a) Film stack used for four point bend experiments by Birringer <i>et al.</i> (b) Fracture energies and yields reported for different test configurations [115].	139
9.1 Super layer test (a) Schematic of test strips with sacrificial layer [116] (b) Delamination observed for Ti-Cr strips with different apex angles for the release layer [116]. . . . .	141
9.2 Schematic of bilayer film with residual stresses [116]. . . . .	142
9.3 Schematic for fabrication of super layer test structures . . . . .	144
9.4 Premature peeling observed in the thin film after deposition. . . . .	146
9.5 Cracking and premature debonding in films with a superlayer. . . . .	146

Figure	Page
A.1 Schematic drawing of heterogeneous adhesive beams (a) Thickness enhancement (b) Material enhancement. . . . .	163
A.2 Schematic drawing heterogeneous film under peel. . . . .	164
A.3 Experimental results from [131] and FEM simulation results compared for two cases with thickness-enhanced and material-enhanced heterogeneous film undergoing peel (a) $D_s/D_c = 8.8$ (b) $D_s/D_c = 2.0$ . . . . .	167
A.4 Schematic drawing of debonding adhesive beam on an elastic foundation under peel loading. . . . .	169
A.5 The bilinear cohesive zone model. . . . .	170
A.6 Different stages of crack propagation in the heterogeneous adhesives. . .	175
A.7 Schematic drawing of bending deformation in a cantilever beam (a) Uniform cantilever beam (b) Adhesion-free portion of heterogeneous strip. .	176
A.8 Schematic drawing for two states of beam before and after unstable crack propagation. . . . .	182
A.9 FEM simulation v.s. Semi-analytical solution for two different bending rigidity ratios (a) $D_s/D_c = 8.8$ (b) $D_s/D_c = 2.0$ . . . . .	183
A.10 Peel force changing with crack tip location under different bending rigidity ratio and loading conditions. . . . .	184
A.11 Variation of force and extra bending moment during unstable crack propagation. . . . .	186
A.12 Energy or work changing with crack tip location under different loading conditions (a) Force-controlled loading (b) Force-controlled loading. . . .	187
A.13 Strain energy and cohesive energy along crack tip. . . . .	189
A.14 Damage zone size changing with crack tip location. . . . .	190
A.15 The effect of cohesive parameter ( $\sigma_{max}$ ) on peeling performance of heterogeneous strip (a) Peel force changing with peel displacement. (b) Strain energy changing with crack tip location (c) Cohesive energy changing with crack tip location. . . . .	192

## ABSTRACT

Singh, Yuvraj Ph.D., Purdue University, August 2019. Characterization of Interfacial Energy of Thin Films through Current Induced Diffusive Interfacial Voiding . Major Professor: Ganesh Subbarayan, School of Mechanical Engineering.

Electromigration in thin films is a well known failure mode for scaled microelectronics. While our understanding of electromigration physics has improved immensely in the last few decades, there are still some gaps in literature. In particular, the influence of interfaces on the mass transport rate is not well understood. Through reliability studies conducted on passivated metals films, marked improvement in electromigration lifetimes was observed. Specifically, some choices of materials for passivation appear to perform better than others. Qualitatively this improvement in electromigration performance is attributed to surface adhesion. However, a theoretical connection is largely missing in the literature. Lane *et al.* through *in-situ* electromigration experiments and separate interfacial debond experiments on sandwich specimens showed that a correlation exists between the void growth rate and the debond energy. However, a fundamental understanding of the relation between the two is missing. In this study we explore the connection between interfacial adhesion and void growth in a current driven system. Several experiments with varying test conditions are carried out on Blech-like test structures with different capping layers. The influence of these capping layers is captured through direct void growth measurements. Comparison of activation energy associated with electromigration was made against existing literature. It was found to be consistent with values reported for surface/interface dominated diffusion mechanisms. Further, an extension is proposed to the phase growth relations derived in existing literature to include the effect of surface adhesion. Interfacial adhesion energy ratios are extracted from the electromigration experiments for two of the test structures (Cu-Ta and Cu-SiN<sub>x</sub>) tested in this

study. This ratio is compared to values reported in literature for the two interfaces and they are in good agreement.

## 1. INTRODUCTION

### 1.1 Motivation

Adhesion at a heterogeneous interface is a subject of growing interest with a wide variety of engineering applications [1–6]. Applications include paints and coatings, microelectronics and metal-plastic interfaces among others.

This thesis is aimed at studying heterogeneous interfaces in microelectronic devices. Fig. 1.1 is a demonstration of some instances of interfacial failure in microelectronic devices. Some of the well documented failure modes for thin films are the "telephone cord" type buckling phenomena due large compressive residual stresses [7–9], straight sided [10, 11], circular blisters [11, 12], debonding/cracking under applied external loads [13, 14] and electromigration induced failure [13, 15–17]. The non-electromigration failures are a result of mechanical stress at the interfaces however current provides the driving force that overcomes the interfacial adhesion during electromigration. Often the approach used to mitigate these failures is to roughen the surface to enhance mechanical interlocking at the interface, add adhesion promoters or introduce diffusion barriers if the failure is accompanied by phase transformation. As a last resort, the material itself may be changed. However, this approach is usually arbitrary and involves extensive parametric studies that may be time consuming.

To characterize the strength of these interfaces, several methods are proposed in prior literature. Methods such as the peel test [1], superlayer tests [19], indentation [20], scratch test [21] and bulge test [22] are some of the more popular methods. While these methods are well established, they have some disadvantages in terms of length scale, surface finish requirements, sample preparation and fixturing. Most significantly, the materials we are interested are ductile in nature. They tend to deform plastically upon loading. During peel, scratch, blister or indentation, the

interface in film is subjected to stresses beyond their yield strength causing them to plastically deform. It becomes challenging to distinguish between the work of adhesion at the interface and the work done in plastically deforming the films. Other challenges associated with the conventional methods are limitations on length scale of the films under consideration and the fixturing for each of these tests. Often these tests end up being more qualitative in nature. Though a qualitative measure of adhesion may be suitable in some instances, quantitative measure of interfacial fracture toughness is desired for studies that extend to reliability of the device.

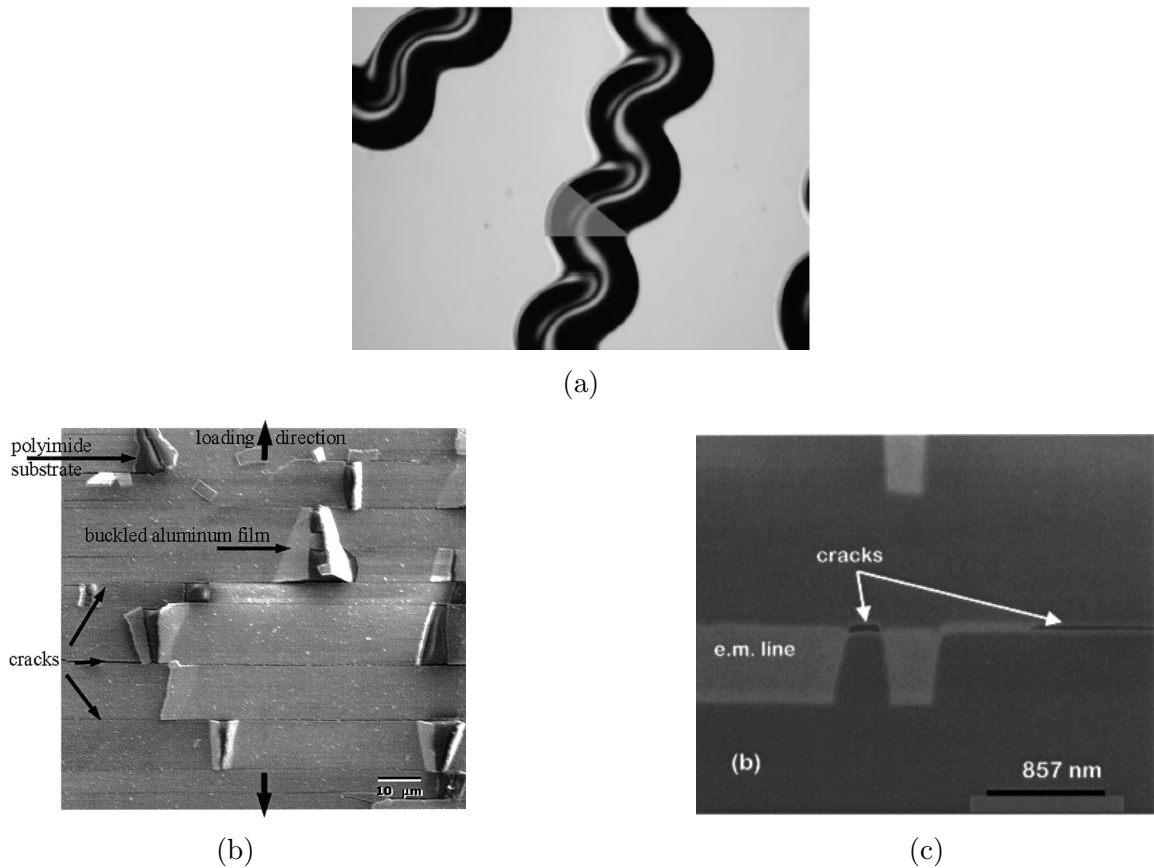


Figure 1.1. Examples of thin film debond (a) Telephone cord buckling in thin film [9] (b) Micrographs of failure in Al thin films on a flexible substrate under externally applied tension [13] (c) SEM micrograph of failure in a copper damascene line after electromigration [18].

## 1.2 Research Objective

In light of the challenges associated with characterization of adhesive strength at a heterogeneous interface, a new technique based on experimental observation by Lane *et al.* [23] on void growth in metal lines during electromigration is proposed. Revisiting the study by Lane *et al.*, we see in Fig. 1.3 the two axes correspond to information obtained through two separate experiments. The void growth rates are obtained through in-situ electromigration experiments and the fracture toughness is obtained through standard four point bending tests on diffusion bonded sandwich specimens. Briefly, electromigration is the phenomena observed in conductive films where the flow of electrons causes the atoms/ions to diffuse in order to conserve momentum. In conductors such as Cu, the diffusion path is found along the interface [24], and more importantly, the adhesion at the interface is believed to control the diffusion at the interface [23,25]. The experiments carried out by Lane involved line-via-line structures with different capping layers. Fig. 1.2b shows the SEM images of the moving metal edge at different times when the structure is subjected to a high current density. It was observed that the rate at which void grow changes under the influence of a cap material. Adding a cap layer to the conductive lines changes the surface energy, which in turn affects nucleation and growth kinetics for voids. Lane hypothesized that the relationship between these two quantities is dependent on the free energy of formation of the interfacial bonds. Further, he argues that the work of adhesion linearly varies with activation energy, leading to a correlation. This however, was found not be the case in our experiments. While the correlation provides some insight about the nature of the relationship between adhesion and mass diffusion, it fails to explain the underlying physics.

Recently Vaitheeswaran *et al.* [26] developed a theoretical framework to study the thermodynamic driving force associated with a moving interface. Conditions for phase growth and nucleation in bodies with multiple diffusing species and arbitrary surface stress at the phase interface were derived without inherent assumptions. The growth

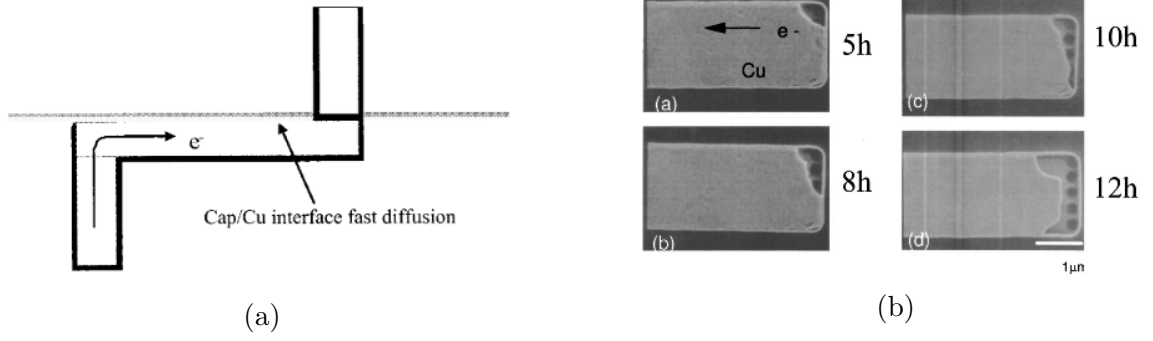


Figure 1.2. (a) Schematic of the line-via-structure [23] (b) SEM micrographs of a moving metal edge in a conductive line subject to electromigration [23].

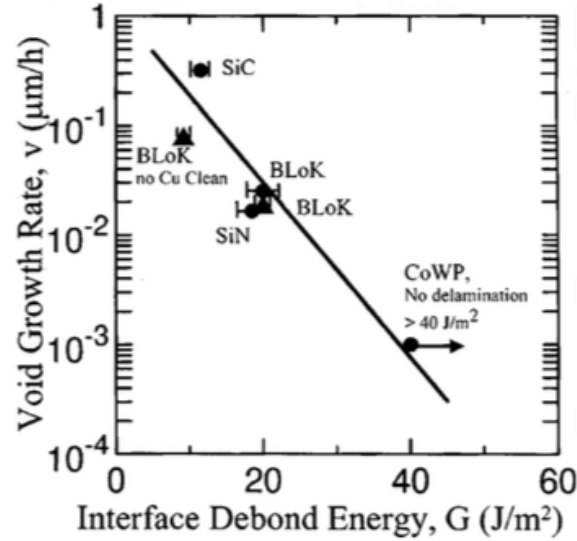


Figure 1.3. Void growth rate as a function of interfacial debond energy [23].

of voids is typically attributed to the coalescence of vacancies, which is dependent on the magnitude of bulk diffusion flux of vacancies [27]. Prior work does not include the effect of interfacial energy on the void growth rates. However, experimental evidence from [24,25] suggests that there is a relationship between the surface energy and the diffusion of species. The driving force (configurational force) for a diffusive system is used to derive a relation for a diffusive phase (void) growth. The derived relation is a consequence of the second law of thermodynamics valid at the interface. In this thesis,



we discuss an extension to this derivation for the case of electromigration by choosing an appropriate form for the driving force in a current driven diffusive system. Further, an analogy to fracture mechanics is drawn, where the computed J-integral [28] has to exceed a critical value for a steady state crack growth. Similarly, for the diffusive void growth, the critical volumetric energy density needs to be exceeded. A relation is derived for the critical volumetric energy density that includes the effect of interfacial adhesion.

The focus of this research is to characterize the interfacial adhesion energy using current induced diffusive voiding. As mentioned earlier, there is evidence from prior work that the connection exists, but, the use of electrical current induced voiding as a means to extract adhesion properties of thin films has not been explored in prior literature. From experiments carried out at varying test temperatures and current densities we obtain the void growth rates from fabricated Blech like test structures. The test structures used for this study are designed to allow ex-situ and in-situ measurements. Blech like structures are designed to eliminate multiple failure modes usually observed in line-via-line structures. TiN is used as a diffusion barrier layer for the base and three different capping materials are chosen for this study. Through the theoretical framework, we derive a relationship between diffusive void growth rate, which depends on the interfacial adhesion energy between the conductor and the capping layer. The additional benefit of this method of passing current through conductive lines is that these conductive lines can be buried, which is representative of their application in microelectronic devices. There is also no restriction on the rigidity of the substrate. The same test can be carried out on a conductive line on a flexible substrate as long as the state of stress on the conductive line can be measured.

### 1.3 Thesis Outline

We start with a survey of the relevant literature on electromigration and describe the factors that affect electromigration behavior in Chapter 2. We specifically include

work by Blech that is used as an inspiration for the test structures designed in this study. Next, we rationalize the choice of the test structure design and the materials choices for this study in Chapter 3. Prior work on relevant existing literature is briefly discussed for void growth measurements in-situ. We also present numerical simulations of the joule heating expected in the test structures. With the design for the test structure, in Chapter 4 we discuss the fabrication methods, process flow and the challenges encountered. Details of overall strategy for fabrication is presented along with the final design of the test specimens. Chapter 5 discusses the custom designed tester development and capabilities that enable measurements and observations made during the study. A set of design requirements are laid out and the final design of the tester is presented. The chapter ends with a discussion of the experimental procedure used, the tests that are to be carried out and the preliminary measurements that are required on the films. The results and observations are presented in Chapter 6. Resistance changes with time, void growth rates and the microstructure of the films are discussed in this chapter. Next, the theory developed by [26] is reproduced in a condensed version in Chapter 7. The derivation of interfacial transport theorem is followed up by the balance of mass, momentum and energy at the interface. Taking the free energy imbalance leads to the second law conditions from which nucleation and growth relations for phase transformations are derived. An extension to this theory that includes charge balance at the interface is proposed to study cases with electromigration. An updated relation for the thermodynamic driving force (configurational force) is then used to extract the surface energy for the interfaces being tested. The driving force required to nucleate and grow voids at heterogeneous interfaces is related to the energy release rate and compared to the existing definition of fracture toughness and the J-integral. Chapter 8 is dedicated to analysis and extraction of surface energy from obtained data. The extracted surface energy is then compared to reported values in literature. We end with a some insights about the nature of the study and future work is proposed. Chapter 9 describes attempted experimental validation of the proposed characterization technique using super layer tests as proposed

by Bagchi. The test method, fabrication process used and the challenges encountered with fabrication are discussed in this chapter. The fabrication of the devices was not successful and so we rely on existing literature for validation. We end with the conclusions and future work in 10

The appendix includes related work published recently [29] on a semi-analytical model to capture instability at a heterogeneous interface during peel tests. Though not directly related to the primary thrust of this thesis on relating adhesion to electromigration experiments, the included work is related to interfacial adhesion for films. This work is focused on modeling peel force required to debond patterned films. The novelty of this work is the ability to model the instability encountered at the interface for the patterned films. It also provides a way to enhance fracture toughness without modifying the interface, which is ideal for applications where interfaces cannot be modified.

## 2. BACKGROUND: ELECTROMIGRATION

This chapter pertains to a review of existing literature on electromigration. Electromigration is a significant reliability concern in microelectronics with several decades of research dedicated to studying lifetimes for different metallizations, use conditions and design features. Our goal therefore is to conduct a preliminary search to identify prior work to determine the fundamental physics associated with the process of electromigration relevant to this work.

### 2.1 Review of Electromigration

Electromigration is defined as the mass transport of atoms/ions due to the momentum exchange with moving electrons in a current carrying conductor. Geradin in 1861 [30] first observed the segregation in molten alloys subject to direct electric currents. It wasn't until 1914 when Skaupy [31] found the interaction between metal atoms and electrons to describe the physical phenomena. Seith and Wever [32] through tracer experiments on Hume-Rothery alloys found the direction of the electrons to have an influence on electromigration. These marker motion experiments revealed that the driving force for electromigration was not solely influenced by the electrostatic force from the applied electric field, but also strongly depended on the direction of motion of the electrons. As a result of these empirical observations they concluded that flowing electrons transferred momentum to atoms causing mass transport. This study further cemented the idea originated by Skaupy of an "electron wind" as the driving force for electromigration. The idea of the "electron wind" as a momentum transfer driving force causing mass transport in metals subjected to an electric field established the theoretical foundation for electromigration. Fiks, Huntington and Grone [33,34] followed this up with mathematical descriptions of the

electromigration driving forces. Their electromigration driving force model was formulated from a semi-classical ballistic approach to explain the collision of the charge carriers with the metal ions to induce mass transport. According to this ballistic model, the electromigration driving force ( $F_{em}$ ) is composed of two distinct contributions. The first component comes from the interaction of the electric field with the charge of the migrating ion called the direct electrostatic force ( $F_{es}$ ). The second is due to the momentum transfer from flowing conduction electrons colliding with the metal ions, and is called the electron wind force ( $F_{wd}$ ). Therefore, the total effective electromigration driving force is expressed as:

$$F_{em} = F_{es} + F_{wd} = Z_{eff}^* e E = (Z_{es} + Z_{wd}) e E \quad (2.1)$$

where  $Z_{es}$  and  $Z_{wd}$  are the charge numbers corresponding to the metal ion and the electron wind.  $e$  is the charge of an electron, and  $E$  is the electric field.  $Z_{eff}^*$  is the combined effective charge number that is dimensionless. Microscopic and quantum mechanical effects of the electromigration phenomenon are comprised in the effective charge number. Typically the values reported in literature are theoretically derived or measured experimentally through marker motion studies.

The force  $F_{es}$  due to the interaction between the ionic core of the atoms and the electric field is directed toward the negative electrode terminal and is not strongly dependent on the temperature. For most metals, the  $F_{es}$  force is negligible in comparison to the  $F_{wd}$  force that is acting in the opposite direction toward the positive terminal. This electron wind force is reported to be an order of magnitude greater than the electrostatic force for gold, copper and aluminum [35]. This idea of electromigration is based on vacancy diffusion as the dominant mechanism in a metal lattice. However, it should be noted that similar biased atomic diffusive motion under an electric field occurs predominantly at grain boundaries and interfaces in thin metal films. Diffusion is a non-equilibrium process, and it occurs until a thermodynamic equilibrium is achieved. It is possible to relate the rate of diffusion to the concentration gradient responsible for the mass transport [36]. Vacancies flow from

regions of high concentration to regions of low concentration. According to the first Fick's law, the flux of vacancies  $J_v^d$  is proportional to the gradient of the vacancy concentration  $C_v$  as follows

$$J_v^d = -D_v \nabla C_v \quad (2.2)$$

$D_v$  is a diffusion coefficient. Electromigration is a highly temperature dependent process. The temperature dependence is captured through an arrhenius relationship for diffusivity. Here diffusivity  $D_v$  is expressed as:

$$D_v = D_o \exp\left(\frac{-E_a}{kT}\right) \quad (2.3)$$

Where,  $D_o$  diffusion coefficient,  $E_a$  is the activation energy related to the diffusion process,  $k$  is the Boltzmann's constant and  $T$  is the test temperature. The driving force from electromigration gives rise to a velocity component which is expressed as:

$$v_d = M F_{em} = Z_{eff}^* e \rho j \frac{D_o}{kT} \exp\left(\frac{-E_a}{kT}\right) \quad (2.4)$$

$M$  is the atomic mobility. The electric field  $E$  is expressed in terms of the resistivity  $\rho$  and the current density  $j$ . Typically the atomic mobility is expressed by the Nernst-Einstien relation where,

$$M = \frac{D}{kT} \quad (2.5)$$

where  $k$  is again the Boltzmann's constant, while  $T$  is the test temperature. The vacancy flux due to electromigration then is expressed as:

$$J_v^{em} = \frac{D_v C_v}{kT} Z_{eff}^* e \rho j \quad (2.6)$$

The net flux of vacancies is the superimposition of the vacancy flux due to diffusion and the vacancy flux due to electromigration.

These are typically opposing fluxes so, the total flux is given as:

$$J_v = J_v^d + J_v^{em} = -D_v \nabla C_v + \frac{D_v C_v}{kT} Z_{eff}^* e \rho j \quad (2.7)$$

### 2.1.1 Effect of Microstructure

Microstructure has an important role to play during electromigration specially for scaled microelectronics where smaller lines and structures have a larger surface area to volume ratio. Mass transport along a current carrying conductor occurs through a few different mechanisms; surface, interface, grain boundary and lattice diffusion. The onset of each of these mechanisms is usually captured through a measurement of an activation energy associated with each diffusion mechanism. To account for the multiple diffusion mechanisms a proposed method is to sum the contributions from each mechanism as follows [24, 37, 38]:

$$D_{eff} = D_b + \sum_j^n D_{gb,j} \left( \frac{\delta_{gb,j}}{d} \right) + D_i \left[ 2\delta_i \left( \frac{1}{w} + \frac{1}{h} \right) \right] + D_s \left( \frac{2}{w} + \frac{1}{h} \right) \quad (2.8)$$

$D_{eff}$  is the effective diffusivity and the subscripts  $b, gb, i$  and  $s$  refer for bulk, grain boundary, interface and surface diffusivities.  $\delta$  is the width of the grain boundary while,  $w$  and  $h$  are the width and height of the conducting line. Fig. 2.1 is a schematic of diffusion paths available for mass transport. Bulk and pipe diffusion are not shown in this schematic. Typically bulk diffusion is ignored if the homologous temperature is low. Through self diffusion studies on copper it is shown that below 400 ° C, bulk diffusion can be ignored due to it's high activation energy which is  $\approx 2.2$  eV [39]. Grain-boundary and surface/interface diffusion are then the remaining dominant diffusion mechanisms. As such the effective diffusivity is then:

$$D_{eff} = \sum_j^n D_{gb,j} \left( \frac{\delta_{gb,j}}{d} \right) + D_i \left[ 2\delta_i \left( \frac{1}{w} + \frac{1}{h} \right) \right] + D_s \left( \frac{2}{w} + \frac{1}{h} \right) \quad (2.9)$$

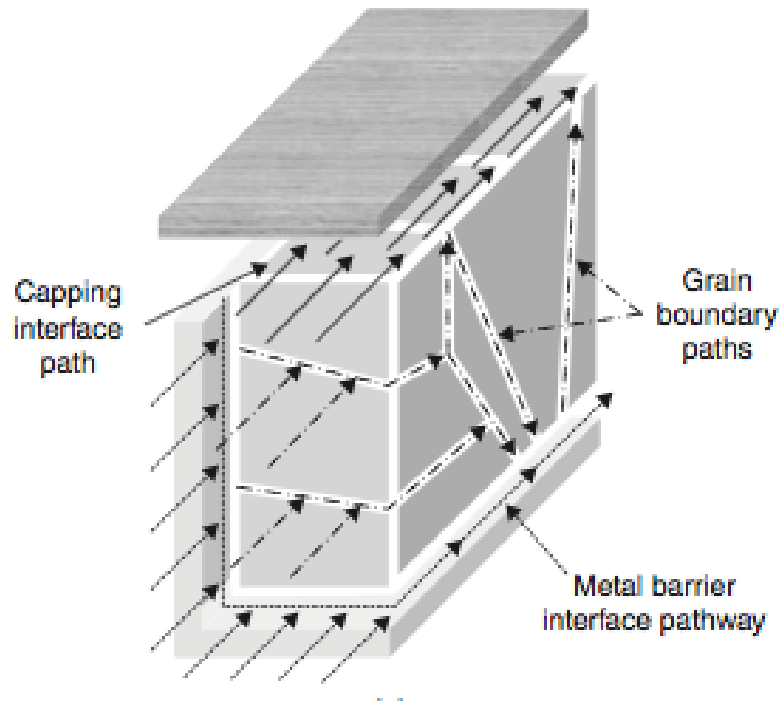


Figure 2.1. Schematic of diffusion paths for atoms in a micro volume [40].

When the geometry is scaled and lines shrink; the grain structure is more “bamboo-like”, with one or two grains spanning the width of the line. In such a scenario mass transport through grain boundary diffusion is limited and interface diffusion becomes the dominant mechanism. An example of such behavior is shown for Aluminum in Fig. 2.2, where the median time to failure is much higher compared to a polygrain structure. This is because of the lack of continuous grain-boundary paths and the fact that the electromigration driving force is perpendicular to the grain-boundaries. If the conductor is then encapsulated or has an interface, the primary path for diffusion is through the interface. For copper there is evidence in literature to show that the surface/interface migration is the dominant path for diffusion in small interconnects [24]. This can be incorporated into Eq. (2.4) for an updated relation:



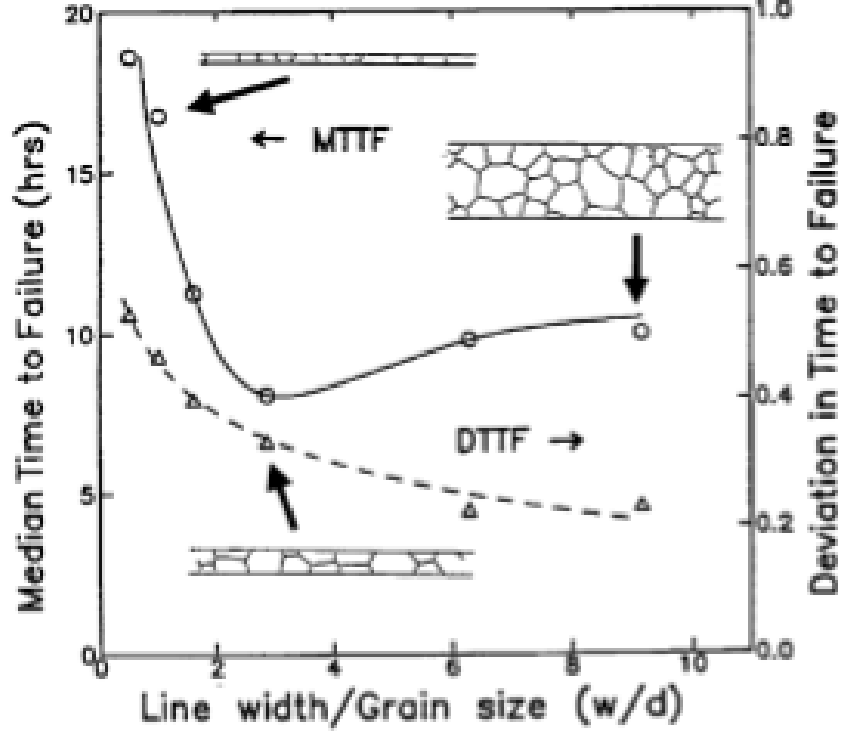


Figure 2.2. Median Time to Failure for Aluminum interconnects with varying microstructures [41].

$$v = Z_{eff}^* e \rho j \frac{D_{eff}}{kT} \exp\left(\frac{-E_a}{kT}\right) \quad (2.10)$$

$$v = Z_{eff}^* e \rho j \frac{D_i \left[ 2\delta_i \left( \frac{1}{w} + \frac{1}{h} \right) \right]}{kT} \exp\left(\frac{-E_a}{kT}\right) \quad (2.11)$$

An illustration of such behavior is shown in Fig. 2.3 where, multiple voids are observed to grow along a line-via-line structure. Grains can accumulate vacancies at different rates and one location may be thermodynamically more favorable for void evolution compared to others. At smaller length scales the local microstructure may play a more critical role where reliability statistics are concerned. In the absence of grain boundary diffusion the only path available for diffusion is through the interface/surface which may be limited. Prior work on reliability studies suggest longer

lifetimes for such structures but also more variability in the location of failure. At larger length scales, a continuum approach may suffice where average behavior among many grains is assumed.

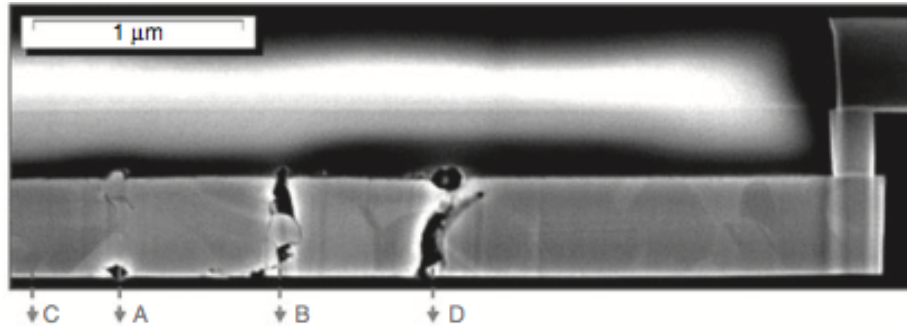


Figure 2.3. Void nucleation and growth sites in a line-via-line structure where grain boundaries span the width of the interconnect [42].

### 2.1.2 Geometric Effects on Electromigration

We have established that the grain size on the order of the width of a conducting line can suppress grain boundary diffusion leading to better electromigration performance. However, there are other factors to consider. Seminal work by Blech [15,43,44] on aluminum conducting lines led to significant breakthroughs in the understanding of electromigration. We will now briefly cover the experiments carried out and the modification to the flux equation to account for the observations. The experiments carried out by Blech involved aluminum lines of varying lengths on a secondary layer of Titanium Nitride (TiN). A schematic of the test structure is shown in Fig. 2.4. The purpose of the secondary layer is to act as a parallel conductor, which has a lower electrical conductivity compared to Aluminum. It also serves as a diffusion barrier for Aluminum. Owing to the lower conductivity of the base layers, most of the current would flow through the Al line during the experiment. As the experiment progresses, metal ions are carried towards the anode while a visible line drift is observed on the cathode side due to vacancy accumulation and void formation. The drift is measured

as a function of the current density ( $j = \frac{i}{A}$ ). The first observation Blech made was that the cathode end only moved if the line was a certain minimum length. Shorter lines did not move or moved very little compared to a longer line for a fixed current density. He attributed this observation to the existence of a “back-flow” stress. This stress is generated due to the pile up of atoms at the anode end of the conductor. Release of stress at the anode end leads to formation of hillocks or extrusion of material that can cause failure in the form a short-circuit. He hypothesized that if a stress gradient develops along the length of the conductor, then a force acts opposite to the electron wind force described earlier. Revisiting the flux of vacancies due to electromigration Eq. (2.6) we introduce a second term with an opposing sign that accounts for the stress gradient driving force. Consider the flux of vacancies which is equal and opposite the flux of atoms:

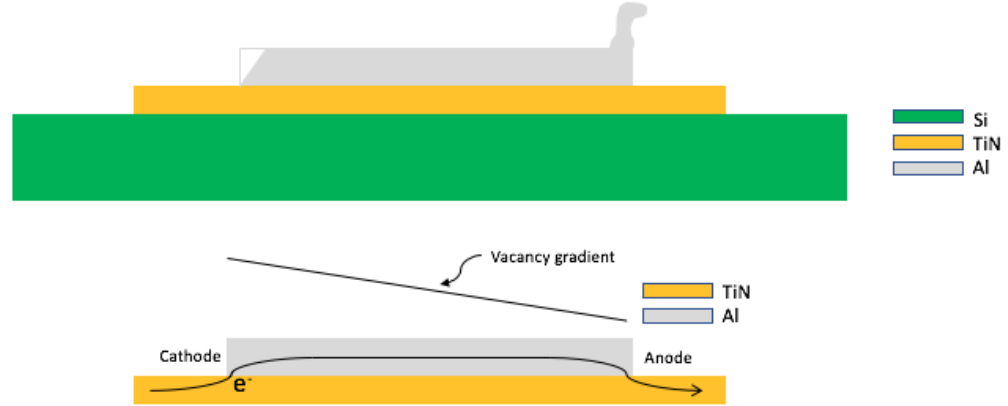


Figure 2.4. Schematic depicting the cross-section of the structure used by Blech.

$$J_c^{em} = \frac{D_c C_v}{kT} \left[ Z_{eff}^* e \rho j - \Omega \frac{\Delta \sigma}{\Delta x} \right] \quad (2.12)$$

where,  $\Omega$  is atomic volume and  $\sigma$  is the hydrostatic stress which varies along the length  $x$ . At equilibrium, when mass transport is halted, the flux of vacancies moving

is zero. At the steady state condition, the electromigration driving force is equal and opposite to the force due to the back flow stress.

$$J_v^{em} = 0 \quad (2.13)$$

$$Z_{eff}^* e \rho j = \Omega \frac{\Delta \sigma}{\Delta x} \quad (2.14)$$

Further rearrangement of the equation leads to a critical threshold, which we will refer to as the “Blech Threshold” going forward. It is the product of a critical current density  $j_c$  and a length  $L$ . This product is unique to the material tested. For a given current density a line can be “immortal” to electromigration failure if the Blech Threshold for the given geometry is lower than the experimentally determined value. We will use this as a guide for designing our test structure in this study.

$$j_c L = \Omega \frac{\Delta \sigma}{Z_{eff}^* e \rho} \quad (2.15)$$

There is some variation in the reported Blech Product values in literature for a given conductor. The presence of a residual stresses from the fabrication process could cause this variation leading to smaller Blech product value, which will fail prematurely [45].

Though the idea of a back-stress was proposed by Blech as the cause of a delayed failure event, the nature of this back stress was not clear until Kirchheim’s work [46]. He included the effect of a transient back stress build-up in a single model. Considering the movement of an atom, with an atomic volume  $\Omega_a$ , from the grain boundary to the surface, the relaxation of the neighboring atoms within the grain boundary leads to a volume contraction of  $f\Omega_a$  around the formed vacancy. The total volume change due to lattice relaxation is  $(1 - f)\Omega_a$ , where  $f$  is the relaxation factor which represents the ratio between the vacancy volume and the atomic volume. The local strain field due to a vacancy formation at the lattice site leads to a stress.

The gradient of the mechanical stress acts as an additional driving force in the total vacancy flux equation as follows:

$$J_v = J_v^d + J_v^{em} + J_v^\sigma = -D_v \nabla C_v + \frac{D_v C_v}{kT} Z_{eff}^* e \rho j - \frac{D_v C_v}{kT} f \Omega_a \nabla \sigma \quad (2.16)$$

A generalization of the Fick's second law of diffusion along with appropriate sink and source terms are then utilized to derive a relation between the equilibrium vacancy concentration and the mechanical stress  $\sigma$ :

$$C_{v,eq} = C_{v,o} \exp \frac{(1-f)\Omega\sigma}{k_b T} \quad (2.17)$$

$C_{v,o}$  is the initial vacancy concentration in the absence of a stress. The stress change in a due to a volume change by  $dV$  as given by the Hooke's law is as follows:

$$d\sigma = B \frac{dV}{V} \quad (2.18)$$

where  $B$  is the bulk modulus. The relation for the evolution of stress can then be derived in conjunction with the equilibrium vacancy concentration equation as follows:

$$\frac{\partial \sigma}{\partial t} = B(1-f)\Omega_a \frac{\delta}{d} \frac{C_{v,eq} - C_v}{\tau_v} \quad (2.19)$$

Here,  $d$  is the grain diameter and  $\delta$  is the boundary thickness. Coupling of the stress evolution and vacancy concentration dynamics in this manner helped explain the origin of the stress development during electromigration.

### 2.1.3 Electromigration Lifetimes

To earliest work on electromigration lifetime predictions is a model proposed by Black in 1960's [47]. Black derived a semi-empirical model for interconnects un-

dergoing failure due to a steady state direct current using the model developed by Huntington and Grone [48]. The mean time to failure (MTTF) relation derived by Black is as follows:

$$MTTF = A \frac{1}{j^n} \exp\left(\frac{E_a}{kT}\right) \quad (2.20)$$

where, A is pre-factor constant, j is the current density and n is the current density exponent. Two critical parameters, the current density exponent and activation energy are extracted by regression from the measured times to failure (TTF). Usually, the current density exponent is considered to be 2. This was later modified by Blair [49] in the form presented in Eq. (2.20). The most plausible explanation for the exponent being 2 was given by Shatkeez and Lloyd [50]. The model solves a time dependent diffusion equation and finds a solution for the MTTF in which the square power dependence was obtained. This was due to the nucleation of voids which needs a supersaturation of vacancies on the cathode side. The incubation time of nucleation is much longer than the time needed to grow a void. While the number of vacancies needed to nucleate an embryo of a critical size is small, the supersaturation of vacancy can be a slow and long process. Additionally, a large number of vacancies can be consumed by sinks before supersaturation can occur. For growth of a void then, the exponent is close to unity and is expressed as:

$$t = B \frac{1}{j} \exp\left(\frac{E_a}{k_b T}\right) \quad (2.21)$$

Here, B is a pre factor usually expressed as  $\frac{V k_b T}{\Omega C D_o Z^* \rho}$ , with V being the volume of the void needed for the circuit to fail. Often, the time for nucleation and the time for void growth is superimposed to describe life under an accelerated test condition.

In most cases the extrapolation of life for a tested device is based on a lognormal fits of the form:

$$F(t) = \int_t^0 \frac{1}{\sqrt{2\pi}\sigma u} \exp\left[\frac{[\log(u) - \log(MTTF)]^2}{2\sigma^2}\right] du \quad (2.22)$$

Similarly the Weibull fit is given by the expression:

$$F(t) = 1 - \exp\left[-0.693 \frac{t^\beta}{MTTF}\right] \quad (2.23)$$

$F(t)$  is the cumulative percent failures at time  $t$  and  $\sigma$  is the standard deviation. Both MTTF and  $\sigma$  are found by plotting the experimental TTF data on a lognormal plot; the coefficient  $\beta$  is extracted from the Weibull plot. All these parameters are extracted from measurements on a variety of test structures designed for different metal layers and different current densities.

### 3. TEST STRUCTURE DESIGN AND MATERIAL SELECTION

In this chapter we discuss relevant background on existing test structures used in prior literature to study electromigration. We then provide an overview of the electromigration characterization in the existing literature where in-situ observations of void growth were attempted. Details for some of these tests and the test setup are discussed. Next, some challenges with the design are discussed along with the materials of interest for this study. Decisions relating to geometry are rationalized for the test structure. Finally, numerical simulations of joule heating expected in the test structure are presented.

#### 3.1 Background: Electromigration Test Structures

Electromigration as discussed in the previous chapter has become more relevant as a design challenge as the interconnects shrink to accommodate smaller form factors and higher density I/O packages. Most experimental studies in literature are concerned with time to failure (TTF). For this reason, we will separate the test structures into two categories. Belonging to first category are test structures and methods meant for TTF statistics that rely on accurate measurement of resistance during testing. These include test structures meant for classical resistometric method (CRM) [51], temperature-ramp resistance analysis to characterize electromigration (TRACE) [52], the breakdown of energy of metal method (BEM) [53], Standard Wafer-level Electromigration Acceleration Test method (SWEAT) [54] and wafer-level isothermal Joule heated electromigration test (WIJET) [55], Highly accelerated electromigration life-time test (HALT) [56]. While these experimental methods are useful for reliability they are usually focused on a particular technology and may suffer from multiple failure modes or locations. An example of such a case is shown in Fig. 3.1 where



multiple voids are observed in a line-via-line structure. Often time to failure is also based on some measure of resistance change, which is not standardized.

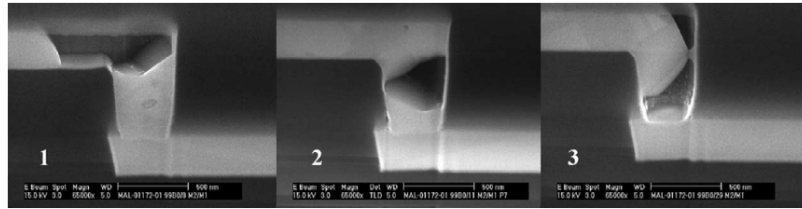


Figure 3.1. Void formation in line-via-line structure imaged post testing [57].

Second type of test structures are idealized ones that are meant to mimic metallizations and geometry in a manner that makes identification of failure locations and modes easier. “Blech” structures discussed in the Chapter 2 falls in this category. Another such design is a single line-via-line structure with a tungsten plug between the two levels of metallization. A simple structure of such a design is shown in Fig. 3.2. This type of structure along with the Belch structure is not limited to a resistance measurement. A velocity for a growing void can be measured using such structures through in-situ measurements.



Figure 3.2. A line-via-line schematic for a test structure with two layers of metallization.

Our focus in this study is not based on lifetime assessment for a particular technology, but, rather a fundamental understanding of electromigration failure and the factors that influence electromigration behavior. For this reason, we turn to idealized structures, where the geometry is simple and the modes of failure can be limited.

With this in mind, we first review test structures in the existing literature that have attempted in-situ electromigration characterization. We then revisit the test structure proposed by Blech [58] that uses a diffusion barrier layer to carry current in parallel to a conductor of interest. This structure is preferred over the line-via-line structures in the literature due its simplicity in design/fabrication. The structure also has the added advantage of low risk of failures that are exacerbated by joule heating. The barrier layer at the bottom of the Blech structure typically has a lower conductivity compared to the primary conductor and so, most of the current flows through the conductor when the strip of material to be tested is encountered. When a void is nucleated, it can grow without severely changing the local temperature, which is a drawback with the line-via-line structure. Once a void grows past the tungsten plug, the liner material, which is typically only a few nanometers, carries a large current and will eventually cause failure in the device.

### 3.2 In-situ Electromigration Testing

In-situ testing is preferred for this study because of the ability to track void growth during the experiment. Most of the electromigration tests in literature use buried devices to assess reliability. Void growth or regions of failure can only be determined post failure through carefully cross-sectioned test specimens or through X-ray tomography. Sometimes, these failures may not be apparent due to complex nature of the devices being tested or poorly cross-sectioned test specimens. As mentioned previously, for line-via-line structures failure may occur in multiple locations especially when the devices are scaled. If the position of these failures is not known apriori then finding the failure site may be a time consuming step. To overcome these obstacles, we will rely on in-situ observations either using a Scanning Electron Microscope or an optical microscope.

There is some existing work on in-situ observation of electromigration tests. Below, we list some of these studies along with the dimensions and the scope of the

study relevant to this work. Meyer *et al.* developed a custom built test rig in an SEM to conduct electromigration tests on line-via-line structures. Since the test structures used in this work are fully embedded a FIB (Focused Ion Beam) cross-section is required to make the observation in the SEM. Fig. 3.3 shows the structure, test setup and the observation from this study. Here, Cu is the interconnect with a Ta liner and the dielectric capping layer of PECVD -  $\text{Si}_3\text{N}_4$ . Details of the test structure are not clear from the paper. Test conditions are  $20 \text{ MA/cm}^2$  at  $250^\circ \text{C}$ .

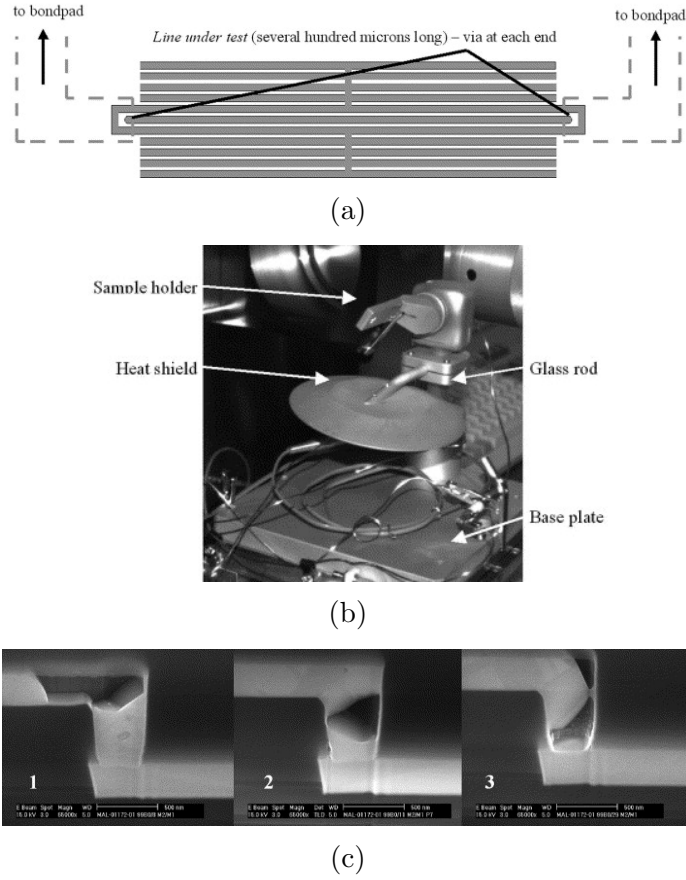


Figure 3.3. Details of (a) Test structure used in the study (b) In-situ test setup for SEM observations (c) Post failure FIB cross-section indicating void growth in line-via-line structures [57].

Vairagar *et al.* had a similar study with line-via-line structures based on the NIST recommendations for structure design [59]. Cu interconnects with Ta diffusion barrier

layer and  $\text{Si}_3\text{N}_4$  as a capping layer was used for this study. Similar to Meyer *et al.*, this study uses a FIB cross-section to track locate the failure site which is at the  $\text{Cu}/\text{Si}_3\text{N}_4$  interface at the cathode end. The test setup used is the same as the previous study. The current density used in this study is  $10 \text{ MA}/\text{cm}^2$  and the test temperature is  $350^\circ\text{C}$ . Fig. 3.4 shows the structure used and the observations made in this study.

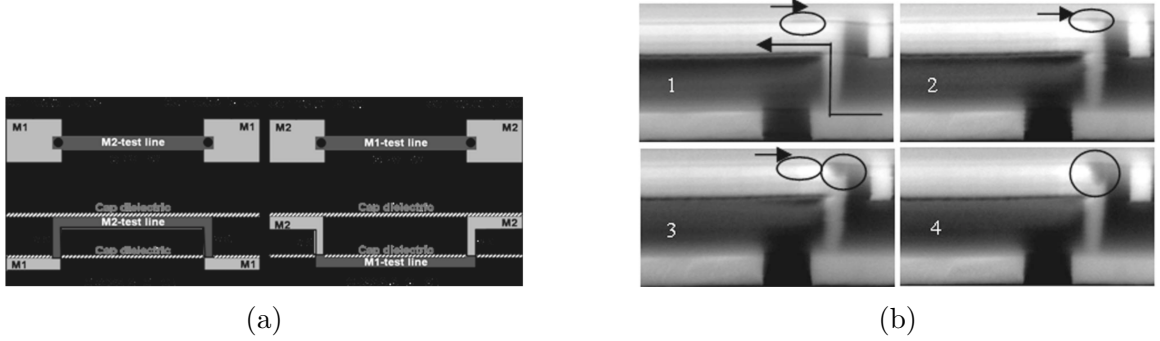


Figure 3.4. Details of (a) Test structure (b) Post failure FIB cross-section indicating void growth in line-via-line structure as a function of time [59].

Next, work by Lee *et al.* [60] on Cu and Cu(Sn) interconnects is also an in-situ electromigration study. This work is the closest in terms of design and procedure to the work in this thesis. Fig. 3.5a is a Blech like structure with a tungsten (W) base layer and Ta as the diffusion barrier layers. These tests were carried out at  $2.1 \times 10^6 \text{ A}/\text{cm}^2$  with test temperatures varying from  $250$  to  $400^\circ\text{C}$ . The focus of this study was to ascertain the benefits of tin (Sn) doping on Cu electromigration lifetimes without changing the liner or the capping materials. Fig. 3.5b is an image of the edge displacement recorded in a SEM over time for one of the experiments in this study. Unlike the studies by Meyer and Viaragar there is no need for a cross-section in this study.

The device fabricated by Kirimura *et al.* are shown in Fig. 3.6. The devices are damascene copper with different cap layers that are limited to  $30 \text{ nm}$  in thickness. This is so the void can be observed through the cap layer in an SEM. The penetration depth of the electrons from the e-beam depends on the accelerating voltage and the material that is encountered by the beam. The test setup involves a temperature

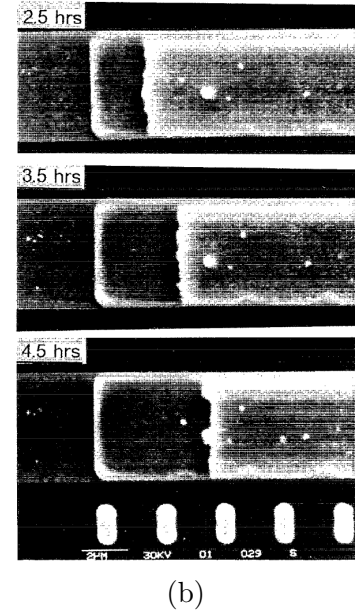
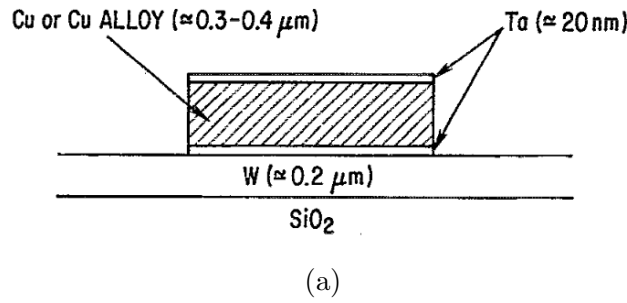


Figure 3.5. Details of (a) Test structure used by Lee *et al.* (b) Edge displacement captured by SEM during electromigration experiments [60].

controlled stage with nano-manipulators to supply the current. On the device there are local and standard probes to measure resistance accurately during the experiment.

The results from the study by Vanstreels, which are an extension of Kiri-mura's work are shown in Fig. 3.7. The voids are clearly visible just beyond the electron injector. Over time, the voids grow and their velocity is tracked. The results for drift velocity are shown in Fig. 3.7b.

We use guidance from these listed studies to determine needs from the test setup along with the advantages and disadvantages of each device structure and test setup. Other works not listed here, but, relevant to in-situ study of electromigration are cited in [61].

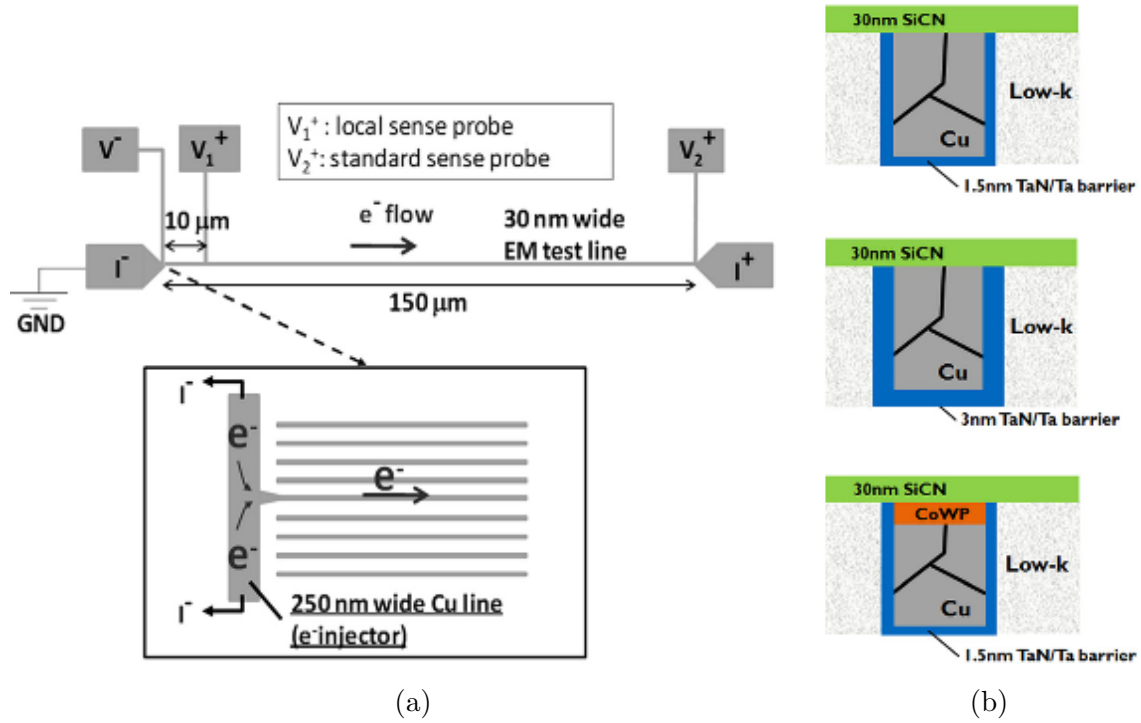


Figure 3.6. Details of (a) Top view of the EM structure used by Kirimura *et al.* (b) Cross-section view of the EM structure [62].

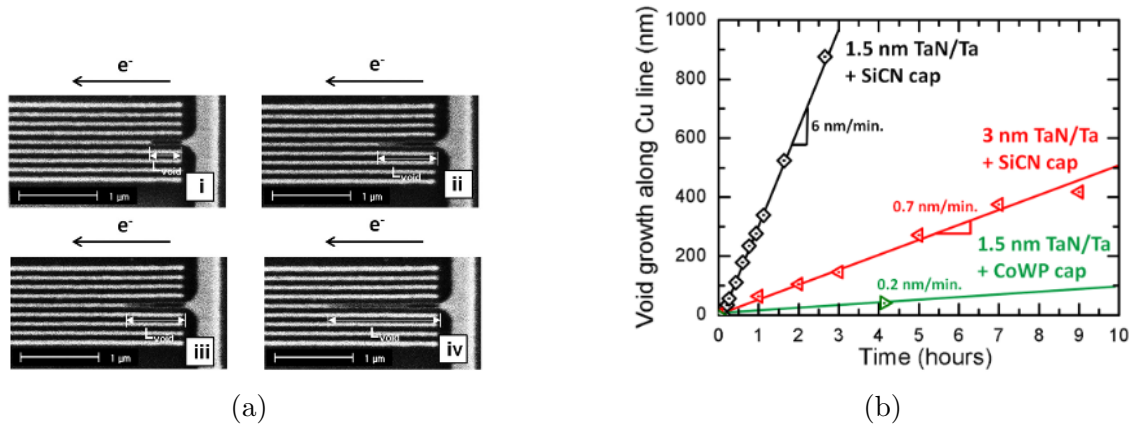


Figure 3.7. (a) Void evolution observed in the EM structure (b) Void drift velocity for different cap materials observed during In-situ experiments by Vanstreels *et al.* [63].

### 3.3 Material Selection

The earliest work on electromigration was carried out on aluminum (Al) and gold (Au). The push for materials of interest is generally a consequence of technology needs of the microelectronics industry. As a whole, the industry has moved from aluminum and gold interconnects to copper where it is feasible. Copper offers good electrical and thermal conductivity, which helps reduce RC delays and better thermal performance. In terms of plating and deposition, it is more convenient compared to silver (Ag). There are some disadvantages when it comes to passivation and processing of copper. Copper oxidizes easily and does not have the self passivation property of aluminum, which forms  $\text{Al}_2\text{O}_3$  that is limited to the surface. Noble metals do not oxidize and have a better corrosion resistance compared to copper. Copper is also stiffer compared to aluminum and gold which may lead to some reliability challenges for packaging, specially with 3-D integration that involves copper pillars and copper TSV (Through Silicon Via). Copper tends to diffuse through silicon dioxide ( $\text{SiO}_2$ ) that would cause device degradation. Therefore, a diffusion barrier is typically required between the copper interconnect and the dielectric layer to inhibit the migration of copper atoms. We will discuss this in more detail when we introduce diffusion barrier layers later in this chapter. Copper has a higher melting temperature (1357 K) compared to aluminum (933 K) and for typical ULSI (Ultra Large Scale Integration) circuits, copper interconnects outperform aluminum interconnects as they are subject to lower homologous temperatures [64]. This fact plays an important role when the resistance of copper to electromigration, thermomigration or stress migration is considered. In general, copper outperforms aluminum and gold in terms of electromigration lifetime, but, as the devices are scaled, microstructure also makes a significant difference to electromigration behavior.

In this study we prefer to focus on Cu because of its surface diffusivity. At temperatures  $< 350^\circ\text{C}$ , the diffusivity of Cu through the surface is several order of magnitude larger than the diffusivity through the grain boundaries. This will help

distinguish the influence of capping layers and diffusion barrier layers on the mass transport rate during electromigration.

### 3.3.1 Diffusion Barrier Layer

Diffusion barrier layers are a critical component of interconnects. In order for a material to be qualified as a diffusion barrier layer, it must meet certain criteria. Consider to materials A and B in contact, where A is a metal copper or aluminum and B is silicon, which is usually doped to meet some electrical performance requirement. Even though silicon would usually form a native oxide, it may not be enough to prevent atoms of aluminum or copper from diffusing through and altering the device performance. As a result, diffusion barriers are typically introduced between the materials A and B that physically separates the two. These materials are usually chosen so that the intermixing of A and B is suppressed under external conditions such as temperature, stress, and time. To qualify as a barrier layer, some criteria must be met. These are outlined by Nicolet [65] and are as follows:

1. Transport rate of A across X and of B across X should be small
2. Loss rate of X into A and B should be small
3. X should be thermodynamically stable against A and B
4. X should have good adhesion to A and B
5. Contact resistance at the interfaces should be minimal
6. X should be laterally uniform in thickness and structure
7. X should be resistant to mechanical stress and thermal stress
8. X should be thermally and electrically conducting

It is clear that all these conditions may not be met and there is some amount of compromise required to relax some of the needs. Even if an identified material meets



all the criteria, additional constraints may inhibit its applicability due to processing constraint during fabrication or cost of implementation to existing fabrication methods. An additional constraint imposed by our need is the requirement for the material to be resistant to electromigration.

A popular choice for diffusion barriers is refractory metals and their nitrides. Refractory metal nitrides are suitable owing to their high melting points, high thermal stability, and high conductivity (tunable) [66]. Refractory metals have good corrosion resistance and barrier properties, however, most of the challenges in implementation arise from fabrication limitations. We discuss this issue in detail with using tantalum as a barrier layer in a later chapter. Refractory metal nitride such as TiN, WN, ZrN, TaN and TiZrN are some that were tested as diffusion barrier layers in existing literature [66]. Among the refractory metal nitrides used on present day devices, currently, TaN is most popular. However, we will focus on TiN because of its versatility and sufficient barrier capabilities. A general method to check the viability of the diffusion barrier is to carry out XRD analysis to determine the highest annealing temperature at which the metal shows significant diffusion through for a known thickness of the barrier layer. Fig. 3.8 shows the XRD spectra of  $Cu/TiN/SiO_2/Si$  stack after annealing in the temperature range of 500 – 800 ° C for 60 minutes in nitrogen. This is work carried out by Kwak *et al.* [67]. The thickness of TiN is 100nm deposited using a sputtering process and the thickness of copper is 100 nm deposited using REPCVD (Remote Plasma Chemical Vapor Deposition). The XRD reveals the diffraction peaks of Cu and TiN for as-deposited, and annealed cases ranging 500 ° C to 800° C. At 700C, the Cu (111) and Cu (200) peaks are reduced in intensity, and subsequently at 800 ° C, diffraction peaks of  $Cu_4Si$  appear at  $2\theta$  values of 44.0 °. It is therefore safe to state that above 700 ° C, the barrier starts to degrade. The disappearance of copper in the XRD pattern indicates that most of the copper has diffused through the barrier film to the silicon substrate where it reacts with silicon to form  $Cu_4Si$  after annealing at 800 ° C. This formation of  $Cu_4Si$  can lead to an increase in sheet resistance of copper.

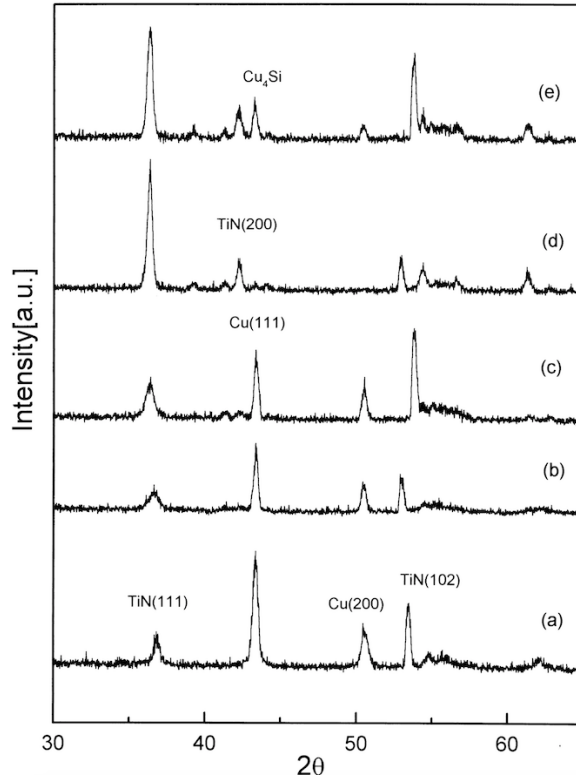


Figure 3.8. XRD spectra for *Cu/TiN/SiO<sub>2</sub>/Si* samples; (a) as-deposited and after annealing in *N<sub>2</sub>* for 1 hour at (b) 500° C, (c) 600° C (d) 700° C and (e) 800° C [67].

Further, AES (Auger Electron Spectroscopy) was carried out by the authors to show the extent of interdiffusion. Fig. 3.9 confirms minimal interdiffusion at or below 500 ° C anneal temperatures. Beyond that temperature, Cu starts to diffuse through the SiO<sub>2</sub> layer which is not ideal. For this reason, as part of our annealing process during fabrication, the annealing temperatures are to be kept below 500 ° C.

Among different refractory metal nitrides the effectiveness of TiN against Cu diffusion can be seen in Fig. 3.10 by comparing the diffusion constants as a function of temperature. These numbers are orders of magnitude lower when compared to the diffusion coefficients for Cu self diffusion.

Another point of contention for diffusion barrier layers is their electrical resistivity. Most refractory metal nitrides have low electrical resistivities that are usually tunable based on the content of nitrogen available during sputtering or variation of ion beam

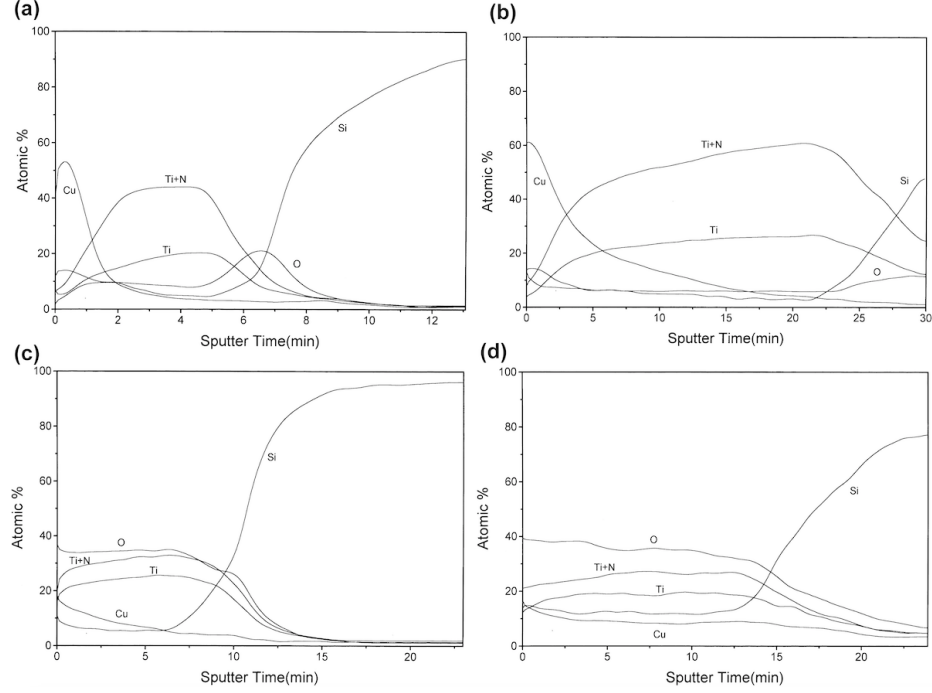


Figure 3.9. AES depth profiles for *Cu/TiN/SiO<sub>2</sub>/Si* samples; (a) as-deposited and after annealing in *N<sub>2</sub>* for 1 hour at (b) 500° C, (c) 700° C (d) 800° C [67].

power, if IBAD (Ion Beam Assisted Deposition) is used. Fig. 3.11 shows variation in electrical resistivity with  $T^2$  (77-300K) for different TiN films sputtered at different conditions [68]. It is observed that the residual resistivity ( $\rho_o$ ) of TiN films is influenced by nitrogen partial pressure during deposition. It also appears that the values of  $\rho_o$  decrease from  $1.0061 \times 10^{-4}$  to  $0.3866 \times 10^{-4} \Omega - cm$  as the nitrogen partial pressure increases from  $2.7 \times 10^{-3}$  to  $6.7 \times 10^{-3}$  Pa, whereas the composition ratio (Ti/N) is almost same at 1.721.73 for the samples TN3, TN4 and TN5, which are deposited under same conditions except for the nitrogen partial pressure. Keeping this in mind we will also need to ensure each new test specimen is tested for electrical resistivity.

### 3.3.2 Capping Layer

Capping layers often act as diffusion barriers and etch stop layers for ILD (Inter-layer Dielectric) stacks. From the perspective of electrical design, one of the require-

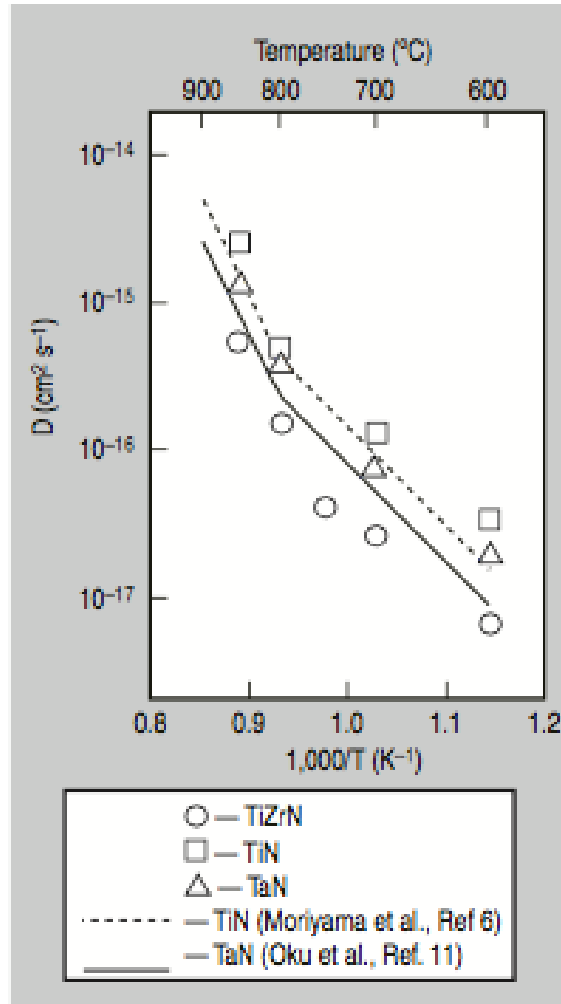


Figure 3.10. The diffusion coefficients of copper in different barriers (TiN, TaN, and TiZrN) in the temperature range of 600–900° C [66].

ments is the need to have a low dielectric constants to avoid parasitic losses. Silicon nitride (SiN) was adopted as a diffusion barrier dielectric for Cu interconnects with PECVD-SiO<sub>2</sub> ILD. It has a  $\kappa$  value over 6. More recently, capping layers with lower  $\kappa$  ILD materials are being introduced; these are namely SiC, SiCN, or SiCOH [69]. Their  $\kappa$  values range between 4 and 5. However, these lower ( $\kappa \leq 5.0$ ) dielectric barriers have scaling issues due to stress cracking and leakage challenges upon UV exposure required to cure low-K films ( $\kappa \leq 3.0$ ). As the ILD layers become thinner, the relative contribution of the diffusion barrier  $\kappa$  to  $\kappa_{eff}$  is growing. As an alternative

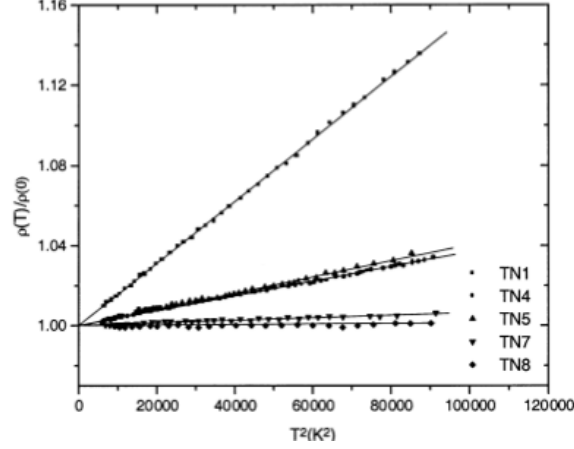


Figure 3.11. Variation of resistivity ratio ( $\rho(T)/\rho(0)$ ) with temperature for different TiN films, where normalizing factor  $\rho(0)$  is taken as residual resistivity [68].

to using low-K materials, thinning of diffusion barriers is done to maintain performance without causing reliability concerns [70,71]. Scaling to a few nanometers still remains a challenge [72].

Hu *et al.*, through electromigration experiments on thin copper lines ( $\leq 2\mu m$ ) found the activation energies for diffusion through the cap surface to be low compared to grain boundary diffusion; confirming the fastest path for diffusion of copper atoms was through the surface/interface [24]. As an added measure, some capping layers have an additional diffusion barrier layer. Fig. 3.12 shows some schematics of cap layers that are proposed or currently in use. Additionally, several steps may be needed to clean the interface, since, residue from planarization steps and etch steps may result in poor adhesion and poor electromigration reliability.

For this study, we will focus on using SiN with TiN or Ta as additional diffusion barrier layers. SiN, as mentioned earlier, is currently in use as an etch stop layer and a barrier layer, it is preferred in this study over  $\text{SiO}_2$  because of its reduced risk for causing copper oxidation. Depending on the method of fabrication, oxidation can be prevented or limited.

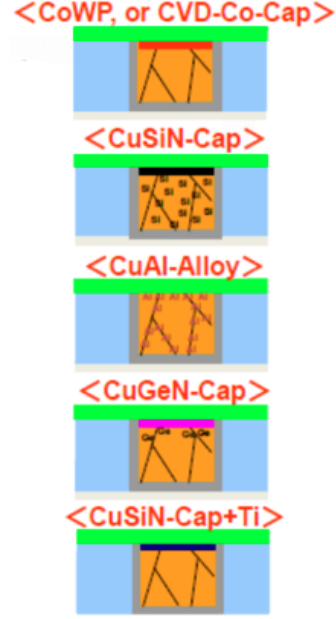


Figure 3.12. Schematic of configurations for capping layers [72].

### 3.4 Geometry

A starting point for choosing the geometry comes from prior work in literature to determining the current densities at which electromigration is observed in the chosen conductor. In our case, the metal is Cu and the current densities reported in literature vary from  $10^5$  to  $10^7 A/cm^2$ . On the lower end, the time to failure is very high and at the high end of test, current densities lifetimes are short primarily due to joule heating failure. Additionally, we consider the trends and expected current densities from technology roadmaps to determine what is most suitable. Fig. 3.13 is the trend for current density of Cu interconnects. At present, the current density imposed on these interconnects is approximately  $3 \times 10^6 A/cm^2$ . We will use this information to determine the length of the line.

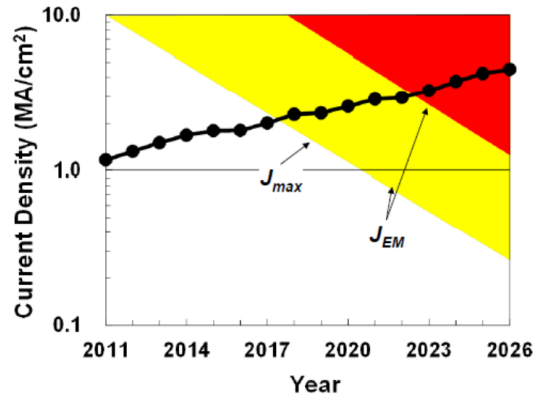


Figure 3.13. Trends in maximum current densities and targeted current densities for Cu interconnects [72].

### 3.4.1 Conductor - Copper

**Length:** Blech’s work on electromigration is key to determine the length of the line needed to induce electromigration failure. The “Blech threshold” is unique to the conductor and is a constant that determines the critical length for a conductor to mitigate risk of electromigration. Often, during circuit design, this is used as a basis to form rules for restricting geometries by either changing the length of the line or the width/thickness to reduce current densities experienced by the line. Our approach to choosing a design length is to conservatively make the line longer for two reasons. First, a longer line will ensure electromigration occurs for the highest chosen current density. Second, a longer line will ensure the gradient of the hydrostatic stress is small. This second reason is important to ensure that we obtain a constant interfacial velocity.

We use the reported values of ‘Blech threshold’ in literature to determine the critical length for current density test range we wish to evaluate. Even though the Blech Threshold is supposed to be a unique value for a conductor, there is some variation in the reported value for Cu. These variations may be attributed to the microstructure or the test conditions. Among the highest value reported in literature is 3700 A/cm [73]. Other sources have reported a lower critical product ( $jL_c$ ), with

the lowest reported value at 1500 A/cm [74]. To stay conservative we use the highest reported critical product value, which in turn yields the longest critical length. For the lowest current density value ( $10^5$  A/cm<sup>2</sup>) in our test range, the critical length is 370  $\mu$ m. In order to observe electromigration failure, any line designed for this study has to be longer than 370 $\mu$ m. At higher current densities, this length is more than sufficient.

**Thickness:** In order to achieve the current densities desired for the tests while keeping the current low requires scaling the cross-sectional area accordingly. The overall current in the circuit is to be chosen to be in the mA range for safe operation. This is chosen as a range predominantly due to concerns about safe operation and the accuracy of the current source. The current source available has a range of 0-40V and a maximum current output of 1 A. If a structure has a resistance of 500  $\Omega$ , the maximum current output possible is 80 mA. Traditionally Cu interconnects are deposited using a plating process with a seed layer deposited either using a chemical vapor deposition (CVD) or a physical vapor deposition (PVD) step. Thickness of the interconnects may vary from several nanometers to a few microns. Plating baths and chemistry can often be complex based on the requirement for a device. For instance, during a dual damascene process, the plated Cu needs to fill a via which may have varying aspect ratio. A high aspect ratio would mean that the via is deeper than its opening. In such cases, a conformal plating process is used which has additives that help with conformal plating to avoid pinch holes in the plating. It is also challenging to maintain a high accuracy in plating thickness and often a planarization step is required to reduce the thickness down to the specification. This CMP (Chemical Mechanical Polish) step is known to cause variations and contamination on Cu surfaces.

To avoid these challenges we resort to using a PVD process where, the thickness is monitored by an oscillating crystal with accuracy in the sub nanometer range. The thickness of the material is however limited by the process. In general a single step deposition in a PVD process is limited to 500 nm. This is more than sufficient for



our purposes. Our goal is to have as large a surface area to volume ratio possible in this study. We therefore use 100 nm of Cu as a baseline in this study.

**Width:** Once the thickness of the Cu strip is known, we move on to selecting a range of widths to study the variation in Cu electromigration. There is experimental evidence to suggest that the a bamboo grain structure has a higher activation energy compared to a polygrain structure. If a conducting strip is made small enough so only one grain spans the width of the specimen, then vacancies are limited to diffusion along the interface unlike a polygrain structures where the vacancies can move along the grain boundaries. In reference [24], Cu lines that were 2  $\mu m$  in width were tested and observed to have a longer electromigration lifetime. The authors concluded that the improvement in lifetime was the result of the “bamboo grain” structure. We therefore use a range of widths; 0.5, 1, 2, 5, 10, 20  $\mu m$  in this study.

The choice of line widths chosen here serves two purposes. First, we wish to determine the line width where the structure transitions from a polygrain structure to a bamboo grain structure. Second, we need to determine the suitable line width at which we have a moving interface where an average velocity can be specified.

### 3.4.2 Diffusion Barrier Layer/Capping Layer

**Capping Layer Thickness:** The only important geometry constraint for the capping layer is the thickness. Passivation layers or capping layers can range between tens of nanometers to a few microns on a real device. However, since the goal of this study is to determine the effect of interface, the cap layer thickness needs to be minimized. Since the capping layer chosen for this study is SiN, the lower limit on the thickness deposited is based on the tool used for deposition. SiN has an elastic modulus  $E=250$  to  $325$  GPa and it can induce residual stresses of the order of  $1$ - $2$  GPa based on the method used for deposition. To minimize residual stress induced by the SiN a thin layer is preferred using a process with a lower temperature for deposition. Depositing a thick capping layer with higher residual stress built up in

the structure may cause variations in resulting electromigration rates from device to device. Additionally, a thick capping layer would mean that a higher hydrostatic stress would build up on the anode end of the tested line causing a larger stress gradient. This is because the transported material will need to induce a higher stress to rupture the capping layer. A thin capping layer for these reasons is preferred which will allow hillocks to form but, also provide sufficient protection against oxidation.

We utilize a plasma based chemical vapor deposition process to deposit the capping layer in this study. We are able to reliably deposit 20 nm of  $\text{SiN}_x$ . At higher thicknesses the residual stress starts to warp the test specimen. We keep this thickness fixed for all the test structures in this study.

**Diffusion Barrier Layer Thickness:** Diffusion barrier layers in microelectronics fabrication are usually on the order of several nanometers. There is ongoing work to shrink these layers to 2-3 nm but, such thin diffusion barriers do not provide sufficient barrier against diffusion. We utilize two diffusion barrier layers in this study.

The first diffusion barrier serves as the base layer for the Blech structure that needs to be sufficiently conductive. This layer carries most of the current until the Cu line is encountered. For this reason, the layer needs to have sufficient conductivity to avoid failure due to joule heating. Given a conductivity, we are able to determine the cross-sectional area that is required for safe operation. We also need to keep in mind that the line may not fail due to joule heating, but, it would create a local hotspot. These hotspots can contribute a higher local temperature and accelerated failures. We discuss this more in detail when we introduce the finite element model in the next section. We use 100 nm of TiN as the base layer thickness in this study. Since the process for deposition is sputtering, the upper limit to depositing TiN on the instrument is a few hundred nanometers. Additionally, a thicker diffusion barrier layer would mean a longer etch time. We therefore focus on changing the width of the structure to control the resistance and thermal conduction.

The second diffusion barrier layer is between the capping layer and the Cu line. This barrier layer serves to modify the interfacial adhesion between the Cu and the

cap layer. A thick diffusion barrier layer here would introduce an additional residual stress on the line. In order to avoid such variation we use barrier layers that are only a few nanometers in thickness (5nm of Ta and 10 nm of TiN). These barrier layers are capped by 20 nm of SiN<sub>x</sub>.

**Diffusion Barrier Layer Width:** We alluded to the variation of the barrier layer in the previous section. In the case of the top barrier layer between the cap and the Cu line, the thickness of the barrier layer is not as important; it only needs to cover the Cu line on all sides. The barrier layer on the bottom needs to be chosen more systematically. If the barrier layer width is small, there are two disadvantages. First, the resistance of the structure will be higher for a given thickness. Second, the surface area for conduction will be smaller. Thus, the width of the structure needs to be chosen appropriately to avoid excessive heat generation in the line. We discuss this in detail as we introduce the finite element model in the next section.

### 3.5 Finite Element Modeling

Two models are presented in this section; first is a 2-D model of the test structure meant to serve as a basis to determine the risk of joule heating. The second model is a 3-D one for the Blech like structure meant to study the difference in current crowding between a narrow and a wide base diffusion barrier layer.

#### 3.5.1 2-D Model

A 2-D model of one of the test structures using the dimensions of real structure is made. Silicon is used as a the base, where, Cu line is 500  $\mu\text{m}$  long and 100 nm thick, while the TiN base layer is 550  $\mu\text{m}$  long and 100nm thick. A 20nm thick layer of SiN is used for the passivation. A coupled electric-thermal study is carried out using the joule heating module in Comsol Multiphysics 4.3b [75]. Linear triangular elements are used for meshing within regions of interest using a refined meshing scheme. A total of 411,772 elements are used. Fig. 3.14 is the schematic of the structure along

with a mesh shown for zoomed in region of the structure. For the thermal problem, a fixed temperature boundary condition is used at the base of Si, set at  $T = 293\text{K}$ . The top surface of the structure uses a heat convection boundary condition to account for natural convection from the top surface. A nominal heat transfer coefficient,  $h_s = 4.0\text{ w/m-K}$  is used on the surface of SiN. The edges of Si have a symmetry boundary condition. For the electrical problem, a bias is applied across the TiN layer. We vary this bias from  $0.2\text{V}$  to  $15\text{ V}$  in this study. Every other boundary is electrically insulated. Fig. 3.15 depicts the boundary conditions described. Material properties used for TiN and Cu are listed in Tab. 3.1 and 3.2 while the material properties of SiN and Si were imported from the Comsol materials library.

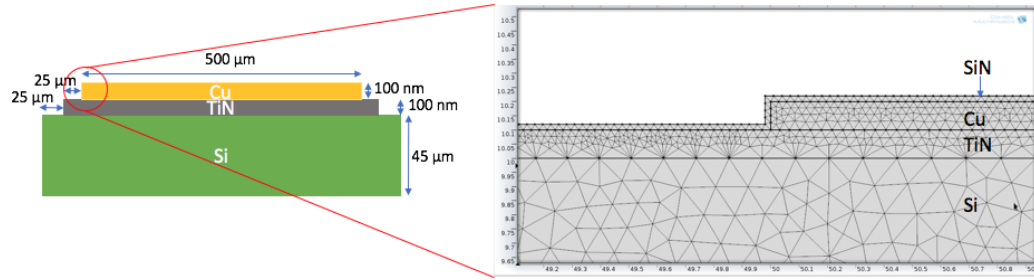


Figure 3.14. Schematic of the 2-D model along with the mesh used for this numerical study.

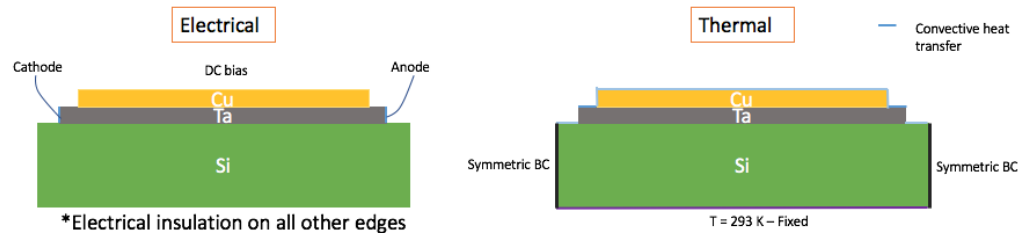


Figure 3.15. Pictorial representation of the boundary conditions used in this study.

The passage of current through the conductive layers leads to generation of heat, which is conducted away from the film to the large sink in the form of Si. From the results obtained, we observe that a hot spot is formed at the cathode and anode end

Table 3.1. TiN Properties.

Property	Value	Units
Electrical Conductivity	1.33E6	S/m
Heat Capacity at Constant Pressure	43.4	J/(kg.K)
Thermal Conductivity	19.2	W/(m.K)
Density	5400	kg/m <sup>3</sup>
Relative Permittivity	1	

Table 3.2. Cu Properties.

Property	Value	Units
Electrical Conductivity	5.998E7	S/m
Heat Capacity at Constant Pressure	385.5	J/(kg.K)
Thermal Conductivity	400	W/(m.K)
Density	8700	kg/m <sup>3</sup>
Relative Permittivity	1	

where TiN carries all the current. Once the Cu strip is encountered, the electrical conductivity of Cu ensures most of the flow of current is through the Cu. Fig. 3.16 is a plot of the current density in the test structure if the thickness is assumed to be 10  $\mu\text{m}$  into the page. A jump in the current density is observed at the junction where Cu is first encountered. In the limit of mesh refinement, this jump would become a singularity. This can be attributed to current crowding and, if left unchecked, can lead to further local heating and aggravation of void formation. Fig. 3.17 is a plot of the local temperature rise in the test structure. A hotspot is observed in TiN and is a function of the geometry and current passing through the test structures. From the parametric study, the maximum temperature rise is plotted as a function of the expected current density in Cu. A quadratic behavior is expected, and the results confirm this behavior. Fig 3.18 is a plot of the maximum temperature observed in the test structure as a function of the current density in the Cu strip. For a different geometry, these results will be different. Two cases are presented here, the first where the base layer of TiN is 10  $\mu\text{m}$  and second, where TiN is considered to be 40  $\mu\text{m}$ . At

the range of current densities of interest,  $<3 \times 10^6 \text{ A/cm}^2$ , the local joule heating will raise the local temperature by  $<5 \text{ }^\circ\text{C}$  for the  $40 \text{ }\mu\text{m}$  wide base layer.

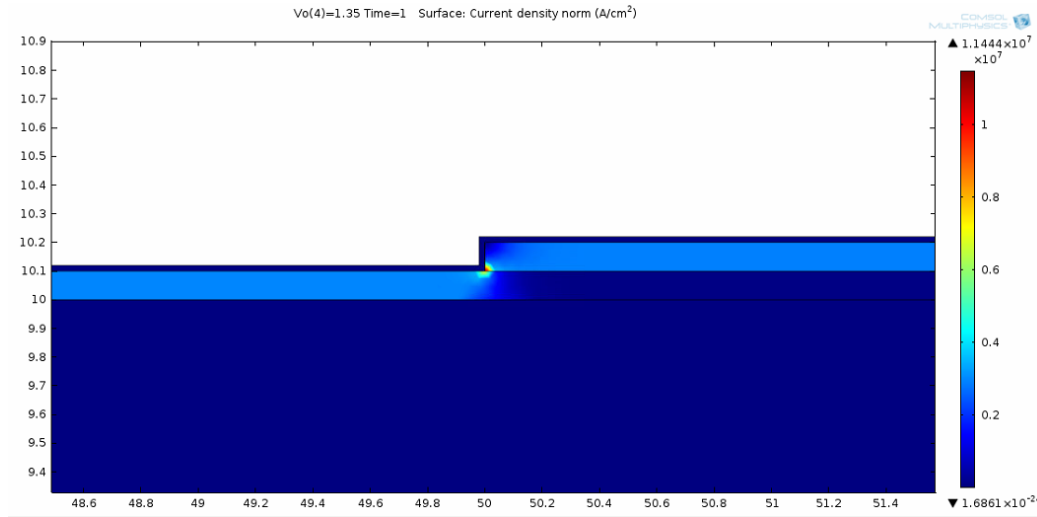


Figure 3.16. Current density distribution in the structure at the cathode end of the Cu line.

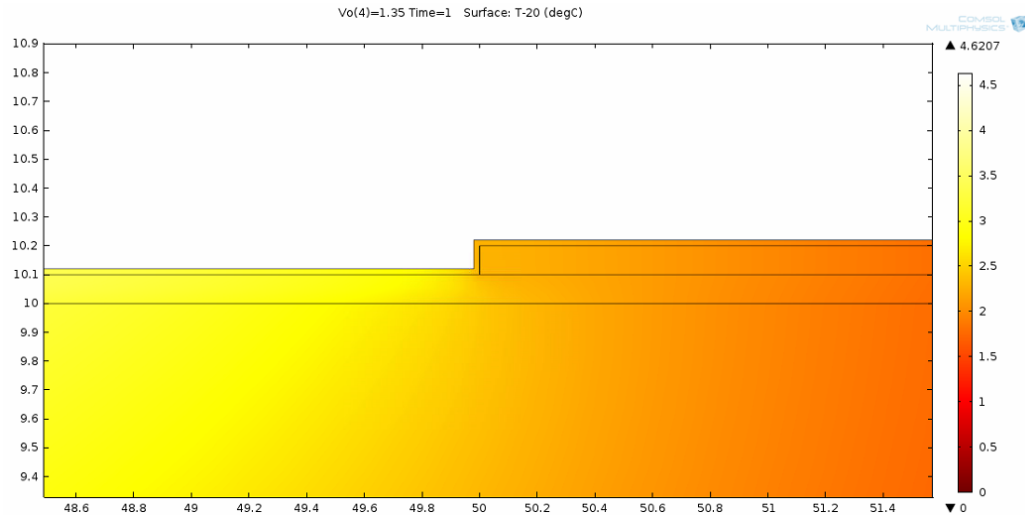


Figure 3.17. Temperature rise at the cathode end due to an applied current.

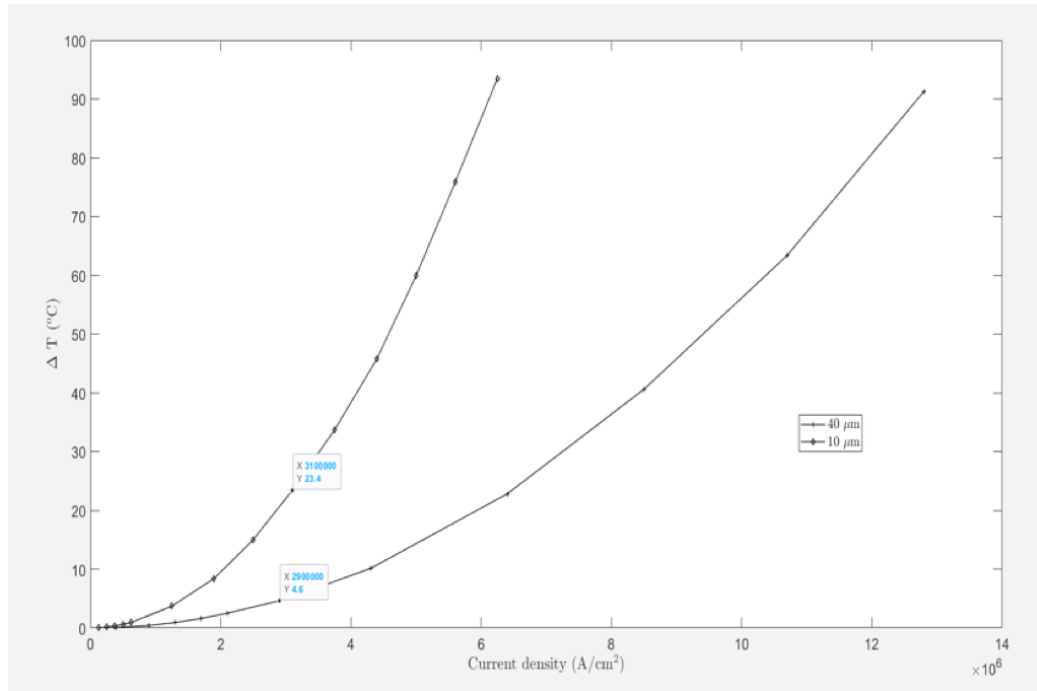


Figure 3.18. Maximum temperature rise as a function of the current density in Cu.

### 3.5.2 3-D Model

A 3-D model of the test structure was also completed. In this model, only the Cu and TiN film are modeled. The purpose of this model is to visualize the current crowding when the base layer width is modified. Two scenarios were simulated, the first is where the base layer of TiN is the same width as the Cu line and the second where TiN is four times as wide as the Cu line. The model uses the same material properties as the ones used in the 2-D model. The Cu line is  $500 \mu\text{m} \times 10 \mu\text{m} \times 1 \mu\text{m}$  and the TiN layer is  $550 \mu\text{m} \times w \times 1 \mu\text{m}$  where,  $w$  is either 10 or 40  $\mu\text{m}$ . No silicon base is used in this study, since this is purely meant for visualization of current flow through the conductive layers. For boundary conditions, a DC bias of 1V is applied on the edge of the TiN layer and all other surfaces are electrically insulated. A fine mesh is used with 28882 and 143732 linear tetrahedral elements respectively for the two cases. Fig. 3.19 is a top view with the mesh for the two cases.

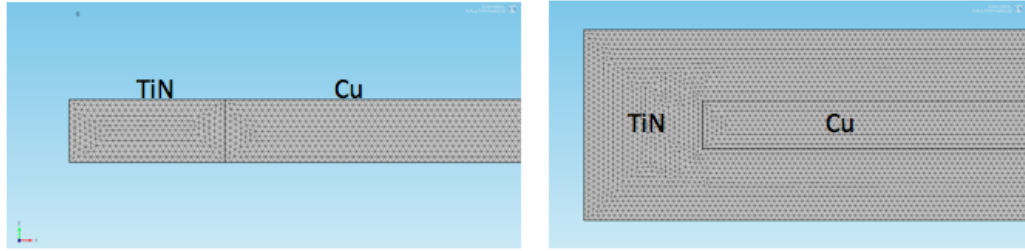


Figure 3.19. Top view of the mesh used for the two cases with varying base layer widths.

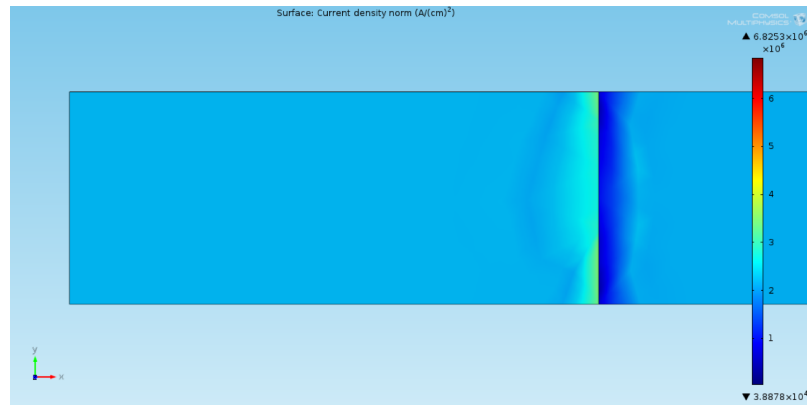


Figure 3.20. Top view of the current density distribution for a Cu line with a narrow TiN base layer.

Fig. 3.20 and Fig. 3.21 are plots of the current density distribution in the films. Note that the boundary condition was a DC bias, so the total current flowing would be different for the two case. We resolve the difference by taking the normalized current density. Fig. 3.22 are plots of the current densities along the top and bottom edge of the Cu line. The normalization is taken with respect to the current density  $10 \mu\text{m}$  from the edge of the Cu line. For a wide base TiN layer, we observe higher current densities at the edge of the lines while, a narrow base layer the current density seems to be consistent along the width. Note, the top and the bottom edge have very different magnitudes, where, the bottom is higher due to the current crowding effect. This visualization helps rationalize the curvature observed in when the Cu lines are subject to a higher current density. With the wide base diffusion barrier layer, a



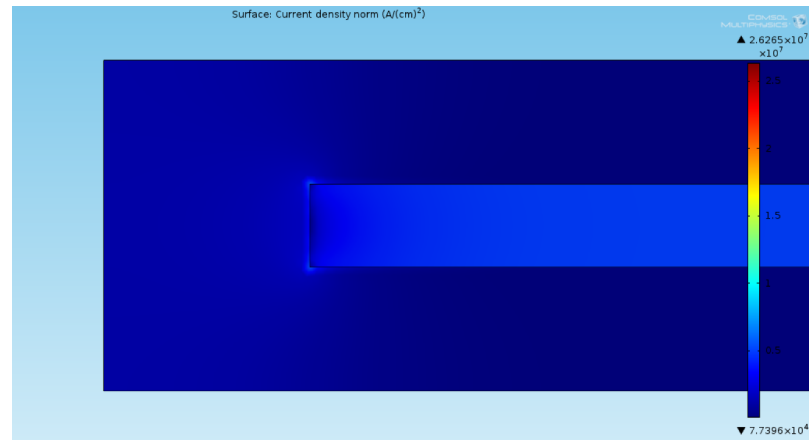
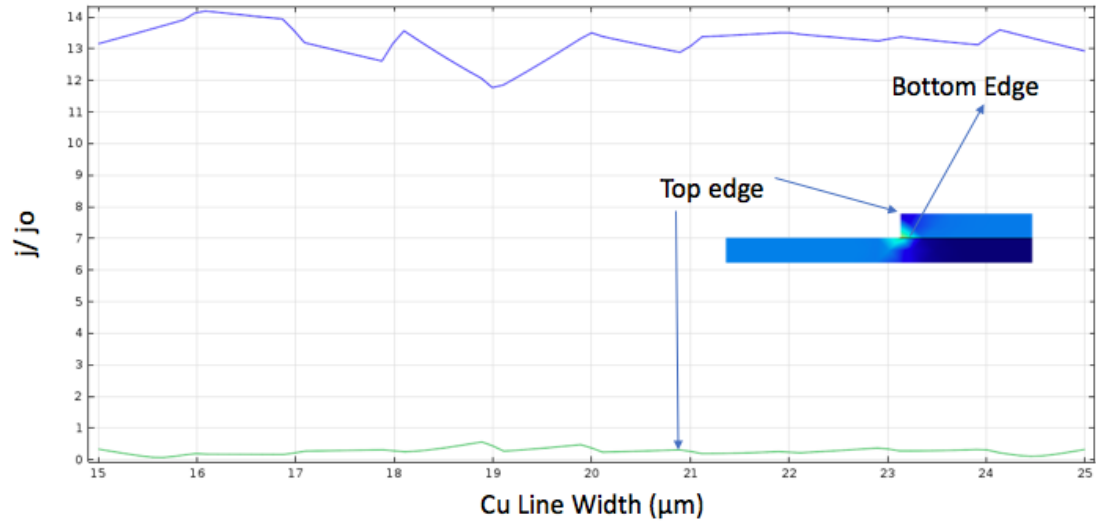
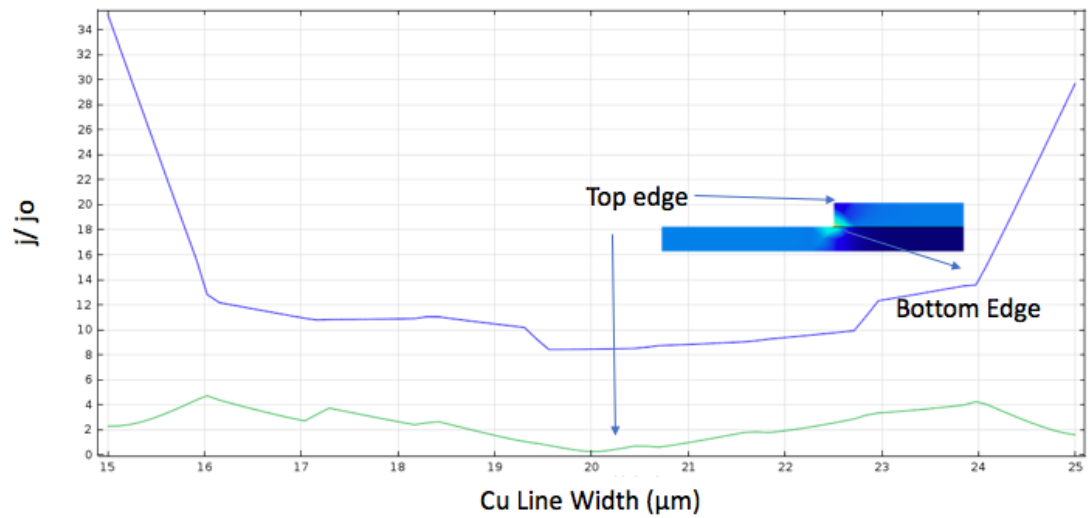


Figure 3.21. Top view of the current density distribution for a Cu line with a wide TiN base layer

higher current density may cause the edges to move at a higher velocity compared to the middle of the line.



(a)



(b)

Figure 3.22. Plot of the normalized current density along the top and bottom edge of the Cu line for (a) Narrow base layer (10  $\mu\text{m}$ ) (b) Wide base layer (40  $\mu\text{m}$ ).

## 4. FABRICATION PROCESS

This chapter focuses on the fabrication process used for the test structures. We begin with a brief description of the main fabrication methods and techniques before discussing the details of the fabrication process steps. Finally, the challenges encountered during fabrication are discussed along with steps used to resolve the challenges.

### 4.1 Process Details

Considering the variety of fabrication methods used for this work, it is most convenient to break the fabrication process by individual sub-steps. These will fall under the categories: Lithography, Deposition, Etching, Growth and Miscellaneous. We first discuss some details about each of these sub-steps before diving into the fabrication. Under each sub-step some of the challenges encountered are discussed at the end of this chapter along with the solution used to overcome the challenge.

#### 4.1.1 Lithography

There are two types of lithography used in this study. The first is E-beam lithography, where an electron beam is used to directly write on the wafer and the other is contact lithography where a hard mask is used to imprint a pattern on to the wafer. The imprint process or the writing process is possible because of a photosensitive polymer referred to as a photoresist (PR). These polymers become active when light of a certain wavelength is shone on it. The benefit of using e-beam lithography is that the device can be scaled down to sub-micron ranges, which is necessary if we wish to fabricate test specimens with sub-micron widths. Contact lithography relies on a light source with different wavelengths on offer. The one that is most commonly used is the g-line which has a 435 nm UV lamp source. Most contact lithography

masks will give a feature size of 1-2  $\mu\text{m}$  at best. To define the geometry of Cu on the wafer we use the e-beam lithography and for the rest of the fabrication we use contact lithography process.

## Photoresist Application

For a particular photoresist, a certain dosage is required before the region that is exposed becomes active. Typically, this is a function of the photoresist chemical composition, thickness of the photoresist and the substrate material. These photoresists are generally categorized as positive tone or negative tone depending on their behavior. For a positive tone, the material that is exposed to the beam becomes active and is removed after chemical development. While the negative tone will have material that is exposed stay after the development process. For the lift process, generally a negative tone resist is used but, it is well known that they leave behind residue that is hard to remove without harsh chemical treatment. For this reason, we use a positive tone photoresist with some modifications to suit our needs in this study. Fig. 4.1 shows the profiles of resist after exposure.

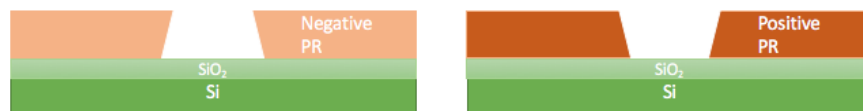


Figure 4.1. Schematic of sidewall profile for negative tone and positive tone resist.

The photoresists are usually spun on at a given rate for a specified time to achieve a desired thickness. This is followed up with a soft bake step to drive out the reducers from the PR. As a rule of thumb, the resist thickness should be 3-5 times the thickness of the metal being deposited. Once the PR is applied and soft baked, it is ready for exposure to activate the photochemical. A certain dosage is required to activate these chemicals which varies from resist to resist. Dosage is measured as energy per unit area or charge per unit area based on the resist being used. Manufacturers will

usually provide a baseline but, dosage tests are required to ascertain the optimal process values.

For this study we used two different photoresists. One that is sensitive to E-beam and another which is sensitive to UV spectra. For the E-beam lithography process, we used a positive tone photoresist. A bi-layer recipe of NANO PMMA (polymethyl methacrylate) from Microchem was optimized for lift-off process. A bi-layer requires two different polymers of the same family with different sensitivities to the E-beam. Here, the bottom layer is more sensitive compared to the top layer. This allows for easier lift off of metal after deposition due to the negative profile of the sidewall.

A second photoresist, AZ1518 is used for the rest of the fabrication process. AZ1518 is also a positive photoresist used with g-line or broad spectrum UV sources. It is a versatile PR with good resolution but, usually needs an adhesion promoter with Si substrates that have SiO<sub>2</sub>. Typical thicknesses for this resist range from 1-3  $\mu\text{m}$ . We used this resist for etching as well as for lift off.

Once the pattern is defined on the resist. A chemical development process is needed where the chemical will dissolve areas that are exposed or unexposed depending on the tone of the resist. These chemical are specific to the resist and their composition may differ. An additional hard bake step may be required after development to drive out any additional reducers/moisture.

## **E-beam Lithography**

E-beam lithography in this study was carried out on JEOL JBX-8100FS . An electron beam is rastered across the substrate at a defined rate and intensity after a pattern is defined. The primary advantage of electron-beam lithography is the ability to define custom patterns (direct-write) with sub-10 nm resolution. This form of maskless lithography has high resolution and low throughput, limiting its usage to photomask fabrication, low-volume production of semiconductor devices or research and development. Since this form of the patterning involves a rastering step, the time

required for writing depends on the dosage, probe current and the area for the write. If there are multiple fields to write, more time is required since the beam can only raster an area 1 mm x1 mm. For larger areas the stage has to move precisely and the fields have to be stitched. This stitching process and the order is defined while fracturing the data along with the the shot size. Shot size is the minimum beam diameter during the write process. A smaller shot size would mean more beam steps are required and the intensity would also need to be changed. The data fracturing is carried out in a standalone software Beamer. Here the data is read as closed polygons for geometry and then split into multiple fields. Shot size, accelerating voltage and the raster sequence is defined next. Instructions are written for a particular instrument make and model which defines some of these parameters. If two features are close or if there is overlap between two fields a proximity correction is required during this step.

## **Contact Lithography**

Contact lithography as a the name suggests uses a hard mask with a predefined pattern to be in contact with the substrate on which the pattern is to be transferred. The contact mask aligner used in this study was the Suss MJB-3 contact mask aligner with a g-line UV source. The substrate with a photoresist is aligned optically to the mask typically with Chrome or Iron Oxide patterns that are dark or light field. The pattern transfer takes place when a UV light source illuminates to the mask and substrate. The chrome or iron oxide regions block the UV from transmission on to the substrate. The light source has a certain intensity which is known apriori and the time for exposure is determined by the dosage required. AZ 1518 for instance requires a dosage of  $900 \text{ mJ/cm}^2$ . If the intensity of the UV source is  $10 \text{ mJ/s}$  then the time to exposure is 90 seconds. This is just a rough guide but this number changes based on the substrate material and the thickness of the photoresist.

This type of lithography is quick but, suffers from diffraction related aberrations for finer feature sizes. Additionally, as the wafer size gets larger the mask may distort the features from center to the edge. Nevertheless, we will use this lithography process for wet and dry etch process along with lift-off for Ta.

#### **4.1.2 Deposition**

Deposition in our case refers to the deposition of metals, metal nitrides and passivation. We will predominantly rely on physical vapor deposition (PVD) of metals and metal nitrides while, chemical vapor deposition (CVD) is used for the capping layer.

#### **Physical Vapor Deposition**

PVD process refers to a process where a target material is first vaporized in a vacuum chamber and then condensed back into a thin film which coats everything in its path. The most common PVD processes are evaporation and sputtering. We used both of these methods in our study. Evaporation relies on a target material being vaporized using either an electron beam or high electrical resistance. The rate is usually controlled by the power supplied to the heating source.

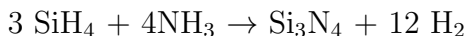
We used electron beam physical vapor deposition where the electrons bombard the target material in a crucible to vaporize it before it condenses back on the cooler work piece and chamber surroundings. PVD relies on calibration between power supplied and the rate of deposition. The instrument used in this study is PVD-1 by Lesker<sup>TM</sup>. Six different materials can be deposited without breaking vacuum, which is important if contamination or oxidation is a concern between films. Typically during deposition, only the deposition rate and the final thickness are defined. The materials are usually calibrated for the instrument apriori. The chamber vacuum pressure also depends on the material being deposited, but, is usually around  $10^{-7}$  torr. The lower the pressure,

the better the quality of film deposited. We used this instrument to deposit Cu and Ta.

Another instrument used in this study is the Magentron nitride sputtering system. A target or a metal precursor that needs to be deposited is bombarded with energetic ions of inert gases (e.g., argon or helium). The forceful collision of these energetic ions with the target ejects target metal atoms. These metal atoms are then deposited on the substrate material forming a metallic film. In the case of nitride sputtering, they react with nitrogen before they are deposited on the substrate. The target is cooled by water so that little radiation heat is generated. We use this method to deposit the TiN films in this study.

### **Chemical Vapor Deposition**

Chemical vapor deposition (CVD) refers to process where some volatile precursors are introduced in a reaction chamber to produce a desired material. There are many different methods used for CVD however, the one we utilized is PECVD (Plasma Enhance Chemical Vapor Deposition). This method utilizes a plasma to enhance chemical reaction rates of the precursors. PECVD processing allows deposition at lower temperatures which is vital if the fabrication process does not allow higher temperature excursions. In this study, we used PECVD by Axic<sup>TM</sup> to deposit SiN<sub>x</sub> films. This process utilizes two precursor gases; silane (SiH<sub>4</sub>) and ammonia (NH<sub>3</sub>). The reaction that follows is:



This reaction takes place in the presence of a RF plasma to enhance at the deposition. A preconditioning step was utilized here before deposition, which requires a pre-heat and plasma step with just ammonia. It is important that all oxygen be removed from the reaction chamber to avoid oxidizing the Cu.



### 4.1.3 Etching

This study required a combination of wet chemical etch processing and dry chemical etch processing. There are advantages to using one or the other but, for our purpose we are constrained by the set of materials that are used.

#### Wet Chemical Etch

Wet chemical etching is the most common etching method used in microfabrication, where a liquid phase etchant is used. We utilized the wet chemical etch in two instances. First, to remove organic residue from the wafer by mixing two acids that undergo exothermic reaction. This is the piranha etch, where,  $\text{H}_2\text{SO}_4\cdot\text{H}_2\text{O}_2$  are mixed in a 3:1 ratio. This step should be carried out with caution due to its aggressive reaction. Second, we used Buffered Oxide Etch (BOE) to remove parts of the  $\text{SiN}_x$  capping layer to open up the contact pads. BOE is a mixture of a buffering agent, ammonium fluoride ( $\text{NH}_4\text{F}$ ) and hydrofluoric acid (HF). Concentration of the mixture may vary, which would change the etch rate slightly.

#### Dry Chemical Etching

Dry chemical etching refers to processes where generally material is removed using a bombardment of ions usually in the presence of a plasma. The advantage of this process is the ability to carry out anisotropic etch of material. We utilized RIE (Reactive Ion Etching) in two cases for this study. First was to etch TiN and the second, was to remove organics from the substrate after PR development or strip. In both cases one or more gases are introduced in the reaction chamber in the presence of a plasma. In the case of the TiN etch we used the Panasonic RIE with Chlorine gas as the precursor. Chlorine reacts with TiN to form volatile byproducts like metal chlorides and  $\text{ClO}_2$  if there is any oxygen present [76]. The gas flow rate, chamber pressure and the RF power influence the etch rate. In our case the etch rate was

found to vary between 2nm/min to 8 nm/min. Silicon dioxide on the wafer acts as an etch stop layer once the TiN is completely etched. A check is required using a needle probe to determine if all the TiN is removed from the desired area.

Photoresist residue was removed in the Branson Asher using a combination of Ar/O<sub>2</sub> plasma. After development of the PR, there is usually a very thin layer of resist residue left behind several nanometers in thickness. In order to remove it, an ashing step is required. This ashing step is usually very brief, but, care must be taken to avoid oxidizing features. If the substrate for instance has Cu on it, it will oxidize rapidly in the O<sub>2</sub> plasma. Appropriately, Ar must be used in such cases for etching.

#### 4.1.4 Miscellaneous

During fabrication a few other instruments were required.

- The first was a nitrogen anneal furnace. This is so that the test structures could be annealed at a high temperature in the absence of oxygen. The anneal furnace was purged and set to the desired temperature several hours before the annealing step. This is so that the temperature in the quartz tube was stabilized with mostly nitrogen present in the tube.
- Second, we used a combination of two surface characterization tools. Alpha Step IQ and KLA-Tencor are two stylus based surface roughness/height measurement tools. We used these tools during the development phase to determine the optimal process conditions especially after development of PR.

## 4.2 Fabrication

Schematic representations of the fabrication process steps are shown in Fig. 4.2. These schematics are the cross-sections of the device as it is processed. There are

some subtle differences in fabrication for the three capping/diffusion barrier layers. These differences are highlighted in the details of the fabrication process.

- We start with a blank 2 inch single side polished Si <100>wafer with P type dopants. This thickness of this wafer is 450  $\mu m$  and it has a thermally grown SiO<sub>2</sub> of 470 nm. The wafer is first cleaned in a Piranha etch solution (3:1 H<sub>2</sub>SO<sub>4</sub>:H<sub>2</sub>O<sub>2</sub>) for 8 minutes which ensures all organic residue is removed from the wafer before any processing.
- This step is followed by a deposition of 100 nm of TiN in a sputtering system. This step is carried out in the Nitride sputtering system at a rate of 1 Å/s at 350 °C. After this step the substrate is cleaned in Toluene/Acetone/Methanol for 3 minutes each in a large beaker. We will refer to this step as solvent clean step from here on. We can no longer use a piranha etch solution as it etches the TiN layer. With this step our wafer is ready for further processing.
- Following the deposition of TiN, a bi-layer of PMMA is applied on the wafer to serve as the resist for Cu PVD deposition. The spin on recipe for the resist is listed in Tab. 4.1 with the details for spin rate and times.

Table 4.1. Spin Coat Recipe Details.

Process	Photoresist	Details	Time
Spin Coat	PMMA 495 A4	Rotate at 3000 RPM	50 seconds
Soft Bake		180 °C	5 minutes
Spin Coat	PMMA 950 A4	Rotate at 3000 RPM	50 seconds
Soft Bake		180 °C	5 minutes

- After the PR is applied and softbaked, load the sample on to a piece holder and locate the coordinates for the test specimen in reference to the piece holder plate. This is necessary to ensure the writing in the E-beam is aligned. A secondary check is made using the SEM mode on the E-beam lithography tool. Once the piece is located and aligned. The probe current settings are changed

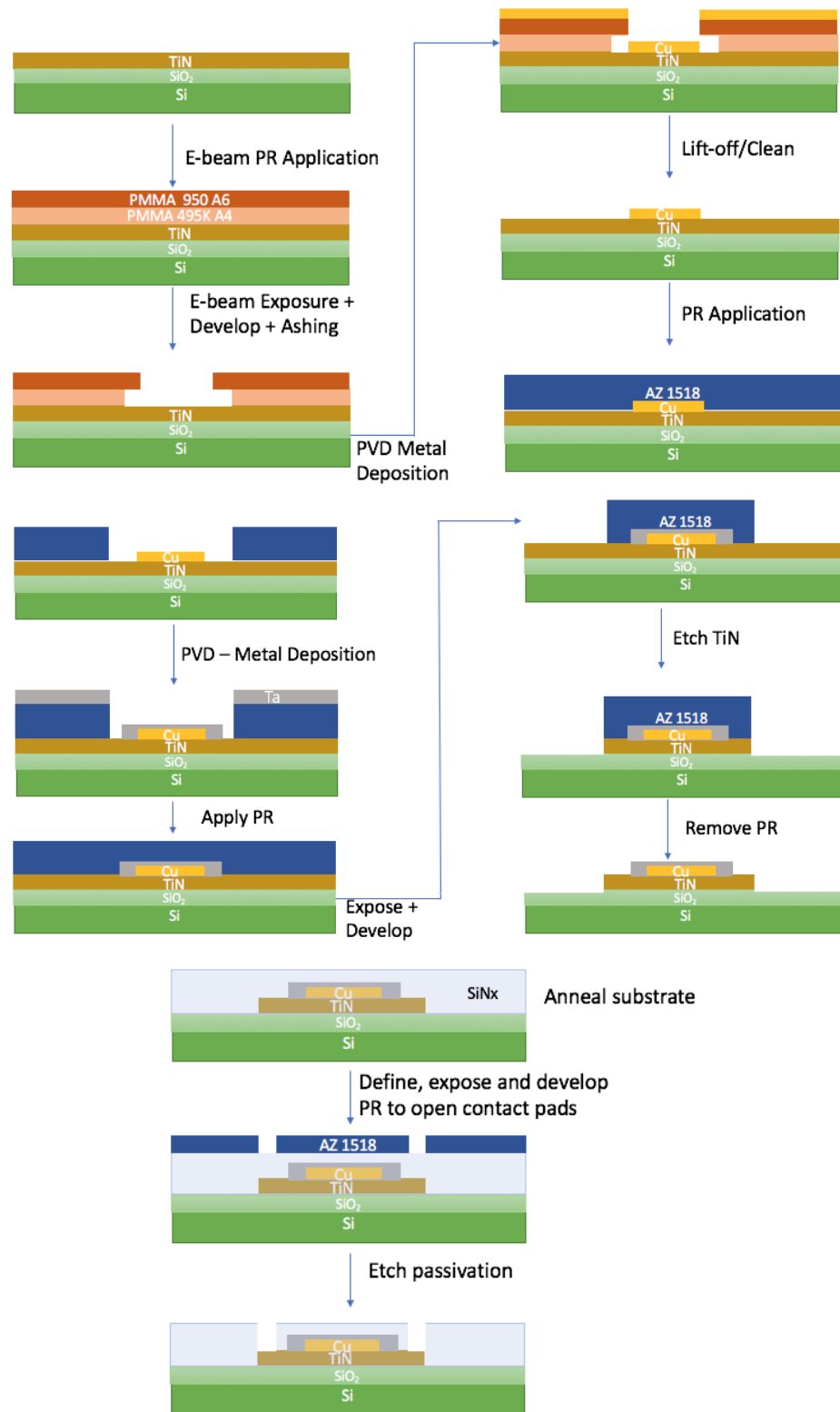


Figure 4.2. Schematics of the fabrication process for electromigration test structures.

to reflect the current to be used and the appropriate calibration file is loaded. Assuming the data is fractured and the pattern is loaded on to the tool, we can begin the write step. Fig. 4.3 is the mask to be exposed on the E-beam. A dosage of  $1400 \mu\text{C}/\text{cm}^2$  was found to be appropriate for this bi-layer recipe after a dosage test. The probe current chosen for the write is 10 nA with a beam spot size of 16 nm and an accelerating voltage of 100 kV. Since PMMA is a positive tone PR, the regions exposed to the beam are the regions that will be removed from the substrate after development. These correspond to the solid color regions in Fig. 4.3. Each row has a different width for the line and while the columns remain the same. In total, each device contains 20 structures and the features at the bottom are the van der pauw structures.

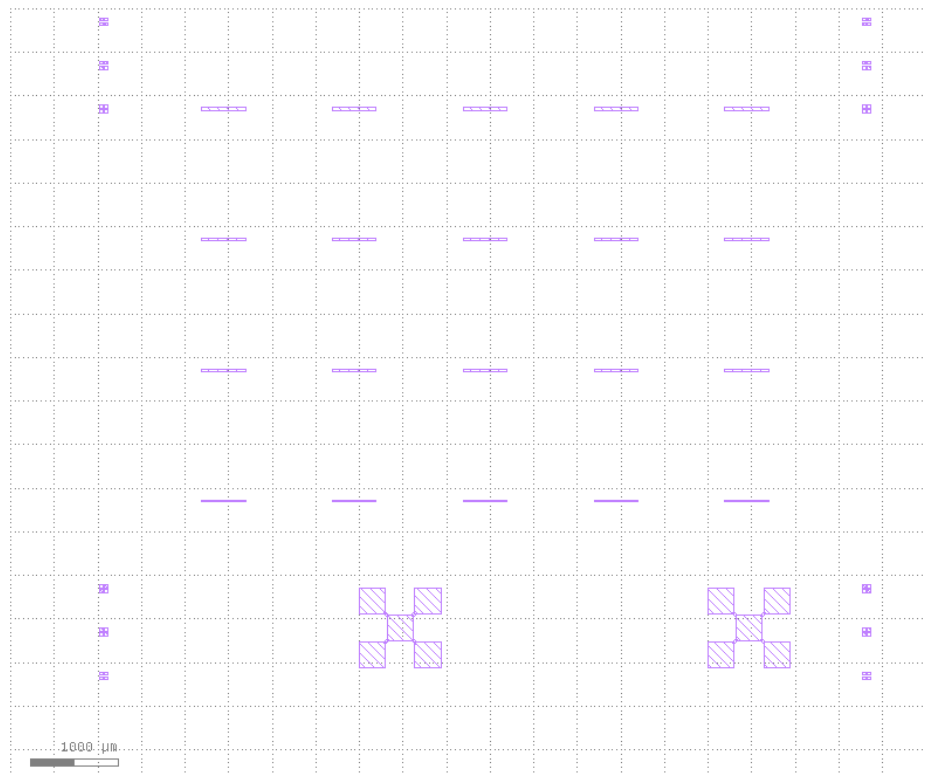


Figure 4.3. Mask to define the pattern for the Cu lines.

- Once the exposure is complete, we develop the PR with 1:3 MIBK:IPA solution for 30 to 45 seconds. No hard bake is required after this. In order to stop the

development, the work piece is immersed in IPA. Fig. 4.4 shows an optical image of the PR after development. These regions are where Cu is to be deposited. Before proceeding to the deposition, a brief ashing step is required to remove the PR residue. Ashing is carried out to carbonize the top surface of the PR and then remove it. We carry out ashing for 45 seconds with gas flow rates for  $O_2$  and Ar set at 12 and 130 sccm. The RF plasma is set at 100 W. If the step is carried out correctly then only a few nanometers of the PR would be removed.

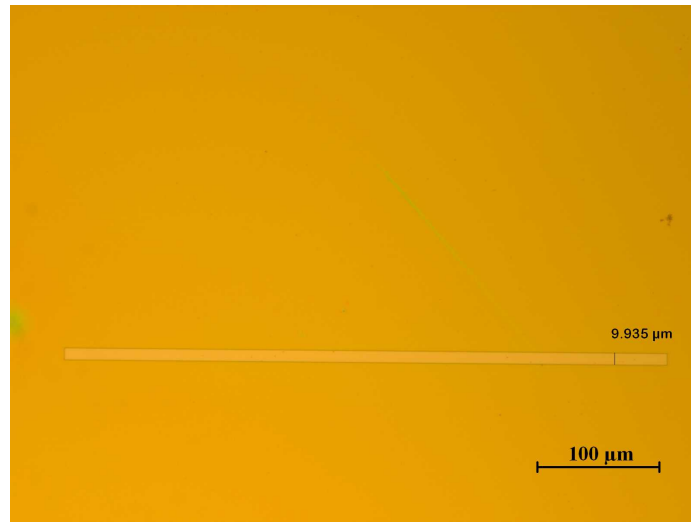


Figure 4.4. Optical image of the exposed and developed region on the substrate.

- Next, we use PVD-1 to deposit 100 nm of Cu on the the substrate with the PR. The deposition rate is set at 2 Å/S. This particular instrument has an automated shutter that will cut power and block additional material from condensing on the workpiece. Thus the thickness can be controlled very precisely. After the deposition, a thin layer of Cu covers the entire surface but, because of the bi-layer recipe we end up with a discontinuous film. A discontinuous film helps eliminate film tear during lift off.
- Lift off for Cu with PMMA resist is carried out with an NMP(N-Methyl-2-pyrrolidone) based solution. Traditional solvent clean process does not work well to remove E-beam resist. PG remover, which is a commercially available

NMP based solvent stripper is heated at 80 °C in a beaker. The test specimen with the Cu film is placed in this beaker for 15 minutes while gently agitating the solution using a glass pipette. There is risk of film tear if the agitation is too strong. After the lift off the test specimen should be thoroughly cleaned using a solvent clean process. Fig. 4.5 is an image of a Cu line on TiN after the lift off process.

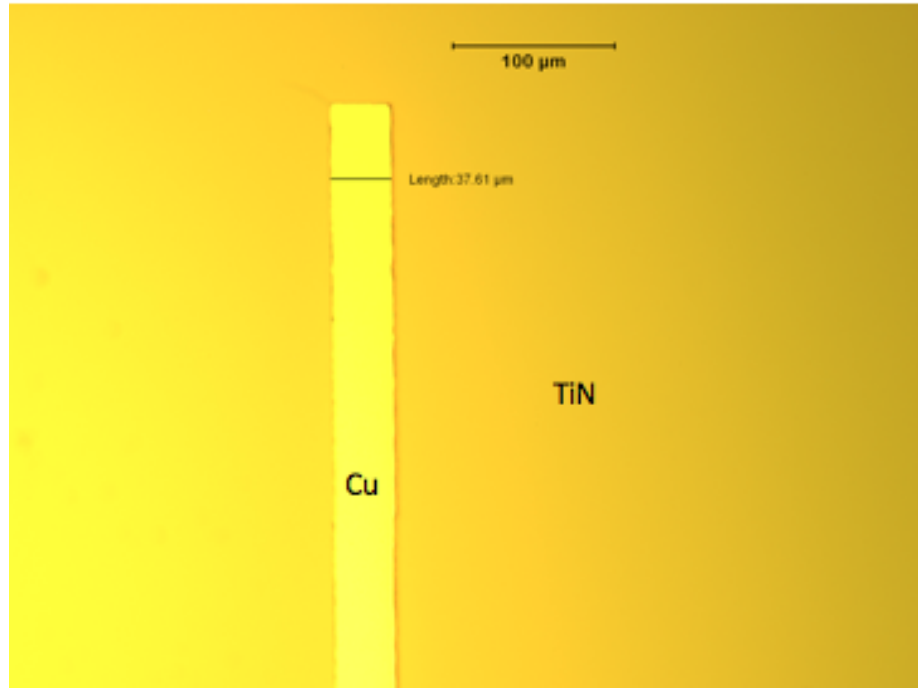


Figure 4.5. Cu lines on TiN post lift off.

- If a Ta diffusion barrier is required we add a new PR layer of AZ1518. This step is optional and can be skipped if there is no diffusion barrier layer between the cap and the Cu layer. Tab. 4.2 contains the details for the spin coat and soft bake for this resist. Once the PR is applied and soft baked, it can be exposed in a contact mask aligner. We use the alignment marks defined in the previous mask step to optically align the workpiece on to the hard mask. Fig. 4.6 is the mask used for this step. The colored regions are the regions that are not illuminated by the UV lamp. After exposure and development for the specified

time, we ensure PR residue is removed by using a brief Ar plasma etch. At this point the substrate is ready for deposition of Ta. A deposition rate of  $3\text{\AA}/\text{s}$  was chosen to keep the exposure time to a minimum. Ta has a high melting temperature of  $3017\text{ }^{\circ}\text{C}$ , which causes cross-linking in the photoresist. If the PR is cross-linked it becomes extremely challenging to remove it. For this reason the thickness of the Ta diffusion barrier layer was limited to  $5\text{ nm}$ .

Table 4.2. Process steps for AZ1518

Process	Details	Time
Spin Coat HMDS	Rotate at 4000 RPM	40 seconds
Spin Coat AZ1518	Rotate at 4000 RPM	40 seconds
Soft Bake	$100\text{ }^{\circ}\text{C}$	2 minutes
Exposure	$10\text{ mJ}/\text{s}$	10 seconds
Develop	1:4 AZ400K:DI water	60 seconds
Hard Bake	-	-

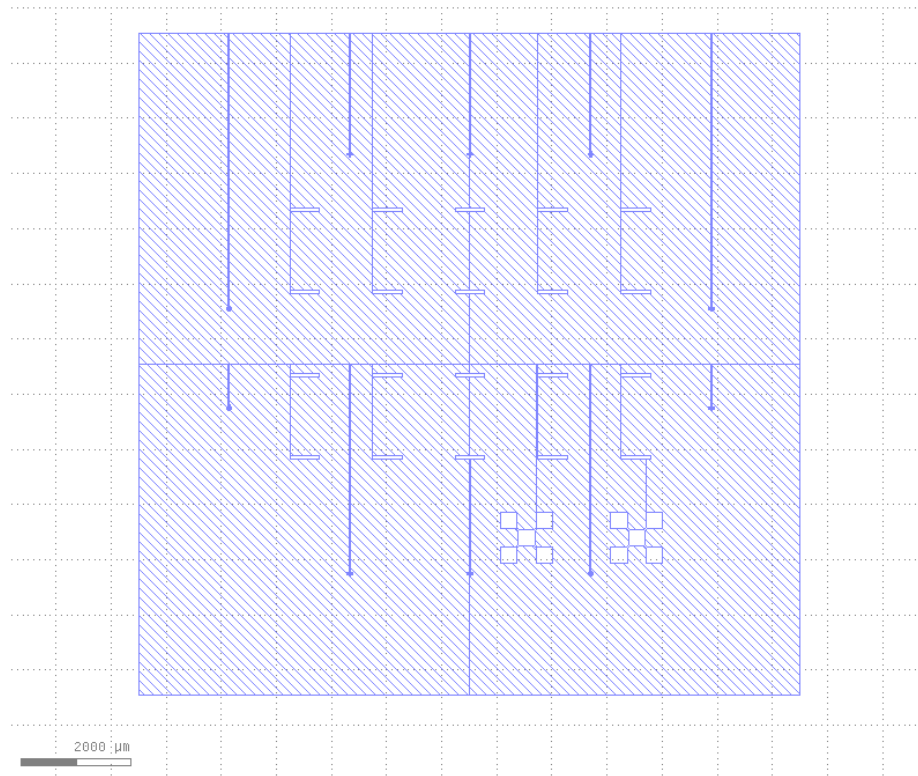


Figure 4.6. Mask used to define the area where Ta is to be deposited.



- If TiN is to be used for the upper diffusion barrier layer, then the next step after the lift off of Cu is to sputter TiN again on the entire workpiece. The sputter tool does not allow use of any organic materials due to concerns of contamination. Therefore, after through cleaning, a substrate with TiN and Cu is coated with 10 nm of TiN at  $1\text{\AA}/\text{s}$ .
- Beyond those two optional steps, the rest of the fabrication process remains the same for the three structures. Post the optional diffusion barrier deposition. A solvent clean is required to ensure all organic contaminants are removed. This is then followed by another mask step to etch the TiN. Again, we use AZ1518 PR on the wafer. This time, the recipe is slightly modified to give a thicker layer of PR. Tab. 4.3 is the modified recipe for this step. The purpose of this mask is to act as a barrier between the chlorine gas and the substrate during TiN etching. Fig. 4.7 is the mask used in this step. It defines the contact pads and the base layer geometry for the Blech structure. After the mask is developed, the regions of exposed TiN will be etched in chlorine gas but, chlorine is known to harden PR. This makes the PR challenging to remove during the strip step. In order to protect the structure underneath, a thicker layer of AZ1518 is coated ( $3\mu\text{m}$ ) compared to  $1.8\mu\text{m}$  in the previous step. The top surface of the PR is removed using Ar plasma etch step in the same RIE chamber. Fig. 4.8 is an optical image of the substrate after the PR is developed for TiN etching.

Table 4.3. Process steps for AZ1518

Process	Details	Time
Spin Coat HMDS	Rotate at 3000 RPM	30 seconds
Spin Coat AZ1518	Rotate at 3000 RPM	30 seconds
Soft Bake	100 °C	4 minutes
Exposure	10 mJ/s	12 seconds
Develop	1:4 AZ400K:DI water	70 seconds
Hard Bake	-	-

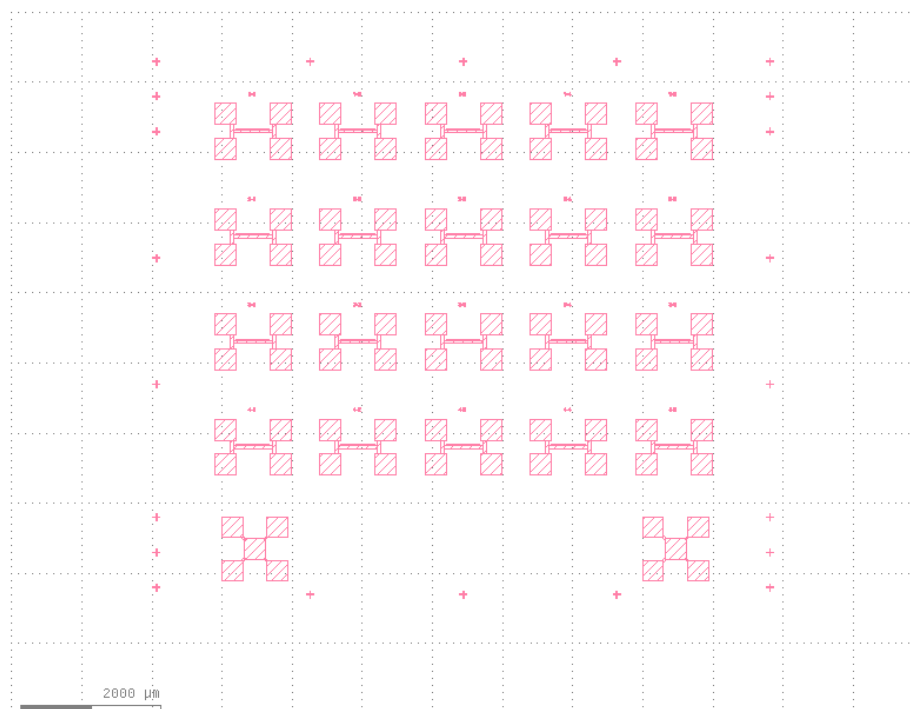


Figure 4.7. Mask for TiN dry etch.

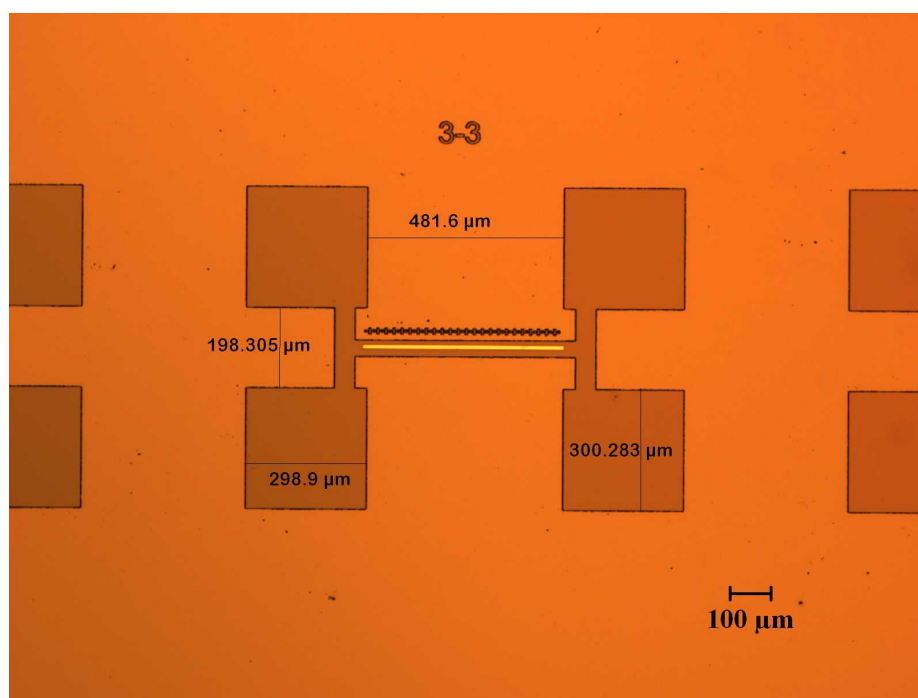


Figure 4.8. Top view of substrate after the PR development for TiN etch mask.

- The RIE etch for TiN is carried out using the process settings shown in Tab. 4.4. This is an abbreviated version of the etch recipe settings. Before the etch step is started, a purge and clean step is required in the chamber to remove any remnants of the contaminants from previous use of the equipment. The test substrate is loaded on to a 6 inch standard Si wafer using crystal bond at 60 °C. The bonded wafer allows better thermal transport and the crystal bond ensures the test specimen does not move during the etch step. The etch times usually vary but were found to be between 2nm/min to 8 nm/min. 5 minute etch steps were carried out each time to determine the etch depth. One way to check complete etch is to check the electrical resistance of the exposed area without the PR and the other is to characterize the depth using a profilometer. After the etch step is completed, Ar gas is used to purge the chamber. Once purged, an Ar plasma is used to etch the top layer of the PR before removal. This helps remove the hardened top layer of PR due to Cl<sub>2</sub>. Details of this process are shown in Tab. 4.5. This etch step was run for 1 minute.

Table 4.4. Process steps for TiN etch recipe

Etch Recipe Details - # 189	
Pressure	0.6 Pa
RF Source	150 W
RF Bias	35 W
Cl <sub>2</sub> Flow Rate	26 cm <sup>3</sup> /min

Table 4.5. Process steps for PR dry etch recipe

Etch Recipe Details - # 134	
Pressure	1.0 Pa
RF Source	100 W
RF Bias	0 W
Cl <sub>2</sub> Flow Rate	40 cm <sup>3</sup> /min

- After confirming complete etching of the TiN, a solvent clean step is used to remove the remainder of the TiN on the substrate. Fig. 4.9 is an optical image

of what the structure looks like after the etch step. Fig. 4.10 is also an optical image after the TiN etch, however this structure has the Ta diffusion barrier layer. Once the substrate is clean it is ready for passivation. PECVD is used to deposit a 20nm layer of  $\text{SiN}_x$  on the substrate. Before deposition is carried out a pre-conditioning step is used where ammonia is used as the only precursor with plasma generated using an RF source of 150W at 300°C. Following this preconditioning step, the test specimens are placed in the chamber which is purged several times to remove oxygen. The settings for the the passivation step are presented in Tab. 4.6.

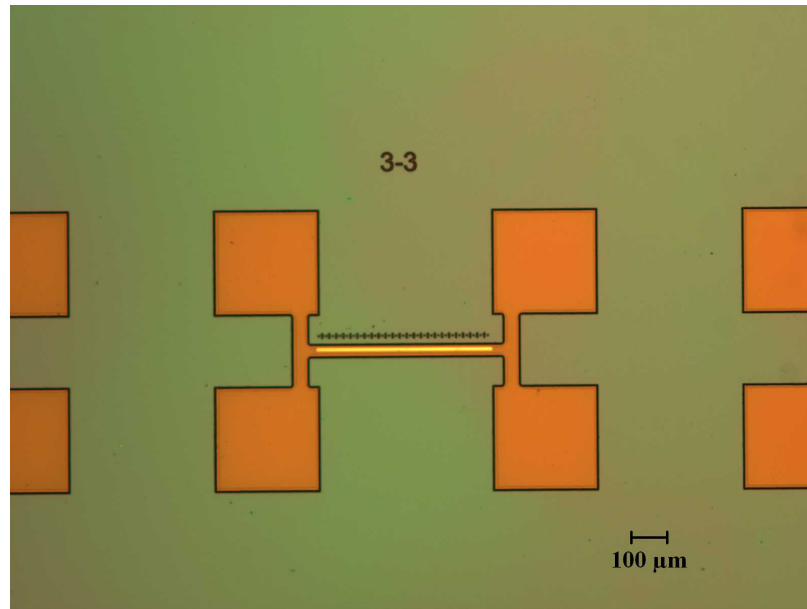


Figure 4.9. Top view of substrate after TiN etch.

- Following the passivation step, we anneal the test specimen in a nitrogen anneal furnace at 350 °C for 3 hours. The anneal step is meant to help facilitate stabilization of the microstructure. The chamber is purged with nitrogen and preheated for several hours before the anneal step.
- The final mask on the test specimen is meant to etch the passivation where the contact pads are present. Fig. 4.11 is the mask used for this step. AZ1518 is

Table 4.6. Passivation process recipe for  $\text{SiN}_x$ 

$\text{SiN}_x$ Passivation Recipe	
Base Pressure	25 mT
Pressure	400 mT
RF Source	150 W
Temperature	300 °C
$\text{SiH}_4$ Flow Rate	120 sccm
$\text{NH}_3$ Flow Rate	100 sccm
Process Time	60 seconds

used with the process recipe discussed in Tab. 4.2. After developing a wet etch in BOE (Buffered Oxide Etch) is carried out for 120 seconds. BOE etches the  $\text{SiN}_x$  passivation with little to no effect on the PR. After the etching step, the wafer is thoroughly rinsed in DI water and the PR is stripped in a solvent clean step. A quick test is performed on the Van der Pauw structure to ensure all passivation is etched.

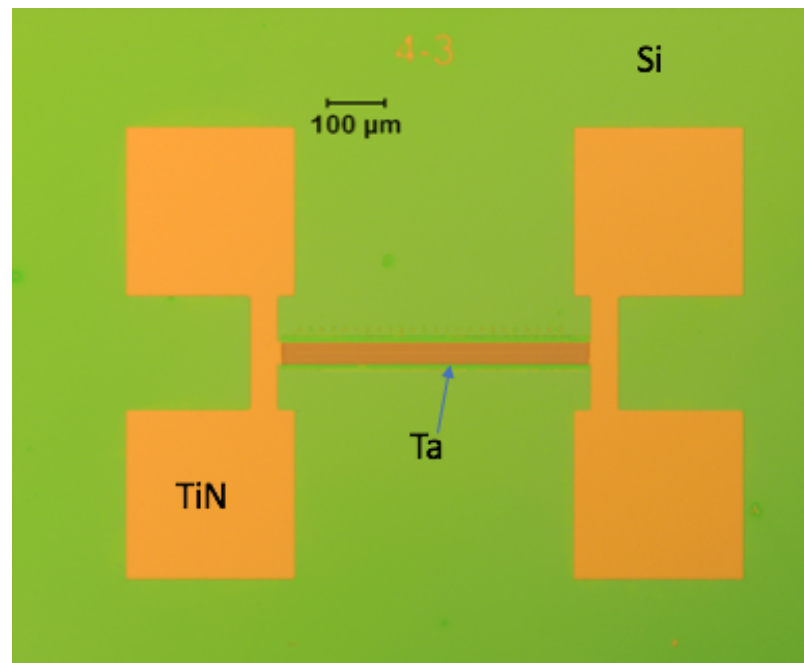


Figure 4.10. Top view of substrate TiN etch with a Ta diffusion barrier layer.

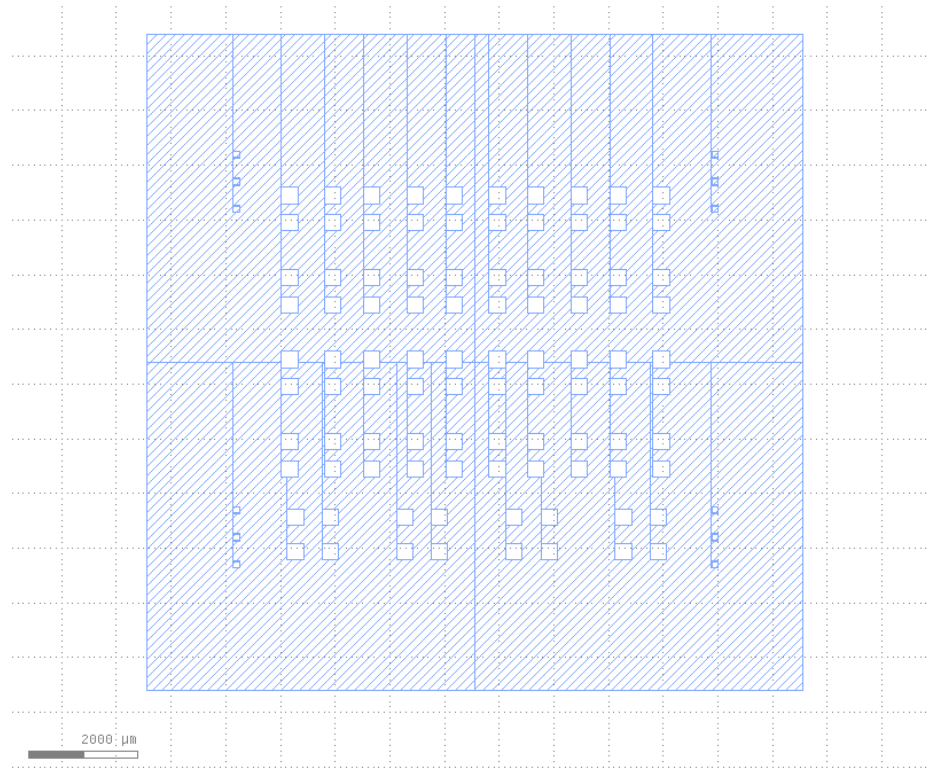


Figure 4.11. Mask for passivation wet etch.

The final cross-section of these test specimens is shown in schematics along with the thickness of each layer in Fig. 4.12.

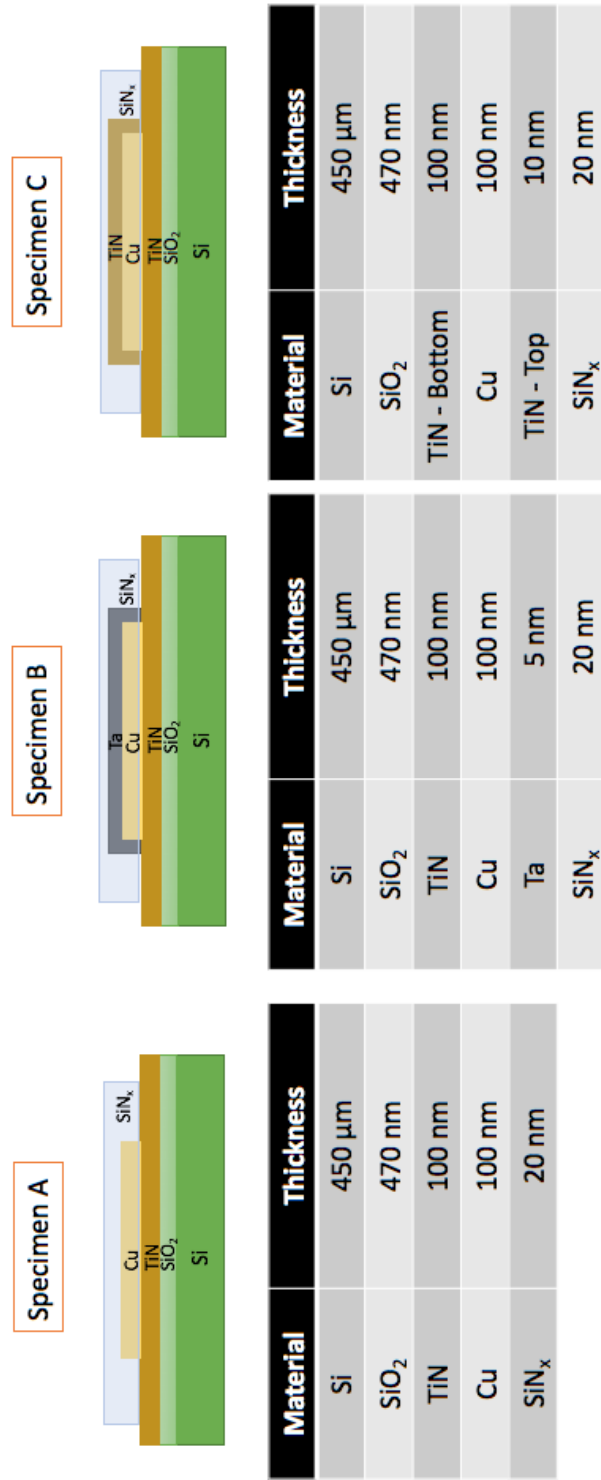


Figure 4.12. Final structure cross-section schematics for the three test specimens.

### 4.3 Fabrication Challenges

Several challenges were encountered during the fabrication of test specimens. We discuss some of the major challenges briefly and the solutions to the process challenges.

- During E-beam lithography, one of the challenges encountered were stitch errors, where a stitched field drifts during the rastering process. These drifts may be due to poor calibration or thermal drifts in the chamber. Fig. 4.13 is an image of the stitch error observed during writing. The discontinuity in the line is where the two fields intersect. However due to thermal drifts, the definition was poor. In some cases the lines were completely disconnected.



Figure 4.13. Stitch error in mask write during E beam lithography leading to poor mask definition.

In order to overcome this challenge all fields were made floating fields with as little overlap as possible. Since the beam can raster a 1mm x 1mm area. All written fields were made smaller than that area.



- During lift-off process for the Cu tear in the film was observed as shown in Fig. 4.14. These tears are a consequence of the deposition of continuous films during evaporation. In order to overcome this issue a thicker photoresist can be used or in the case of E-beam lithography, we used a bi-layer recipe that mimics the negative tone PR sidewall profile. In general, the PR needs to be 3 to 5 times the thickness of the deposited layer.

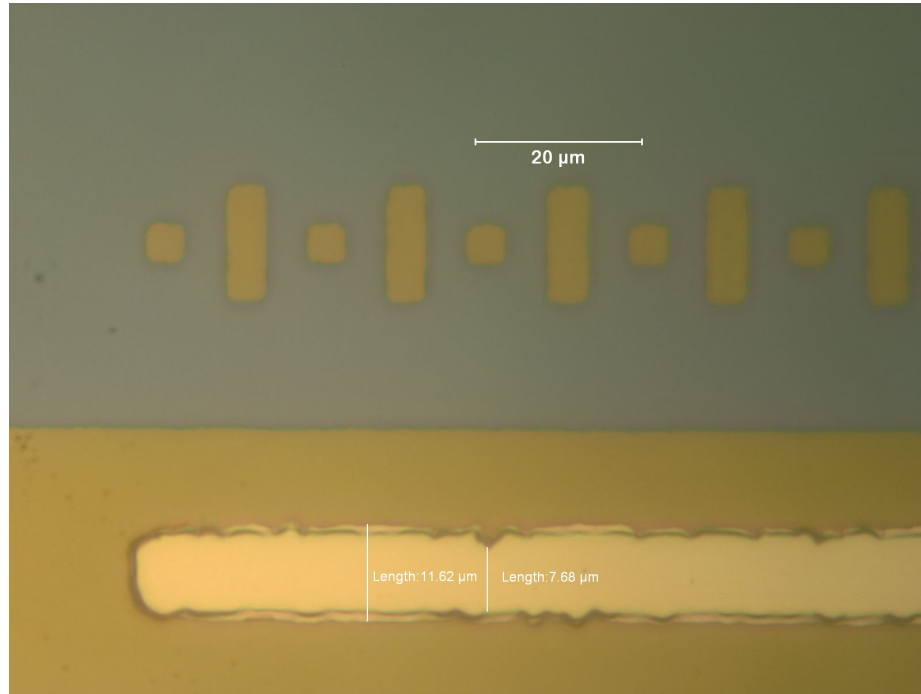


Figure 4.14. Tear in the thin film observed after lift-off.

- During the deposition of Ta, it was observed that the PR had cross-linked due to the high melting temperature of Ta. Images of the cracks developed in the PR after deposition are shown in Fig. 4.15. In order to avoid this issue, we limit the thickness of Ta to 5nm at a high deposition rate to reduce the amount of time the PR is exposed to high temperatures. Additionally, a different method may be used for deposition like plating or sputtering. These options were unfortunately not available at the time.

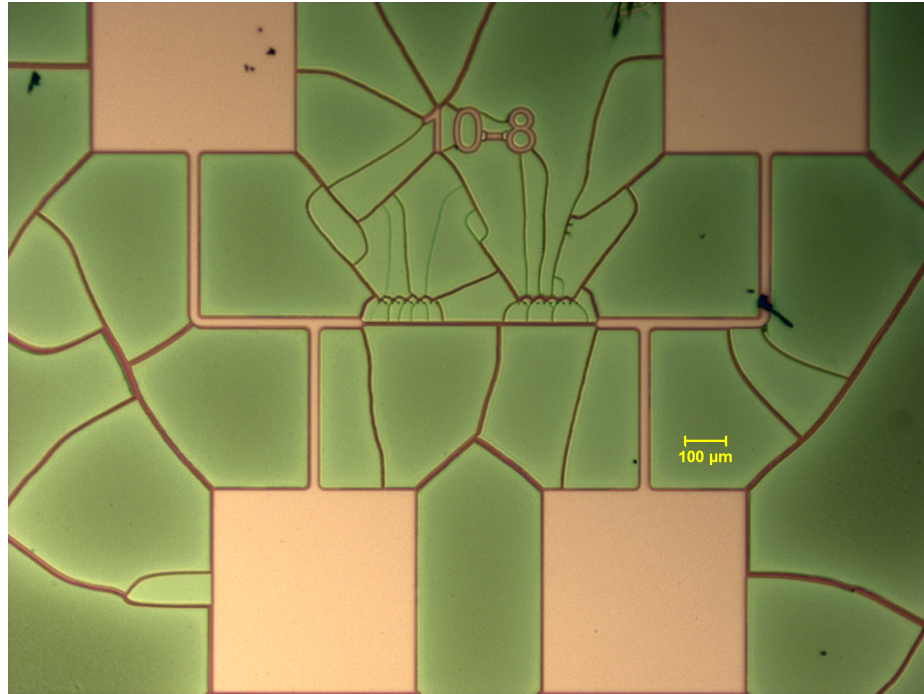


Figure 4.15. Crack formation in PR due to high temperature exposure during Ta deposition.

- Initially a wet etch recipe was used for etching TiN. BOE was used as the etchant with a known etch rate of 5nm/min [77]. However, the etching was not ideal as it caused bubbling of the film and non uniform etch rates over the entire test specimen. In order to etch TiN we now rely on a dry etch recipe that utilizes chlorine in the presence of a plasma. The etching recipe seems to work well, though the etch rates may vary a bit requiring far more intermediary etch steps and monitoring.
- Even though the dry etch recipe for TiN works well, one of the challenges with the dry etch is the definition of a mask for the etch. Traditionally a hard mask such as SiO<sub>2</sub> or Nickel (Ni) are used for dry etching. However, with our test structure this is not a possibility as it would require further steps to etch the hardmask which may damage/corrode the Cu lines. We rely on photoresist as

a mask for this step. Chlorine used in this recipe is known to dry and harden the top layer of the photoresist, making it a challenge to remove post etch.

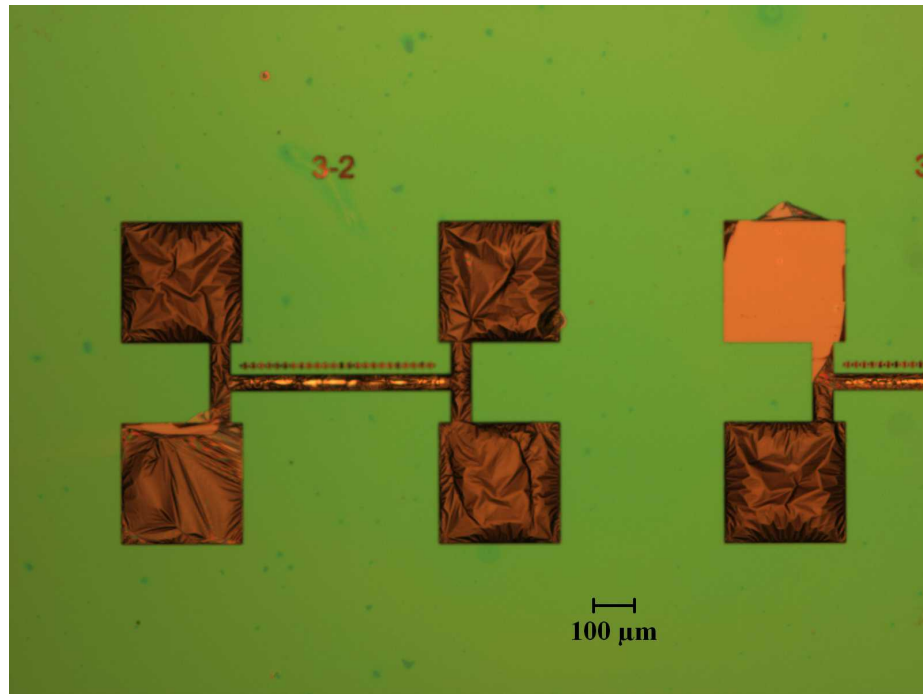


Figure 4.16. Hardened top surface of the PR mask for TiN etching.

Since, we use PR as the mask with TiN and Cu both already deposited, we cannot use piranha etch, sonication in solvents or ashing to clean the PR residue. Each of these steps will oxidize/corrode or crack the Cu film. Our solution is to do a short Ar plasma etch to remove the top layer of the PR. Using Ar ensures oxidation is not a concern. Once the top layer of the PR is removed the rest of the PR can be stripped in a solvent solution.

## 5. TEST SETUP AND EXPERIMENTAL PLAN

In this chapter, the needs for a tester listed based on the scope of the study. The final design for the testing apparatus is presented along with the capabilities. A set of experiments and the testing procedure are then presented at the end of the chapter

### 5.1 Development of Test Setup

#### 5.1.1 Tracking Voids and Failures

Most of the in-situ electromigration studies described earlier involve the development of a custom built test bench to monitor failures. Blech's original work also involved tracking interface velocity using an optical microscope. However, since our devices are scaled down to a few microns, accurately measuring the void growth rate is challenging. Most optical microscopes are diffraction limited by the visible spectra of light at high magnifications. Rayleigh's diffraction limited resolution is used to calculate the resolution of a microscope and is given by the expression:

$$r = \frac{1.22\lambda}{NA_{Obj} + NA_{Cond}} \quad (5.1)$$

Here,  $r$  represents the minimum spacing between easily distinguishable or well resolved objects,  $\lambda$  is the average wavelength of illumination in visible light and NA is the objective numerical aperture. NA is based on the refractive index ( $n$ ) of the medium between the objective and the sample multiplied by the sine of the aperture angle  $\theta$ . The constant 1.22 is derived from Rayleighs work on Bessel Functions. These are used for calculating problems in systems such as wave propagation. The maximum angular aperture of an objective is around  $144^\circ$ . The sine of half of this angle is 0.95. If using an immersion objective with oil, which has a refractive index of 1.52, the

maximum NA of the objective will be 1.45. If using a dry (non-immersion) objective, the maximum NA of the objective will be 0.95 (as air has a refractive index of 1.0). Taking the NA of the condenser into consideration, air (with a refractive index of 1.0) is generally the imaging medium between the condenser and the specimen. Assuming the condenser has an angular aperture of  $144^\circ$ , then the NA<sub>cond</sub> value will equal 0.95. Using green light of 514 nm, an oil immersion objective with an NA of 1.45, condenser with an NA of 0.95, then the (theoretical) limit of resolution will be 261 nm [78]. Most optical systems are not as complex and will typically have a resolution lower than the one predicted by the Rayleigh criterion. For this reason, we will need to rely on an SEM to track displacements after each interval of testing. That is the first requirement for the test setup. The test rig should be compatible with a SEM.

### 5.1.2 Resistance Measurements

Since, our test structure is a Blech like structure, there is a possibility that the base layer fails due to some critical flaw during fabrication or poor design. If the resistance of the base layer is large or the current flowing through it is large, it is possible for joule heating to be a concern. One way to ensure such failures are correctly identified is to monitor resistance change over time. If the failure is not visible from imaging then the failure in the base layer is captured by the resistance change in the structure. One issue with subjecting multiple test structures to electromigration is that this method may not determine which structure failed unless they are checked individually. For this reason we will focus on single structures at a time. We also need to be able to measure the resistivity of Cu, TiN and Ta separately as a function of temperature. A known method in literature for accurate resistance monitoring is based on 4-wire Kelvin measurements. Here two probes act as the current carrying source and the other two are used to measure the voltage drop across that length. The advantage of using a 4-wire measurement is that it eliminates the additional resistance that comes

from the leads and the probe itself. Fig. 5.1 shows the basic circuit diagram for a 4-wire setup.

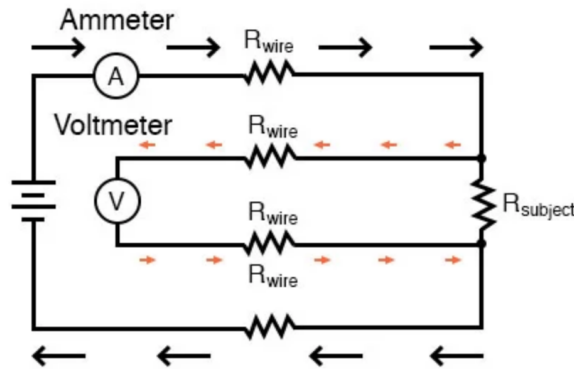


Figure 5.1. Circuit for a 4-wire resistance measurement setup [79].

At first, it may appear that any advantage is lost by measuring resistance this way, because the voltmeter now has to measure voltage through a long pair of lead wires, introducing stray resistance back into the measuring circuit. However, the voltmeter's wires carry minuscule current. Thus, those long lengths of wire connecting the voltmeter across the subject resistance will drop insignificant amounts of voltage, resulting in a voltmeter indication that is very nearly the same as if it were connected directly across the subject resistance.

### 5.1.3 Temperature Control

Final consideration for the test setup is the ability to carry out tests at an elevated temperature. Diffusion processes like electromigration are dependent on the local temperature. In order to subject the test specimen to a higher temperature, there are two options. Either the test is carried out in an environmental chamber where the ambient temperature is raised to the desired value or the test specimen is heated locally. Many reliability studies rely on carrying out tests on several boards at a given time and for those studies it is usually suitable to carry out the test in a controlled environment. However, since we require the test setup to be usable in a SEM we need

to utilize a local heat source. Accurate measurement of the temperature and control of the heating is crucial to this study.

## 5.2 Design of Test Apparatus

### 5.2.1 Design Requirements

The design for the test setup is dictated by the restrictions on size and weight allowable in the SEM. The SEM used in this study is a field emission FEI Quanta 650 SEM. It has a magnification capability up to 1,000,000x with resolution as low as 1.2nm (30kV, high vacuum). It comes equipped with two detectors (EDT - Everhart Thornly Detector and CBS - Concentric Backscatter). It has a slightly larger chamber compared to other benchtop SEM's however, size is still a constraint with the motorized stages for sample manipulation. The weight constraint is set at 1.2kg and the size of the device is required to fit over the existing stage without interfering with the other electronics. In order to probe the test structures, we chose to use needle probes to make contact with the device. The other approach would be to wirebond and route the circuit through a custom printed circuit board. We chose the former approach for its flexibility specially, in the early part of the testing where designs might need to be changed. As discussed previously we require a four wire resistance measurement so at least four needle probes are needed. In order to place the needles on the device and manipulate them in the SEM separate stages are required which are compatible in vacuum. Finally a good current source is required and a power supply to a heating source. We require atleast four such needle probes that can be moved within the SEM. Independent stages that are capable of moving in three directions are needed. The stages would need to be vacuum compatible and have a small step size for motion. Lastly we need to be able to carry out tests at an elevated temperature. To achieve this we must rely on a local heat stage that has low power consumption and the capability to be controlled with a feedback loop. One of the challenges to overcome with the test setup is the ability to make connection

between the electronics outside the chamber and the stages/probes inside the SEM chamber. This requires designing custom flanges with hermetic connectors that will hold under vacuum.

### 5.2.2 Final Design

First, we break down functionality and determine the overall design strategy for the test setup. Fig. 5.2 is an overview of the various components on the instrument and their input/outputs.

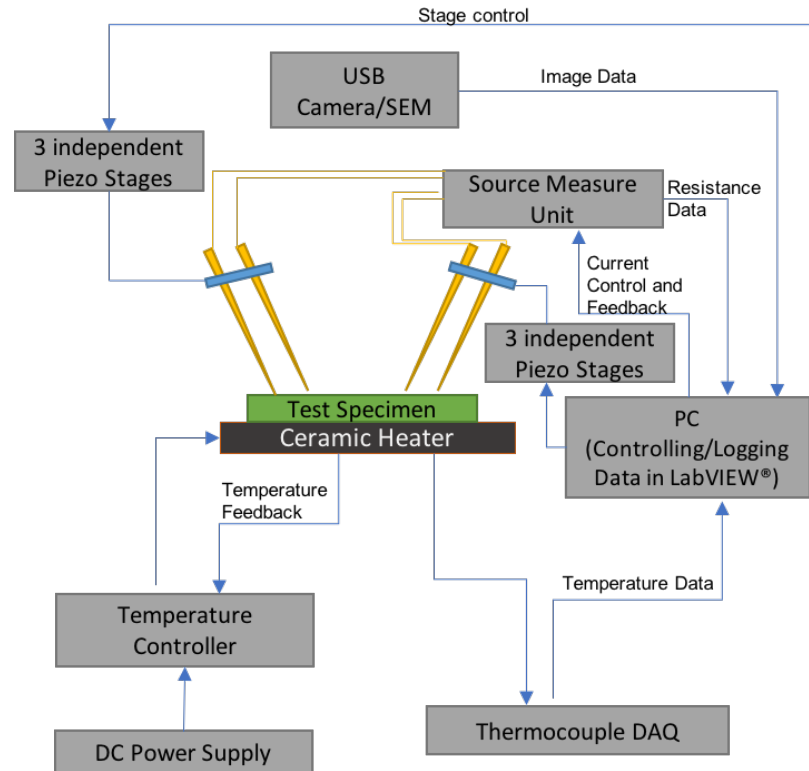


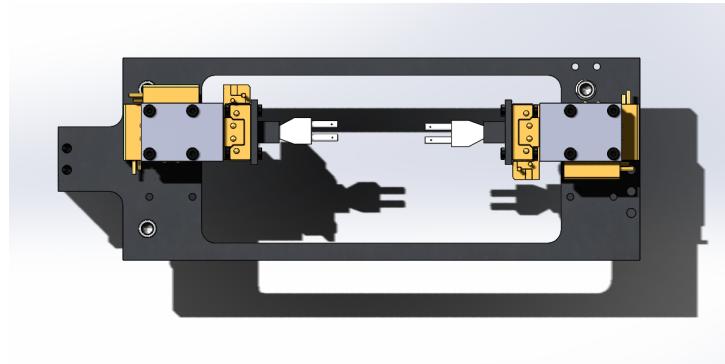
Figure 5.2. Schematic of test setup control and feedback loop.

One the decisions made early in the design phase was to select motorized stages rather than manual manipulators which were bulky and vacuum incompatible. An advantage to using motorized stages is that it allows manipulation without breaking vacuum in the chamber. The stages chosen for this setup were the AG-LS25V6 series

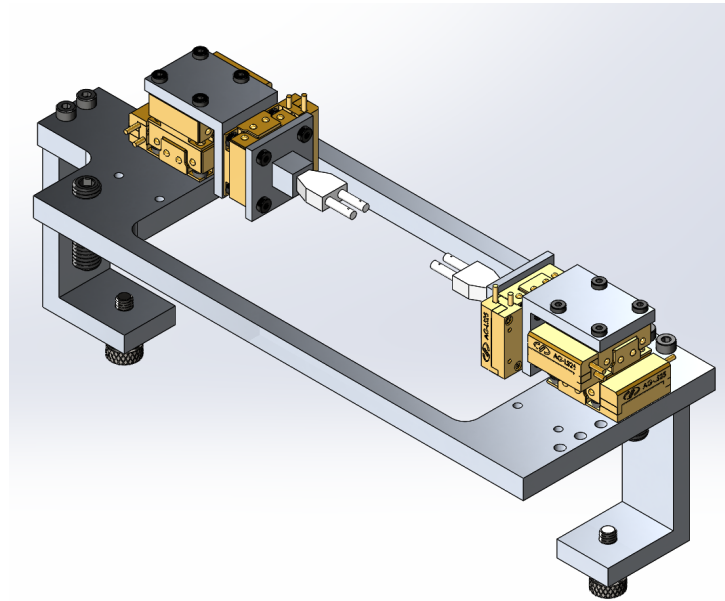


from Newport. These stages are vacuum compatible piezo motor driven linear stages rated for  $10^{-6}$  hPa. They have a 12 mm travel and precision motion is achieved by calibrated, pre-stressed linear ball bearings. The minimum step size for this stage is  $0.05\mu\text{m}$  with no secondary feedback. The stages are controlled through an 8 channel AG-UC8 controller that comes with a stand alone software. In order to reduce the number of stages required for the 4 wire resistance measurements we chose dual needle probe holder from American Probe Technologies. These probe holders are designed to accept 20 mil replaceable probes. The probe holder comes with two 74B-1/45 x 1" holders mounted into an Ultem insulator with a single 0.125" mounting shank. A twinaxial cable is connected to each holder for electrical connections. With this design, we have six independent linear stages with two mounted probe holders. Fig. 5.3 is a top view of the stages and probe holder mounted on an aluminum plate. Three stages are mounted on each side to allow motion in all three directions.

The plate shown in this schematic rests upon the existing stage on the SEM. If the setup is placed outside the SEM, then it rests on the three M-10 screws with ball bearing ends that can be adjusted for planarity. For imaging outside the SEM, we use a Keyence VH-250L long distance working lens mated to a FLIR camera. With this imaging, it is possible to resolve objects down to  $1\mu\text{m}$  at the highest magnification (500X). The advantage of this lens is the large field of view so the entire line being tested can be imaged. To heat the sample, we use the HTS24 (20mm x 20mm) 24W resistive ceramic heater from Thor Labs. The heater is connected to a temperature controller 5B7-388 from Oven Industries with a T-type thermocouple feedback attached to ceramic heater. The temperature controller comes with standalone software with PID control for the heater. Finally, the most critical component for this setup is the current source. We use the Keithely 2450 sourcemeter that is capable of nA resolution as a constant current source. Fig. 5.4 is the final test setup in ambient conditions with the optical imaging system. Fig. 5.5 is the same system in the Quanta 650 SEM.

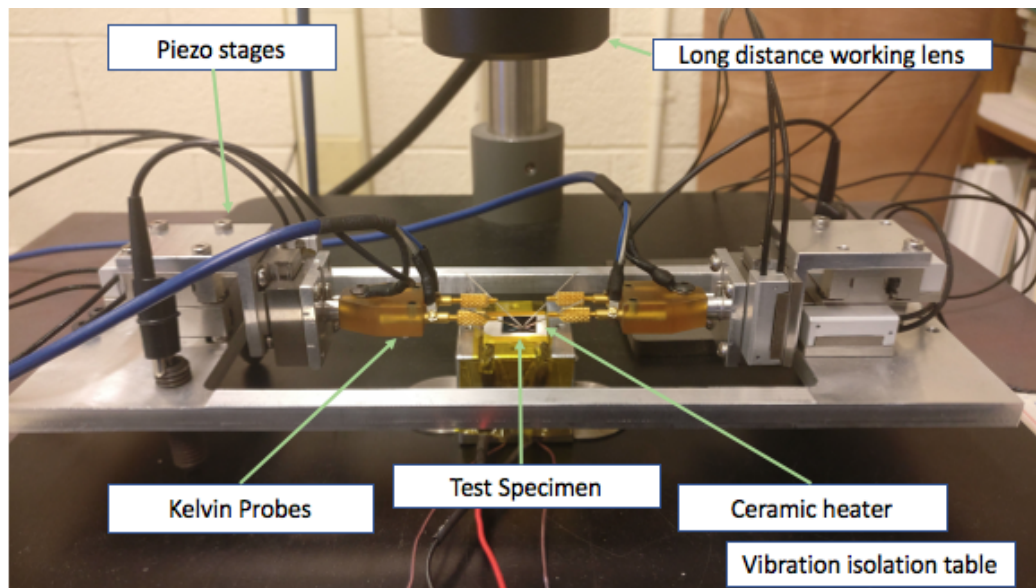


(a)

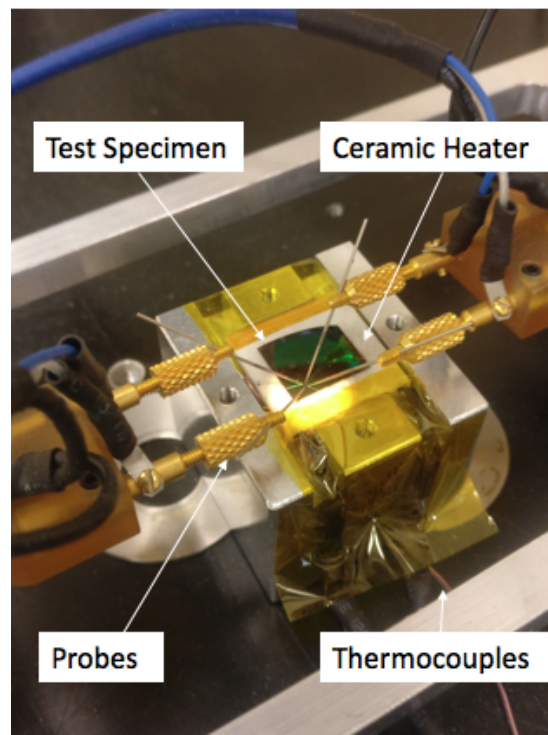


(b)

Figure 5.3. CAD image for the designs of the test setup (a) Top view of the CAD model with the aluminum plate with the stages and probe holder (b) Isometric view of CAD model with the aluminum plate with the stages and probe holder.



(a)



(b)

Figure 5.4. (a) Test setup for ex-situ experiments under an optical microscope (b) Test specimen holder with the ceramic heater and needle probes.

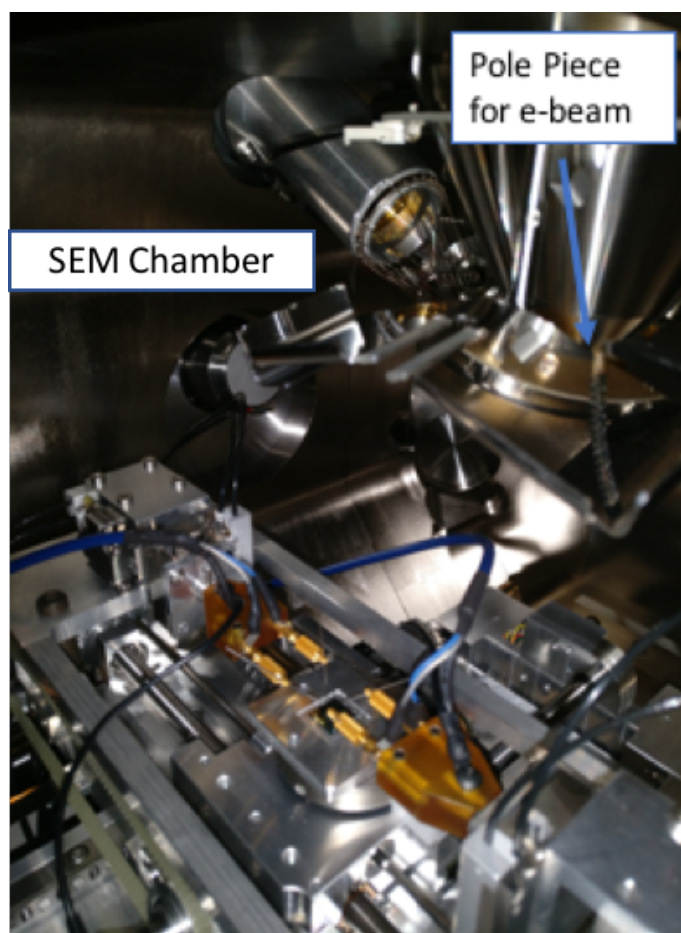


Figure 5.5. Test Setup in the SEM chamber for in-situ experiments.

For logging data and images, we use an integrated National Instruments Labview program. Fig. 5.6 is a snapshot of the GUI for the tester in Labview. This is so that information is synced in time. The information logged is the resistance value obtained from the sourcemeter and the optical images if the test is being carried out in ambient conditions.

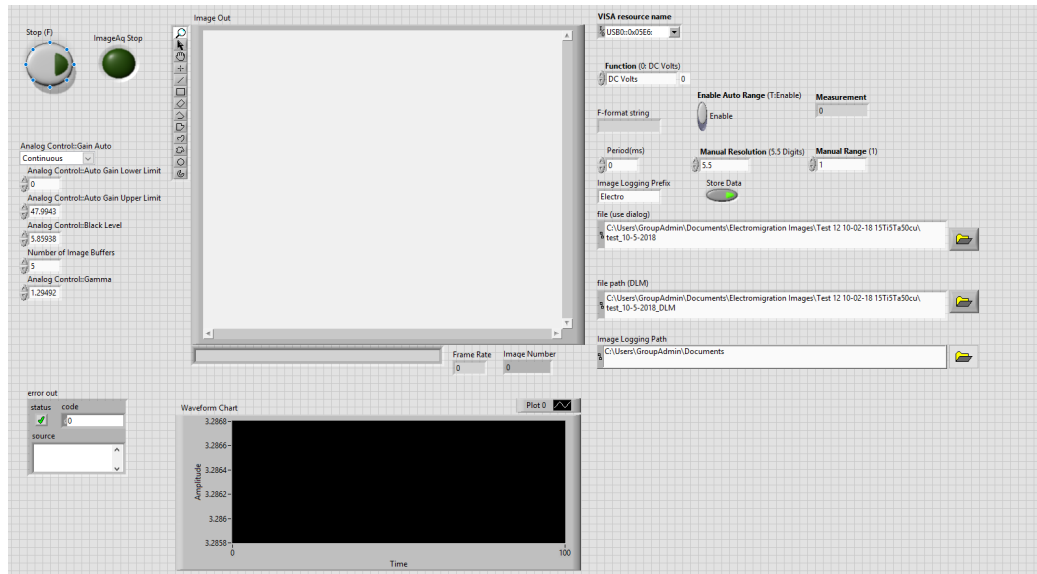


Figure 5.6. Image of the front diagram GUI in Labview.

The highlights of the tool capabilities are as follows:

1. Ex-situ and in-situ testing capability
2. Vacuum compatible setup with 6 independent piezo stages for probe manipulation
3. 4-wire resistance measurement with current control in the nA range
4. Temperature controlled heating stage for local temperature excursions with accuracy of 1 % of test temperature
5. Integrated control and data logging through Labview

Table 5.1. Table of resistivity measured at room temperature.

Material	Resistivity $\rho$ [ $\Omega - \mu m$ ]
<i>Cu</i>	0.16
<i>Ta</i>	0.74
<i>TiN</i>	3.13

### 5.3 Preliminary Measurements

Before any electromigration experiments are carried out we need to characterize the resistivity of the films that are deposited. We use Van der Pauw method and structure to capture the resistivity of different conductive materials used in our test structure. These are, namely, Cu, Ta and TiN. Most importantly we need to characterize this as a function of temperature. We incorporated these features on the test specimen during fabrication, so each sample is individually characterized.

For the Van der Pauw structure certain conditions have to be met [80]:

1. The sample must have a flat shape of uniform thickness
2. The sample must not have any isolated holes
3. The sample must be homogeneous and isotropic
4. All four contacts must be located at the edges of the sample
5. The area of contact of any individual contact should be at least an order of magnitude smaller than the area of the entire sample.

Tab. 5.1 are the resistivities noted for each material at room temperature. We can see that the resistivity of copper is the lowest, hence, during testing a large portion of the current would be diverted from the TiN into Cu. Additionally, Ta is only 5nm in the structure so its resistance would be large and the current carried by Ta will be very low.

On each device, there are two additional test structures with no Cu on them. These serve as structures where the resistance is measured for the TiN or TiN/Ta. In a real test structure the Cu strip would act as a parallel circuit. In the absence of a large contact resistance, the difference between the two structures can be used to quantify the resistance of the Cu line. We will this approach to determine the fraction of the current is flowing through the Cu line. We use these base structures to also characterize the change in the resistance of the structure as a function of temperature. Fig. 5.7 is an example of the characterization of resistance when the temperature is increased from RT to 275 °C. As expected the resistance increases fairly linearly with increase in temperature. There is however, some variation between devices. For this reason we characterize the base resistance separately for every substrate.

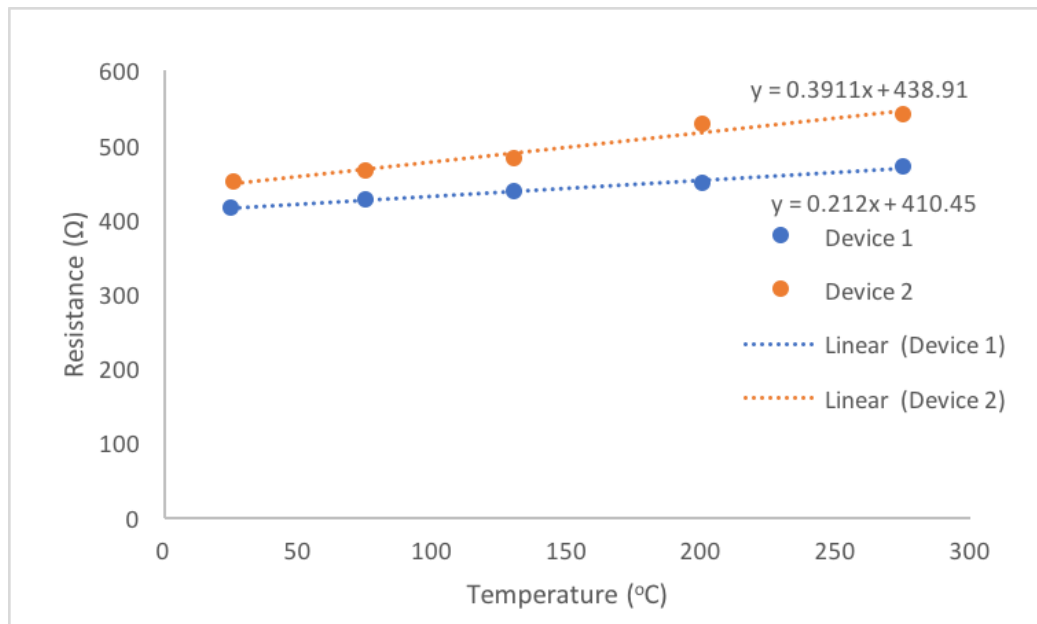


Figure 5.7. Variation in resistance for two TiN structures (deposited at different times) as a function of temperature.

## 5.4 Test Plan and Procedure

A process flow for the experiments is shown in Fig. 5.8. As mentioned in the previous section, we start with a preliminary evaluation of the film sheet resistance and the resistance of the base TiN structure without the Cu lines at varying temperatures. Once the trends are known for the particular substrate we assume similar behavior for all test structures on that substrate. Next, the test specimen is heated to the desired test temperature and the needle probes are lowered on to the test structure. Some of heat is lost to due to conduction once the needle probes are lowered. A small current is passed (1 mA) through the test structure to ensure the circuit is closed. This also serves to provide a resistance value for the test structure from which the resistance of the Cu line is calculated. The portion of current flowing through the Cu line is then determined and a new current output value is chosen. This current represents the total current flowing through the circuit which will split at the junction between Cu and TiN giving the desired current density for Cu. The desired current value, test length interval and image acquisition intervals are input into the Labview program. Once the test interval is complete the current source and heater source can be turned off. Images of the test structure are taken after the interval of testing and the void growth is measured. Once the measurement is complete the test can be resumed.

We start by considering the variation in the test structure geometry. Most of the test structure features are kept constant except the width. The rational behind this decision was discussed in Chapter 3. The details of the geometry are shared in Tab. 5.2. The purpose here is to determine the width of test specimen that gives the most consistent interface velocity and where the continuum approximation holds.

In another set of experiments, the temperature is varied while keeping the geometry and current density fixed. The temperature range is chosen such that the homologous temperature  $T_m < 0.5$  for the tests. At higher temperatures, bulk diffusion starts to becomes prevalent along with grain boundary diffusion. Diffusion rates for Cu at 100 °C and 350 °C are shown in Fig. 5.9.



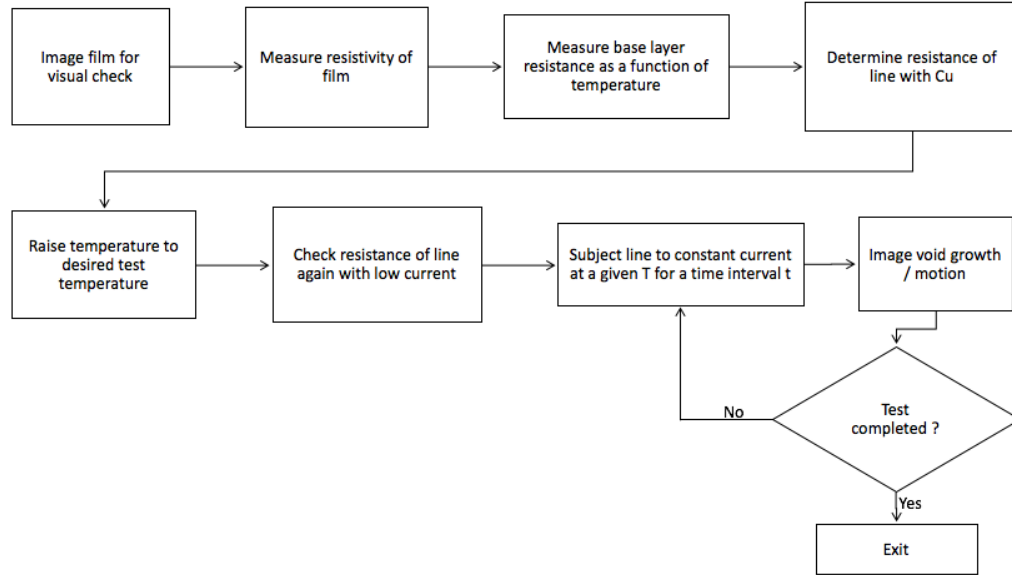


Figure 5.8. Process flow used for the electromigration tests.

	Melting point (K)	Temperature ratio 373 K/(T m)	Diffusivities at 100°C (cm <sup>2</sup> /s)	Diffusivities at 350°C (cm <sup>2</sup> /s)
Cu	1356	0.275	$D_l = 7 \times 10^{-28}$ $D_{gb} = 3 \times 10^{-15}$ $D_s = 10^{-12}$	$D_l = 5 \times 10^{-17}$ $D_{gb} = 1.2 \times 10^{-9}$ $D_s = 10^{-8}$
Al	933	0.4	$D_l = 1.5 \times 10^{-19}$ $D_{gb} = 6 \times 10^{-11}$	$D_l = 10^{-11}$ $D_{gb} = 5 \times 10^{-7}$

Figure 5.9. Diffusivities for surface, grain boundary and lattice diffusion of Cu and Al [81].

The next set of tests is meant to study the effect of current density variation on the void interface velocity. The range of test current densities chosen here are based on prior literature on Cu electromigration, details are shown in Tab. 5.3. The test temperature is fixed in this case at 275 °C to accelerate the rate of diffusion.

Beyond the electromigration tests, evaluation of the microstructure of the films is also required. EDS and EBSD will be used for analysis of the chemical composition and characterization of orientation and average grain size of the films.

Table 5.2. Test Structure Variation

Interface	Length $\mu\text{m}$	Width $\mu\text{m}$	Thickness nm	Base layer thickness nm	Base layer width $\mu\text{m}$
TiN/Cu/SiN <sub>x</sub>	500	0.5	100	100	40
		2			
		5			
		10			
		20			
TiN/Cu/TiN	500	0.5	100	100	40
		2			
		5			
		10			
		20			
TiN/Cu/Ta	500	0.5	100	100	40
		2			
		5			
		10			
		20			

Table 5.3. Test plan: Current density variation

Interface	Test Current density A/cm <sup>2</sup>	Test Temperature °C
TiN/Cu/SiN <sub>x</sub> (500 $\mu\text{m}$ / 100 nm/ 10 $\mu\text{m}$ wide)	1x10 <sup>5</sup>	275
	5x10 <sup>5</sup>	
	1x10 <sup>6</sup>	
	2x10 <sup>6</sup>	
	3x10 <sup>6</sup>	
TiN/Cu/Ta (500 $\mu\text{m}$ / 100 nm/ 10 $\mu\text{m}$ wide)	1x10 <sup>5</sup>	275
	5x10 <sup>5</sup>	
	1x10 <sup>6</sup>	
	2x10 <sup>6</sup>	
	3x10 <sup>6</sup>	

Table 5.4. Test plan: Temperature variation

Interface	Test Temperature °C	Test Current density A/cm <sup>2</sup>
TiN/Cu/SiN <sub>x</sub> (500 $\mu$ m/ 100 nm/ 10 $\mu$ m wide)	130	3x10 <sup>6</sup>
	200	
	230	
	250	
	275	
TiN/Cu/TiN <sub>x</sub> (500 $\mu$ m/ 100 nm/ 10 $\mu$ m wide)	130	3x10 <sup>6</sup>
	200	
	230	
	250	
	275	
TiN/Cu/Ta (500 $\mu$ m/ 100 nm/ 10 $\mu$ m wide)	130	3x10 <sup>6</sup>
	200	
	230	
	250	
	275	

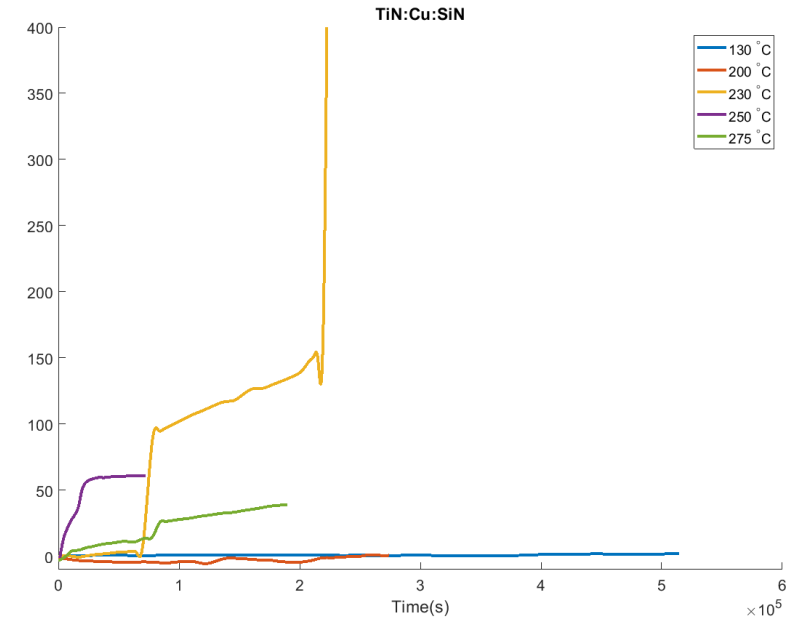
## 6. EXPERIMENTAL RESULTS

In this section we present the results from electromigration tests. Results from resistance monitoring are discussed for the different test conditions. EDS and EBSD characterization is carried out to obtain information on the chemical composition and the microstructure of the films. Length of voids as a function of time, temperature and current density are plotted for the different capping/diffusion barrier layers to obtain interface velocities.

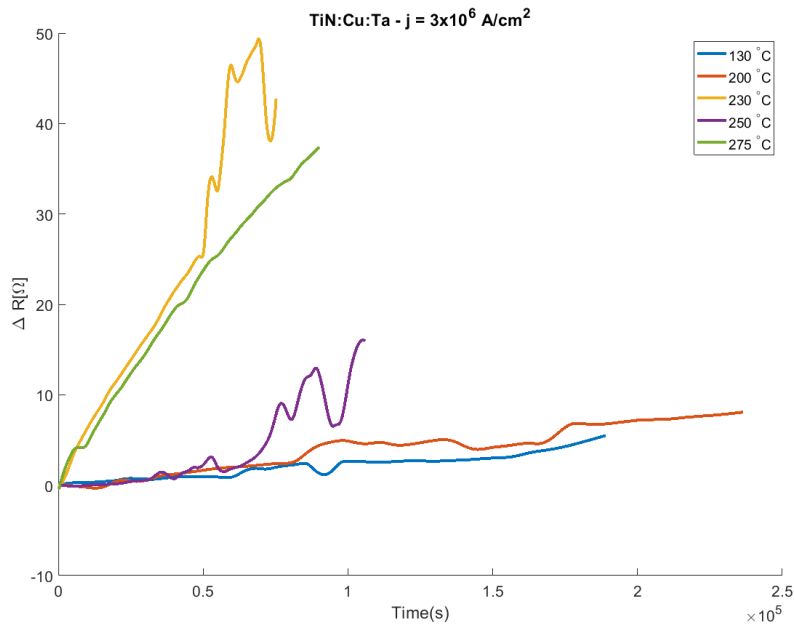
### 6.1 Resistance Measurement

Resistance measurement in this study serves to determine the base resistance of the the Cu line and the TiN base layer. Data is collected at 1Hz using the 4-wire resistance method. Fig. 6.1 shows the change in resistance for varying temperatures in the range 130°C to 275°C. Each of these lines is an evaporated Cu line that is 10  $\mu m$  in width and 500  $\mu m$  long with a thickness of 100  $nm$ . At higher temperatures and higher current densities, the time for testing is shorter. The shortest interval for testing is 2 hours at 275°C with a current density of  $3 \times 10^6$  A/cm<sup>2</sup> and the longest interval for testing is 48 hours at 130°C and current density of  $3 \times 10^5$  A/cm<sup>2</sup>.

As discussed in the previous chapter, these tests were carried out in intervals for measurement of the length of voids that form at the cathode end. The presented data is spliced together for the entirety of the test. A smoothing function (leoss) is used in Matlab to filter out abrupt jumps that were recorded due to vibrations in in surroundings. This was later resolved using a vibration isolation table. During the tests, there are multiple samples on the same substrate, even though they are not subject to a direct current, they experience a temperature excursion which results in oxidation of the TiN contact pads. Following SEM imaging after each interval



(a)



(b)

Figure 6.1. Resistance change observed for test structures subject to varying temperatures at a fixed current density  $j = 3 \times 10^6$  A/cm<sup>2</sup> (a) Test structures with SiN capping layer (b) Test structures with Ta diffusion barrier layer (c) Test structures with TiN diffusion barrier layer.

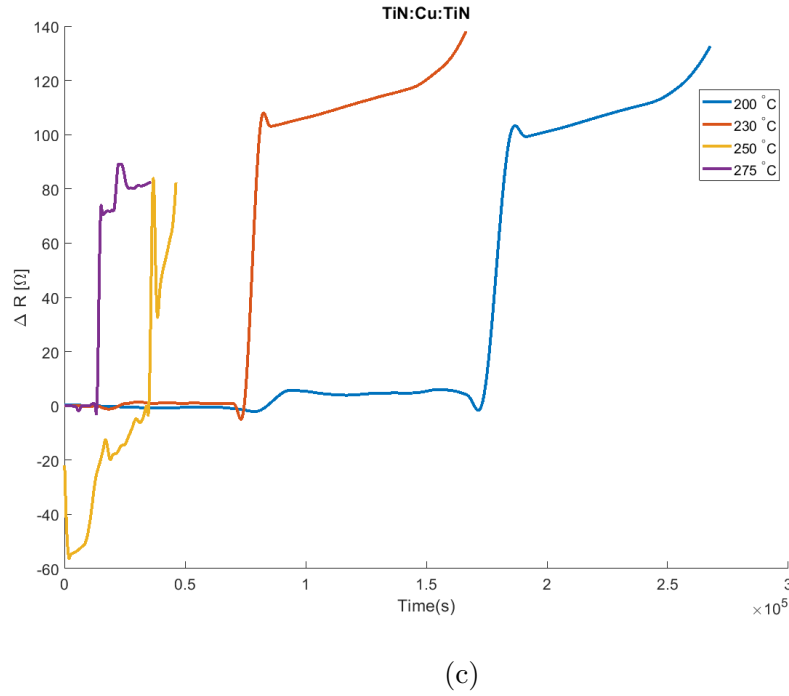


Figure 6.1. Continued.

of testing, these jumps in resistance were consistently recorded. During the test, specially at higher temperatures and high current densities the contact pads undergo some oxidation.

Even though TiN is relatively resistant to oxidation some surface oxidation is expected over time which would lead to a lowering of its electrical conductivity. We confirm this through EDS (Energy dispersive spectroscopy). Usually during reliability tests, this is not a concern because the structures are either completely embedded or tested in an  $N_2/Ar$  environment.

Some tests failed after a few intervals of testing like the 230 °C for the SiN capping layer and 250 °C for Ta diffusion barrier layer. The test structure with  $SiN_x$  failed because of a scratch formed when the test structure was being transferred from under the needle probes. As a general trend, resistance values increased more rapidly if the test temperature was higher. At 130°C and 200 °C the resistance change was

minimal. The test structures with TiN appeared to have a larger jump in resistance after the interval of testing, suggesting a pronounced oxidation of the test specimen.

A second set of experiments were carried out with varying current densities at fixed temperature of  $T = 275^\circ\text{C}$ . Fig. 6.2 is the resistance change noted for the different tests as a function of the varying current densities. At higher current densities the resistance change is rapid and so the test intervals were kept short. At low current densities there is very minimal change in the resistance. Here the data is presented without the smoothing function. Similar behavior is observed for both the Ta diffusion barrier layer structures and the SiN capping layer structures.

The abrupt jump in resistance values for Fig. 6.2b correspond to the second interval of testing. However, none of these cases presented fail due to joule heating, which is confirmed through SEM imaging. The rise in resistance values does however affect the local temperatures. If the rise in temperature is gradual, the temperature controller compensates for the temperature change by lowering the power supplied to the resistive heater.

Some, test specimens early on in this study were of a smaller cross-section with a thinner base layer. These devices failed due to joule heating. We present cases where such failures were observed in the next section.

### 6.1.1 Joule Heating

Joule heating failure is a major concern for electromigration testing. We briefly discussed monitoring resistance to determine joule heating failures in an earlier chapter. These failures usually appear as abrupt and rapid rise in resistance values. The power for joule heating is given by the expression:

$$P = I^2 R = j^2 \rho V \quad (6.1)$$

where,  $I$  is the current and  $R$  is the resistance of the line. The rewritten form is expressed in term of  $j$ , the current density.  $\rho$  is the resistivity and  $V$  is the volume

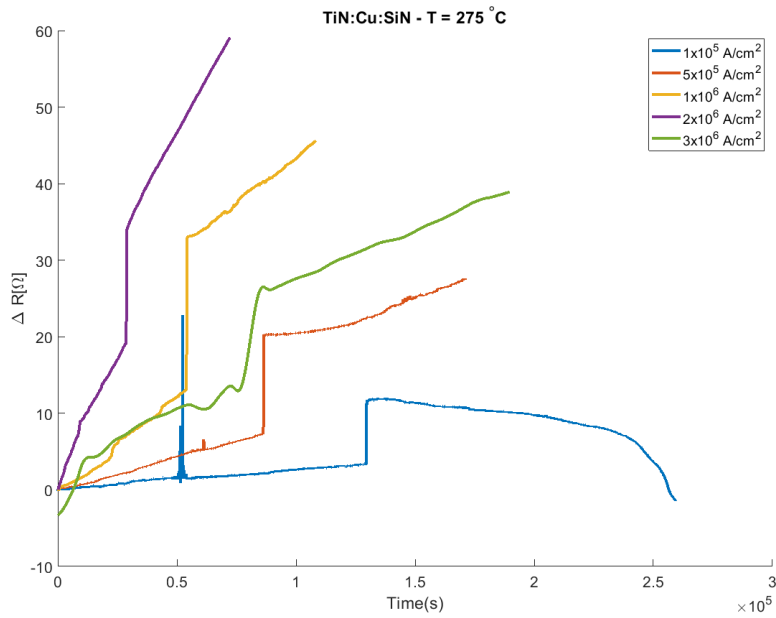
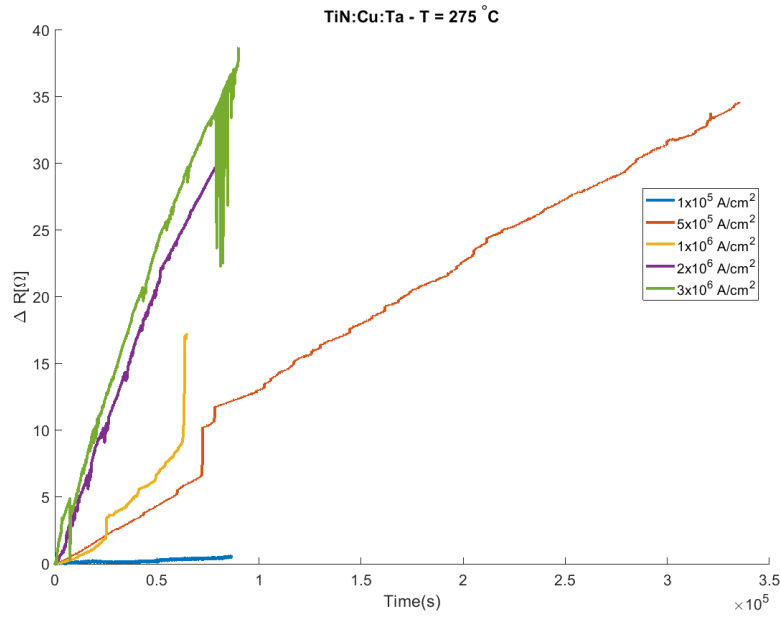
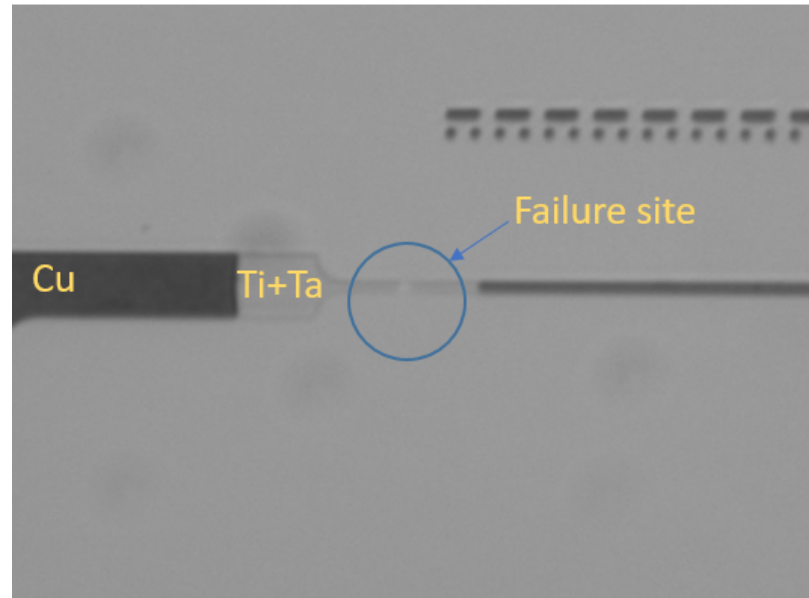


Figure 6.2. Resistance change observed for devices subject to varying current stressing conditions at a fixed test temperature  $T = 275\text{ }^{\circ}\text{C}$  (a) Test structure with Ta diffusion barrier layer (b) Test structure with  $\text{SiN}_x$  capping layer.

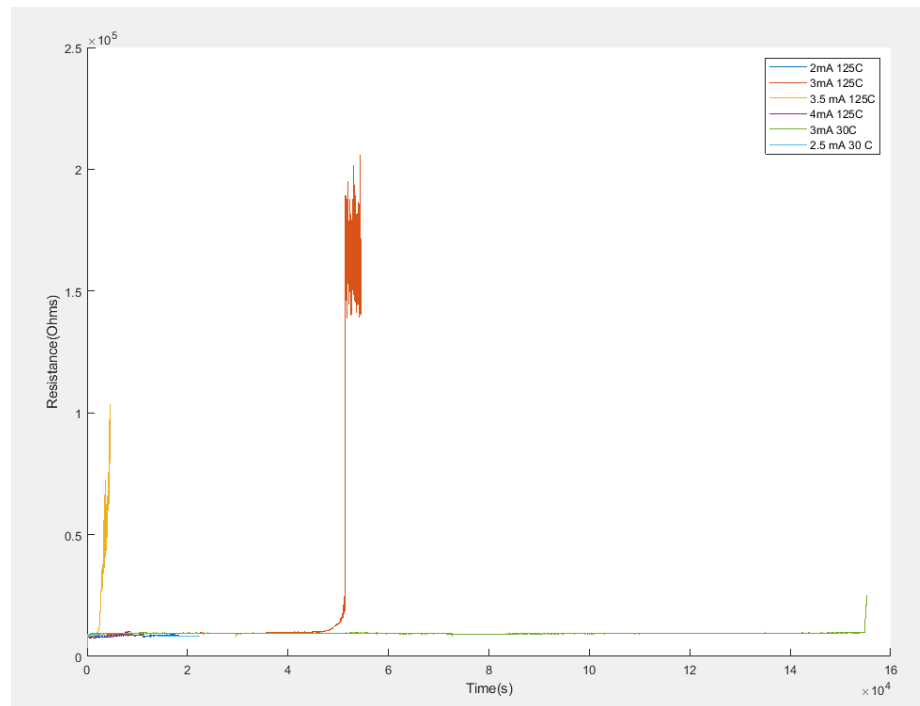


of the strip. Joule heating failures generally occur when the current density flowing through a conductor is large or a flaw is present. We observed two such cases of failure during our study. One of these failures occurred in the base layer Fig. 6.3 which was initially captured by the rise in resistance value and then confirmed through imaging. The current density used during this experiment was set at  $1.5 \times 10^6$  A/cm<sup>2</sup> and the test temperature was  $T=125$  °C. This is during the early phase of testing when a combination of Ti and Ta were being considered as adhesion/diffusion barrier layers at the base of the structure. A second failure due to joule heating occurred in an aluminum line which was captured only through imaging initially Fig. 6.4. This test was carried out at a high current density  $j = 8 \times 10^6$  A/cm<sup>2</sup> at  $T=125$  °C. The failure here looks different from electromigration due to the abrupt nature of voiding and the absence of material accumulation on the anode end of the line.

Joule heating may not contribute to failure, but, it still provides local energy in the form of heat, which contributes to shorter electromigration lifetimes. A local hotspot created due to a flaw or high current densities is undesirable for these tests. A local change in temperature causes changes in resistivity values and may contribute to a higher interface owing to a gradient of temperature across the test structure. We carried out finite element analysis to estimate the local temperature rise due to joule heating. These results were presented in Chapter 3. Experimentally, there are a few different techniques available to evaluate joule heating, however, the scale of the problem makes it challenging to resolve local hot spots. Some experimental techniques used in literature are nanoIR, thermorefectance spectroscopy, scanning joule expansion microscopy (SJEM), scanning thermal microscopy (SThM), Raman thermometry, AC conductance measurements and pulsed I-V measurements [82]. An experimental characterization is beyond the scope of this study at present. However, one of the benefits of the Blech structure used in this study is that, local joule heating is limited compared to the line-via-line structure, due to the alternate path available for current to flow.



(a)



(b)

Figure 6.3. Joule heating failure observed in the base layer with Ti (15nm) and Ta (5nm) (a) Optical image of failure location (b) Resistance change observed during testing.

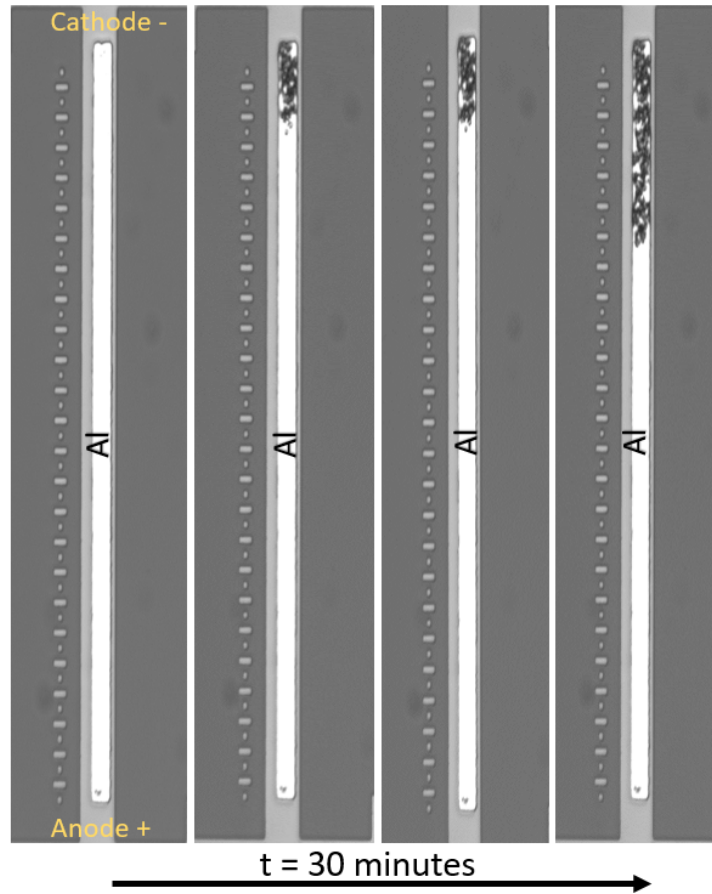


Figure 6.4. Joule heating failure observed in Al.

## 6.2 Morphology of Interface

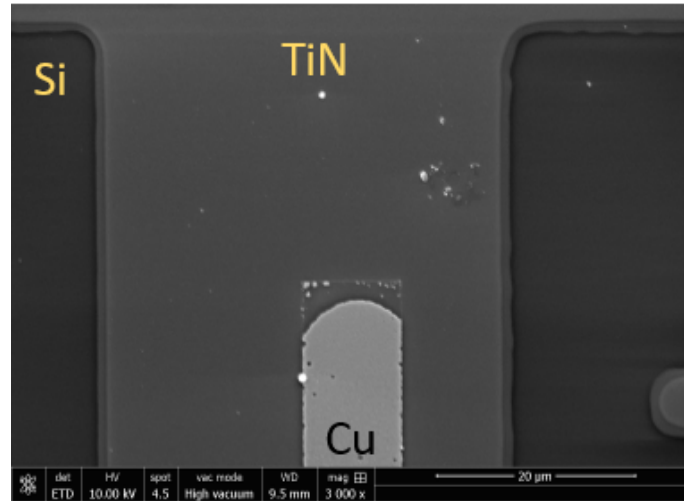
### 6.2.1 Cathode End

There are some differences in the way the interface moves for each of the capping/diffusion barrier layers. Fig. 6.5 is a comparison of the cathode end for three different structures after the first measurement of length of void. We notice motion for all three interfaces, but, TiN has a cleaner interface at this given test conditions. This may be because the rates at the top and bottom are the same for diffusion in the case of TiN. If Ta or SiN are used as a capping/barrier layer then the top surface may diffuse at a different rate compared to the bottom and this would lead to some

islands of material to be left behind. This is visible in the SEM image for the Ta barrier diffusion layer.

Additionally, at lower test temperatures, the islands of material are seen for all three interfaces. Similar observations were noted by [58] for gold films. Generally, islands were observed for lower current densities or lower test temperatures. This may be attributed to smaller contribution of mass transport through grain boundary as the test temperature is lowered. Fig. 6.6 is a comparison of the cathode end at 200 °C at the same current density for the three different test structures. Islands of material are visible at the cathode while the interface has moved ahead. Once the island of material is separated from the moving interface, further testing reveals no significant change in these islands.

One other observation made from tests at higher current densities and test temperatures is the existence of the curvature of the moving interface. This curvature was observed in numerical simulations of Chapter 3 for the wide base layer due to the the additional surface available for diffusion along the sides of the metal film and the jump in current density at the edge. A surface stress in the metal film is unlikely to be responsible for driving the diffusion to form a curvature in the Cu film.



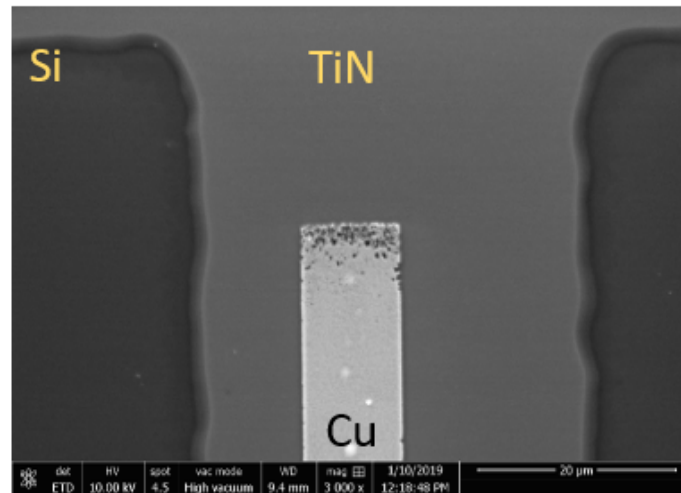
Test Time:  $t = 4$  hours

Current Density:  $j = 3 \times 10^6 \text{ A/cm}^2$

Test Temperature:  $T = 275 \text{ }^\circ\text{C}$

Capping Layer: 10 nm TiN + 20 nm SiN

(a)



Test Time:  $t = 2$  hours

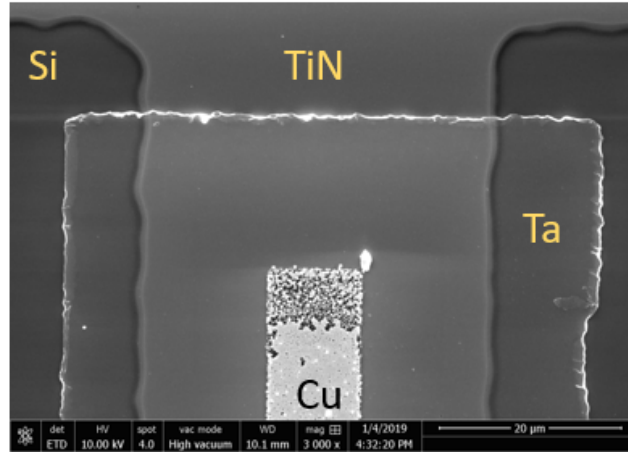
Current Density:  $j = 3 \times 10^6 \text{ A/cm}^2$

Test Temperature:  $T = 275 \text{ }^\circ\text{C}$

Capping Layer: 20 nm SiN

(b)

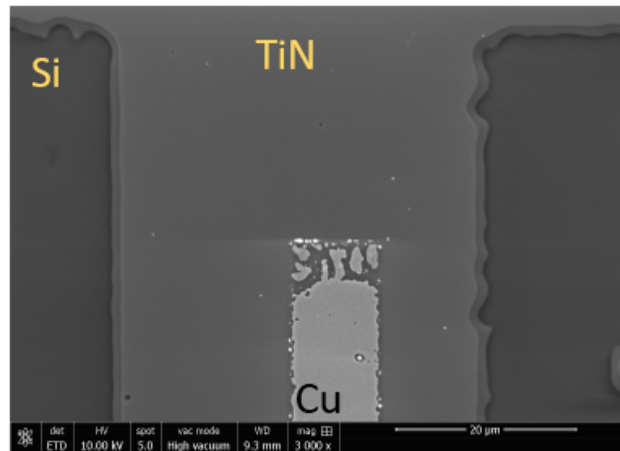
Figure 6.5. SEM images of the cathode end of test specimens after testing at  $T = 275 \text{ }^\circ\text{C}$  and  $j = 3 \times 10^6 \text{ A/cm}^2$  (a) Test Structure with TiN diffusion barrier layer (b) Test Structure with SiN<sub>x</sub> capping layer (c) Test Structure with Ta diffusion barrier layer.



Test Time:  $t = 2$  hours  
 Current Density:  $j = 3 \times 10^6 \text{ A/cm}^2$   
 Test Temperature:  $T = 275 \text{ }^\circ\text{C}$   
 Capping Layer: 5 nm Ta + 20 nm SiN

(c)

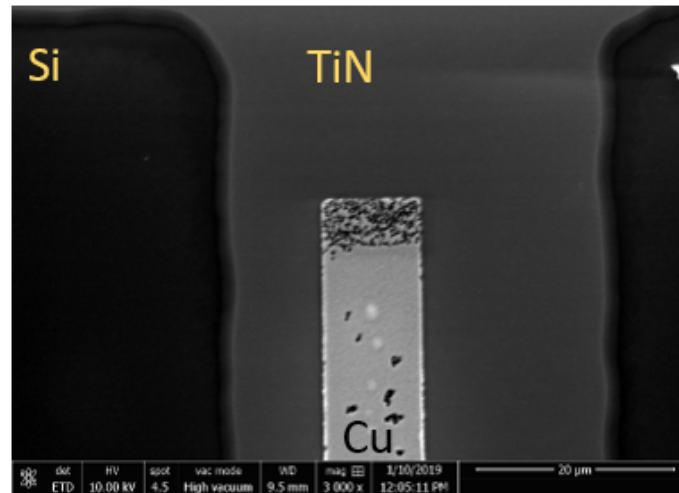
Figure 6.5. Continued.



Test Time:  $t = 24$  hours  
 Current Density:  $j = 3 \times 10^6 \text{ A/cm}^2$   
 Test Temperature:  $T = 200 \text{ }^\circ\text{C}$   
 Capping Layer: 10 nm TiN + 20 nm SiN

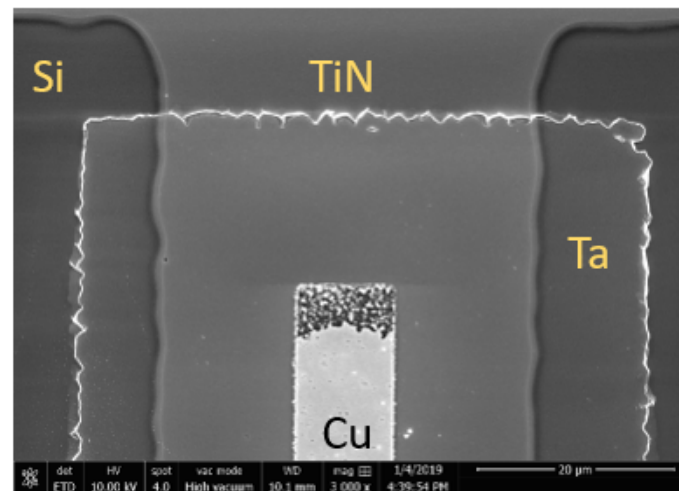
(a)

Figure 6.6. SEM images of the cathode end of test specimens after testing at  $T = 200 \text{ }^\circ\text{C}$  and  $j = 3 \times 10^6 \text{ A/cm}^2$  (a) Test Structure with TiN diffusion barrier layer (b) Test Structure with SiN<sub>x</sub> capping layer (c) Test Structure with Ta diffusion barrier layer.



Test Time:  $t = 36.6$  hours  
 Current Density:  $j = 3 \times 10^6$  A/cm<sup>2</sup>  
 Test Temperature:  $T = 200$  °C  
 Capping Layer: 20 nm SiN

(b)



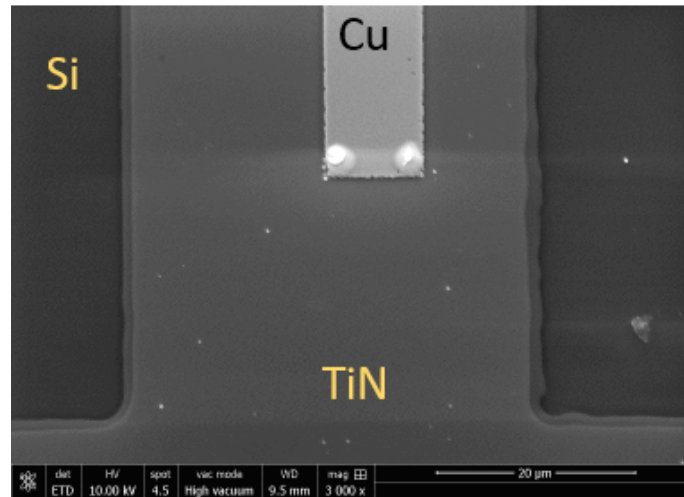
Test Time:  $t = 24$  hours  
 Current Density:  $j = 3 \times 10^6$  A/cm<sup>2</sup>  
 Test Temperature:  $T = 200$  °C  
 Capping Layer: 5 nm Ta + 20 nm SiN

(c)

Figure 6.6. Continued.

### 6.2.2 Anode End

The anode end of the test structures helps confirm that the voiding or interface motion observed on the cathode end is indeed due to electromigration. Fig. 6.7 are the anode ends of the same test structures as Fig. 6.5 where, the test temperature was  $T = 275\text{ }^{\circ}\text{C}$  and the current density was fixed at  $j = 3 \times 10^6\text{ A/cm}^2$ . In this case growth is observed on the anode side after testing. In some cases the growth is not pronounced enough to break through the passivation layer. In the case where the growth breaks through, we carried out EDS to confirm the composition. Fig. 6.8 is a point analysis of the region where a hillock is observed. The spectra confirms the composition being primarily Cu.



Test Time:  $t = 4$  hours

Current Density:  $j = 3 \times 10^6\text{ A/cm}^2$

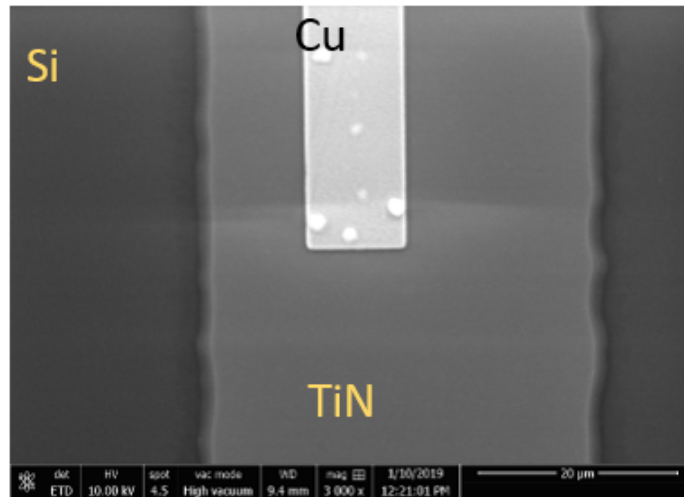
Test Temperature:  $T = 275\text{ }^{\circ}\text{C}$

Capping Layer: 10 nm TiN + 20 nm SiN

(a)

Figure 6.7. SEM images of the anode end of test specimens after testing at  $T = 275\text{ }^{\circ}\text{C}$  and  $j = 3 \times 10^6\text{ A/cm}^2$  (a) Test Structure with TiN diffusion barrier layer (b) Test Structure with  $\text{SiN}_x$  capping layer (c) Test Structure with Ta diffusion barrier layer.





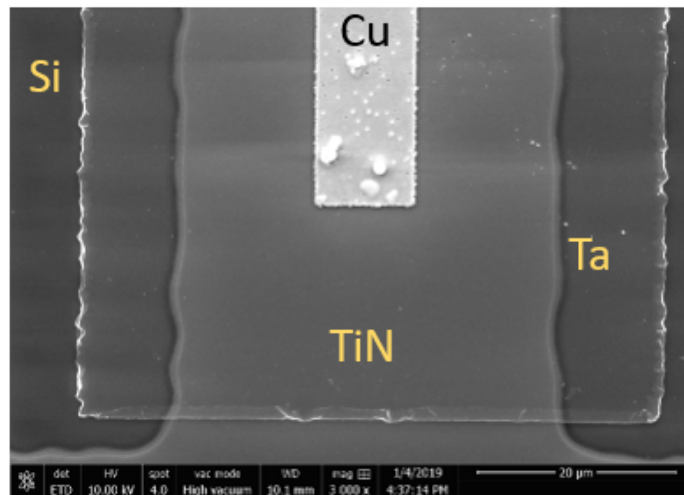
Test Time:  $t = 2$  hours

Current Density:  $j = 3 \times 10^6 \text{ A/cm}^2$

Test Temperature:  $T = 275 \text{ }^\circ\text{C}$

Capping Layer: 20 nm SiN

(b)



Test Time:  $t = 2$  hours

Current Density:  $j = 3 \times 10^6 \text{ A/cm}^2$

Test Temperature:  $T = 275 \text{ }^\circ\text{C}$

Capping Layer: 5 nm Ta + 20 nm SiN

(c)

Figure 6.7. Continued.

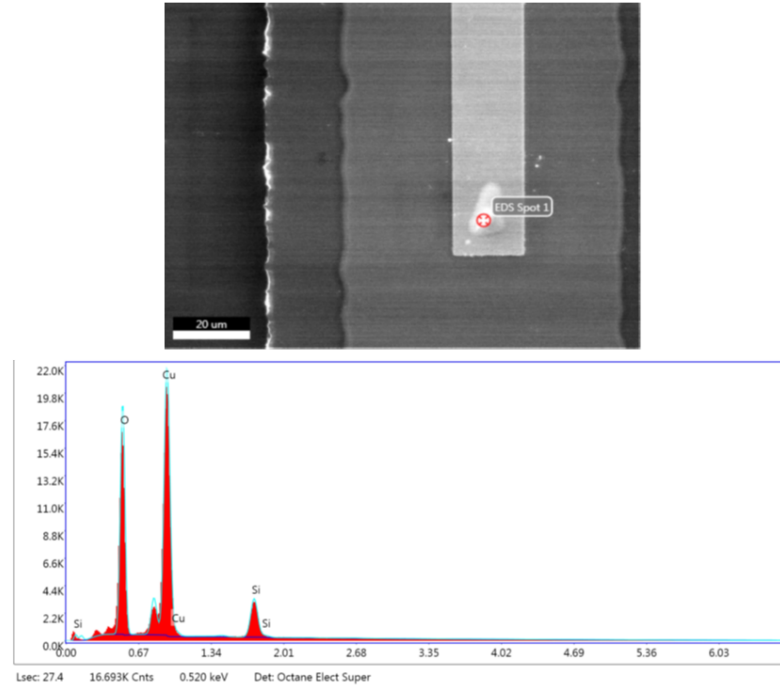


Figure 6.8. EDS spectra of the hillock formation on the anode end of the line.

### 6.2.3 Surface Texture

The surface texture for the evaporated Cu is quite even with a small grain size. Plated Cu versus Cu deposited using PVD or CVD often differ in microstructure due to the process conditions and thickness of deposited films [83]. In general, evaporated films like the one in this study tend to have smaller grain sizes before anneal. Fig. 6.9 is an image taken on a blanket film of Cu (100nm) before annealing. This film was evaporated on a different substrate in the chamber during deposition for a real test specimens. The fabricated test specimens are passivated with SiN to prevent oxidation. It is therefore challenging to obtain grain size and distribution from those test specimens without damaging the thin layer of Cu. In order to obtain information on the grain size and distribution blank samples were placed in the same chamber during deposition of Cu film. These blank films are subject to anneal conditions of 350 ° C as the rest of the test specimens for 3 hours.

EBSD (Electron Backscattered Detector) characterization was carried out on the film. Since the films are very thin, polishing cannot be carried out on them and so they are characterized as deposited. For EBSD mapping, the FEI Quanta 650 electron microscope with an EDAX-TSL Hikari EBSD detector was used. Each pixel was 20 nm in size with a hexagonal grid shape used for data capture. OIM analysis software version 5.3 was used to analyze the EBSD measurement results. Sparse set of grains were observed with the evaporated film. For the grains that were identified an average size of 374.58 nm was observed on the surface.

### 6.3 Measurements of Void Length

Measurements of the void length are primarily carried out in the SEM. Optically, voids of a few microns are visible but, the resolution is not sufficient to make accurate measurements. Fig. 6.10 is one such example where voided region is visible optically, but, not resolved enough to make accurate measurements. After each interval of

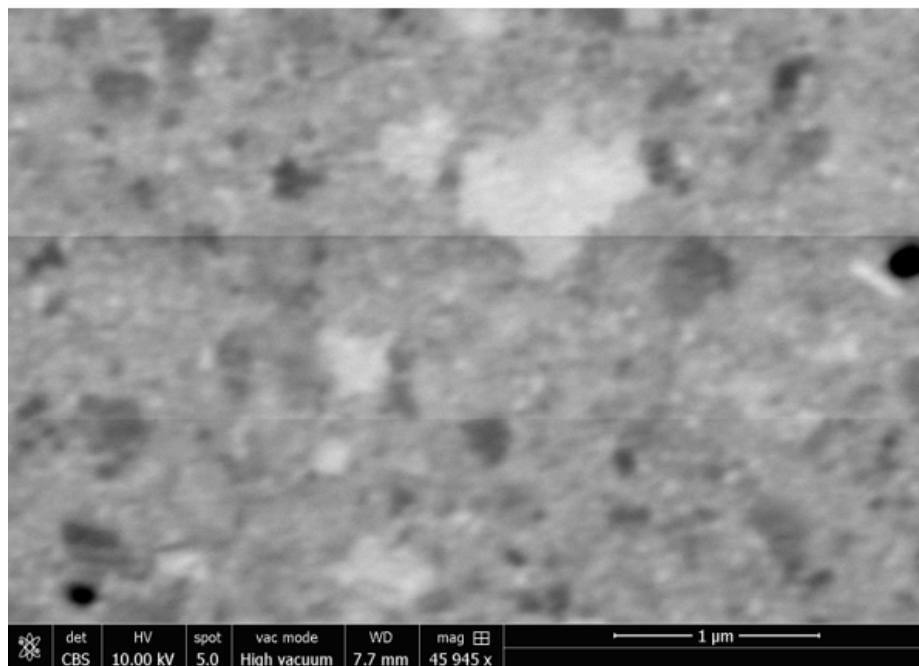


Figure 6.9. Surface texture of a blank Cu film before anneal.

testing the device, images are taken in the SEM and measurements at the cathode end are made using Image J.

Fig. 6.11 is an example of such a measurement. If the curvature is present at the interface is clean then the minimum and maximum void lengths are measured. If the curvature is irregular then the measurements are made by finding the minimum and maximum points that are disconnected from the islands of material behind the moving interface.

Fig. 6.12 is a compilation of measurements for each test as a function of the temperature and the interface. Each plot corresponds to fixed temperature and fixed current density  $j = 3 \times 10^6$  A/cm<sup>2</sup>. Each marker corresponds to an mean displacement measured from the images and the error comes from the curvature of the interface.

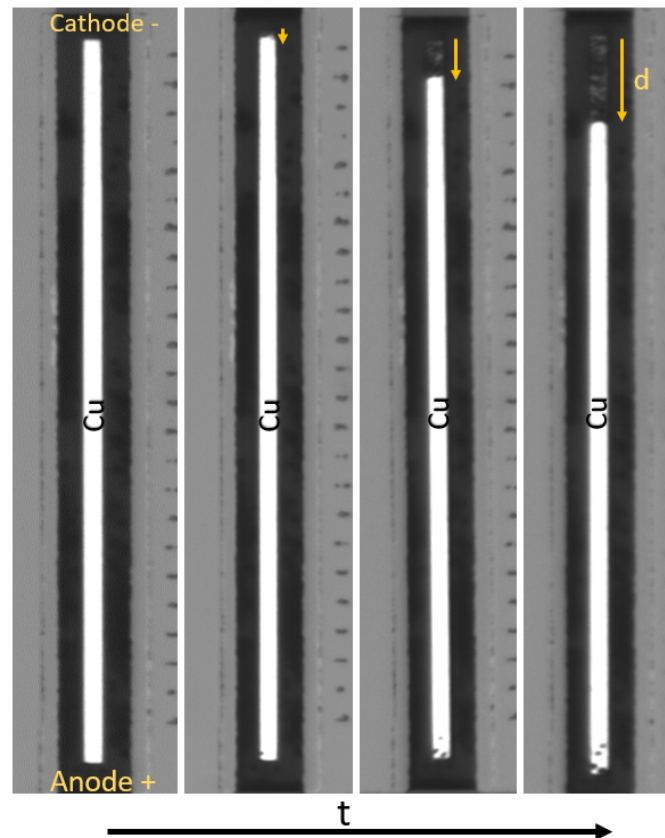


Figure 6.10. Optical images of void length recorded for 10  $\mu\text{m}$  wide Cu lines.

## 6.4 Velocity of Interface

The velocity for each of these tests is obtained through a linear fit to the void length measurement data. Most of the data points seem to suggest a linear velocity profile for the interface. This linear behavior is expected if the test structure lines are long. Blech like structures that are short are known to produce a back stress, which changes the interface velocity. Theoretically the line would move with a linear velocity until the stress gradient is large enough to diminish the growth rate, and finally the line would reach a critical length. This critical line length would be the line length predicted by the “Blech Product” for the given test current density.

## 6.5 Width Variation

Several devices were tested with varying widths of the Cu line while keeping all the other geometry features the same. Fig. 6.13 is a compilation of some of the devices tested. At 0.5 and 2  $\mu\text{m}$  width the line starts to develop several opens at the cathode end. While this is expected for narrow lines with bamboo grained structures, this is not ideal to determine the growth rate of the voids. At 5  $\mu\text{m}$ , we start to

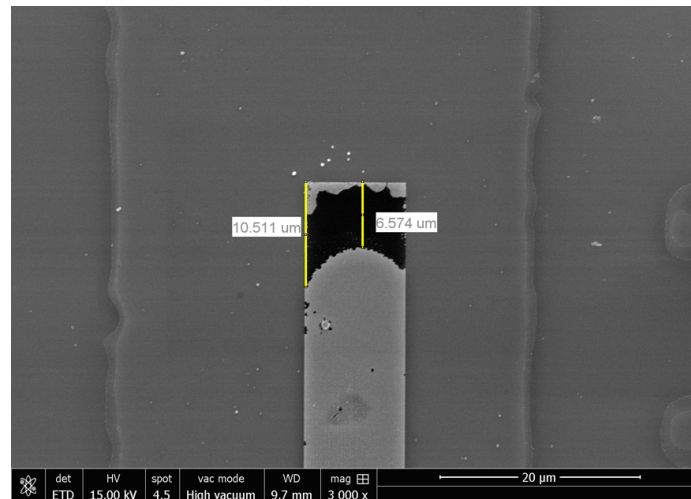
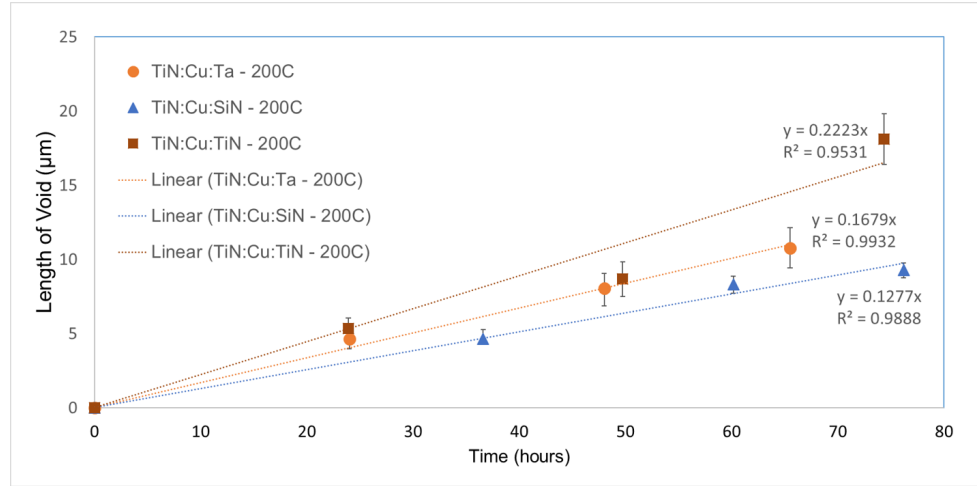
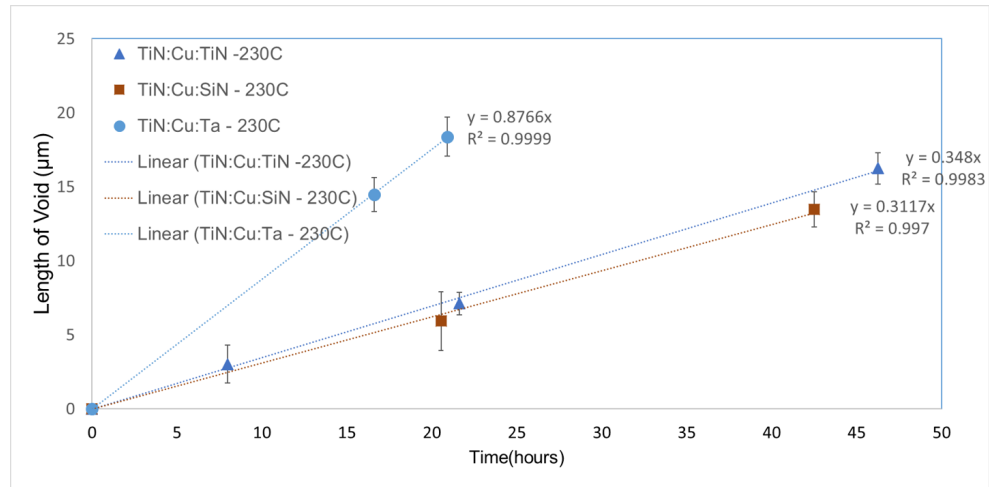


Figure 6.11. Measurement made in Image J for one of the test structures after an interval of testing.

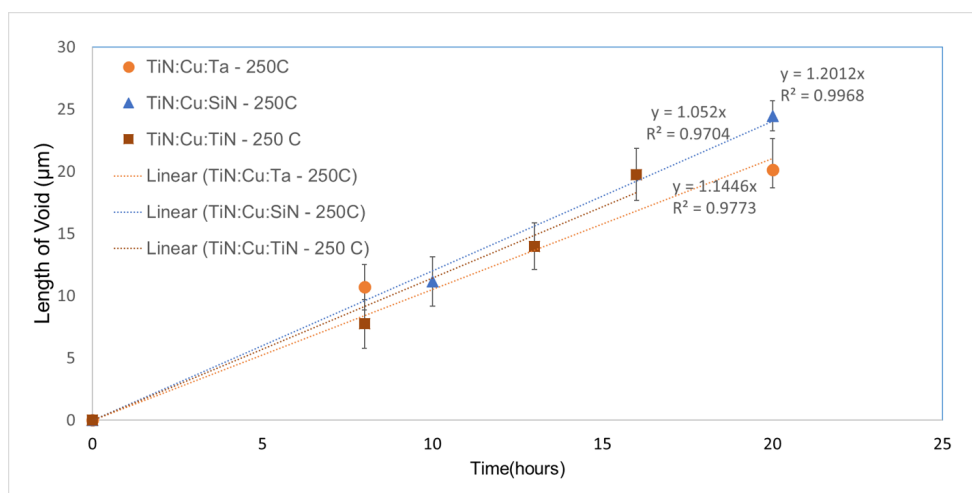


(a)

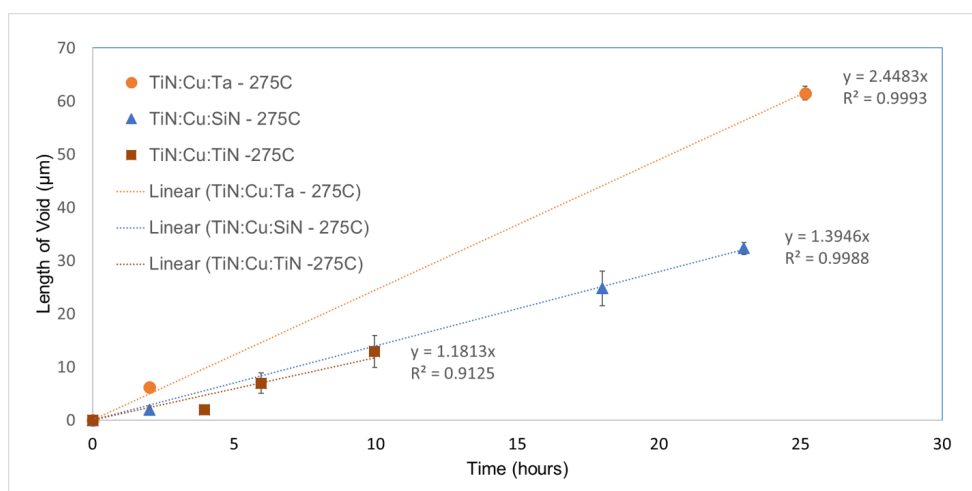


(b)

Figure 6.12. Record of the length of voids as a function of varying test temperatures and fixed current density  $3 \times 10^6$  A/cm<sup>2</sup> for different test structures (a) Test temperature  $T = 200$  °C (b) Test temperature  $T = 230$  °C (c) Test temperature  $T = 250$  °C (d) Test temperature  $T = 275$  °C.



(c)



(d)

Figure 6.12. Continued.

observe a moving interface but, the interface is not consistent across the width of the line. At 10 and 20  $\mu m$  widths, the interface is much more easily discernible. The last two cases are the same interface with  $SiN_x$  capping layer tested at the same current density  $j = 3 \times 10^6$  A/cm<sup>2</sup> and test temperature  $T = 275^\circ C$ . Even though the 20  $\mu m$  seems to have the cleanest interface, the current required to achieve the desired test current density is more than double the current required for the 10  $\mu m$  wide line. This would not be an issue if the base layer was scaled correctly to avoid a large local hotspot ahead of the Cu line. The TiN base layer is of the same width and thickness in both cases so its resistance only increases with the local rise in temperature. If the current is doubled, the power of joule heating will be four times as much, which would lead to a larger temperature gradient. A large temperature gradient as the one observed in this case may lead to a significant change in the interfacial velocity. The two cases were compared at identical test conditions and the velocity of the Cu line was found to be 2.669  $\mu m/hr$  for the wider 20  $\mu m$  line compared to 1.395  $\mu m/hr$  for the 10  $\mu m$  line width. This is a significant difference and in order to stay conservative, we rely on the 10  $\mu m$  wide lines to keep the joule heating limited in all experiments moving forward. The 10  $\mu m$  wide line has a polygrain structure which can approximate continuum behavior without a large temperature gradient.

### 6.5.1 Temperature Variation

Based on the measurements of void length from the images, we compare the change in velocity as a function of temperature. The data suggests an exponentially increasing velocity with an increase in temperature from 130 to 275  $^\circ C$  while the current density was kept fixed at  $j = 3 \times 10^6$  A/cm<sup>2</sup>. Fig. 6.14 are plots of the velocity as a function of temperature with a simple exponential fit. There are differences in the displacement rates for the three different capping/diffusion barrier layers. Each marker point is the mean velocity from the linear fits.



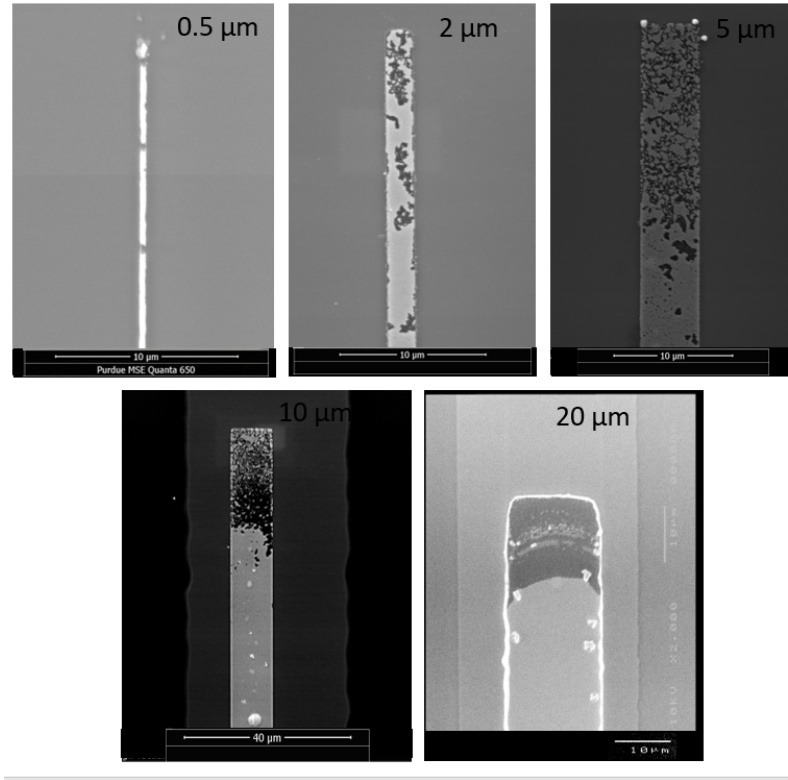
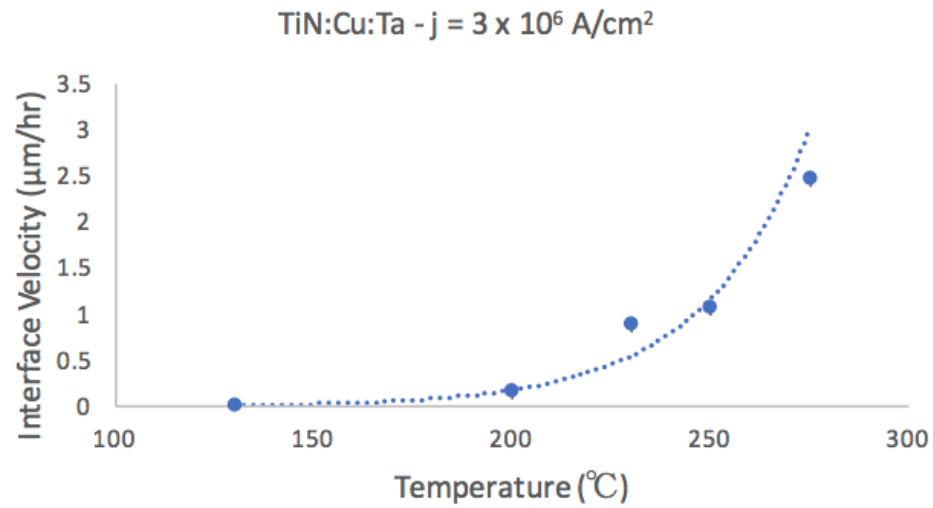
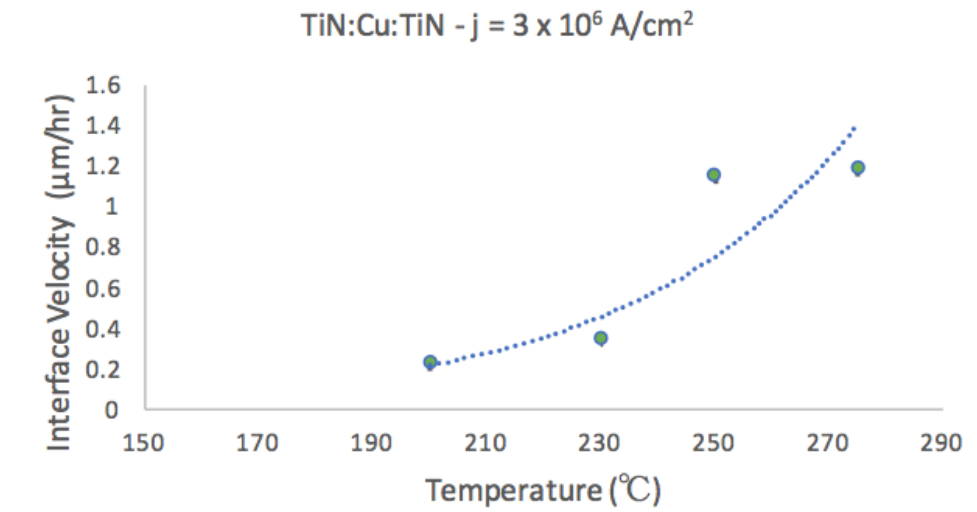


Figure 6.13. Interface motion in Cu lines of varying widths.

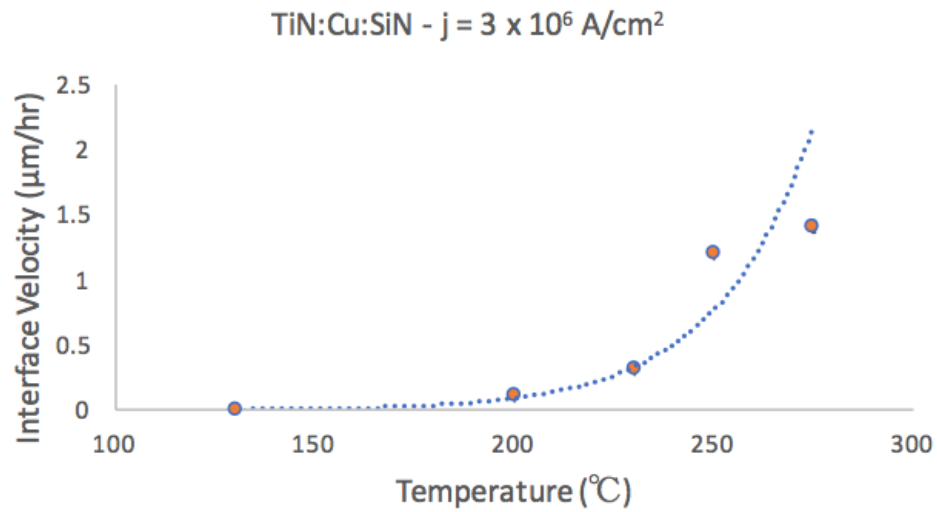


(a)

Figure 6.14. Velocity recorded for different test structures at  $j = 3 \times 10^6 \text{ A/cm}^2$  and varying temperatures (a) Test structure with Ta diffusion barrier layer (b) Test structure with TiN diffusion barrier layer (c) Test structure with SiN capping layer.



(b)



(c)

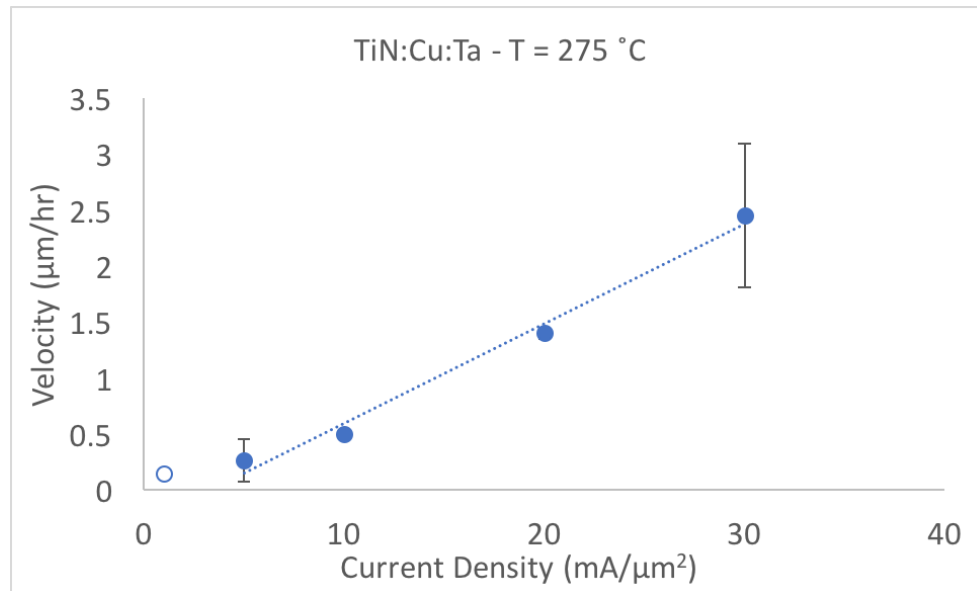
Figure 6.14. Continued.

### 6.5.2 Current Density Variation

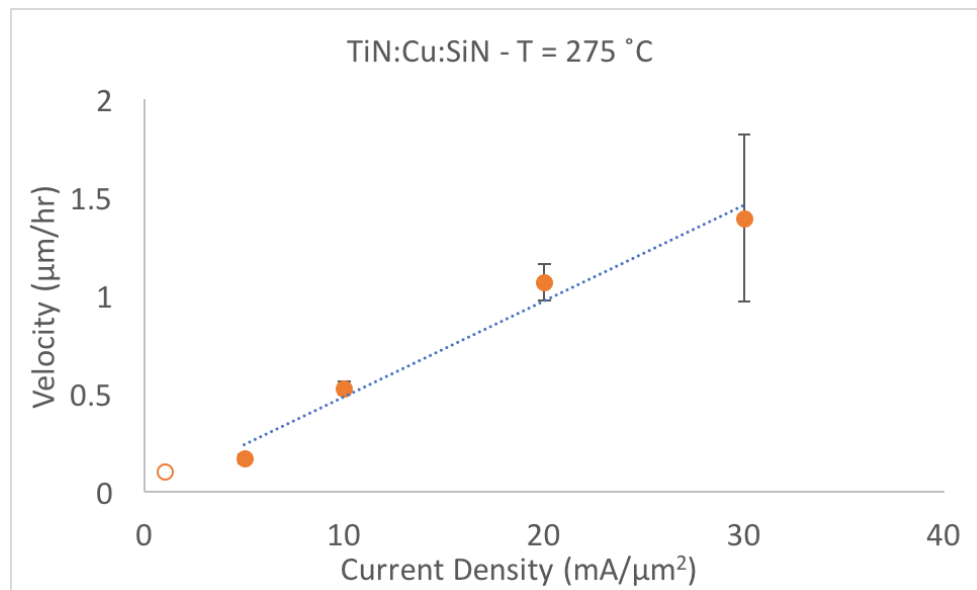
The test structures were subject to different current densities at a fixed temperature of 275 °C. For each of these current densities, we expect to see electromigration. The higher temperature helps accelerate the diffusion rates. Fig. 6.15 is a comparison

of the velocities obtained for Ta diffusion barrier and a SiN<sub>x</sub> capping layer. In both cases the velocity changes linearly as a function of the current density though the rates of change are different. Electromigration was observed at the lowest test current density however, a moving interface was not clear from the images. We exclude the lowest current density data from our analysis going forward.

Below a current density of  $5 \times 10^5$  A/cm<sup>2</sup>, the diffusion rates are extremely slow. For a Blech Product of 3700 A/cm with a line length of 500  $\mu m$  the critical current density would correspond to  $7.4 \times 10^4$  A/cm<sup>2</sup>. It is expected that at this current density there is no observable electromigration phenomena. The intercept from these fits give a slightly different critical current density value. We will revisit this in Chapter 8 when we examine the intercept values along the axis.



(a)



(b)

Figure 6.15. Velocity recorded for different test structures at  $T = 275^\circ\text{C}$  and varying current densities (a) Test structure with Ta diffusion barrier layer (b) Test structure with SiN capping barrier layer.

## 7. A CONTINUUM MODEL FOR ELECTROMIGRATION

### 7.1 Overview

This chapter is a condensed version of the theory developed in reference [26] where, the thermodynamic configurational force associated with a moving interface is used to derive the conditions for phase growth and nucleation in bodies with multiple diffusing species and arbitrary surface stress at the phase interface. We start with the derived interfacial transport theorem for a general scalar field. Analogous to the bulk field, the balance of mass, momentum and energy are derived next. The thermodynamic conditions that result from free-energy inequality at the interface are derived leading to the analytical form of the configurational force for bodies subject to mechanical loads, heat, and multiple diffusing species. The derived second law condition naturally extends the Eshelby energy-momentum tensor to include species diffusion terms. The above second law restriction is then used to describe the condition for the growth of new phases in a body undergoing finite deformation. The growth conditions are derived in both current as well as reference configurations. Finally, a statistical, temperature-dependent growth velocity is derived using the Boltzmann distribution.

### 7.2 Derivation of Balance Laws at the Interface

The development in this section is motivated by the pioneering work of Truesdell and Toupin [84]. The approach followed is to make a systematic analogy to the bulk balance laws presented in [26], including in the explicit use of an entropic inequality condition on the interface. Additionally, analogous to bulk derivation, surface quantities corresponding to mass, momentum, internal energy, entropy and free energy are introduced as variables and resolved through the derived thermodynamic restrictions. The resulting form of the driving force on the phase interface is similar to that de-

rived in [85,86], but the derivation here allows inhomogeneous and anisotropic surface stress.

### 7.2.1 Interface Transport Theorem

An interfacial transport theorem is derived by [26] using the idea of an interface “pillbox” shown in Fig. 7.1, to connect bulk fields with the interface. The interface transport theorem is valid for a scalar field on the interface and is the basis for derivation of the mass, momentum and energy balance equations.

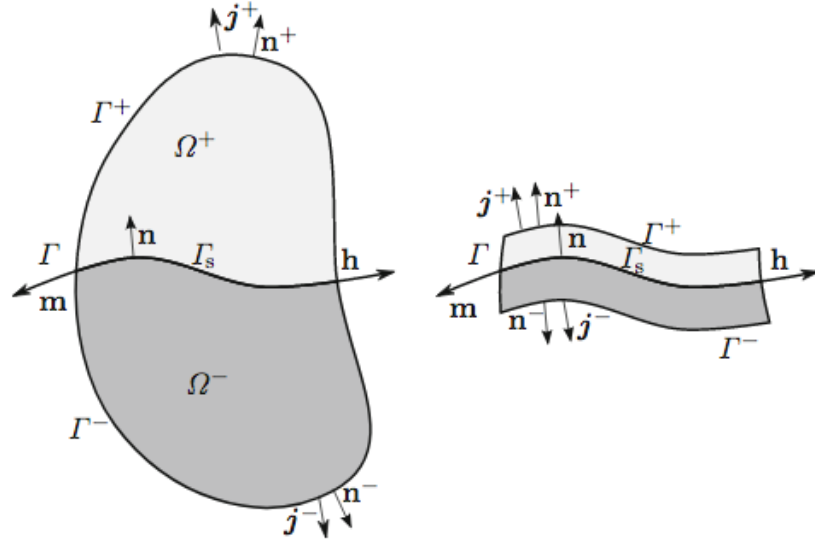


Figure 7.1. Control volume (interface pillbox) with generalized field and fluxes.

The local form of the interface transport theorem is given by the expression:

$$- \llbracket \phi (v_{s_n} - v_n) \rrbracket + \dot{\phi}_s + \phi_s \nabla_s \cdot \mathbf{v}_s = - \llbracket \mathbf{j}^\phi \rrbracket \cdot \mathbf{n} - \nabla_s \cdot \mathbf{h}_t^\phi + r_s^\phi \quad \text{on } \Gamma \quad (7.1)$$

where, the left hand side of the above expression represents the accumulation of bulk and interface fields due to bulk normal fluxes and the interface flux.  $\mathbf{j}$  refers to the flux of the field  $\phi$  while  $r$  denotes volumetric generation. The interface is considered as a separate domain, bounded by the curve  $\partial\Gamma_s$  (Fig. 7.1). The superficial field

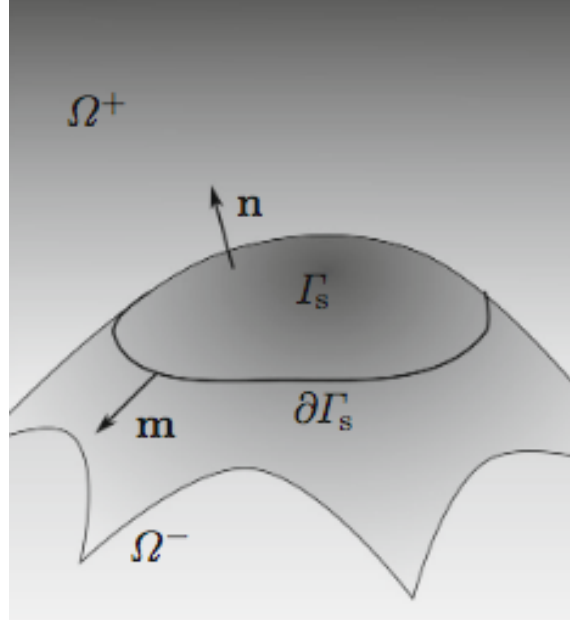


Figure 7.2. Schematic showing the definition of the normals to the interface and to the boundary of the interface subregion  $\Gamma_s$ .

on the interface  $\phi_s$  is changed by inflows due to a flux  $\mathbf{h}$  on the boundary  $\partial\Gamma_s$  of the interface, the flux exchanges  $\mathbf{j}^i$  with the bulk domains on either side, and the spontaneous generation rate  $r_s$ . At the interface the jump in the field and fluxes are defined as  $\llbracket \cdot \rrbracket = (\cdot^+ - \cdot^-)$ .

### 7.2.2 Balance Laws at the Interface

The general interface transport theorem of Eq. (7.1) is applied to various conserved quantities such as species mass, momentum and energy, by replacing  $\phi$  with the appropriate conserved quantity to obtain the balance law. The species mass balance at the interface is obtained by replacing the bulk field  $\phi$  by  $\rho\nu^\alpha$ , the mass flux  $\mathbf{j}^\phi$  of the diffusing species  $\alpha$  by  $\mathbf{j}^\alpha$ , and the tangential interface flux  $\mathbf{h}_t^\phi$  by the surface mass flux  $\mathbf{h}_t^\alpha$ . The interface is considered massless, and therefore, surface mass excess,  $\phi_s$  is ignored. The rate of spontaneous generation of species  $\alpha$  at the surface (as due to

a chemical reaction) is denoted  $r_s^\alpha$ . Substituting in Eq. (7.1) the species mass balance is expressed as:

$$- \llbracket \rho \nu^\alpha (v_{s_n} - v_n) \rrbracket = - \llbracket \mathbf{j}^\alpha \rrbracket \cdot \mathbf{n} - \nabla_s \cdot \mathbf{h}_t^\alpha + r_s^\alpha \quad (7.2)$$

The momentum balance at the interface is obtained by considering momentum in an arbitrary, but fixed direction  $\hat{\mathbf{n}}$ . Analogous to bulk field, the field  $\phi$  is chosen to be  $\phi = \rho \mathbf{v} \cdot \hat{\mathbf{n}}$  in the direction  $\hat{\mathbf{n}}$ . Accounting for the appropriate bulk and interface flux terms, while ignoring the spontaneous generation of momentum we obtain the momentum balance as:

$$- \llbracket \rho \mathbf{v} (v_{s_n} - v_n) \rrbracket \cdot \hat{\mathbf{n}} = \llbracket \boldsymbol{\sigma} \hat{\mathbf{n}} \rrbracket \cdot \mathbf{n} - \nabla_s \cdot \mathbf{h}_t^\mathbf{v} \quad (7.3)$$

where,  $\boldsymbol{\sigma}$  is the traction on the interface. Furthermore, the tangential component of the surface flux  $\mathbf{h}_t^\mathbf{v} = \mathbf{P} \mathbf{h}^\mathbf{v} = -\mathbf{P} \boldsymbol{\sigma}_s \hat{\mathbf{n}}$ . Since  $\hat{\mathbf{n}}$  is arbitrary, constant and non-zero, Eq. (7.3) yields:

$$- \llbracket \rho \mathbf{v} (v_{s_n} - v_n) \rrbracket = \llbracket \boldsymbol{\sigma} \rrbracket \mathbf{n} + \nabla_s \cdot (\mathbf{P} \boldsymbol{\sigma}_s) \quad (7.4)$$

If the surface stress is homogeneous and isotropic we obtain the Laplace-Young equation:

$$- \mathbf{n} \cdot \llbracket \boldsymbol{\sigma} \rrbracket \mathbf{n} = \gamma \kappa \quad (7.5)$$

where,  $\kappa$  is the total curvature of the interface.

As with momentum balance, the interface energy balance is obtained by analogy of the balance of bulk internal energy. Thus, the bulk field is  $\phi = \rho e + \frac{1}{2} \rho \mathbf{v} \cdot \mathbf{v}$ , bulk energy flux is  $\mathbf{j}^e = -\boldsymbol{\sigma} \mathbf{v} + \mathbf{j}^q + \sum_{\alpha=1}^N \mu^\alpha \mathbf{j}^\alpha$ . The surface field  $\phi_s$  is given by the internal energy per unit area,  $e_s$ . The tangential component of the surface flux corresponding



to internal energy accumulation is given by  $\mathbf{h}_t^e = -\mathbf{P}\boldsymbol{\sigma}_s\mathbf{v}_s + \mathbf{h}^q + \sum_{\alpha=1}^N \mu_s^\alpha \mathbf{h}_t^\alpha$ . Thus, the interface energy balance relation is:

$$\begin{aligned} & -\llbracket \phi(v_{s_n} - v_n) \rrbracket + \dot{\phi}_s + \phi_s \nabla_s \cdot \mathbf{v}_s = \\ & - \left[ \left[ -\boldsymbol{\sigma}\mathbf{v} + \mathbf{j}^q + \sum_{\alpha=1}^N \mu^\alpha \mathbf{j}^\alpha \right] \cdot \mathbf{n} - \nabla_s \cdot \left( -\mathbf{P}\boldsymbol{\sigma}_s\mathbf{v}_s + \mathbf{h}^q + \sum_{\alpha=1}^N \mu_s^\alpha \mathbf{h}_t^\alpha \right) \right. \\ & \left. + r_s^q + \sum_{\alpha=1}^N \mu_s^\alpha r_s^\alpha \right] \end{aligned} \quad (7.6)$$

The interface entropy inequality can now be obtained analogous to the bulk entropy inequality. Let  $\eta$  denote the bulk specific internal entropy using the pillbox procedure. The entropy imbalance inequality is expressed as,

$$-\llbracket \rho\eta(v_{s_n} - v_n) \rrbracket + \dot{\eta}_s + \eta_s \nabla_s \cdot \mathbf{v}_s \geq - \left[ \left[ \frac{\mathbf{j}^q}{T} \right] \cdot \mathbf{n} - \nabla_s \cdot \frac{\mathbf{h}_t^q}{T_s} + \frac{r_s^q}{T_s} \right] \quad (7.7)$$

where,  $\eta_s$  denotes the entropy per unit area of the interface. The external sources of entropy are the bulk heat flux  $\mathbf{j}^q$ , surface heat flux  $\mathbf{h}^q$  and the surface heat generation  $r_s^q$ .  $T_s$  is the surface temperature.

Defining the specific free energy,  $\psi = e - \eta T$  and its interface equivalent  $\psi_s = e_s - \eta_s T_s$ , the free energy inequality is obtained by using the first and second laws of thermodynamics. Assuming continuity of chemical potential across the interface, i.e.,

$$\llbracket \mu^\alpha \rrbracket = 0, \quad \mu_s^\alpha = \mu^\alpha \quad (7.8)$$

and under the assumption of continuity of temperature, i.e.,

$$\llbracket T \rrbracket = 0, \quad T_s = T \quad (7.9)$$

we get:

$$\begin{aligned}
& - \left[ \left( \rho\psi + \frac{1}{2}\rho\mathbf{v} \cdot \mathbf{v} \right) (v_{\text{sn}} - v_n) \right] + \dot{\psi}_s + \eta_s \dot{T}_s \\
& \quad + \psi_s \nabla_s \cdot \mathbf{v}_s + \frac{1}{T_s} \mathbf{h}_t^q \cdot \nabla_s T_s \leq \\
& - \left[ \rho \mathbf{v}_s \cdot \mathbf{v} (v_{\text{sn}} - v_n) \right] - \left[ \boldsymbol{\sigma} (\mathbf{v}_s - \mathbf{v}) \right] \cdot \mathbf{n} - [\nabla_s \cdot (\mathbf{P} \boldsymbol{\sigma}_s)] \cdot \mathbf{v}_s \\
& - \sum_{\alpha=1}^N (\left[ \rho \mu^\alpha \nu^\alpha (v_{\text{sn}} - v_n) \right] + \mathbf{h}_t^\alpha \cdot \nabla_s \mu_s^\alpha) \\
& \quad + \nabla_s \cdot (\mathbf{P} \boldsymbol{\sigma}_s \mathbf{v}_s)
\end{aligned} \tag{7.10}$$

The right hand side indicates the work that is being done on the control volume due to surface tractions and diffusion. The free energy increase of the system is given to be less than or equal to the right hand side by the second law.

The inequality leads to the following conditions that have to hold at the interface:

$$- \left[ (\mathbf{v}_s - \mathbf{v}) \cdot \left( \rho\psi \mathbf{I} - \boldsymbol{\sigma} - \rho \sum_{\alpha=1}^N \mu^\alpha \nu^\alpha \mathbf{I} \right) \mathbf{n} \right] \leq 0 \tag{7.11}$$

$$\mathbf{h}_t^\alpha \cdot \nabla_s \mu_s^\alpha \leq 0 \quad \forall \alpha \tag{7.12}$$

$$\mathbf{h}_t^q \cdot \nabla_s T_s \leq 0 \tag{7.13}$$

The conditions Eqs. (7.12) and (7.13) are satisfied by constitutive relations of the following form:

$$\mathbf{h}_t^\alpha = -\mathbf{M}_s^\alpha \nabla_s \mu_s^\alpha \tag{7.14}$$

$$\mathbf{h}_t^q = -\mathbf{k}_s \nabla_s T_s \tag{7.15}$$

where,  $\mathbf{M}_s^\alpha$  is a positive definite surface mobility tensor for the species  $\alpha$ , and  $\mathbf{k}_s$  is a positive definite heat conductivity tensor on the surface. The above equations are the surface analogs of the bulk versions of Fick's law and Fourier's Law.

In the absence of inertial forces, Eq. (7.11) can be restated in the reference configuration as:

$$\mathbf{V}_S \cdot \llbracket \boldsymbol{\Sigma}_\nu - \boldsymbol{\sigma}_I \rrbracket \mathbf{N} \geq 0 \quad \text{on } \Gamma_{s_0} \quad (7.16)$$

where,

$$\boldsymbol{\Sigma}_\nu = \boldsymbol{\Sigma}_0 - \rho_0 \sum_{\alpha=1}^N \mu_0^\alpha \nu_0^\alpha \mathbf{I} \quad (7.17)$$

is an extension to the Eshelby energy momentum tensor [87]  $\boldsymbol{\Sigma}_0 = (\rho_0 \psi_0 \mathbf{I} - \nabla_0 \mathbf{U} \boldsymbol{\sigma}_I)$ , with  $\boldsymbol{\sigma}_I$  being the first Piola-Kirchhoff stress tensor;  $\mathbf{U}$  is the displacement in reference coordinates and  $\Gamma_{s_0}$  is the subsurface viewed in the reference configuration. Eshelby also suggests  $\boldsymbol{\Sigma}_0^* = \boldsymbol{\Sigma}_0 - \boldsymbol{\sigma}_I$  as an energy-momentum tensor with greater utility for estimating the force on a defect [87].

The jump  $\llbracket \boldsymbol{\Sigma}_\nu - \boldsymbol{\sigma}_I \rrbracket$  represents a conserved quantity that will integrate to zero within a homogeneous domain. In this sense, it is an extension to the path-independent J-integral of fracture mechanics [28] to bodies with multiple diffusing species. The conjugate to the reference interface velocity  $\mathbf{V}_s$ , namely  $\llbracket \boldsymbol{\Sigma}_\nu - \boldsymbol{\sigma}_I \rrbracket \mathbf{N}$ , is the reference configurational force associated with the motion of the interface.

### 7.3 Conditions for Phase Growth

During the growth of the phases, Eq. (7.11) should be satisfied at each point on  $\Gamma$  and at all instants of time. It is convenient, however, to derive the growth criterion in the reference configuration using Eq. (7.16). We begin by decomposing the surface velocity into tangential and normal components in the reference configuration  $\mathbf{V}_S = \mathbf{V}_{S_T} + V_{S_N} \mathbf{N}$ , where  $\mathbf{N}$  is the surface normal vector with the convention that  $\mathbf{N}$

points from Phase  $-$  into Phase  $+$  (see Fig. 7.1). Thus, the left hand side of Eq. (7.16) can be written as

$$\begin{aligned} (\mathbf{V}_{\mathbf{S}_T} + V_{\mathbf{S}_N} \mathbf{N}) \cdot \llbracket \boldsymbol{\Sigma}_\nu - \boldsymbol{\sigma}_I \rrbracket \mathbf{N} = & \mathbf{V}_{\mathbf{S}_T} \cdot \left[ \rho_0 \left( \psi_0 - \sum_{\alpha=1}^N \mu_0^\alpha \nu_0^\alpha \right) \mathbf{I} - \mathbf{F}^T \boldsymbol{\sigma}_I \right] \mathbf{N} \\ & + V_{\mathbf{S}_N} \mathbf{N} \cdot \llbracket \boldsymbol{\Sigma}_\nu - \boldsymbol{\sigma}_I \rrbracket \mathbf{N} \end{aligned} \quad (7.18)$$

where,  $\mathbf{F}$  is the deformation gradient with the inverse  $\mathbf{F}^{-1} = \mathbf{G}$ . Simplifying, the second law condition of Eq. (7.18) reduces to requiring:

$$- \llbracket \mathbf{F} \mathbf{V}_{\mathbf{S}_T} \cdot \boldsymbol{\sigma}_I \mathbf{N} \rrbracket + V_{\mathbf{S}_N} \mathbf{N} \cdot \llbracket \boldsymbol{\Sigma}_\nu - \boldsymbol{\sigma}_I \rrbracket \mathbf{N} \geq 0 \quad \text{on } \Gamma_{s_0} \quad (7.19)$$

Now, treating the dissipation due to tangential slip independent of the normal velocity causing the growth, the thermodynamic second law conditions for growth, Eq. (7.19), may be stated as:

$$V_{\mathbf{S}_N} \mathbf{N} \cdot \llbracket \boldsymbol{\Sigma}_\nu - \boldsymbol{\sigma}_I \rrbracket \mathbf{N} \geq 0 \quad \text{on } \Gamma_{s_0} \quad (7.20)$$

$$- \mathbf{V}_{\mathbf{S}_T} \cdot \llbracket \mathbf{F}^T \boldsymbol{\sigma}_I \rrbracket \mathbf{N} \geq 0 \quad \text{on } \Gamma_{s_0} \quad (7.21)$$

with  $\mathbf{N} \cdot \llbracket \boldsymbol{\Sigma}_\nu - \boldsymbol{\sigma}_I \rrbracket \mathbf{N}$  representing a jump in volumetric energy density. The second condition is trivially satisfied in the absence of slip.

Recalling that the positive normal velocity points in the direction  $\mathbf{N}$  of the interface, from the  $-$  Phase to the  $+$  Phase in the reference configuration, we will assume a convention that Phase  $-$  is the growing phase and therefore,  $V_{\mathbf{S}_N}$  is positive during the growth. Although it is not necessary to choose *a priori* the observed quantity,

we choose the surface normal speed  $V_{\text{S}_N}$  as a macroscopic, positive observed quantity. Therefore, we restate Eqs. (7.20) and (7.21) to require that:

$$\mathbf{N} \cdot \llbracket \boldsymbol{\Sigma}_\nu - \boldsymbol{\sigma}_I \rrbracket \mathbf{N} \geq 0 \quad \text{on } \Gamma_{\text{s}_0} \quad (7.22)$$

$$V_{\text{S}_N} = C_{V_N} \mathbf{N} \cdot \llbracket \boldsymbol{\Sigma}_\nu - \boldsymbol{\sigma}_I \rrbracket \mathbf{N} \quad \text{on } \Gamma_{\text{s}_0} \quad (7.23)$$

$$\mathbf{V}_{\text{S}_T} = -C_{V_T} \llbracket \mathbf{F}^T \boldsymbol{\sigma}_I \rrbracket \mathbf{N} \quad \text{on } \Gamma_{\text{s}_0} \quad (7.24)$$

where,  $C_{V_N}$  and  $C_{V_T}$  are arbitrary positive quantities.

#### 7.4 Statistical Growth Condition

In general, the atomistic phenomena that lead to phase nucleation and growth are statistical in nature. Thus, in experimental observations, the growth condition of Eq. (7.22) requires a treatment keeping in mind the inherent variability at microscopic length scales. Considering now the growth conditions in the current configuration that is the alternative form of Eq. (7.22), we rewrite the equation as

$$g_{sn} \equiv \left( H - \frac{G}{l} \right) \geq 0 \quad \text{on } \Gamma_{\text{s}_0} \quad (7.25)$$

where,  $H$  and  $G$  are volumetric and surface energy densities respectively, and  $l$  is a characteristic length scale in the current configuration as explained below. The definitions of  $H$  and  $G$  follow from growth conditions:

$$H(\mathbf{F}, \nu^\alpha, T) = \left[ \sqrt{\mathbf{n} \cdot \mathbf{F} \mathbf{F}^T \mathbf{n}} \left( \rho \psi - \sum_{\alpha=1}^N \rho \mu^\alpha \nu^\alpha \right) - \frac{\mathbf{n} \cdot \mathbf{F} (\mathbf{F}^T - \mathbf{I}) \boldsymbol{\sigma} \mathbf{n}}{\sqrt{\mathbf{n} \cdot \mathbf{F} \mathbf{F}^T \mathbf{n}}} \right] \quad (7.26)$$

$$G(\mathbf{F}, \boldsymbol{\sigma}_s, T) = -l \frac{\mathbf{F}^T \mathbf{n}}{\sqrt{\mathbf{n} \cdot \mathbf{F} \mathbf{F}^T \mathbf{n}}} \cdot (\kappa \boldsymbol{\sigma}_s \mathbf{n} + \nabla_s \cdot \boldsymbol{\sigma}_s) \quad (7.27)$$

The arguments in the above expressions explicitly indicate the independent physical variables that influence the quantities. For ease of reading, henceforth, we will not explicitly include the arguments when referring to these quantities. The explicit

introduction of the length scale  $l$  in the definition of  $G$  nullifies the length scale dependence inherent in the expression due to the curvature and surface divergence terms.

Since, for an applied configurational force, the observed velocity in general is influenced by microstructural arrangement influenced by atomic scale uncertainty, we now consider a probabilistic treatment of the observed velocity for a given (deterministic) configurational force. The statistical growth form derived in [26] in the reference configuration is

$$\langle V_{S_N} \rangle = C_{V_N} (\mathbf{N} \cdot [\boldsymbol{\Sigma}_\nu - \boldsymbol{\sigma}_I] \mathbf{N}) \exp \left[ - \left( \frac{E_c}{k_B T} \right) \right] \quad (7.28)$$

#### 7.4.1 Application to Small Deformation Diffusive Void Growth

Under the assumption of small deformation the growth condition in the current configuration reduces to:

$$\begin{aligned} \left[ \mathbf{n} \cdot \boldsymbol{\Sigma} \mathbf{n} - \sum_{\alpha=1}^N \rho \mu^\alpha \nu^\alpha \right] &\geq - \frac{\mathbf{F}^T \mathbf{n}}{\sqrt{\mathbf{n} \cdot \mathbf{F} \mathbf{F}^T \mathbf{n}}} \cdot (\kappa \boldsymbol{\sigma}_s \mathbf{n} + \nabla_s \cdot \boldsymbol{\sigma}_s) \\ &\geq - \frac{1}{\sqrt{1 + 2\varepsilon_{nn}}} (\mathbf{I} + \nabla \mathbf{u}) \mathbf{n} \cdot (\kappa \boldsymbol{\sigma}_s \mathbf{n} + \nabla_s \cdot \boldsymbol{\sigma}_s) \end{aligned} \quad (7.29)$$

Now, if the surface stress is homogeneous and isotropic ( $\boldsymbol{\sigma}_s = \gamma \mathbf{I}$ ), and if strains are small  $\varepsilon_{nn} \ll 1$ , the above equation simplifies to,

$$\left[ \mathbf{n} \cdot \boldsymbol{\Sigma} \mathbf{n} - \sum_{\alpha=1}^N \rho \mu^\alpha \nu^\alpha \right] + \kappa \gamma \geq 0 \quad \text{on } \Gamma_s \quad (7.30)$$

Now, a growing phase is locally required to have negative curvature. Thus, we define a local radius of curvature  $r = -\frac{1}{\kappa} > 0$ , and assuming Phase  $-$  to be void (values are zero inside the jump term), we get the condition for diffusive void growth as

$$\mathbf{n} \cdot \boldsymbol{\Sigma} \mathbf{n} - \sum_{\alpha=1}^N \rho \mu^\alpha \nu^\alpha - \frac{\gamma}{r} \geq 0 \quad \text{on } \Gamma_s \quad (7.31)$$

Finally, applying the statistical arguments of § 7.4, we arrive at the small deformation diffusive void normal velocity as:

$$v_{s_n} = c_{v_n} \left( \mathbf{n} \cdot \boldsymbol{\Sigma} \mathbf{n} - \sum_{\alpha=1}^N \rho \mu^\alpha \nu^\alpha - \frac{\gamma}{r} \right) \exp \left[ - \left( \frac{E_c}{k_B T} \right) \right] \quad (7.32)$$

## 8. EXTRACTION AND VALIDATION OF INTERFACIAL ADHESION ENERGY

### 8.1 Activation Energy

In order to compare the data from this study to others in literature, we check the activation energy for electromigration. Due to the variety of test methods used in literature for assessment of electromigration, we first describe the test structure and the criteria used for failure in Tab. 8.1. For these studies the test conditions used and the activation energies calculated are presented in Tab. 8.2. While all these studies are not comparable to this work, we can draw some general conclusions. In general, the activation energies reported in literature may be based on different failure criteria which may make direct comparisons less reliable. For narrow test structures  $< 1 \mu\text{m}$  where, surface diffusion dominates mass transport, the activation energies are  $< 1.0 \text{ eV}$  [88]. This also requires the temperature ranges and current densities to be relatively low.

In order to obtain an activation energy from the resulting data, we revisit the growth condition from Chapter 7 and linearize the equation to yield:

$$\ln v_{\text{sn}} = \ln(c_v H) - \frac{E_c}{k_B T} \quad (8.1)$$

where, we lump the free energy term and the energy dissipated during diffusion as:

$$H = \left( \mathbf{n} \cdot \Sigma \mathbf{n} - \sum_{\alpha=1}^N \rho \mu^\alpha \nu^\alpha \right) \quad (8.2)$$

The left hand side is known and when the data is plotted against the inverse of  $T$ , we obtain the activation energy from the slope. In addition, we obtain an intercept value that corresponds to  $\ln(c_v H)$ . The term is unique to the current density at which the test is carried out. The plots for the three different interfaces are shown



in Fig. 8.1. The activation energies found in this study are listed in Tab. 8.3. The test structures with Ta diffusion barrier layer and capping layer  $\text{SiN}_x$  seem to be in agreement with results reported in literature where, the activation energy falls in the range of values reported for surface/interface diffusion. The structure with TiN as the diffusion barrier layer has a lower activation energy. A low activation energy is a symptom of either poor adhesion at the interface or surface oxidation of Cu during the fabrication process. Poor adhesion at the interface may be inherent to the combination of materials or the presence of PR residue.

Table 8.1. Summary of structures and methods used in copper electromigration tests.

Reference	Copper deposition	Liner/Cu/cap thickness (nm/ $\mu\text{m}$ /nm)	Test line width x length ( $\mu\text{m}$ x $\mu\text{m}$ )	Passivation	Remarks
[89]	Evaporated	20-50(Al,Cu,Ti)/0.3/-	13 x 1000	None	Test done at $3 \times 10^{-7}$ Torr 0.5% $\Delta R$ criterion
[90]	Sputtered	10(Ta)/0.4/10(Ta)	5.4 x 200 2.5 x 5 - 1000	None	Test done in He at 50 Torr Drift velocity test
[91]	Sputtered?	30(Ta)/1.4/-	2.0 x 300	0.1 $\mu\text{m}$ nitride + 1.2 $\mu\text{m}$ polyimide	Via chain structure Fail by opens
[92]	Sputtered	150( $\text{Al}_2\text{O}_3$ )/0.4/-	1.5 x 1000	0.8 $\mu\text{m}$ nitride	Fail by opens
[93-95]	Sputtered	-/ $\approx$ 1.0/-	4-5 x 80	None	Test done in air (oxidation) 5% $\Delta R$ criterion
[96]	Sputtered	-/ $\approx$ 1.0/-	4-5 x 80	None	Test done in nitrogen 5% $\Delta R$ criterion
[97]	Sputtered	100(TiN)/0.4/100(TiN)	0.2-1.0 x 22,000	0.2 $\mu\text{m}$ oxide + 0.8 $\mu\text{m}$ nitride	Fail by opens
[98]	Plated	$\approx$ 125( $\text{Pd}_2\text{Si}$ )/0.3/-	1.5,2.5 x 100	0.6 $\mu\text{m}$ oxide	Fail by opens
[99]	Plated CVD	$\approx$ 125( $\text{Pd}_2\text{Si}$ )/0.3?/- 100(TiW)/?/-	1-1.5 x 100 1-1.5 x 100	0.6 $\mu\text{m}$ oxide 0.6 $\mu\text{m}$ oxide	50% $\Delta R$ criterion Fail by opens
[100]	CVD	100(TiW)/ $\approx$ 0.4/-	1.5 x 100-800	None	50% $\Delta R$ criterion
[101]	Sputtered	20(Ti) + 100(TiN)/0.5/-	2 x 2000	0.8 $\mu\text{m}$ nitride	0.0-0.70 wt. % Ti in Cu

Table 8.1. Continued.

Reference	Copper deposition	Liner/Cu/cap thickness (nm/ $\mu\text{m}$ /nm)	Test line width x length ( $\mu\text{m}$ x $\mu\text{m}$ )	Passivation	Remarks
[102]	PVD,CVD	60(TiN)/0.5/40(TiN)	800 x 1-4	None	20% $\Delta R$ criterion
[103]	?	?(Ta)/0.135/?(SiC <sub>x</sub> N <sub>y</sub> H <sub>z</sub> )	5-200 x 0.09	None	5% $\Delta R$ criterion
[24]	Evaporation	15(Ta)/0.3/-	200 x 0.15-10	None	Tested in Nitrogen at 15 Torr
[104]	Evaporation	-/?/10(CoWP)	0.27-2 x ?	Nitride/oxide	10% $\Delta R$ criterion
[105]	Sputtering CVD	150(TaN,Ta)/1/-	100 x 10	0.1 $\mu\text{m}$ Nitride	
		20(Ti)/1/-	100 x 10	0.1 $\mu\text{m}$ Nitride	
		100(TiN)/1/-	100 x 10	0.1 $\mu\text{m}$ Nitride	
[106]	Evaporation	100(TiN)/0.5/-	2.5-85 x 11.5	None	Tested under vacuum
[107]	Evaporation	20(Ta)/0.4/20(Ta)	300 x 2-5	None	
[108]	Various methods	20(Ta)/0.3/20(Ta)	300 x 2	Ta	
[60]	Evaporation	200(W)+20(Ta)/0.3/20(Ta)	5-300 x 5	None	Tested under vacuum
[73]	?	0.25(Ta)/0.5/100(SiN <sub>x</sub> )	10-300 x 0.5	Nitride	
[74]	?	!20(Ta)/?/?	10.5-210 x 0.21	si <sub>3</sub> N <sub>4</sub>	
[109]	?	?/?/?	5-250 x 0.18	Oxide/Nitride	10% $\Delta R$ criterion

Table 8.2. Summary of copper electromigration test results.

Reference	$\Delta H$ (eV)	Temperature range (°C)	Current density (MA cm <sup>-2</sup> )	Temperature (°C)	Remarks
[89]	0.79	282-401	8.7 - 9.4	342	
[90]	0.66	177-407	1.6,3.1	-	
[91]	0.95 - 1.3	276-415	2.0	350	
[92]	-	-	10	135	
[93-95]	0.86	150-195	16-18	-	As deposited
	1.26	150-195	15-18	-	After 450 °C anneal (large grains)
	$\approx 0.8$	$\approx 180-250$	$>10$	-	After 450 °C anneal (large grains)
[97]	-	-	8	8	0.6 $\mu$ m linewidth
	-	-	8	100	0.2 $\mu$ m linewidth
[98]	-	-	15	$\approx 1$	
[99]	0.81	225 - 300	8	28-63	Pd <sub>2</sub> Si under/plated Cu
	-	-	8	$\approx 160$	TiW under/CVD Cu
[100]	0.41	150-300	8	22	TiW liner/CVD Cu

Table 8.2. Continued.

Reference	$\Delta H$ (eV)	Temperature range (°C)	Current density (MA cm <sup>-2</sup> )	Mean time to failure (h)	Temperature (°C)	Remarks
[101]	-	-	5	40	250	Pure Cu
[102]	0.7-1.02	170-250	8-12	0.08-36	125	PVD, CVD samples have different results
[103]	0.9-1.0	250-325	1-5	-	275	
[24]	0.9-1.1	255-405	1.5	-	-	
[104]	0.9-1.0	280	3.6	2.8/1100	280	
[106]	1.09	175-275	0.6	-	-	
[108]	0.77	250-400	1.5	-	269	
[107]	0.77	200-394	3.6	-	250	
[60]	0.77	250-400	2.1-3.5	-	400	
[73]	0.8	340-400	1-3	-	-	-
[74]	0.9	55	-	-	55	
[109]	0.92	300-350	0.75-4.5	-	-	
[105]	1.09	170-230	1	-	-	

Table 8.3. Activation energies calculated in this study

Interface	Base/Cu/Barrier/Cap Layer Thickness (nm/nm/nm/nm)	Test Conditions		Activation Energy eV
		$j$ (A/cm <sup>2</sup> )	$T$ Range(K)	
TiN/Cu/Ta/SiN	100/100/5/20	3x10 <sup>6</sup>	403.15 - 548.15	0.710
TiN/Cu/SiN	100/100/20	3x10 <sup>6</sup>	403.15 - 548.15	0.788
TiN/Cu/TiN/SiN	100/100/10/20	3x10 <sup>6</sup>	473.15 - 548.15	0.556

## 8.2 Extraction of Interfacial Adhesion

One of the goals for this study is to determine the interfacial adhesion between Cu and the diffusion barrier/capping layers through current induced diffusive voiding. We revisit the expression derived for the growth condition. The free energy for a system with an applied current density may be expressed as:

$$H = \left( \mathbf{n} \cdot \boldsymbol{\Sigma} \mathbf{n} - \sum_{\alpha=1}^N \rho \mu^{\alpha} \nu^{\alpha} - \frac{\gamma}{r} \right) = -c_j \mathbf{J} \cdot \mathbf{n} \quad (8.3)$$

where  $\mathbf{J}$  is the current density expressed here as a vectorial quantity and  $\mathbf{n}$  is normal to the moving interface plane. The negative sign follows convention from the derivation of the phase growth condition where,  $-\mathbf{n}$  points away from the void interface. Such a relation would capture the behavior during electromigration where,  $c_j$  captures the relation between diffusion of species and the flow of charge along the conductor. Note that we have ignored other terms that may be a part of the free energy of the system like strain energy density, since these terms are negligible for the current system. We can write the expression for void growth again in terms of the chosen form of  $H$  in Eq. (8.3):

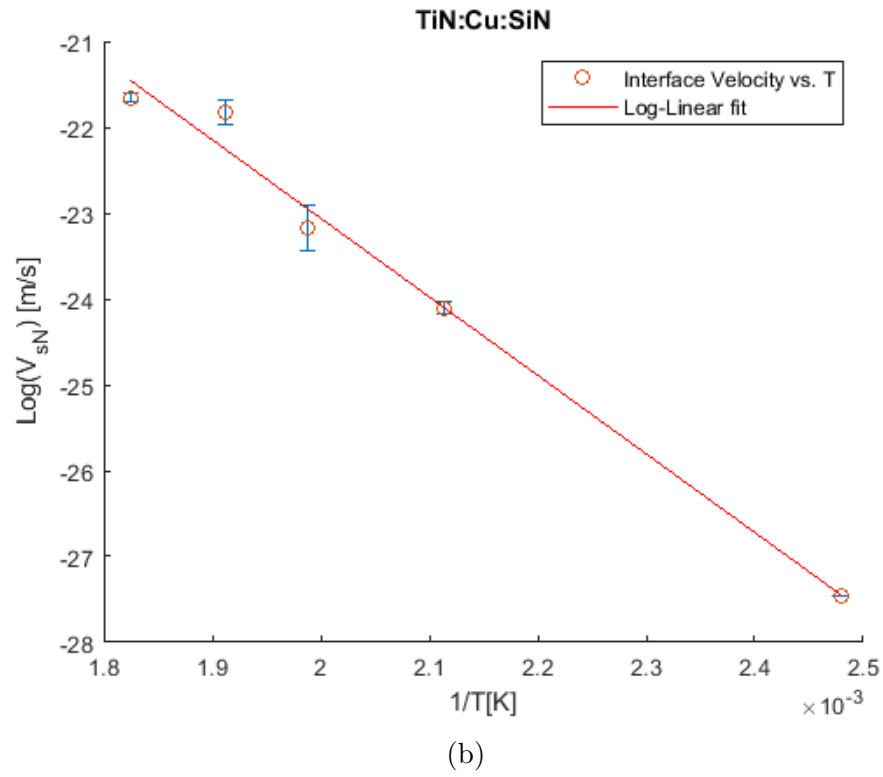
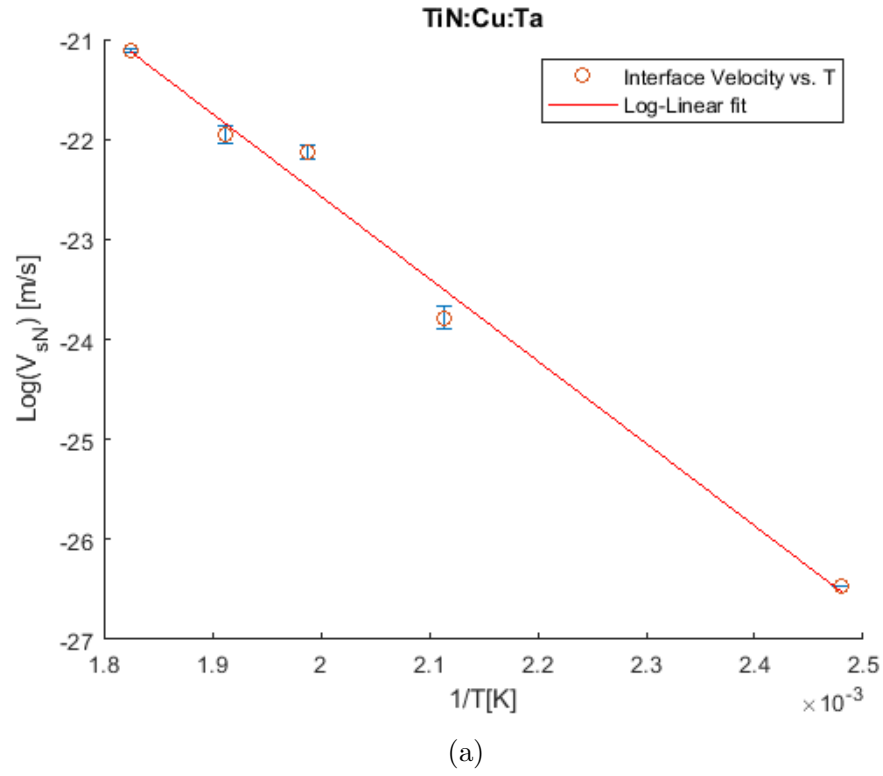


Figure 8.1. Log-linear fit to velocity data for different test structure at fixed current density  $j = 3 \times 10^6 \text{ A/cm}^2$  and varying temperatures (a) Test structure with Ta diffusion barrier layer (b) Test structure with  $\text{SiN}_x$  capping layer (c) Test structure with TiN diffusion barrier layer

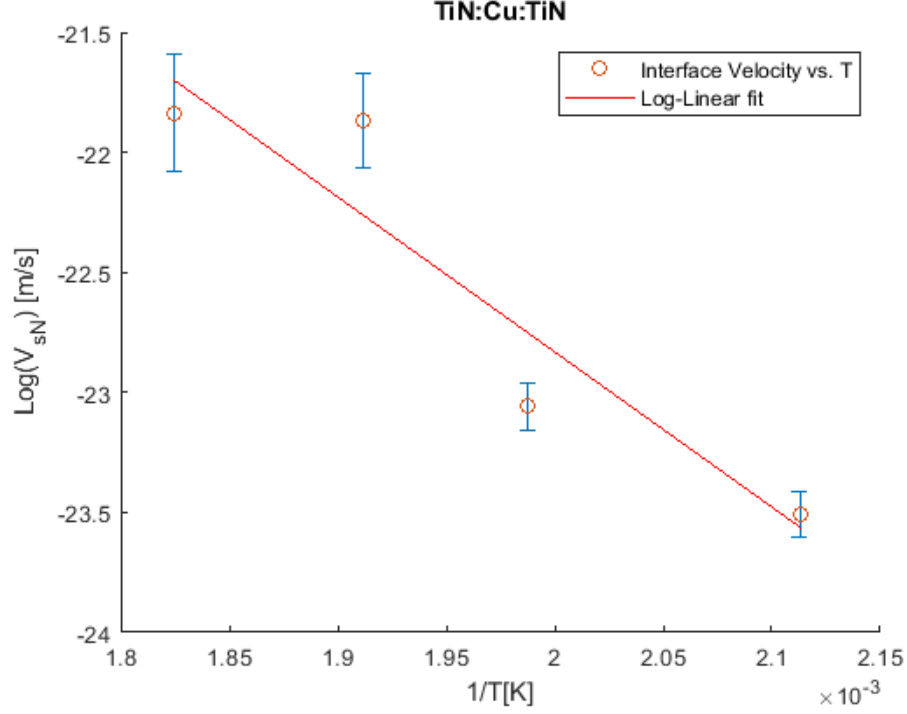


Figure 8.1. Continued

$$v_{sn} = (-c_v c_j \mathbf{J} \cdot \mathbf{n}) \exp \left[ \frac{-E_c}{k_B T} \right] = (c_{vj} \mathbf{J} \cdot \mathbf{n}) \exp \left[ \frac{-E_c}{k_B T} \right] \quad (8.4)$$

Now, based on the experiments carried out at the different current densities at a fixed test temperature we are able to determine the constant  $c_{vj}$  for given set of experiments. Fig. 8.2 is the plot of the normalized current density versus the normalized velocity multiplied with the exponential term. The activation energy used here comes from the activation energy derived using the temperature variation data in the previous section. The inverse of the slope from this plot gives the constant  $c_{vj} = -c_v * c_j$  while, the intercept provides an idea of the critical current density at which electromigration is no longer observed. Note the lowest current density data is omitted for the two structures at present. Electromigration was observed at these current densities however, there was no discernible interface.



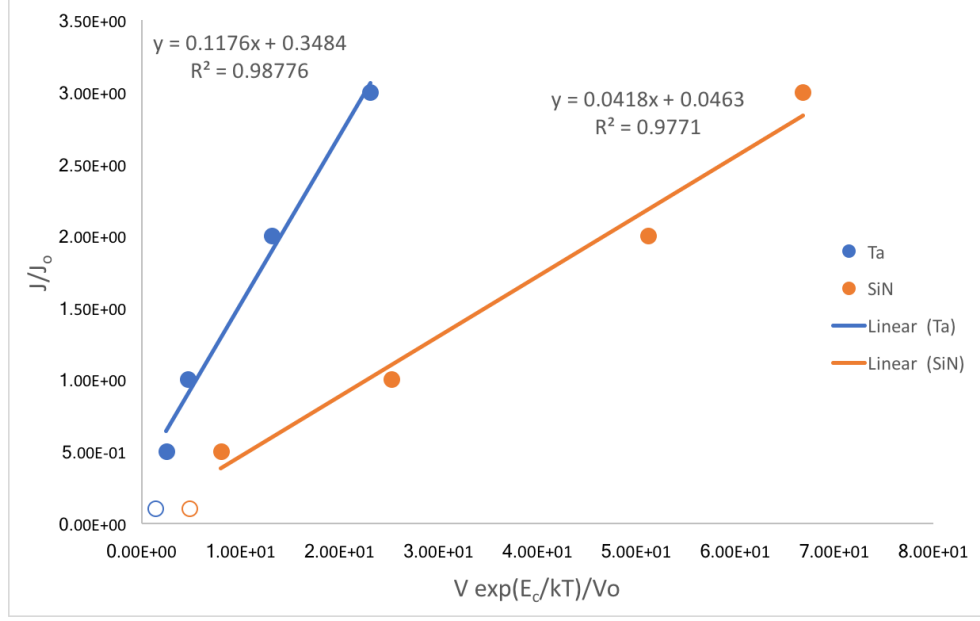


Figure 8.2. Plot of current density variation test data for the Ta and SiN diffusion/cap layer structures.

Next, we draw an analogy to fracture mechanics where, J-integral which is a path independent integral quantity used to calculate the energy release rate must achieve a critical value  $J_c$  for steady state crack progression [28]. In other words  $J \geq J_c$  for a crack to grow. For the case of electromigration we use a similar argument such that,  $H \geq H_c$ .  $H_c$  represents the critical volumetric energy density required for the void to grow during electromigration. Revisiting the void growth condition 7.31 we add an additional term for the interfacial energy  $\gamma_f$  and rearrange the terms:

$$H \geq H_c \quad (8.5)$$

$$\mathbf{n} \cdot \Sigma \mathbf{n} - \sum_{\alpha=1}^N \rho \mu^\alpha \nu^\alpha - \frac{\gamma}{r} \geq \sum_{i=1}^n \gamma_{f_i} \frac{L_i}{A} \text{ on } \Gamma_s$$

The right hand side of this equation represents the critical energy barrier that needs to be overcome for the void to grow. Locally, the curvature  $r$  is very large if the moving front is planar which makes the first term on the right hand side negligible.

$L$  is the perimeter of the interface and  $A$  is the cross-sectional area of a moving front. If there is more than one interface then the interfacial energy and perimeter for that interface are accounted for separately. For steady state diffusive void growth the  $H = H_c$ , thus, the flowing electrons must impart enough energy to debond the atoms from the interface. Rewriting  $H$  as 8.3 we obtain:

$$H = H_c$$

$$c_{vj} \mathbf{J} \cdot \mathbf{n} = \sum_{i=1}^n \gamma_{fi} \frac{L_i}{A} \text{ on } \Gamma_s \quad (8.6)$$

If we now consider taking the ratio of the interfacial energy for the two cases where SiN and Ta are the only interfaces along Cu conductor we obtain the relation:

$$\frac{c_{vj, SiN} \mathbf{J} \cdot \mathbf{n}}{c_{vj, Ta} \mathbf{J} \cdot \mathbf{n}} = \frac{\gamma_{SiN}}{\gamma_{Ta}} \quad (8.7)$$

The length and area terms cancel out on the right hand side as they are the same in both case. Tab. 8.4 are the results from the fit and the ratio of the interfacial energy using this relation. The ratio for these energies is what we can compare to other experimental data for validation.

Table 8.4. Fit results for variation in current density

Interface	$c_{vj}$	$\frac{J_c}{A/\text{cm}^2}$	Ratio $\gamma/\gamma_{Ta}$
TiN/Cu/SiN <sub>x</sub>	23.92	4.63 x 10 <sup>4</sup>	2.81
TiN/Cu/Ta	8.50	3.48 x 10 <sup>5</sup>	1

### 8.3 Validation of Extracted Interfacial Adhesion

Adhesion measurements on thin films are quite challenging to obtain for the interfaces of interest to this study. Fabrication of superlayer structures inspired by Bagchi's work [19] were attempted in this work for validation however, those structures failed during fabrication. More details on those structures are discussed in the next chapter. We rely on measurements made through four point bend experiments on sandwich specimen tests available in literature.

Sandwich specimen tests are modifications of the macroscopic fracture tests and samples for these tests are prepared by incorporating a thin film into a macroscopic fracture test specimen. This is typically done through diffusion bonding, which can alter both the film microstructure and interfacial adhesion, since the bonding process takes a long time (several hours) and occurs at temperatures close to the melting point. Many different sandwich test specimen geometries (see Fig. 8.3) are used. These include four point bend, double cantilever and Brazil-nut sandwich specimen. The type of the sandwich samples considered here is the four-point bend test [110–113]. To date this is the most popular adhesion test for the microelectronics industry. In this test, two elastic substrates with thin films on them are bonded together with another material (typically Cu or epoxy). The upper substrate has a notch in it, and a crack propagates through the substrate and kinks into the interface of interest upon loading. At this point the strain energy release rate reaches steady state, which corresponds to the load plateau in the load-displacement curve. The strain energy release rate can then be calculated from the steady state plateau load  $P$  at fracture [110] as follows:

$$G = \frac{21(1 - \nu^2)P^2L^2}{16Eb^2h^3} \quad (8.8)$$

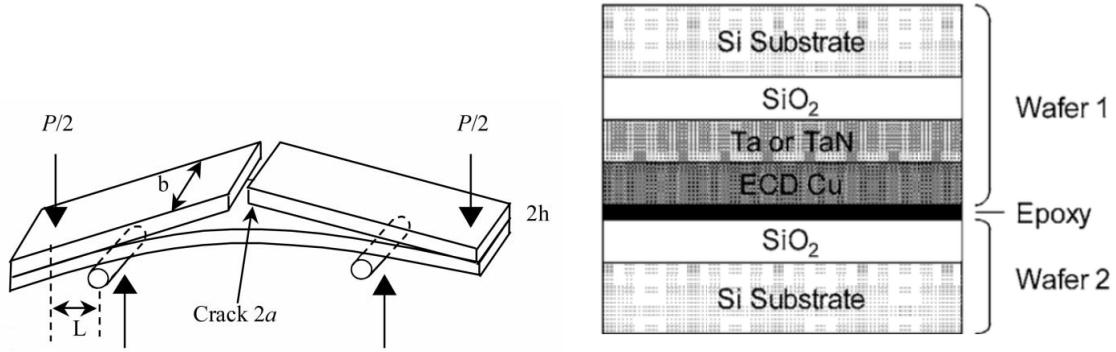


Figure 8.3. (a) Sandwich specimen test schematic [112] for a four point bend test, (b) Schematic of the cross-section of a sandwich specimen test structure [114].

The challenge in sandwich specimen tests is the complicated processes that go into specimen preparation. The specimen are prepared by means of diffusion bonding. This process introduces the possibility of altering film microstructure and interface adhesion. Also, films plastically yield in strongly bonded interfaces which, is observed in the adhesion measurements made by Kim et al. [114].

The data sets we use for validation comes from [23] for the Cu-SiN<sub>x</sub> interface and [114] for the Cu-Ta interface. For Cu-SiN<sub>x</sub> Lane reports a interfacial adhesion  $G_{SiN} = 18.5 \pm 1.8 \text{ J/m}^2$ . There isn't much information on the geometry of the test specimen used and more importantly the thickness of the Cu layer. Cu being complaint allows energy dissipation in the form of plastic deformation. A thicker layer of Cu would mean, the measured interfacial energy would include a larger portion of energy attributed to plasticity. This is observable in the results reported by Kim *et al.*. Fig. 8.5 shows the steady state debond energy measured for Cu-Ta and Cu-TaN interfaces as a function to the Cu layer thickness. In the limit where the Cu layer is 200 nm thick, the reported  $G_{Ta} \approx 5 \text{ J/m}^2$ . This gives a ratio for the upper bound:

$$\frac{G_{SiN}}{G_{Ta}} = 3.7$$

This value is in 18.5 % larger than the value we obtained through our calculations. A second study using the four point bend experiment reported a lower value for the interfacial energy between Cu and SiN<sub>x</sub> [115]. This study uses a stack shown in

Fig. 8.6a with 200nm of Cu on a Ta liner and 50 nm of SiN. A notch is introduced on the side of the coupon where SiN is present and fractures are observed along the Cu-SiN interface during testing. Fig. 8.6b are results plotted for various configurations of the test technique used in the study. We will rely on the value reported with the standard test, since the test method is well established. The reported strain energy release rate is  $G_{SiN} = 10.5 \pm 1.2 \text{ J/m}^2$ . This value is lower compared to the fracture energy reported by Lane *et al.* highlighting the variability in data across different studies. We use this as a separate data point to establish a known lower bound for the purpose of validation where,

$$\frac{G_{SiN}}{G_{Ta}} = 2.1$$

The value obtained from this study fits within these bounds. This is a promising result given the complexity involved in most adhesion characterization methods in literature. Additionally, the value we obtain through our experiments are bound to be slightly lower because, the ratio of the interfacial energy is a combination of the interfacial energy of TiN and Ta or SiN. This is because the base of the Cu line is in contact with TiN which allows diffusion tangential to it's surface. Mathematically, the expression in Eq. (8.7) should read as follows:

$$\frac{c_{vj,SiN}}{c_{vj,Ta}} = \frac{\gamma_{SiN}(2t + w) + \gamma_{TiN}(w)}{\gamma_{Ta}(2t + w) + \gamma_{TiN}(w)} \quad (8.9)$$

where w and t are known geometric width and thickness of the Cu film. The interfacial energy of Cu-TiN is to be determined but, early indications suggests this value may be small compared to Cu-Ta and Cu-SiN interfacial energies. However, further verification is required to confirm this.

Cap	SiC	BLoK™	SiN	CoWP	BLoK™ (no Cu clean)
$G(\text{J/m}^2)$	11.5	20.0	18.5	>40	9.2
Error	1.1	2.0	1.8	N/A <sup>a</sup>	0.9
Growth rate @310 °C ( $\mu\text{m/h}$ )	0.32	0.023	0.017	0.001	0.08
$\Delta H_m$ (eV)	0.87	0.92	0.90	1.22	N/A

<sup>a</sup>N/A indicates not applicable.

Figure 8.4. Results for steady state energy release rate obtained through four point bend tests on sandwich specimen tests by Lane et al. [23].

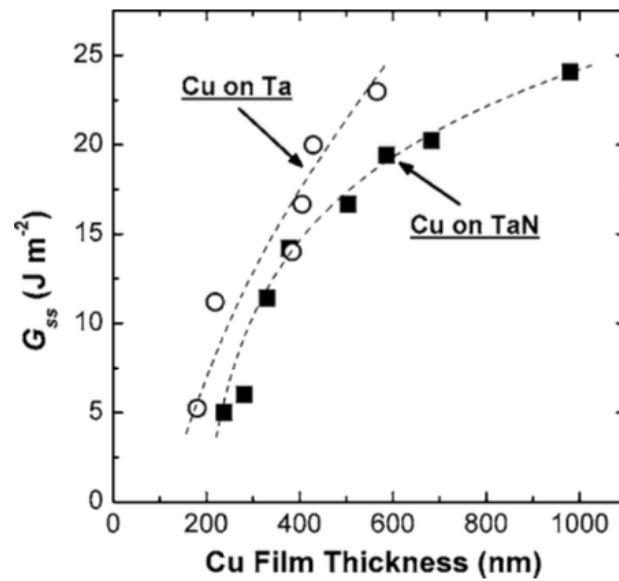


Figure 8.5. Results for steady state energy release rate obtained through four point bend tests on sandwich specimen tests. [114]

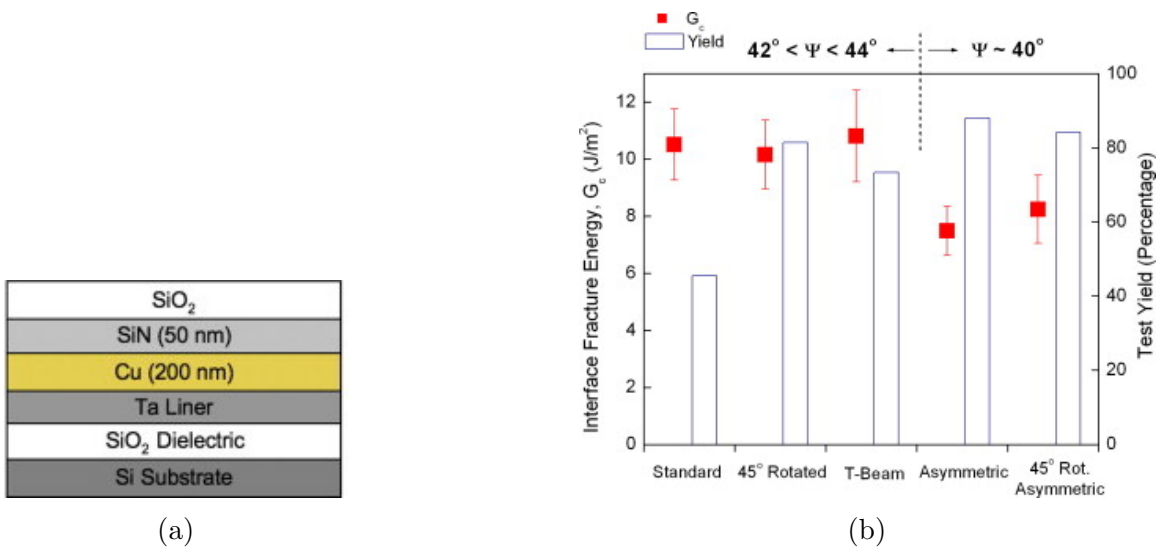


Figure 8.6. (a) Film stack used for four point bend experiments by Birringer *et al.* (b) Fracture energies and yields reported for different test configurations [115].

## 9. VALIDATION OF FRACTURE TOUGHNESS: SUPER LAYER TEST

### 9.1 Overview

This section describes the superlayer method for interfacial adhesion measurement. Originally these structures were meant to serve as a baseline study to validate experimental results from the electromigration tests. We begin by introducing the super layer test method. The fabrication steps for the test method are discussed along with the preliminary requirements for the built-up layers. Next, we describe the challenges encountered with this method during fabrication that led to premature failure of the devices.

### 9.2 Super Layer Test

This method was originally proposed by Bagchi *et al.*, where the interfacial adhesion energy between Cu and  $\text{SiO}_2$  was characterized by inducing a debonding event at the interface by depositing a film with a high residual stress. By varying the thickness of the added layer (superlayer), energy is provided at the interface to drive a crack. Typically, a metal film like Chromium(Cr) is used for the superlayer because of its high melting temperature which, ensures a large residual stress upon cooling. Zheng *et al.* modified the test structure using a sacrificial Au layer to linearly vary the adhered portion of the film that is delaminated Fig. 9.1a. This modification to the geometry allows for a more accurate measure of energy release rate as the available energy to drive the crack reduces. The change in the contact area between the film and the substrate increases along the length of the film however, the energy available through the intrinsic residual stress remains the same. As the film decoheres from the interface, the crack driving force ultimately reduces to the critical value below which there is no more propagation unless any external force is applied.



The energy release rate for the interfacial crack in a multi layer stack shown in Fig. 9.2 is given by [19]:

$$G = \sum_i \frac{\sigma_k^2 h_i}{E'_i} - \sum_i \frac{1}{E'_i} \left[ \frac{P^2}{h_i} + \frac{12M_i^2}{h_i^3} \right] \quad (9.1a)$$

$$P = \kappa \left[ \frac{E'_1 h_1^3 + E'_2 h_2^3}{6(h_1 + h_2)} \right] \quad (9.1b)$$

$$\kappa = \frac{6(h_1 + h_2)(\varepsilon_1 - \varepsilon_2)}{h_1^2 + E'_2 h_2^3 / E'_1 h_1 + E'_1 h_1^3 / E'_2 h_2 + h_2^2 + 3(h_1^2 + h_2^2)} \quad (9.1c)$$

$$M'_i = E'_i \kappa \quad (9.1d)$$

where  $i = 1, 2$  refer to the materials in the bilayer,  $h_1$  and  $h_2$  refer to the film and superlayer thicknesses,  $E'_i$  are the biaxial elastic moduli  $E_i/(1 - \nu_i)$ , load  $P$  is associated with the residual tensile stress  $\sigma_i$  in each layer,  $\kappa$  is the curvature of the debonded layer,  $\varepsilon_i$  are misfit strains and  $M_i$  are the bending moments along the centerline of each layer due to load  $P$ . Since, the interfacial toughness is mode

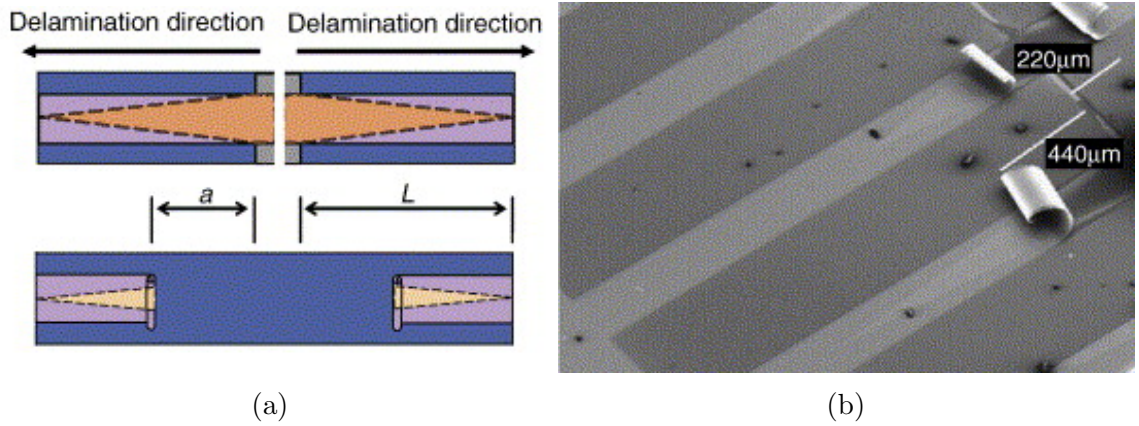


Figure 9.1. Super layer test (a) Schematic of test strips with sacrificial layer [116] (b) Delamination observed for Ti-Cr strips with different apex angles for the release layer [116].

dependent the phase angle also needs to be specified corresponding to the estimated interfacial toughness.

The energy release rate in the modified superlayer test is given by:

$$G_c = G \frac{L}{a} \quad (9.2)$$

When the film and the superlayer combination is cut, the composite film debonds over the central weak region. The initiated crack then propagates over the varying width region. The propagating crack arrests at a width of the varying width region such that the energy release rate is equal to the interfacial fracture toughness.

### 9.2.1 Super Layer Test Specimen Fabrication

The fabrication of the test specimen conforms to the standard of IC fabrication with compatible material sets. Cr is the super layer chosen to introduce tensile stress. The only possible drawback of using the modified version of the super layer test structures is the use of gold or carbon as a the sacrificial layer. Though it is possible to etch gold from the stack, it is not a clean process. The etch chemical may even etch other films that are present, worse it may cause corrosion and sub critical debonding in the film structure. In order to avoid this we propose a modified

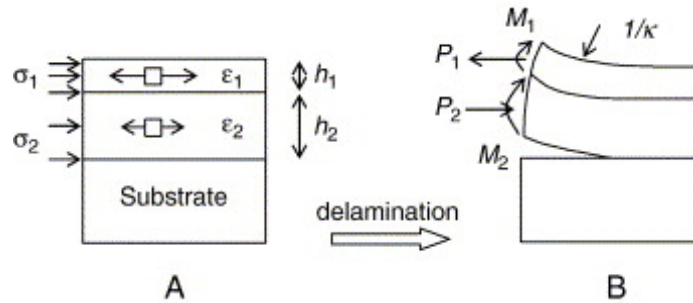


Figure 9.2. Schematic of bilayer film with residual stresses [116].

fabrication scheme using image reversal photoresist as a possible substitute for gold as a sacrificial layer. Briefly, the steps are as follows:

1. Start with a wafer that has a combination of Ti and Au as the sacrificial layer. Based on Zheng's work we used 5 nm of Ti and 25 nm of Au. Next spin coat and expose photoresist with mask 1 which, creates the profile for the sacrificial layer to be etched. Au and Ti are both etched using commercially available etchants.
2. Spin and expose positive photoresist AZ1518 with mask 2 to form the pattern for the metal lift-off. Before developing the resist, dip the specimen in Toluene for 5 minutes. This hardens the top layer of the photoresist and gives it a desirable negative profile for metal lift off. No post bake is required after this step.
3. Evaporate the metal film stack on the substrate to the desired thickness. Note, the superlayer residual stress is based on the thickness of the film and it's elastic modulus. Choosing the correct thickness is critical to the design. If the residual stress induced is small, there is no debond event and if the stress is too large, uncontrolled debonding occurs. After deposition strip the photoresist. Ensure that there is little to no agitation when the photoresist is being stripped.
4. Once the metal lift off is carried out spin AZ 1518 positive photoresist and expose mask 3. This mask pattern is used to define areas where the Cr and Cu film are to be etched. After developing the resist, wet etch the Cr and Cu films. Once the etch is complete. Lift off the resist by dipping in a solvent and transfer quickly to IPA. Follow this step by carrying out CPD (Critical point drying) to avoid stiction.
5. Measure the length of the film that peeled back to assess the energy release rate.

These steps are shown in a schematic in Fig. 9.3.

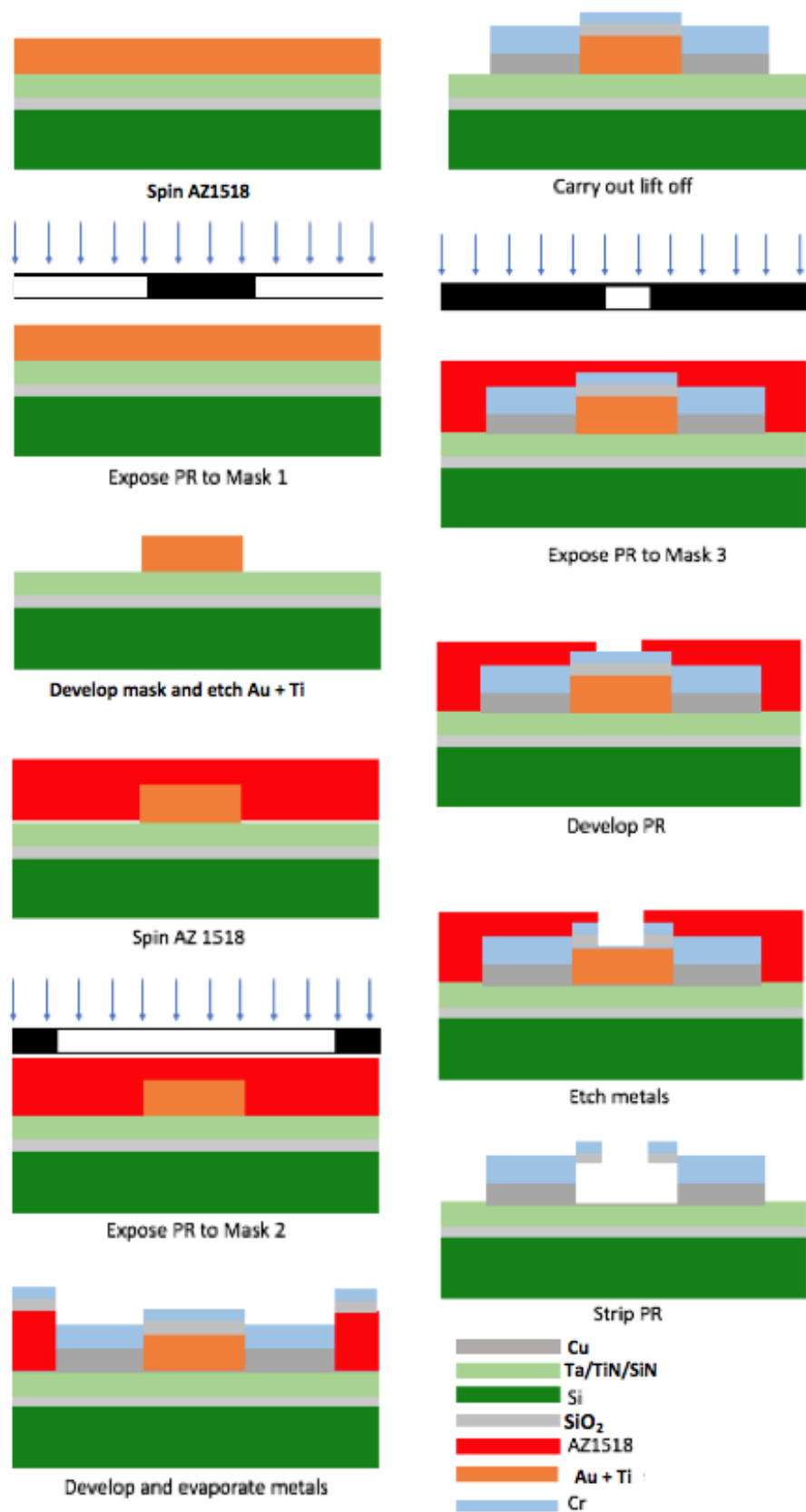


Figure 9.3. Schematic for fabrication of super layer test structures

### 9.2.2 Results: Super Layer Test

Test structures were fabricated with 100nm of Cu and 100nm of Cr on  $\text{SiN}_x$ . Ti and Au were used as the sacrificial layers following [116]. There were several issues that were encountered during the fabrication process.

1. Most chemical etchants that etch Cr also etch Cu to some extent. This is still manageable if the etch rates are known and relatively slow. However, it was found that as the Cr layer is etched, the Cu layers start to crack underneath.
2. The Au sacrificial layer is not ideal for use with Cu as it has better adhesion with Au compared to  $\text{SiN}$ . When Au etching was carried out, the etch solution did not penetrate far enough under the Cu film for it to be effective. The thickness of the sacrificial layer is crucial, a thin layer will not allow etching solutions to penetrate and a thick layer will cause the film to tear.
3. Calibrating a film to induce a known amount of residual stress is challenging. Residual stress measurements will vary from one deposition step to another and if the metal under the superlayer is ductile, it will plastically yield to conform to the substrate.

Due to the fabrication challenges, the idea to use superlayers was abandoned for the given study. Fig. 9.4 and Fig. 9.5 are images from the failed fabricated devices. We instead use reported values of interfacial energies in literature for the material sets of interest.

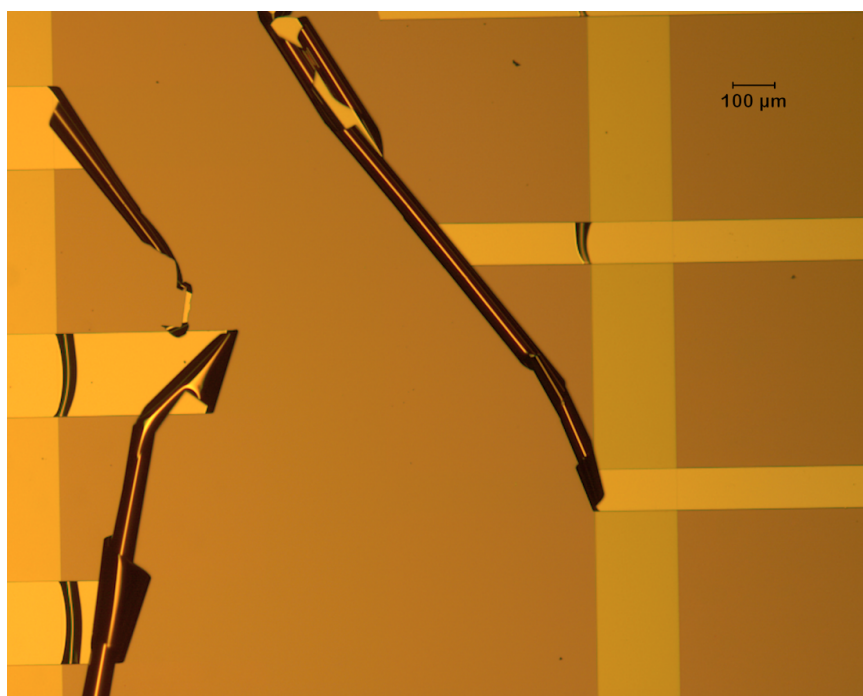


Figure 9.4. Premature peeling observed in the thin film after deposition.

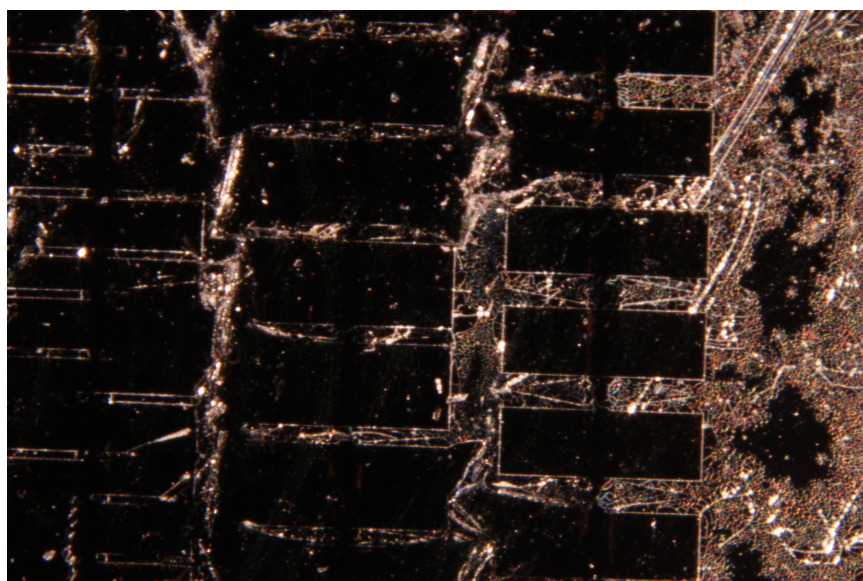


Figure 9.5. Cracking and premature debonding in films with a superlayer.

## 10. CONCLUSIONS AND FUTURE WORK

### 10.1 Summary of Work

In this study we designed test structures using Blech's work as inspiration. The test structures were made such that they would not develop large stress gradients during testing which, is confirmed by the nearly linear void growth measurements. Three different test structures were fabricated to allow a comparative study with varying line widths. The width variation was used to determine the line width most feasible to allow average void growth measurements. Additionally, numerical simulations were carried out to determine the local temperature change for a chosen test current density and width of the conducting line. A custom tester was built with the flexibility to allow ex-situ or in-situ experiments. The developed test setup can be used in an SEM for test specimens or test conditions where, optical measurement may not be sufficient. The tool has the ability to provide nA current source resolution while taking 4-wire resistance measurements. Tests can be carried at elevated temperatures using a local heat source in the form a ceramic heater.

Three different test structures with varying capping interfaces (Cu-Ta, Cu-SiN<sub>x</sub> and Cu-TiN ) were subject to electromigration stress conditions. First, temperature was varied between 130 °C and 275 °C at a fixed current density of  $3 \times 10^6$  A/cm<sup>2</sup>. An exponential change in void growth rate was observed as the temperature was changed. After data fitting, the activation energy was extracted for each test structure. The results for Cu-Ta and Cu-SiN<sub>x</sub> interface were found to be in good agreement with activation energies reported in literature for cases where surface or interface diffusion is the primary diffusion mechanism. The test structure with Cu-TiN interface yielded a lower activation energy of 0.56 eV indicating possible oxidation in the test structure. A second set of experiments were carried out on two of three device structures (Cu-

Ta and Cu-SiN<sub>x</sub>) where, the test temperature was kept constant at 275 °C and the current densities were varied. The results from both test structures confirmed linearly varying void growth rates. Using the phase growth condition derived by [26] and using a simple analogy to fracture mechanics, we derived a condition where, the driving force for diffusion of species needs to exceed a critical value for diffusion to occur. Using the data fits from the two different test conditions we were able to extract a ratio for the interfacial energies  $\frac{\gamma_{SiN}}{\gamma_{Ta}}$  of the two tested interfaces (Cu-SiN<sub>x</sub> and Cu-Ta). We obtained a ratio of 2.81 from our experiments. This ratio was validated against published data from literature that used four point bend experiments on sandwich specimens. The ratio of interfacial energies from existing literature was found to be 2.1 and 3.7 which, puts the calculated values in this study within the bounds. However, it is noted that the value we calculate should include interfacial energy for TiN as well. Since the test structures all have an interface with TiN as the base layer. The adhesion characterization of the Cu-TiN interface needs to be carried out separately to verify the exact ratio but, the results seem promising.

Superlayer test structures were fabricated to initially serve as validation for the interfacial energy however, several fabrication challenges were encountered which led to premature failure of the devices.

## 10.2 Implications of the study

The study has a few fundamental and technological implications:

1. This method and structure can be used to evaluate the viability of new diffusion/capping barrier layers without the need for extensive reliability studies on real structures that may take a long time to carry out.
2. It provides a fundamental basis to explain the variation in electromigration lifetimes observed for different material interfaces. Improving adhesion at the interface by chemical treatments or surface cleaning will provide better electromigration performance if the material interface cannot be changed.



3. This method to extract adhesion energy from current driven diffusive systems is the only other work in literature apart from [23] where a fundamental relation between adhesion and void growth kinetics is derived. However, Lane *et al.* use a correlation that was derived using the assumption of a linear behavior between work of adhesion and activation energy.
4. Potentially, the method proposed here for adhesion characterization can be extended to flexible substrates and embedded structures, which is currently not possible with any of the existing thin film adhesion characterization methods

### 10.3 Future Work

Interfacial adhesion at the Cu-TiN needs to be characterized using a different method so a more accurate comparison can be made with the extracted values through the electromigration experiments. Additionally, test structures with silicon carbide (SiC) as the passivation layer are to be fabricated for testing. This will allow a second data set to validate the extracted interfacial adhesion values.

The current data set for test temperature variation uses a fixed a current density at  $3 \times 10^6$  A/cm<sup>2</sup>. For a given interface, the extracted value of  $\ln(c_v H)$  through data fits is a unique value that changes with the current density. In order to estimate the constant  $c_v$  additional tests will be required at a different current density. Furthermore, a thorough investigation of the Cu microstructure after annealing is required to ascertain average grain sizes.

## REFERENCES

## REFERENCES

- [1] R. Rivlin. The effective work of adhesion. *Paint Technology*, 9:215–218, 1944.
- [2] K. Kendall. Control of cracks by interfaces in composites. *Proceedings of the Royal Society of London A: Mathematical, Physical and Engineering Sciences*, 341(1627):409–428, 1975.
- [3] W. T. Chen and T. F. Flavin. Mechanics of film adhesion: Elastic and elastic plastic behavior. *IBM Journal of Research and Development*, 23:203–213, 1972.
- [4] D. H. Kaeble. Theory and analysis of peel adhesion. In *Transaction of Society of Rheology*, volume 3, pages 161–180, 1959.
- [5] D. H. Kaeble. Peel adhesion: Influence of surface energies and adhesive rheology. *Journal of Adhesion*, 1:102–123, 1969.
- [6] K.-S. Kim and N. Aravas. Elastoplastic analysis of the peel test. *International Journal of Solids and Structures*, 24(417-435), 1988.
- [7] M. Moon, H. Jensen, J. Hutchinson, K. Oh, and A. Evans. The characterization of telephone cord buckling of compressed thin films on substrates. *Journal of the Mechanics and Physics of Solids*, 50:2355–2377, 2002.
- [8] A. Volinsky, P. Waters, J. Kiely, and E. Johns. Sub-critical telephone cord delamination propagation and adhesion measurements. *Materials Research Society, Warrendale, PA*, 2004.
- [9] A. Lee, C. Litteken, R. Dauskardt, and W. Nix. Comparison of the telephone cord delamination method for measuring interfacial adhesion with the four-point bending method. *Acta Materialia*, 53(3):609–616, 2005.
- [10] M. Moon, K. Lee, K. Oh, and J. Hutchinson. Buckle delamination on patterned substrates. *Acta Materialia*, 52(10):3151–3159, 2004.
- [11] J. Hutchinson, M. Thouless, and E. Liniger. Growth and configurational stability of circular, buckling-driven film delaminations. *Acta Metallurgica et Materialia(USA)*, 40(2):295–308, 1992.
- [12] A. Evans and J. Hutchinson. Mechanics of delamination and spalling in compressed films. *International Journal of Solids and Structures*, 20(5):455–466, 1984.
- [13] B. E. Alaca, M. T. A. Saif, and H. Sehitoglu. On the interface debond at the edge of a thin film on a thick substrate. *Acta Materialia*, 50(5):1197–1209, 2002.
- [14] C. Muhlstein, S. Brown, and R. O. Ritchie. High cycle fatigue in single crystal silicon thin films. *Journal of Microelectromechanical Systems*, 10(4):593–600, 2001.

- [15] I. A. Blech. Electromigration in thin aluminum films on titanium nitride. *Journal of Applied Physics*, 47(4):1203–1208, 1976.
- [16] E. C. Yeh, W. Choi, K. Tu, P. Elenius, and H. Balkan. Current-crowding-induced electromigration failure in flip chip solder joints. *Applied physics letters*, 80(4):580–582, 2002.
- [17] K. Tu, C. Yeh, C. Liu, and C. Chen. Effect of current crowding on vacancy diffusion and void formation in electromigration. *Applied Physics Letters*, 76(8):988–990, 2000.
- [18] L. Arnaud, T. Berger, and G. Reimbold. Evidence of grain boundary versus interface diffusion in electromigration experiments in copper damascene interconnects. *Journal of Applied Physics*, 93(1):192–204, 2003.
- [19] A. Bagchi. A new procedure for measuring the decohesion energy for thin ductile films on substrates. *Journal of materials research*, 9(7):1734–1741, 1994.
- [20] D. B. Marshall and A. G. Evans. Measurement of adherence of residually stressed thin films by indentation i. mechanics of interface delamination. *Journal of Applied Physics*, 56(10):2632–2638, 1984.
- [21] P. J. Burnett and D. S. Rickerby. The relationship between hardness and scratch adhesion. *Thin Solid Films*, 154(1-2):403–416, 1987.
- [22] J. J. Vlassak and W. D. Nix. A new bulge test technique for the determination of young's modulus and poisson's ratio of thin films. *Journal of materials research*, 7(12):3242–3249, 1992.
- [23] M. Lane, E. Liniger, and J. Lloyd. Relationship between interfacial adhesion and electromigration in cu metallization. *Journal of Applied Physics*, 93(3):1417–1421, 2003.
- [24] C. K. Hu, R. Rosenberg, and K. Lee. Electromigration path in cu thin film lines. *Applied Physics Letters*, 74(20):2945–2947, 1999.
- [25] J. Lloyd, M. Lane, E. Liniger, C.-K. Hu, T. Shaw, and R. Rosenberg. Electromigration and adhesion. In *IEEE Transactions on Device and Materials Reliability*, volume 5, 2005.
- [26] P. Vaitheeswaran, A. Udupa, S. Sadasiva, and G. Subbarayan. Interface balance laws, phase growth and nucleation conditions for multiphase solids with inhomogeneous surface stress. *Continuum Mechanics and Thermodynamics*, pages 1–24, June 2019.
- [27] R. Gleixner and W. Nix. A physically based model of electromigration and stress-induced void formation in microelectronic interconnects. *Journal of applied physics*, 86(4):1932–1944, 1999.
- [28] J. R. Rice. A path independent integral and approximate analysis of strain concentration by notches. *Journal of Applied Mechanics*, pages 379–386, 1968.
- [29] Y. Xu, Y. Singh, C. Pan, and G. Subbarayan. Adhesive toughness and instability in bonded heterogeneous films. *International Journal of Solids and Structures*, 169:41–54, 2019.

- [30] M. Gerardin. Bestimmung des schmelzpunktes von die wärme schlecht leitenden körpern. *Fresenius' Journal of Analytical Chemistry*, 1(1):453–453, 1862.
- [31] F. Skaupy. Verh. dtsch. *Phys. Ges*, 18:230, 1916.
- [32] H. Weber. Transport experiments on solid copper. *Z.[101] Elektrochem*, 60:1170–1175, 1956.
- [33] V. Fiks. On the mechanism of mobility of ions in metals. *Soviet Physics-Solid State*, 1(1):14–28, 1959.
- [34] A. Grone. Current-induced marker motion in copper. *Journal of Physics and Chemistry of Solids*, 20(1-2):88–93, 1961.
- [35] F. M. d'Huerle. Electromigration and failure in electronics: An introduction. In *Proceedings of the IEEE*, volume 59, pages 1409–1418, 1971.
- [36] M. E. Gliksmann. *Diffusion in Solids: Field Theory, Solid-State Principles, and Applications*. Wiley, 2000.
- [37] E. T. Ogawa, K.-D. Lee, V. A. Blaschke, and P. S. Ho. Electromigration reliability issues in dual-damascene cu interconnections. *Reliability, IEEE Transactions on*, 51(4):403–419, 2002.
- [38] K. D. Lee, X. Lu, E. T. Ogawa, H. . Matsuhasi, and P. S. Ho. Electromigration study of cu/low-k dual damascene interconnects. In *International Reliability Physics Symposium*, 2001.
- [39] S. J. Rotham and N. L. Peterson. Isotope effect and divacancies for selfdiffusion in copper. *Physica Status Solidi(b)*, 35(1):305–312, 1969.
- [40] E. T. Ogawa. *Electromigration in Thin Films and Electronic Devices*, chapter Electromigration Failure in Nanoscale Copper Interconnects. Woodhead Publishing Limited, 2011.
- [41] J. Cho and C. Thompson. Grain size dependence of electromigration-induced failures in narrow interconnects. *Applied Physics Letters*, 54(25):2577–2579, 1989.
- [42] M. A. Meyer and E. Zschech. New microstructure-related em degradation and failure mechanisms in cu interconnects with cowp coating. In AIP, editor, *AIP Conference Proceedings*, volume 945, 2007.
- [43] I. A. Blech and C. Herring. Stress generation by electromigration. *Applied Physics Letters*, 29(3):131–133, 1976.
- [44] I. A. Blech and K. L. Tai. Measurement of stress gradient generated by electromigration. *Applied Physics Letters*, 30(8):387–389, 1977.
- [45] J. R. Lloyd. Electromigration and mechanical stress. *Microelectronic Engineering*, 49:51–64, 1999.
- [46] R. Kirchheim. Stress and electromigration in al-lines of integrated circuits. *Acta Metallurgica et Materialia*, 40(2):309–323, 1992.
- [47] J. R. Black. *Electron Devices, IEEE Transactions on*, 16(4):338–347, 1969.

- [48] H. Huntington and A. Grone. Current-induced marker motion in gold wires. *Journal of Physics and Chemistry of Solids*, 20(1-2):76–87, 1961.
- [49] J. C. Blair, P. B. Ghate, and C. T. Haywood. Concerning electromigration in thin films. In *IEEE*, volume 59, pages 1023–1024, 1971.
- [50] M. Shatzkes and J. Lloyd. A model for conductor failure considering diffusion concurrently with electromigration resulting in a current exponent of 2. *Journal of applied physics*, 59(11):3890–3893, 1986.
- [51] R. Rosenberg and L. Berenbaum. Resistance monitoring and effects of non-adhesion during electromigration in aluminum films. *Applied Physics Letters*, 12(5):201–204, 1968.
- [52] R. W. Pasco and J. A. Schwarz. Temperature ramp resistance analysis to characterize electromigration. *Solid State Electronics*, 26(5):445–452, 1983.
- [53] C. Hong and D. L. Crook. Breakdown energy of metal (bem) - a new technique for monitoring reliability at wafer level. In *Proceedings of the 23rd International Reliability Physics Symposium*, pages 108–114, 1985.
- [54] B. Root and T. Turner. Wafer-level electromigration tests for production monitoring. In *IEEE*, editor, *International Reliability Physics Symposium*, pages 100–107, 1985.
- [55] R. E. Jones Jr and L. D. Smith. A new waferlevel isothermal jouleheated electromigration test for rapid testing of integratedcircuit interconnect. *Journal of Applied Physics*, 61(9):4670–4678, 1987.
- [56] O. Aubel, W. Hasse, and M. Hommel. Highly accelerated electromigration lifetime test (halt) of copper. In *IEEE Transactions on Device and Materials Reliability*, volume 3, pages 213–217, 2003.
- [57] M. A. Meyer, M. Hermann, E. Langer, and E. Zschech. In-situ sem observation of electromigration phenomena in fully embedded copper interconnect structures. *Microelectronics Engineering*, 64:376–382, 2002.
- [58] I. A. Blech and E. Kinsboro. Electromigration in thin gold films on molybdenum surfaces. *Thin Solid Films*, 25(2):327–334, 1975.
- [59] A. V. Vairagar, S. G. Mhaisalkar, A. Krishnamoorthy, K. N. Tu, A. M. Gusak, M. A. Meyer, and E. Zschech. In situ observation of electromigration-induced void migration in dual-damascene cu interconnect structures. *Applied Physics Letters*, 85(13):2502–2504, 2004.
- [60] K. L. Lee, C. K. Hu, and K. N. Tu. In situ scanning electron microscope comparison studies on electromigration of cu and cu(sn) alloys for advanced chip interconnects. *Journal of Applied Physics*, 78(7):4428–4437, 1995.
- [61] Q. Huang, C. M. Lilley, and R. Divan. An in situ investigation of electromigration in cu nanowires. *nanotechnology*, 20:1–6, 2009.

- [62] T. Kirimura, K. Croes, Y. K. Siew, K. Vanstreels, P. Czarnecki, Z. El-Mekki, M. H. van der Veen, D. Dictus, A. Yoon, A. Kolics, J. Bommels, and Z. Tokei. Void nucleation and growth during electromigration in 30 nm wide cu lines: Impact of different interfaces on failure modes. In *Interconnect Technology Conference (IITC)*. IEEE, 2013.
- [63] K. Vanstreels, P. Czarnecki, T. Kirimura, I. D. Wolf, J. Bommels, Z. Tokei, and K. Croes. In-situ scanning electron microscope observation of electromigration-induced void growth in 30 nm pitch cu interconnect structures. *Journal of Applied Physics*, 2014.
- [64] B. Li, T. Sullivan, T. C. Lee, and D. Badami. Reliability challenges for copper interconnects. *Microelectronics Reliability*, 44:365–380, 2004.
- [65] M. A. Nicolet. Diffusion barriers in thin films. *Thin Film Solids*, 52:415–443, 1978.
- [66] C. Lee and Y.-L. Kuo. The evolution of diffusion barriers in copper metalization. *Journal of the Minerals, Metals and Materials Society*, pages 44–49, 2007.
- [67] M. Y. Kwak, D. H. Shin, T. W. Wang, and K. N. Kim. Characteristics of tin barrier layer against cu diffusion. *Thin Solid Films*, 339(1-2):290–293, 1999.
- [68] K. Lal, A. K. Meikap, S. K. Chattopadhyay, S. K. Chatterjee, M. Ghosh, K. Baba, and R. Hatada. Electrical resistivity of titanium nitride thin films prepared by ion beam-assisted deposition. *Physica B: Condensed Matter*, 307(1-4):150–157, 2001.
- [69] S. W. King. Dielectric barrier, etch stop, and metal capping materials for state of the art and beyond metal interconnects. *ECS Journal Of Solid State Science and Technology*, 4(1):3029–3047, 2015.
- [70] M. H. Van der Veen, K. Vandermissen, D. Dictus, S. Demuyne, R. Liu, X. Bin, P. Nalla, A. Lesniewska, L. Hall, K. Croes, and L. Zhao. Cobalt bottom-up contact and via prefill enabling advanced logic and dram technologies. In IEEE, editor, *International Interconnect Technology Conference*, pages 25–28, May 2015.
- [71] J. F. Zheng, P. Chen, T. H. Baum, R. R. Lieten, W. Hunks, S. Lipsey, A. Frye, W. Li, J. O’Neill, J. Xu, and J. Zhu. Selective co growth on cu for void-free via fill. In IEEE, editor, *International Interconnect Technology Conference*, number 265-268, May 2015.
- [72] International technology roadmap for semiconductors 2.0 - interconnect, 2015.
- [73] K.-D. Lee, E. T. Ogawa, H. Matsushashi, P. R. Justison, K.-S. Ko, and P. S. Ho. Electromigration critical length effect in cu oxide dual-damascene interconnects. *Applied Physics Letters*, 79(20):3236–3238, 2001.
- [74] C. S. Hau-Riege, A. P. Marathe, and V. Pham. The effect of line length on the electromigration reliability of cu interconnects. In *Advanced Metallization Conference*, page 169, 2002.
- [75] Comsol multiphysics 4.3b, comsol inc, 2009.

- [76] Y.-Y. Wang, T.-H. Lee, and C.-I. Kim. Etching characteristics of titanium nitride in chlorine based plasma. *Journal of nanoscience and nanotechnology*, 16(12):12933–12935, 2016.
- [77] P. Walker and W. H. Tarn. *handbook of Metal etchants*. CRC press, 1991.
- [78] June 2019.
- [79] Kelvin resistance measurement, June 2019.
- [80] J. G. Webster. *The measurement, instrumentation, and sensor handbook*. CRC press LLC, 1999.
- [81] K. Tu. Recent advances on electromigration in very-large-scale-integration of interconnects. *Journal of Applied Physics*, 94(9):5451–5473, 2003.
- [82] E. Pop. Thermal resistance(measurement and simulation) in electronic devices. Presentation - Online, 2019.
- [83] J. Gupta, J. M. E. Harper, J. L. Mauer, P. G. Blauner, and D. A. Smith. Focused ion beam imaging of grain growth in copper thin films. *Applied Physics Letters*, 61(6):663–665, 1992.
- [84] C. Truesdell and R. Toupin. The classical field theories. In *Principles of classical mechanics and field theory/Prinzipien der Klassischen Mechanik und Feldtheorie*, pages 226–858. Springer, 1960.
- [85] E. Fried and M. E. Gurtin. Coherent solid-state phase transitions with atomic diffusion: a thermomechanical treatment. *Journal of statistical physics*, 95(5-6):1361–1427, 1999.
- [86] M. E. Gurtin and M. E. Jabbour. Interface Evolution in Three Dimensions with Curvature-Dependent Energy and Surface Diffusion: Interface-Controlled Evolution, Phase Transitions, Epitaxial Growth of Elastic Films. *Archive for Rational Mechanics and Analysis*, 163(3):171–208, 2002.
- [87] J. Eshelby. The elastic energy-momentum tensor. *Journal of Elasticity*, 5(3-4):321–335, 1975.
- [88] C. Hua-Riege. An introduction to cu electromigration. *Microelectronics Reliability*, 44:195–205, 2004.
- [89] C. W. Park and R. W. Vook. Activation energy for electromigration in cu films. *Applied Physics Letters*, pages 175–177, 1991.
- [90] C. K. Hu, M. B. Small, and P. S. Ho. Electromigration in cu/w structure. In *MRS Online Proceedings Library Archive*, volume 260, 1992.
- [91] H. Yamada, T. Hoshi, T. Takewaki, T. Shibata, T. Ohmi, and T. Nitta. Evaluation of electromigration and stressmigration reliabilities of copper interconnects by a simple pulsed-current stressing technique. In *Proceedings of IEEE International Electron Devices Meeting*, pages 269–272, 1993.
- [92] S. Shingubara, Y. Nakasaki, and H. Kaneko. Electromigration in a single crystalline submicron width aluminum interconnection. *Applied Physics Letters*, 58(1):42–44, 1990.



- [93] T. Ohmi, T. Hoshi, T. Yoshie, T. Takewaki, M. Otsuki, T. Shibata, and T. Nitta. Large-electromigration-resistance copper interconnect technology for sub-half-micron ulsi's. In *International Electron Devices Meeting*, pages 285–288, 1991.
- [94] T. Nitta, T. Ohmi, M. Otsuki, T. Takewaki, and T. Shibata. Electrical properties of giantgrain copper thin films formed by a low kinetic energy particle process. *Journal of the Electrochemical Society*, 139:922–927, 1992.
- [95] T. Nitta, T. Ohmi, T. Hoshi, T. Sakai, K. Sakaibara, S. Imai, and T. Shibata. Evaluating the large electromigration resistance of copper interconnects employing a newly developed accelerated lifetest method. *Journal of the Electrochemical Society*, 140(4):1131–1137, 1993.
- [96] B. Luther. Planar copper/polymide back end of the line interconnections for ulsi devices. In *VMIC Conference*, pages 15–21, 1993.
- [97] Y. Igarashi, T. Yamanobe, H. Jinbo, and T. Ito. Sub-quarter micron copper interconnects through dry etching process and its reliability. In *Proceedings of 1994 VLSI Tehcnology Symposium*, pages 57–58, 1994.
- [98] J. H. Tao, N. W. Cheung, C. Hu, H.-K. Kang, and S. S. Wong. Electromigration performance of electroless plated copper/pd-silicide metallization. *Electron Devices Letters*, 13(8):433–435, 1992.
- [99] H.-K. Kang, J. S. H. Cho, I. Asano, and S. S. Wong. In *VLSI Multilevel Interconnection Conference(VMIC)*, volume 337, pages 9–10, 1992.
- [100] J. S. H. Cho, H.-K. Kang, C. Ryu, and S. S. Wong. Reliability of cvd cu buried interconnections. In *Proceedings of the IEEE International Electron Devices Meeting*, pages 265–268, 1993.
- [101] K. Hoshino, H. Yagi, and H. Tsuchikawa. Tin-encapsulized copper interconnects for ulsi applications. In *Sixth International IEEE VLSI Multiulevel International Conference*, pages 226–232, 1989.
- [102] D. Save, F. Braud, J. Torres, F. Binder, C. Müller, J. O. Weidner, and W. Hasse. Electromigration resistance of copper interconnects. *Microelectronic Engineering*, 33:75 – 84, 1997.
- [103] C. Christiansen, B. Li, and J. Gill. Blech effect and lifetime prediction for cu/low-k interconnects. In *IEEE 2008 International Interconnect Technology Conference*, pages 114 – 116, 2008.
- [104] C. K. Hu, L. Gignac, R. Rosenberg, E. Liniger, J. Rubino, C. Sambucetti, A. Domenicucci, X. Chen, and A. K. Stamper. Reduced electromigration of cu wires by surface coating. *Applied Physical Letters*, 81(10):1782 – 1784, 2002.
- [105] J. Proost, T. Hirato, T. Furhara, K. Maex, and J. P. Celis. Microtexture and electromigration-induced drift in electroplated damascene cu. *Journal of Applied Physics*, 87(6):2792 – 2802, 1995.
- [106] R. Frankovic and G. H. Bernstein. Electromigration drift and threshold in cu thin-film interconnects. volume 43, pages 2233–2239, 1996.

- [107] C. K. Hu, K. Y. Lee, C. Cabral Jr, E. G. Colgan, and C. Stanis. Electromigration drift velocity in al-alloy and cu-alloy lines. *journal of electrochemical society*, 143(3):1001–1006, 1996.
- [108] C. K. Hu, B. Luther, F. B. Kaufman, J. Hummel, C. Uzoh, and D. J. Pearson. Electromigration drift and threshold in cu thin-film interconnects. *Thin Solid Films*, 262:84–92, 1995.
- [109] C. S. Hau-Riege, A. P. Marathe, and V. Pham. The effect of low-k ild on the electromigration reliability of cu interconnects with different line lengths. In *IEEE Annual Reliability Conference*, volume 41, pages 173–177, 2003.
- [110] P. Charalambides, J. Lund, A. Evans, and R. McMeeking. A test specimen for determining the fracture resistance of bimaterial interfaces. *Journal of Applied Mechanics (Transactions of ASME)*, 56(1):77–82, 1989.
- [111] I. Hofinger, M. Oechsner, H. Bahr, and M. Swain. Modified four-point bending specimen for determining the interface fracture energy for thin, brittle layers. *International Journal of Fracture*, 92(3):213–220, 1998.
- [112] R. Dauskardt, M. Lane, Q. Ma, and N. Krishna. Adhesion and debonding of multi-layer thin film structures. *Engineering Fracture Mechanics*, 61(1):141–162, 1998.
- [113] B. Wang and T. Siegmund. A modified 4-point bend delamination test. *Micro-electronic Engineering*, 85(2):477–485, 2008.
- [114] S. Kim and D. Duquette. Quantitative measurement of interfacial adhesion between seedless electrodeposited copper and tantalum based diffusion barriers for microelectronics. *Electrochemical and Solid State Letters*, 10(1):D6–D9, 2007.
- [115] R. P. Birringer, P. J. Chidester, and R. H. Dauskardt. High yield four-point bend thin film adhesion testing techniques. *Engineering Fracture Mechanics*, 78(12):2390–2398, 2011.
- [116] J. Zheng and S. K. Sitaraman. Fixtureless superlayer-driven delamination test for nanoscale thin-film interface. *Thin Film Solids*, 515(11):4709–4716, 2007.
- [117] K. Kendall. *Molecular Adhesion and its Applications: The Sticky Universe*. Kluwer Academic Publishers, New York, NY, 2004.
- [118] K. Kendall, M. Kendall, and F. Rehfeldt. *Adhesion of Cells, Viruses and Nanoparticles*. Springer Science+Business Media B.V., Dordrecht, Netherlands, 2011.
- [119] H. Gao, X. Wang, H. Yao, S. Gorb, and E. Arzt. Mechanics of hierarchical adhesion structures of geckos. *Mechanics of Materials*, 37(2-3):275–285, 2005.
- [120] K. Johnson, K. Kendall, and A. Roberts. Surface energy and the contact of elastic solids. *Proceedings of the Royal Society of London A: Mathematical, Physical and Engineering Sciences*, 324:301–313, 1971.
- [121] B. Derjaguin, V. Muller, and Y. Toporov. Effect of contact deformations on the adhesion of particles. *Journal of Colloid and Interface Science*, 53(2):314–326, 1975.

- [122] A. Ghatak, L. Mahadevan, J. Y. Chung, M. K. Chaudhury, and V. Shenoy. Peeling from a biomimetically patterned thin elastic film. *Proceedings of the Royal Society of London A: Mathematical, Physical and Engineering Sciences*, 460(2049):2725–2735, 2004.
- [123] J. Y. Chung and M. K. Chaudhury. Roles of discontinuities in bio-inspired adhesive pads. *Journal of The Royal Society Interface*, 2(2):55–61, 2005.
- [124] N. S. Pesika, Y. Tian, B. Zhao, K. Rosenberg, H. Zeng, P. McGuiggan, K. Autumn, and J. N. Israelachvili. Peel-zone model of tape peeling based on the gecko adhesive system. *The Journal of Adhesion*, 83(4):383–401, 2007.
- [125] B. Chen, P. Wu, and H. Gao. Geometry-and velocity-constrained cohesive zones and mixed-mode fracture/adhesion energy of interfaces with periodic cohesive interactions. *Proceedings of the Royal Society of London A: Mathematical, Physical and Engineering Sciences*, 465(2104):1043–1053, 2009.
- [126] M. R. Begley, R. R. Collino, J. N. Israelachvili, and R. M. McMeeking. Peeling of a tape with large deformations and frictional sliding. *Journal of the Mechanics and Physics of Solids*, 61(5):1265–1279, 2013.
- [127] P. Gialamas, B. Völker, R. R. Collino, M. R. Begley, and R. M. McMeeking. Peeling of an elastic membrane tape adhered to a substrate by a uniform cohesive traction. *International Journal of Solids and Structures*, 51(18):3003–3011, 2014.
- [128] E. Hernandez, M. Alfano, D. Pulungan, and G. Lubineau. Toughness amplification in copper/epoxy joints through pulsed laser micro-machined interface heterogeneities. *Scientific reports*, 7(1):16344, 2017.
- [129] S. R. Ranade, Y. Guan, R. B. Moore, J. G. Dillard, R. C. Batra, and D. A. Dillard. Characterizing fracture performance and the interaction of propagating cracks with locally weakened interfaces in adhesive joints. *International Journal of Adhesion and Adhesives*, 82:196–205, 2018.
- [130] R. Tadepalli, K. T. Turner, and C. V. Thompson. Effects of patterning on the interface toughness of wafer-level cu–cu bonds. *Acta Materialia*, 56(3):438–447, 2008.
- [131] S. Xia, L. Ponson, G. Ravichandran, and K. Bhattacharya. Adhesion of heterogeneous thin films—i: Elastic heterogeneity. *Journal of the Mechanics and Physics of Solids*, 61(3):838–851, 2013.
- [132] C. Cuminatto, G. Parry, and M. Braccini. A model for patterned interfaces debonding—application to adhesion tests. *International Journal of Solids and Structures*, 75:122–133, 2015.
- [133] S. Heide-Jørgensen and M. K. Budzik. Crack growth along heterogeneous interface during the DCB experiment. *International Journal of Solids and Structures*, 120:278–291, 2017.
- [134] L. Avellar, T. Reese, K. Bhattacharya, and G. Ravichandran. Effect of cohesive zone size on peeling of heterogeneous adhesive tape. *Journal of Applied Mechanics*, 85(12):121005, 2018.

- [135] R. Garg and N. V. Datla. Peeling of heterogeneous thin films: Effect of bending stiffness, adhesion energy, and level of heterogeneity. *The Journal of Adhesion*, pages 1–18, 2018.
- [136] S. Heide-Jørgensen and M. K. Budzik. Effects of bondline discontinuity during growth of interface cracks including stability and kinetic considerations. *Journal of the Mechanics and Physics of Solids*, 117:1–21, 2018.
- [137] D. Garrivier, E. Decave, Y. Brechet, F. Bruckert, and B. Fourcade. Peeling model for cell detachment. *The European Physical Journal E*, 8(1):79–97, 2002.
- [138] A. Molinari and G. Ravichandran. Stability of peeling for systems with rate independent decohesion energy. *International Journal of Solids and Structures*, 50(11):1974–1980, 2013.
- [139] J. A. Williams. Adhesional instabilities and gecko locomotion. *Journal of Physics D: Applied Physics*, 48(1):015401, 2014.
- [140] Y. Gao and A. Bower. A simple technique for avoiding convergence problems in finite element simulations of crack nucleation and growth on cohesive interfaces. *Modelling and Simulation in Materials Science and Engineering*, 12(3):453, 2004.
- [141] Y. Xu, X. Li, X. Wang, and L. Liang. Inverse parameter identification of cohesive zone model for simulating mixed-mode crack propagation. *International Journal of Solids and Structures*, 51(13):2400–2410, 2014.
- [142] Z. Ouyang and G. Li. Cohesive zone model based analytical solutions for adhesively bonded pipe joints under torsional loading. *International Journal of Solids and Structures*, 46(5):1205–1217, 2009.
- [143] J. Williams and H. Hadavinia. Analytical solutions for cohesive zone models. *Journal of the Mechanics and Physics of Solids*, 50(4):809–825, 2002.
- [144] M. Dado and S. Al-Sadder. A new technique for large deflection analysis of non-prismatic cantilever beams. *Mechanics Research Communications*, 32(6):692–703, 2005.
- [145] K. Bisshopp and D. Drucker. Large deflection of cantilever beams. *Quarterly of Applied Mathematics*, 3(1), 1945.
- [146] A. Magnusson, M. Ristinmaa, and C. Ljung. Behaviour of the extensible elastica solution. *International Journal of Solids and Structures*, 38(46):8441–8457, 2001.
- [147] B. Golley. The solution of open and closed elasticas using intrinsic coordinate finite elements. *Computer methods in applied mechanics and engineering*, 146(1):127–134, 1997.
- [148] L. Chen. An integral approach for large deflection cantilever beams. *International Journal of Non-Linear Mechanics*, 45(3):301–305, 2010.
- [149] M. H. Ang Jr, W. Wei, and L. Teck-Seng. On the estimation of the large deflection of a cantilever beam. In *Industrial Electronics, Control, and Instrumentation, 1993. Proceedings of the IECON'93., International Conference on*, pages 1604–1609. IEEE, 1993.

## APPENDIX

## A. INSTABILITY AT BONDED HETEROGENEOUS FILM INTERFACE

### A.1 Motivation

Loss of adhesion between two films as evidenced by peeling is an important and common occurrence in nature and in engineered systems with molecular forces being the fundamental cause [117–119]. Research into understanding the mechanics of contact with adhesion including peeling has a long and significant history [1, 120, 121]. More recently, several studies have modeled the peeling of homogeneous films in biological and non-biological applications including [122–129].

The bond toughness of an interface can be quantified by adhesion energy, which is the amount of energy required to debond a unit area of the interface. In his pioneering work, Rivlin [1] suggested that the effective work of adhesion might vary with Young’s modulus due to the fact that the stored energy in the film is dependent on its elastic modulus. In another landmark study, Kendall [2] showed that the fracture toughness of a heterogeneous film depends on the bending rigidity of the structure. He derived the quantitative relationship between the bending rigidity of the film, the interfacial fracture energy and the fracture toughness of the peeled structure. Recently, several studies in the literature [119, 128–135] have demonstrated the influence of the arrangement of the geometry or the material of the adherends to the increase in force required for a crack propagating perpendicular to the adherend patterns. In general, these studies demonstrated that the bond toughness or the effective adhesive energy can be dramatically increased by manipulating the extrinsic heterogeneity due to geometry or material stiffness without modifying the intrinsic interfacial adhesion characteristics.

In general, arguments based on energy stored in the films during the peel tests are used to explain the dependence of effective adhesion energy on film heterogeneity.

Models proposed in the literature to describe the above experimental observations vary broadly in their treatment of (1) deformation of the unbonded film (2) description of the fracture process zone and (3) modeling of unstable crack propagation. Xia et al. [131] derived the governing conditions of the peeling process by modeling the film as a beam and minimizing the total potential energy of the system consisting of the stored bending energy in the heterogeneous film, potential of the peel force and the adhesion energy in the bonded portion of the film. Inherent in their formulation were assumptions of small curvature as well as debond without progressive damage in the bonded portion. Cuminatto et al. [132] modeled a periodically bonded film to finite thickness substrate as a beam on elastic foundation with normal (opening) and torsional stiffness. The film deformation was assumed to be small. They then derived an algebraic expression for the energy release rate available for crack growth as a function of film/substrate thickness relative to crack length and film stiffness relative to foundation stiffness. Heide-Jorgensen and Budzik [133] also modeled a periodically bonded film as a beam on elastic foundation under the same assumptions as Cuminatto et al. [132]. Their model differed from that of Cuminatto et al. [132] in the geometrical description of the problem and in the estimation of the applied moment at the crack tip. Heide-Jorgensen and Budzik [136] expanded their earlier study to analyze the interaction between the crack tip and the region where positive peeling stress exists (foundation ‘process’ zone,  $\lambda^{-1}$ ). They showed that when the unbonded portion (discontinuity) was a large fraction of the foundation process zone, then the crack propagation is unstable resulting in a ‘snap-down’ in the load-displacement response. Avellar et al. [134] carried out finite element simulations using a cohesive zone model of the fracture process zone. They demonstrated that the peel force enhancement in adhesive tapes (unlike in bond between brittle structures) depends on the adhesive strength as well as the cohesive-zone size. Arguably, an analytical description of, the impact of finite deformation of the film or the impact of the fracture process zone size and the resulting damage at the interface would provide insight into the peeling of heterogeneous films that the above cited models have not consid-

ered. For the same interfacial adhesive properties, a smaller fracture process zone size signifies the existence of a larger stress concentration. The relationship between the intrinsic adhesive strength of the interface as well as the bending rigidity of the adherent and the fracture process zone size is elaborated in the present study.

The instability in the force-displacement response during the peeling test is another important phenomenon that requires careful study. The experimental evidence presented in Xia et al. [131] and Heide-Jorgensen and Budzik [136] suggests that the adhesive strength improvement is accompanied by instability in the force-displacement response. Furthermore, the instability during the peeling process is not well controlled, and parts of the load-displacement response are unreachable under load-control as several studies have shown [137–139]. In the present study, we demonstrate that an analysis based on forced-controlled response modeled in the previous analytical studies does not fully describe the instability phenomenon. To address this challenge, in this study, a semi-analytical solution is developed, which can describe the unstable crack propagation during peel test of heterogeneous films.

The above cited analytical models of the peeling process [1,2] use work of adhesion to describe the peel force, but generally do not solve for stresses and displacements near the crack tip. In the present study, we use a cohesive zone model (CZM) to describe the debonding process and through it extend the description of the interface state beyond what one can obtain from interfacial energy alone. Unstable crack propagation is also simulated using the CZM. In general, instability is challenging to model in numerical simulations. Solutions often diverge when unstable crack growth is encountered. Although techniques exist to overcome the numerical challenges of modeling the instability caused by a sudden debond [134,140], an alternative analytical approach might be more efficient and might help in more fully understanding the instability phenomena. Therefore, a semi-analytical method based on the cohesive zone model is developed in this study to describe the peel process for the heterogeneous film. The unstable crack propagation process is clearly demonstrated



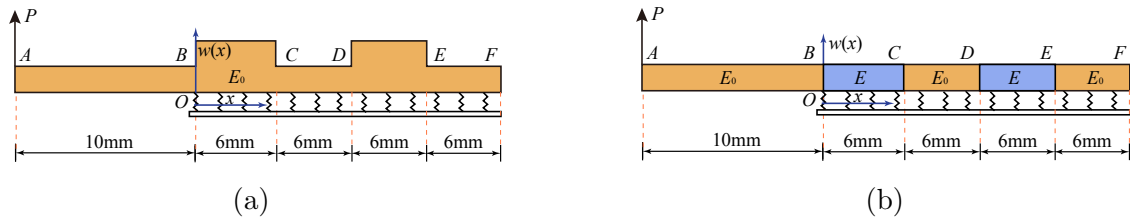


Figure A.1. Schematic drawing of heterogeneous adhesive beams (a) Thickness enhancement (b) Material enhancement.

and information including the distribution of energy and fracture process zone size is obtained with the model.

## A.2 Scope of the Present Study

References [2, 131] demonstrated that the bending rigidity has a substantial influence on the adhesion of a heterogeneous film to a substrate. Therefore, we begin with an approximation of the heterogeneous film as an Euler-Bernoulli beam with bending rigidity ( $D = EI$ ) that is related to both the elastic module ( $E$ ) and the second moment of cross-sectional area ( $I$ ). Figure A.1 shows the schematic of two types of composite adhesive films. Both composite structures consist of alternating stiff and compliant segments. The schematic shown in Figure A.1(a) is a homogeneous material with changing cross-sectional thickness, while the one shown in Figure A.1(b) is a film composed of two materials with different Youngs moduli. For a beam with a rectangular cross-section the second moment of cross-sectional area will change by three orders of magnitude with the thickness, i.e., from the standpoint of bending rigidity, twice the cross-section thickness in Figure A.1(a) is numerically equal to eight times the elastic modulus increase in Figure A.1(b). This idea provides flexibility to choose between material heterogeneity and thickness variation for equivalent improvement in peel resistance.

Xia et al. [131] carried out a series of peeling tests for the thickness-enhanced heterogeneous adhesive film. In order to validate the semi-analytical method devel-

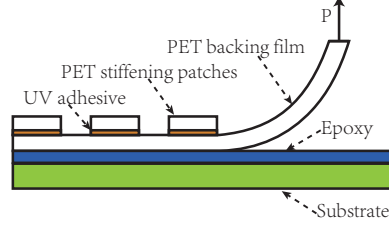


Figure A.2. Schematic drawing heterogeneous film under peel.

oped in this paper, the composite film shown in [131] is considered. The specimen geometry and test conditions used by Xia et al. are repeated below for convenience. The tested specimen consisted of a heterogeneous adhesive film, a plastic substrate and an epoxy layer as shown in Figure A.2. The base of the composite film was a thin polyester (PET) sheet. To introduce heterogeneity in bending stiffness, an array of PET stiffeners with uniform thickness were bonded onto the base using UV curable glue. The elastic modulus and the Poissons ratio of polyester were  $E_0 = 3.8$  GPa and  $\nu = 0.42$ , respectively. The modulus of the UV curable glue was  $E_1 \approx 4$  MPa. The flat side of the composite film was bonded to the plastic substrate using a two part epoxy. During the peel test performed under displacement controlled loading, failure was observed at the adhesion interface between the composite strip and the epoxy layer. The intrinsic adhesion energy of the polyester-epoxy interface was  $G = 5.1$  J/m<sup>2</sup>, which was measured by a separate peel test conducted at  $\theta = 90^\circ$ .

Two composite films with different cross-sectional thickness presented in [131] are investigated in the present work. (1) Geometric parameters of the first specimen are: width of the composite strip  $w = 38.0$  mm, thickness of its base film is  $t_1 = 0.161$  mm, thickness of the UV curable glue is  $t_2 = 0.01$  mm, thickness of the stiffeners is  $t_3 = 0.025$  mm, length of the stiffeners is  $l = 6$  mm, and center-to-center spacing of the stiffeners is set at  $p = 12$  mm. In this case, the bending rigidity ratio of stiff (with stiffeners) to compliant (without stiffeners) regions is  $(D_s/D_c)$  approximately 2.0. (2) Geometric parameters of the second specimen are: width of the composite film  $w = 38.0$  mm, thickness of its base film is  $t_1 = 0.161$  mm, thickness of the UV

curable glue is  $t_2 = 0.03$  mm, thickness of the stiffeners is  $t_3 = 0.161$  mm, length of the stiffeners is  $l = 10$  mm, and center-to-center spacing of the stiffeners is set at  $p = 12$  mm. In this case the bending rigidity ratio ( $D_s/D_c$ ) is about 8.8.

In addition to the thickness-enhanced specimens, two material-enhanced specimens were also investigated. This is because it is relatively easier to implement the material-enhanced case in a theoretical framework. Also, we want to study the differences between these scenarios. For the material-enhanced case, the base film thickness is the same as in the thickness-enhanced cases except the thickness is kept uniform and not varied. Two different elastic moduli  $E$  and  $E_0$  marked in Fig.1(b) were considered.  $E_0$  is the elastic modulus of a homogeneous polyester film and  $E$  in the material-enhanced regions is taken as either  $2.0E_0$  or  $8.8E_0$  for it to match the rigidity in the equivalent thickness-enhanced cases.

### A.3 Finite Element Simulation of Peeling Failure in Heterogeneous Films

Prior to discussing the semi-analytical solution method developed in this study, preliminary finite element simulations of peeling in the composite film are carried out using CZM to demonstrate the ability of numerical solutions in capturing the experimentally observed response. The simulations were performed in ABAQUS<sup>(R)</sup> using the standard implicit mode. Linear 8-noded brick elements (C3D8) were used to mesh the film. The adhesion between the composite film and the epoxy layer was simulated using the bilinear 8-noded three dimensional cohesive elements (COH3D8). The parameters set for the CZM were as follows: the energy release rate  $G$  is set equal to the intrinsic adhesion energy of the polyester-epoxy interface at  $5.1$  J/m<sup>2</sup>. The maximum strength  $S_0$  is  $0.51$  MPa and the elastic rigidity  $K_1$  is set at  $1500$  MPa. With these cohesive parameters, the critical separation at failure can be calculated. In general, these cohesive parameters (e.g., the maximum strength or the critical separation) can be obtained by an inverse analysis using experimental data [141]. For the present work, we found these parameters by trial-and-error. To reduce the com-

putational expense, only half the width of the specimen was modeled by imposing a symmetric boundary condition. Since the solidified epoxy layer has higher toughness compared to the composite film, its influence on peeling failure was neglected in our work and the bottom of the plastic substrate was constrained with an encastre boundary condition. During the peel test, a steady-state peeling force is applied at the end of composite film with the peel angle fixed at  $\theta = 90^\circ$ . Since the deformation of composite film is dominated by bending, the in-plane stretch is neglected. Additionally, large deformation of the composite film was simulated through the geometric nonlinearity mode in ABAQUS<sup>(R)</sup>.

Figure A.3 shows the simulated peeling force-displacement response curves as well as the experimental results from [131]. Here the two different bending rigidity ratios ( $D_s/D_c = 8.8$  and  $D_s/D_c = 2.0$ ) were investigated. Both the thickness-enhanced and material-enhanced composite films were simulated. For the thickness-enhanced case, one can see that the simulated force-displacement response curve for  $D_s/D_c = 8.8$  shown in Figure A.3(a) is in good agreement with the experimental results except for the first peak. This difference arises as a result of the initial free non-adhered length of the film ahead of the bonded interface in our simulation. In the simulations, this length was chosen arbitrarily. However, it does not significantly influence the force-displacement response curves for the following peaks. From Figure A.3(b) one can see that the simulation results and the experimental results for  $D_s/D_c = 2.0$  don't agree as well as they do for the case where  $D_s/D_c = 8.8$ . This difference though relatively small is a result of the chosen cohesive parameters.

As discussed previously, the material-enhanced and the thickness-enhanced films' dimensions and properties were chosen to make them numerically equivalent in terms of bending rigidity. Therefore, the response of these two cases coincide except near the peaks. The material-enhanced film is slightly more rigid compared to the thickness-enhanced film. This difference is the result of the differing constraints at the stiff-compliant interface compared to the homogenous film with varying thickness. For the thickness-enhanced film, the edge is partially free. Going from a thick cross-section

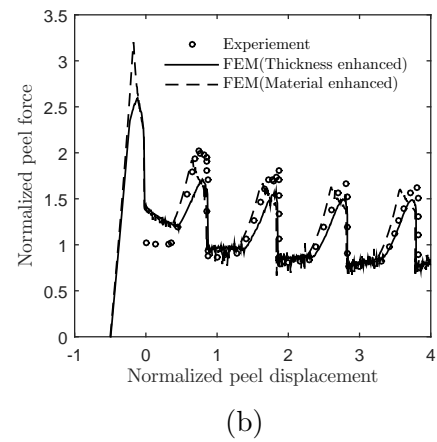
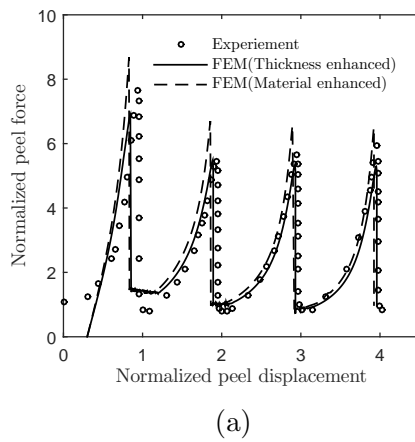


Figure A.3. Experimental results from [131] and FEM simulation results compared for two cases with thickness-enhanced and material-enhanced heterogeneous film undergoing peel (a)  $D_s/D_c = 8.8$  (b)  $D_s/D_c = 2.0$ .

to a thin cross-section only a part of the edge is constrained unlike the material-enhanced case where the entire edge is constrained between the stiff and compliant segments. This effect is insignificant away from the interface due to Saint Venant's principle. Thus, these two cases of heterogeneous films are similar in terms of bending performance except for the regions where the film is unconstrained as described above.

The agreement between the simulations and the experimental results show that cohesive zone models can be used to simulate the adhesive failure of a heterogeneous film faithfully. However, one significant challenge encountered with the finite element simulations is obtaining a convergent solution during unstable crack propagation. In order to circumvent this issue appropriate element size and time increments need to be chosen. Further a viscous damping force can be used to deal with the convergence issues. Note, there is a tradeoff with solution accuracy when damping is applied. Alternatively the convergence criteria can be loosened. However, even with these steps obtaining a convergent solution may still be challenging.

#### **A.4 Semi-Analytical Solution for Peeling Failure of Heterogeneous Film**

During unstable crack propagation, information on variation of fracture process zone size and stored energy in the film cannot be obtained. Moreover, simulations based on force-controlled loading are challenging to simulate using the current finite element method since two solutions may exist for the same force. This caveat will be discussed further in future sections. To this end, a semi-analytical solution is developed, which can describe the unstable crack propagation during peel test of heterogeneous films.

In this study, the heterogeneous film is simplified as an EulerBernoulli beam, shown in Figure A.4. The derivation for an analytical solution of beam bending with large deformation is quite challenging, especially for cases subjected to complex and nonlinearly distributed loads. To simplify the derivation we start by splitting the film into two sections. One is the adhesion-free section, considered a cantilever beam,

where the loads are applied at its free end and another is the section that is adhered to the substrate. In general, the bending deformation of the adhered section is rather small despite being subject to a complex nonlinear adhesive force. For this reason the small deformation assumption is made for the adhered part, while large deformation theory is used for the adhesion-free section. Continuity and smoothness constraints need to be imposed at the interface that connects the two sections.

#### A.4.1 Analytical Solution for Adhesion Portion

Since the loading direction is along  $\theta = 90^\circ$ , the tangential component of the adhesion tractions can be neglected and only the normal tractions are considered in the present study. A bilinear traction-separation law only considering mode I fracture, schematically shown in Figure A.5, is adopted here. This CZM is the same as the one implemented in ABAQUS<sup>(R)</sup>. Once the framework of the analytical method is

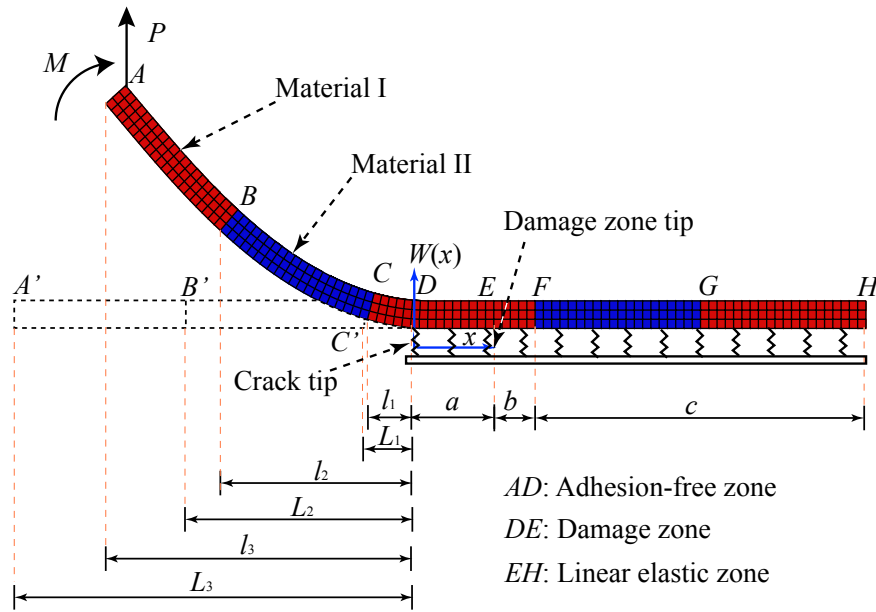


Figure A.4. Schematic drawing of debonding adhesive beam on an elastic foundation under peel loading.

established, an extension to mixed-mode failure is relatively easy to implement. The traction-separation law can be written as

$$T(\delta) = \begin{cases} \frac{\sigma_{max}}{\delta_1} \delta & \text{if } 0 \leq \delta \leq \delta_1 \\ \frac{\delta_f - \delta}{\delta_f - \delta_1} \sigma_{max} & \text{if } \delta_1 \leq \delta \leq \delta_f \\ 0 & \text{if } \delta_f \leq \delta \end{cases} \quad (\text{A.1})$$

where  $\delta_1$  is the characteristic length denoting the onset of damage at adhesion interface, to which the maximum traction  $\sigma_{max}$  corresponds;  $\delta_f$  is the critical separation when failure occurs. When  $\delta < \delta_1$ , the mechanical behavior of adhesion interface always follows the linear elastic relationship. Once the separation  $\delta$  exceeds  $\delta_1$ , the adhesion interface starts to damage, and finally, total separation occurs when  $\delta > \delta_f$ , i.e., there is no traction transmitted across the interface.

From Figure A.4, one can see that the adhered region is further separated into two zones. They are referred to as: the linear elastic zone and the damage zone. They correspond to two stages of the traction-separation law (linearly increasing and linearly decreasing) as shown in Figure A.5. If the separation  $\delta$  in the damage zone reaches  $\delta_f$ , both the crack tip and the damage zone tip will move forward. As the crack length increases a new adhesion-free surface is formed. In the following section,

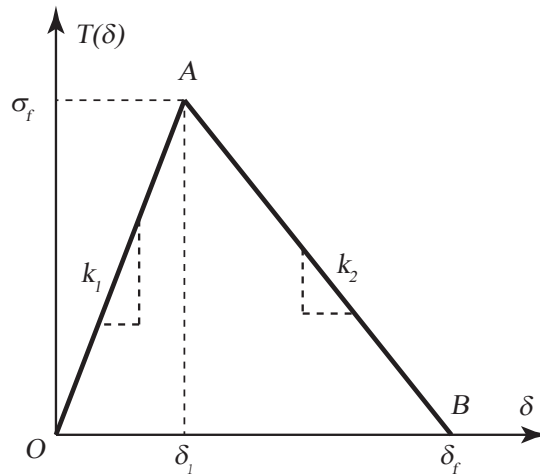


Figure A.5. The bilinear cohesive zone model.



the analytical solutions for deformation in the linear elastic zone and the damage zone are derived. Next, discussion of some issues associated with solving the equilibrium equations in this framework are presented. Though there is prior work in literature where a similar approach was used [142,143], the derivation is limited to homogeneous films.

### Governing Equation in Damage Zone

In order to simplify the derivation, the origin of the coordinate system is always fixed at the crack tip. In the damage zone ( $0 \leq x \leq a$ ), tractions degrade with separations along branch (A-B) in the CZM, and separation of interface, i.e., the vertical deflections ( $w_1(x)$ ), changes in the range  $[\delta_1, \delta_f]$ . The governing equation for  $w_1(x)$  is expressed as

$$\frac{d^4 w_1(x)}{dx^4} = \frac{-bk_2[\delta_f - w_1(x)]}{EI} \quad (\text{A.2})$$

where  $k_2$  is transverse stiffness of the CZM at the descending stage. Eq. (A.2) is rewritten as:

$$\frac{d^4 w_1(x)}{dx^4} = 4\beta^4[w_1(x) - \delta_f] \quad (\text{A.3})$$

where  $\beta = \sqrt[4]{\frac{bk_2}{4EI}}$ ,  $\delta_f = \frac{2G_f}{\sigma_{max}}$ , and  $k_2 = \frac{\sigma_{max}}{\delta_f - \delta_1}$ . The general solution to this fourth order differential equation:

$$w_1(x) = \delta_f + C_1 \cos(\sqrt{2}\beta x) + C_2 \sin(\sqrt{2}\beta x) + C_3 \cosh(\sqrt{2}\beta x) + C_4 \sinh(\sqrt{2}\beta x) \quad (\text{A.4})$$

where  $C_1, C_2, C_3, C_4$  are unknown coefficients obtained using boundary and continuity conditions.

### Governing Equation in Linear Elastic Zone

If the interface separation (equivalent to the beam deflection  $w_2(x)$ ) is less than  $\delta_1$ , its traction will vary linearly with  $w_2(x)$ . In the adhesion region ( $a \leq x \leq a+b+c$ ), the traction-separation relationship is controlled by branch (O-A) shown in Figure A.5. In this case, the governing equation of  $w_2(x)$  is written as

$$\frac{d^4 w_2(x)}{dx^4} = -4\alpha^4 [w_2(x)] \quad (\text{A.5})$$

where  $\alpha = \sqrt[4]{\frac{bk_1}{4EI}}$ ,  $k_1 = \frac{\sigma_{max}}{\delta_1}$ . The general solution of Eq. (A.5) is written as

$$w_2(x) = \exp(-\alpha x) (C_5 \sin(\alpha x) + C_6 \cos(\alpha x)) + \exp(\alpha x) (C_7 \sin(\alpha x) + C_8 \cos(\alpha x)) \quad (\text{A.6})$$

where  $C_5$ ,  $C_6$ ,  $C_7$  and  $C_8$  are unknowns that need to be solved by using boundary and continuity conditions. As  $x \rightarrow \infty$ ,  $w_2(x) \rightarrow 0$ . So  $C_7$  and  $C_8$  both turn out equal to 0. Only the first term remains, i.e., Eq. (A.6) reduces to

$$w_3(x) = \exp(-\alpha x) (C_9 \sin(\alpha x) + C_{10} \cos(\alpha x)) \quad (\text{A.7})$$

### Solution Cases and Boundary Conditions

Based on the general solution for deflections  $w_1(x)$ ,  $w_2(x)$  and  $w_3(x)$ , the governing equations that describe peeling failure of heterogeneous films are derived. As the crack extends during the peel process, the damage zone size changes along with the film material properties and geometry. To accommodate this change different analytical solutions considering different situations have been constructed. For the present study, five cases (or analytical solutions) are derived to obtain the entire solution to crack propagation along the heterogeneous film-substrate interface. Figure A.6 illustrates these five solution cases. In Case 1, the crack tip is located at the first material

interface and no damage exists at the adhesion interface. In Case 2 and Case 3, the crack tip is still at the material interface, but the damage zone  $E'E$  occurs at the adhesion interface. Unlike Case 2, the crack tip in Case 3 is ready to extend forward. Here, the same governing equations are used for the two cases. In Case 4, both the crack tip ( $E'$ ) and the damage zone tip ( $E$ ) propagate and leave the material interface, but no damage is accumulated at the next material segment. In Case 5, the damage zone ( $E$ ) extends through the new material interface but the crack tip ( $E'$ ) is still at the previous material segment. When the crack tip reaches the new material segment, a new cycle based on the above 5 solution cases is repeated.

Now, Case 4 is considered as an example to further illustrate how boundary and continuity conditions are established. All the other cases can be derived in a similar manner. From Case 4 shown in Figure A.6, the crack tip ( $E'$ ) and damage zone tip ( $E$ ) separate the stiff (or the compliant) material segment ( $DF$ ) into three parts.  $DE'$  is the adhesion-free,  $E'E$  is the damage zone and  $EF$  is the elastic zone  $EF$ . Here the latter two are still adhered to the substrate. The governing equations for  $E'E$  and  $EF$

Table A.1. Boundary conditions at the different points for Case 4.

At Point <b>D</b>	At Point <b>E</b>	At Point <b>F</b>
$w_1(x) _{x=0} = \delta_f$	$w_1(x) _{x=a} = \delta_1$	$w_2(x) _{x=a+b} = w_3(x) _{x=a+b}$
$\frac{dw_1(x)}{dx} _{x=0} = \theta_0$	$w_1(x) _{x=a} = w_2(x) _{x=a}$	$\frac{dw_2(x)}{dx} _{x=a+b} = \frac{dw_3(x)}{dx} _{x=a+b}$
$\frac{d^2w_1(x)}{dx^2} _{x=0} = \frac{M + PL_3}{EI}$	$\frac{dw_1(x)}{dx} _{x=a} = \frac{dw_2(x)}{dx} _{x=a}$	$\frac{d^2w_2(x)}{dx^2} _{x=a+b} = \frac{d^2w_3(x)}{dx^2} _{x=a+b}$
$\frac{d^3w_1(x)}{dx^3} _{x=0} = \frac{P}{EI}$	$\frac{d^2w_1(x)}{dx^2} _{x=a} = \frac{d^2w_2(x)}{dx^2} _{x=a}$	$\frac{d^3w_2(x)}{dx^3} _{x=a+b} = \frac{d^3w_3(x)}{dx^3} _{x=a+b}$
	$\frac{d^3w_1(x)}{dx^3} _{x=a} = \frac{d^3w_2(x)}{dx^3} _{x=a}$	

are different though, derived in the previous section they are Eq. (A.4) and Eq. (A.6), respectively. For  $FG$ , the governing equation is Eq. (A.7). Since the length of the stiff/compliant segments in the present study is larger than the damage zone size, and the interface separation in the elastic zone is rather small, the effect of periodically changing adhered materials at the elastic zone on its adhesion force are neglected. The boundary and continuity conditions along the length of the film where these zones exist are listed in Tab. A.1. At each location, four equilibrium equations (deflection, rotation angle, force and moment) are used. In Tab. A.1,  $a$  is the damage zone size, which is as unknown and  $b$  is dependent on  $a$ . The external force  $P$  and the rotation angle  $\theta_0$  at the crack tip are unknowns that satisfy the critical crack propagation condition. Lastly, the distance from the loading point to the crack tip,  $l_3$ , shown in Figure A.4, and the moment applied at the loading point,  $M$ , are variables calculated from iterative solution in the adhesive-free part of the beam. For the analytical solution in the adhered portion, these two parameters  $l_3$  and  $M$  are assumed as known quantities. Therefore a total of 13 equilibrium equations listed in Tab. A.1 are used to solve the 13 unknowns ( $C1, C2, C3, C4, C5, C6, C7, C8, C9, C10, P, \theta_0, a$ ) at each crack propagation step. However, the unknown  $a$  has infinitely many solutions to the set of Eqs. (A.4, A.6, A.7). To circumvent this issues during the iterative analysis two groups of equilibrium equations are constructed by deleting one relatively non-important equilibrium equation at point  $F$ . For instance, in the first equilibrium equation system, the force balance equation at point  $F$  is deleted and in the second equilibrium equation system the moment balance equation is deleted. If is taken  $a$  as a known value now, we obtain the force ( $P$ )-damage zone size ( $a$ ) response curves wherein many intersection points exist. Only the first solution is usually of practical interest since it corresponds to the lowest strain energy stored in the strip during the peel test. The damage zone size ( $a$ ) is then determined by searching the first intersection point of the two curves. It follows that the force ( $P$ ), the rotation angle ( $\theta_0$ ) and the deflection ( $w_0$ ) at the crack tip are written as a function of  $l_3$  and  $M$ .

Since the analytical solution is rather complex, the following simplified expressions are given for the convenience of explanation.

$$P = F(l_3, M) \quad (\text{A.8})$$

$$\theta_0 = F'(l_3, M) \quad (\text{A.9})$$

$$w_0 = F''(l_3, M) \quad (\text{A.10})$$

If we know  $M$  and  $l_3$ , the force( $P$ ), the rotation angle( $\theta_0$ ) and the deflection( $w_0$ ) at the crack tip are solvable. The results are then transferred to the adhesion-free part to solve for its bending deformation. Note,  $M$  is zero when the force controlled loading condition is used and  $M$  varies for displacement controlled loading condition based on the deformation state. This is discussed in detail in future sections of the paper.

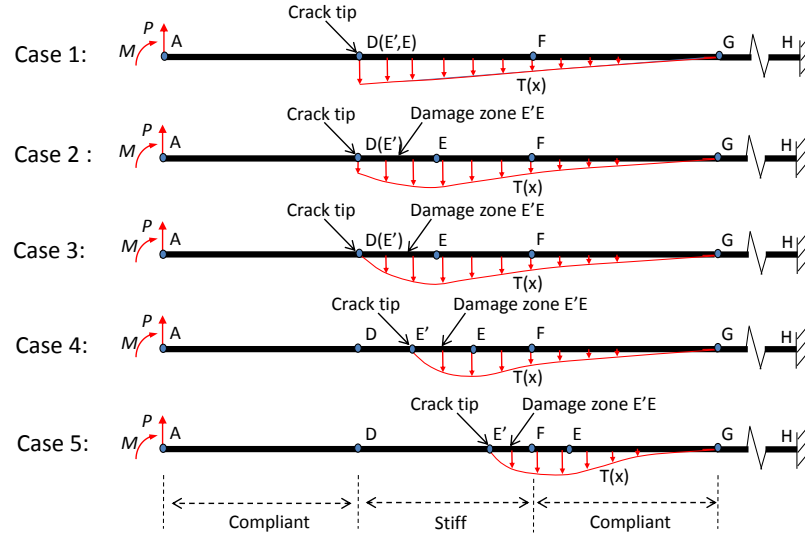


Figure A.6. Different stages of crack propagation in the heterogeneous adhesives.

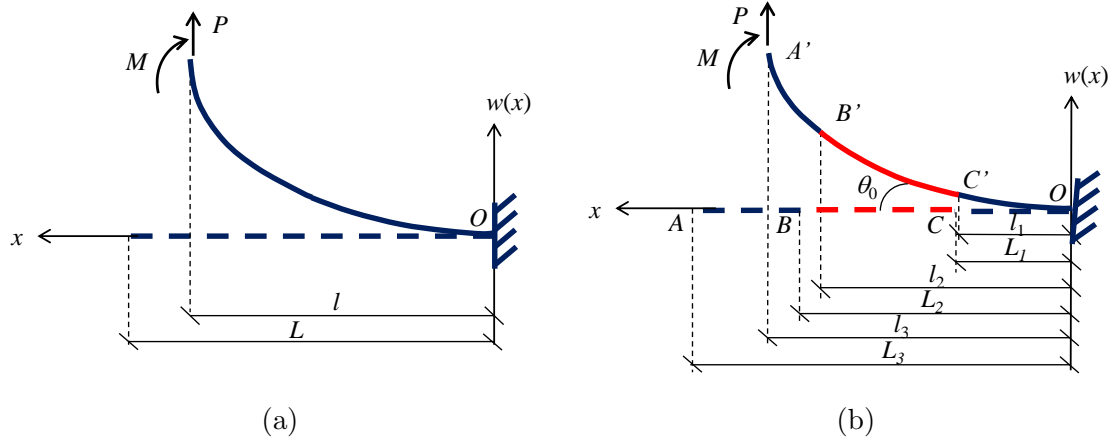


Figure A.7. Schematic drawing of bending deformation in a cantilever beam (a) Uniform cantilever beam (b) Adhesion-free portion of heterogeneous strip.

#### A.4.2 Semi-Analytical Solution for Adhesion-Free Portion

##### Uniform Cantilever Beam

The adhesion free portion of the film is subject to large deformations during the peel test, as such a rigorous treatment that takes into account the large deformations is needed. The large deflection of a bending beam was extensively studied in prior literature. Dado and Al-sadder [144] summarized several existing approaches: the elliptic integral approach [145], the numerical integration approach with iterative shooting techniques (e.g., [146]), incremental finite difference or finite element method with Newton-Raphson iteration technique (e.g., [147]), and other approximation methods. However, there are particular drawbacks in terms of applicability, complexity and stability with the listed methods. Recently, Chen [148] developed an integral approach based on the formulation proposed by Ang et al [149], which is easier to apply compared to the traditional approaches. In the following section, Chen's work is briefly reviewed and its application to the peel test on a heterogeneous film is introduced.

The differential equation for a beam under large deflections is written as:

$$\frac{\frac{d^2 w(x)}{dx^2}}{[1 + \frac{dw(x)}{dx}]^{3/2}} = \frac{M(x)}{EI} \quad (\text{A.11})$$

where  $w(x)$  is the deflection and  $x$  is the coordinate axis that is parallel to the original beam, as shown in Figure A.7. The left-hand side of this equation is the curvature of the bending beam. The curve length of the bending beam is then:

$$s(l) = \int_0^l \sqrt{1 + \left(\frac{dw(x)}{dx}\right)^2} dx \quad (\text{A.12})$$

where  $l$  denotes the projection length of the deformed beam. Let us define

$$z = \frac{dw(x)}{dx} \quad (\text{A.13})$$

Thus we obtain

$$\frac{ds}{dx} = \sqrt{1 + z^2} \quad (\text{A.14})$$

Eq. (A.11) is converted to

$$\frac{dz}{(1 + z^2)^{3/2}} = \frac{M(x)}{EI} dx \quad (\text{A.15})$$

This equation is integrated and we obtain

$$\frac{z}{\sqrt{1 + z^2}} = \int_0^x \frac{M(x)}{EI} dx + \frac{\theta_0}{\sqrt{1 + \theta_0^2}} = G(x) \quad (\text{A.16})$$

where  $\theta_0$  is the rotation angle between the beam and the  $x$  axis. This  $\theta_0$  is obtained from the adhered section of the beam.

From Eq. (A.13), Eq. (A.14) and Eq. (A.16) we obtain

$$\frac{ds}{dx} = \frac{1}{\sqrt{1 - G^2(x)}} \quad (\text{A.17})$$

and

$$\frac{dw}{dx} = \frac{G(x)}{\sqrt{1 - G^2(x)}} \quad (\text{A.18})$$

Eq. (A.17) and Eq. (A.18) become the new governing equations dictating large deflection bending in cantilever beam. For the simple loading case with a concentrated force and uniform beam properties, the governing equation yields a first order ODE which is easily integrated.

If a homogeneous cantilever beam with uniform material property as shown in Figure A.7(a) is considered, its deformation is solved numerically using Eq. (A.16) through Eq. (A.18) in an optimization scheme. For a given value of projection length  $l$ ,  $G(x)$  is calculated according to Eq. (A.16) and then the curve length  $s$  and the deflection  $w$  is obtained by integrating Eq. (A.17) and Eq. (A.18). By changing  $l$ , once  $s$  approaches its original length of beam ( $L$ ), the iterative search is terminated. It is worth noting here that the axial deformation (stretch) of the beam is ignored since it is small compared to the bending deformation. Also note that  $G(x)$  is less than 1 by definition. During the searching process if  $G(x) > 1$  is encountered, it means that the present assumed value  $l$  is too large, a smaller value needs to be provided.

### Heterogeneous Strip

For a heterogeneous film, the solution method is similar to the case of a homogeneous cantilever beam. Nevertheless, the boundary conditions and the construction of the objective function for the optimal solution are different. Prior to introducing the solution procedure, let us first prescribe  $m$  as the total number of segments of the adhesion-free portion where material property changes; and let  $n$  be the current segment number, ( $1 \leq n \leq m$ ). As an example to illustrate the procedure consider a heterogeneous film with the adhesion-free portion containing three segments ( $m=3$ ) with different rigidities. The adhesion-free portion is considered to be a cantilever beam with the right side subjected to a rotation constraint  $\theta_0$  and initial deflection



$w_0$ , and at its left end subjected to a concentrated force  $P$  along with a bending moment  $M$ , as shown in Figure A.7(b). Note that the boundary conditions  $\theta_0$ ,  $w_0$  and the loading  $P$  are not known aprior. These are values that need to be calculated from the solution of adhered portion using Eq. (A.10). As discussed previously, the solution for the adhered portion is based on an initial guess for  $M$  on the adhesion-free portion and the projection length of the adhesion-free portion ( $l_m$ ). The final solution lies somewhere between these two extremes and is solved iteratively.

In order to accurately calculate the deformation of a composite beam, all the curve lengths of the bent beam  $s_n$  (e.g., OC', OB' and OA', shown in Figure A.7(b)) are required to approach their original lengths  $L_n$  (corresponding to L1, L2 and L3). Therefore, a multi-objective optimal scheme is adopted. The calculation of each curve length  $s_n$  requires a corresponding  $G(x)$ . For the uniform beam calculating  $G(x)$  is straightforward but, for the beam with varying material properties, the calculating  $G(x)$  is bit more challenging. Treating each segment separately,  $G(x)$  for  $n$  such sections is written as:

$$G_m^n(x) = \sum_{i=2}^n \left[ \left( \frac{P}{E_{i-1}I_{i-1}} - \frac{P}{E_iI_i} \right) \left( l_m l_{i-1} - \frac{l_{i-1}^2}{2} \right) + \left( \frac{M}{E_{i-1}I_{i-1}} - \frac{M}{E_iI_i} \right) l_{i-1} \right] + \frac{P}{E_n I_n} \left( l_m x - \frac{x^2}{2} \right) + \frac{M}{E_n I_n} x + \frac{\theta_0}{\sqrt{1 + \theta_0^2}} \quad (\text{A.19})$$

Note that the first item in the equation above starts with  $n = 2$ . For the present example,  $G_3^1(x)$ ,  $G_3^2(x)$  and  $G_3^3(x)$  need to be calculated separately. Once the ideal  $G(x)$  values are obtained from the optimization, the deflection of the adhesion-free portion in the heterogeneous film is calculated.

### Solution Construction for Different Loading Conditions

The iterative optimization solution scheme is dependent on the loading conditions. We categorically separate the two scenarios into force-controlled loading and

displacement-controlled loading conditions. When the crack propagates stably, both the loading conditions yield the same results. However, for unstable crack propagation, the force-controlled loading condition only predicts initiation, while the displacement-controlled loading captures the whole process of instability. As such, displacement-controlled loading has more practical significance but, it is more challenging to implement in a general theoretical framework. For this reason, most of the prior work in literature deals only with solutions based on force-controlled loading.

Instability occurs when external work reaches a critical value and the crack continues to propagate without addition of any more energy to the system. The dissipation of energy during crack propagation comes from the release of accumulated elastic strain energy in the beam. Therefore, during displacement-controlled loading, although no additional external work is applied the instability still occurs. This leads to a drop in the peel force which is accounted for with the inclusion of a passive bending moment at the loading point. As illustrated in Figure A.8, Point  $A$  is the crack tip location before the instability occurs. Since the driving force that cause the instability is the released strain energy, the beam bends minimally after dissipation of energy. If this additional bending moment  $M$  is not applied during unstable crack propagation, Point  $A$  moves to Point  $A'$  and our loading point shifts from its original location. The additional bending moment term  $M$  ensures that the loading location remains unchanged during the peel process. However, in the case of stable crack propagation or in the case of force-controlled loading, this extra bending moment will not appear.

The following section introduces the solution scheme for the two loading scenarios and their respective objective functions in the optimal iterative solution are constructed.

#### (i) Force-controlled loading

Following the discussion in the previous section, when force-controlled loading is considered, the extra bending moment  $M$  does not appear here in Figure A.7(b), i.e.,

$M = 0$ . For this case, the constrained nonlinear multi-objective optimization problem describing peeling failure in composite film is:

$$\min_{l_i} U = \sum_{i=1}^n w_i \frac{|s_i(l_i) - L_i|}{L_i} \quad (\text{A.20})$$

$$\text{Subject to } \begin{cases} G_m^n(l_i) < 1 & i = 1, 2, \dots, n \\ \frac{l_i}{L_i} \leq \frac{l_{i+1}}{L_{i+1}} & i = 1, 2, \dots, n-1 \\ lb \leq l_i \leq ub & i = 1, 2, \dots, n \end{cases} \quad (\text{A.21})$$

In this optimization procedure, the projection lengths of  $l_i$  are taken as optimization variables and the curvature lengths  $s_i$  are used to construct sub-objective functions. A weighted global criterion scheme is adopted here, where all the sub-objective functions are combined to form a single global function  $U$ .  $w_i$  the weight function here  $w_i = \frac{L_i}{\sum_{i=1}^n L_i}$  is constructed such that  $\sum_{i=1}^n w_i = 1$ . For some specific cases, this weight function is appropriately adjusted. The global objective function  $U$  is minimized subject to the three constraints listed. The first one,  $G_m^n(l_i) < 1$ , arises from the requirement of integral equation construction (see the previous discussion). The second constraint comes from the requirement of deformation compatibility. The third sets the variable range, where  $lb$  and  $ub$  represent the lower limit and the upper limit, respectively.

The general procedure to obtain the optimal solution is as follows: (1) An initial guess for the optimum variables, i.e., the projection lengths for different segments  $(l_1, l_2, \dots, l_m)$  is made. Once  $l_m$  is known, the effective loads at the interface between the adhered portion and the adhesion-free portion is the force  $P$  and the bending moment  $P * l_m$  (2)  $P$ ,  $\theta_0$  and  $w_0$  are calculated using the analytical expression Eq. (A.10) (3) Based on those values, a new deformation configuration of the bent beam is calculated using Eq. (A.17) and Eq. (A.18). Simultaneously the curvature lengths  $s_i(l_i)$  in Eq. (A.20) are calculated (4) The iterative optimization scheme in Eq. (A.20) is used and step 1 to step 3 are repeated. The optimal variables  $(l_1, l_2, \dots, l_m)$  are iteratively searched and the final deformation of the bent strip is calculated.

## (ii) Displacement controlled loading

For displacement-controlled loading in addition to the applied concentrated vertical force a bending moment is passively triggered when instability occurs. The objective function for the displacement-controlled loading is then described as:

$$\min_{l_i, M_0} U = \sum_{i=1}^n w_i (1 - w_d) \frac{|s_i(l_i, M_0) - L_i|}{L_i} + w_d \frac{|d(l_i, M_0) - d_0|}{d_0} \quad (\text{A.22})$$

$$\text{Subject to } \begin{cases} G_m^n(l_i) < 1 & i = 1, 2, \dots, n \\ \frac{l_i}{L_i} \leq \frac{l_{i+1}}{L_{i+1}} & i = 1, 2, \dots, n-1 \\ lb \leq l_i \leq ub & i = 1, 2, \dots, n \end{cases} \quad (\text{A.23})$$

The displacement related sub-objective function in Eq. (A.22) contains another optimization variable,  $M$ . Here,  $d_0$  and  $d(l_i, M_0)$  represent the prescribed displacement and the calculated displacement at the loading point during the iterative process.  $w_d$  is the weight function prescribed to the displacement term in the global objective function. The constraints are kept the same as that for the force-controlled loading. The optimal solution procedure is also the same as that for the force-controlled loading. The only difference is the change of optimization variables and the objective-function.

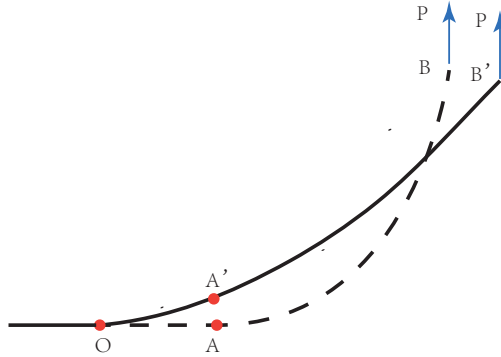


Figure A.8. Schematic drawing for two states of beam before and after unstable crack propagation.

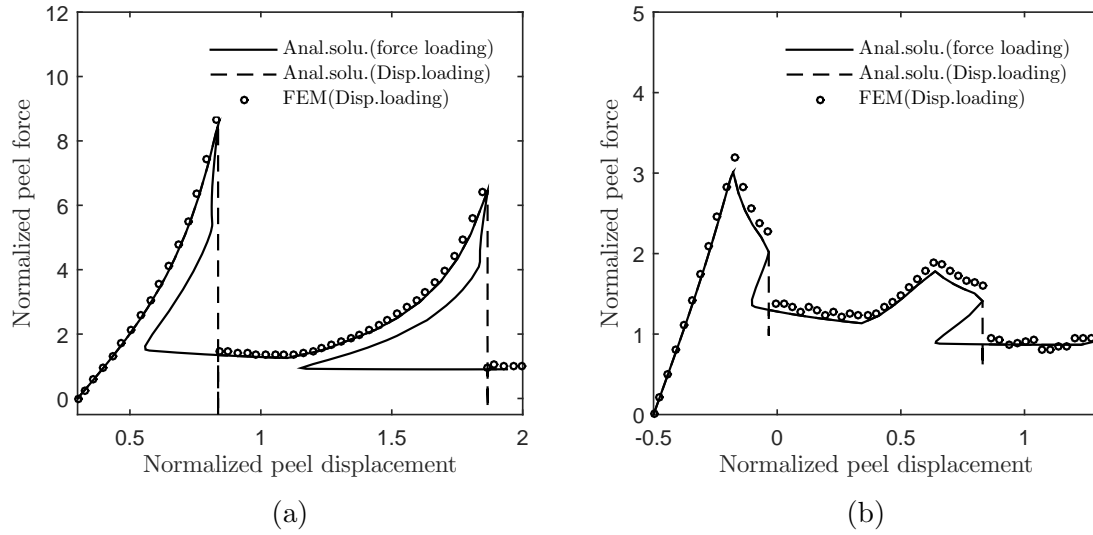


Figure A.9. FEM simulation v.s. Semi-analytical solution for two different bending rigidity ratios (a)  $D_s/D_c = 8.8$  (b)  $D_s/D_c = 2.0$ .

## A.5 Results and Discussion

The example discussed in Section A.3 is further investigated using the proposed semi-analytical method. It is shown that the thickness-enhanced heterogeneous film is equivalent to the material-enhanced film in terms of peel performance. The material-enhanced film (with the width  $b=0.4$  mm) is studied. Here, two bending rigidity ratios  $D_s/D_c=8.8$  and  $D_s/D_c=2.0$  are considered. The results from the displacement-controlled loading and the force-controlled loading scenarios are also discussed.

### A.5.1 Discussion on Peel Force Variation

Figure A.9 shows the normalized peel force-displacement response curves obtained from the semi-analytical solution based on the two loading conditions and two bending rigidity ratios. In this figure, the finite element results from the displacement-controlled loading are included as well. Here, two force peaks are shown, which correspond to the crack being allowed to extend through two heterogeneous segments. Each heterogeneous segment contains one stiff portion and another compliant

portion. From Figure A.9 we observe that the semi-analytical solutions are in good agreement with the FEM results for the displacement controlled case except where the load drops. During this stage, instability is encountered, so the crack instantaneously extends in a dynamic fashion. Force balance here cannot be established without considering an extra bending moment at loading point. As such, the FEM simulation does not converge where the snap back occurs. No information on the loading condition is available at this stage as shown in Figure A.9. Due to the instantaneous crack propagation this force variation cannot be captured by existing experimental methods. However, the present semi-analytical method provides a basis for describing the unstable crack propagation process. From the results of semi-analytical method we see that the force drops first to a smaller value, and then snaps back to a certain value where the crack starts to grow again in a stable manner.

Figure A.10 depicts the relationship between the peel force and the crack tip location, which clearly shows the force fluctuation during crack extension. Based on both Figure A.9 and Figure A.10, it is easy to predict when the force peaks occur, when the instability occurs and how far the crack will propagate in an unstable manner. For the heterogeneous film the lengths of the stiff segments and compliant segments

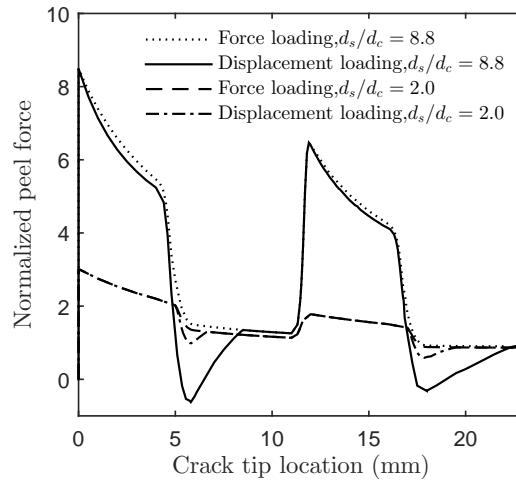


Figure A.10. Peel force changing with crack tip location under different bending rigidity ratio and loading conditions.

are both 6 mm. The peak force occurs at the interface going from a compliant material segment to a stiff one, while unstable crack propagation occurs going vice-versa. The unstable crack propagation starts when the crack tip is located at  $x = 0$  mm and ends at  $x = 8.3$  mm for  $D_s/D_c = 8.8$ . In the case of a lower bending rigidity  $D_s/D_c = 2.0$  it starts at  $x = 5.0$  mm and ends at  $x = 6.4$  mm (i.e. the beam first experiences stable crack propagation before instability takes place). Thus, for the smaller rigidity case the instability occurs closer to the material interface when the crack traverses for a stiff to a compliant segment. In addition, the maximum force to debond is lower for the beam with a lower bending rigidity. It is important to note here that unstable crack propagation through the stiff segment has no influence on the force required to debond in the compliant region. Force to debond in the compliant region coincides for both cases of bending rigidities  $D_s/D_c=8.8$  and  $D_s/D_c=2.0$  as shown in Figure A.10. This implies that the local rigidity enhancement in the heterogeneous film has little influence on the debond characteristics of the compliant region except in the zone where unstable crack propagation occurs. If the force to debond in the compliant region is considered the baseline then, the maximum force to peel in the heterogeneous film is improved 8 fold for  $D_s/D_c=8.8$ , and nearly 2 times for  $D_s/D_c=2.0$ . To summarize, the higher bending rigidity ratio in the heterogeneous film increases the maximum peeling force and increases the length for which the crack propagates unstably.

As discussed previously, unstable crack propagation is triggered by displacement-controlled loading and it is a consequence of release of stored elastic strain energy in the beam. A bending moment term is then required at the loading location to satisfy the constraints when the energy is released. Figure A.11 shows the change in force together with the change in moment during unstable crack propagation for  $D_s/D_c = 8.8$ . It is observed that the force decreases when the bending moment increases and vice versa, the effect is shown in Figure A.9. Once crack propagation returns to the stable regime, this extra bending moment vanishes ( $M = 0$ ). These results obtained through the semi-analytical model are validated against the FEM results presented

in Figure A.9. Those FEM results in turn were validated by experimental results presented in Section A.3.

Figure A.9 compared results from the force-controlled loading case to the displacement-controlled loading. The two response curves coincide at all locations except in regions along the film where unstable crack propagation occurred in the displacement-controlled loading case. This similarity is down to the fact that the extra bending moment term disappears in the displacement-controlled loading case when the crack propagates stably. As a consequence the same set of governing equations describe peel in both cases. The load-displacement response curves from the semi-analytical model for force-controlled loading case are validated against the results presented in [131] as shown in Figure A.9. The results seem to agree well with the existing set of data. However, the present method provides more insight about the variation of the fracture process zone size and the traction-separation relationship around the crack tip.

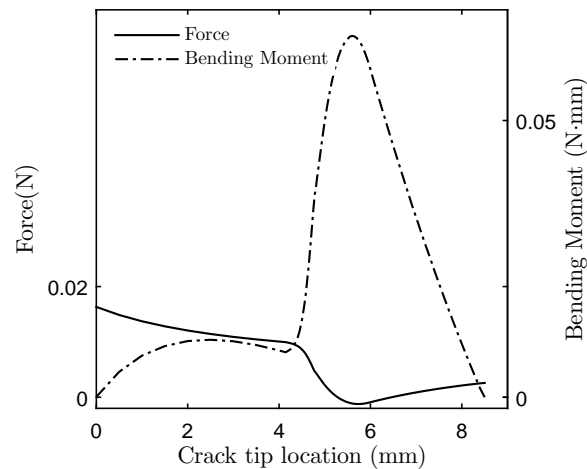


Figure A.11. Variation of force and extra bending moment during unstable crack propagation.



### A.5.2 Discussion on Energy Variation

Improvement in film fracture toughness and unstable crack propagation discussed earlier are related to the bending rigidity ratio of the heterogeneous film. However, the fundamental reason for this correlation is not well understood. In order to explain this dependence one viable approach is to study the transfer and distribution of energy in the film during the peel process.

Figure A.12 (a) and (b) show the variation of work or energy in the peeling film for both loading conditions. Here,  $D_s/D_c=8.8$  is taken as an example to explain the variation of energy during crack propagation. Each sub-figure in Figure A.12 contains four curves: the external work, the internal energy, the difference in external work and the internal energy, and the theoretical fracture energy (equal to the area of crack extension zone multiplied by the fracture energy in CZM). Both sub-figures suggest the differences between external work and internal energy approaches the theoretical fracture energy, and only small errors exist. The small deviation is caused by numerical integration. If the number of discrete points along the curves is increased

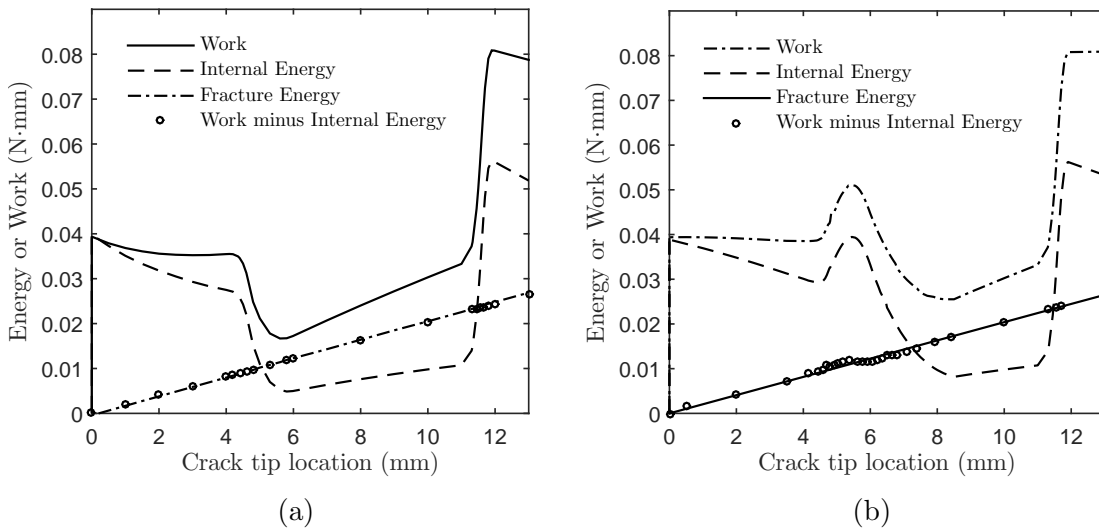


Figure A.12. Energy or work changing with crack tip location under different loading conditions (a) Force-controlled loading (b) Force-controlled loading.

these errors can be further reduced. From an energy balance standpoint the result verifies that the calculated energy variation with crack extension is reasonable.

A closer inspection of the two sub-figures in Figure A.12 shows similarity in behavior for the two different loading conditions. When the external work is increases, the internal energy is increases in the film but, the increase is not as significant. This observation signifies that a part of the external work is dissipated in the creation of two new surfaces when the crack front progresses. More importantly, external work is crack driving force in this case. On the contrary when the external work is kept the same or decreases, the internal energy decreases more rapidly. This implies that during this stage of crack propagation the release of accumulated internal energy adds to the crack driving force. As such, the released strain energy is responsible for unstable crack propagation. For the displacement-controlled loading case, the slight jump in external work at  $x=5.00$  mm corresponds to the addition of the extra bending moment term. As discussed earlier, this is a passive load introduced as a result of the release of accumulated internal energy.

In Figure A.12, at locations  $x = 0$  mm and  $x = 12$  mm of the crack tip where the transition occurs from a complaint segment to a stiff segment, the external work and the internal energies follow the same trend for the two cases. Rapidly increasing external work is converted to stored internal energy at that point. A similar effect is observed with the peel force at those points as shown in Figure A.9. Rivlin [1] had showed that fracture toughness is only dependent on the peel force and the peel angle. We can thus conclude that the sudden improvement in fracture toughness is related to the increase in the internal energy. However, it is still unclear why the external energy rather than resulting in failure at the adhesive interface is converted to internal energy in the beam.

The internal energy in the present case contains the bending strain energy and the cohesive energy of the beam. Stretch in the film is ignored by choice as the angle for peel  $\theta = 90^\circ$  is imposed. The stretch energy term is negligible compared to the bending energy as dicussed early on in the paper. Figure A.13 shows the

variation of the bending strain energy and the cohesive energy in the peeling system under force-controlled loading condition. Comparison of the magnitude of the two energies suggests that the bending energy is the dominant term, by as much as 20 times the cohesive energy. The bending beams acts as a large reservoir of energy. Through this reservoir, external work is transferred to the adhesive interface. When the beam absorbs energy upon bending, the fracture toughness of peeling system is improved. However, when it releases this excess energy, it risks triggering unstable crack propagation.

Cohesive energy in the beam maintains a stable value as the crack progresses until an interface between a stiff segment and a compliant segment is encountered as shown in Figure A.13. In stiffer sections where the material rigidity is higher, the stored cohesive energy is larger. Figure A.14 shows the variations of fracture process zone(damage zone) size for two different bending rigidity ratios. Comparing these with the cohesive energy in Figure A.13, it is clear that the two follow a similar trend. This implies that the cohesive energy is linked to the fracture process zone size. The higher the rigidity, the larger the fracture process zone size and cohesive energy in the beam. This correlation is validated for two different bending rigidity ratios, as

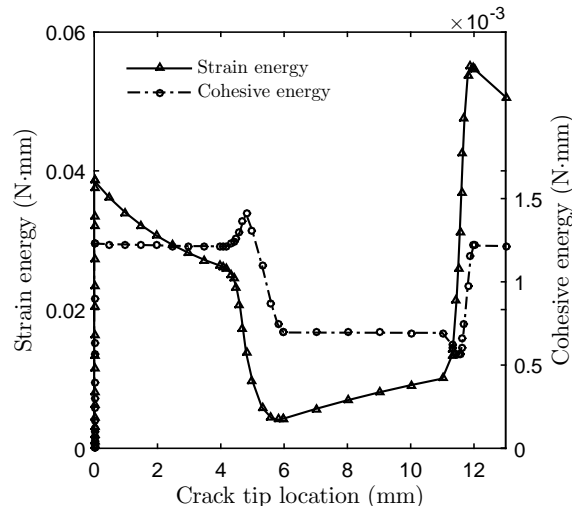


Figure A.13. Strain energy and cohesive energy along crack tip.

shown in Figure A.14. Sections of the beam with a higher bending rigidity resist the extension of cracks more than the sections with a lower bending rigidity. The beam in those sections has a larger fracture process zone size and therefore absorbs more energy. From a different viewpoint, if the same traction-separation law is considered a larger fracture process zone results in a lower stress concentration at the crack tip. Crack growth resistance is higher when the stress concentration is lower. This intricate relationship is the reason for substantial improvement in fracture toughness of the heterogeneous adhesive film.

Interestingly the cohesive energy increases slightly when the strain energy is released from the film. Figure A.13 shows a rise in cohesive energy just before reaching the interface between the stiff and compliant segment, this is followed by a rapid decrease in cohesive energy to the next stable value. In Figure A.13 when the crack tip is located at  $x = 4.2\text{mm}$ , the accumulated strain energy is released, but the cohesive energy increase before it changes direction halfway through the transition into the next segment. On the contrary, when the crack tip located at  $x = 11.2\text{mm}$  and the strain energy increases near the next interface, the cohesive energy drops below the stable value. Halfway through the increase in strain energy, the cohesive energy

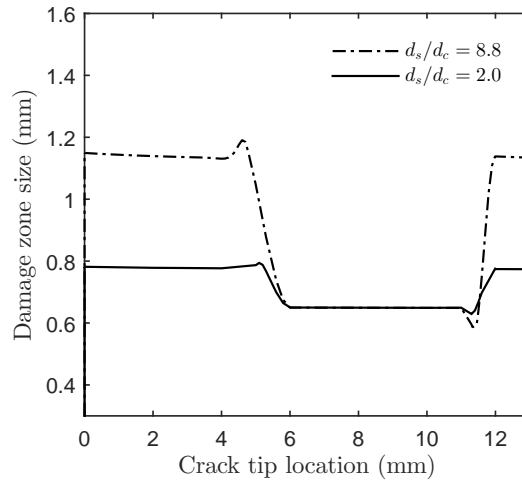


Figure A.14. Damage zone size changing with crack tip location.

begins to increase as well. That is to say, when the bending heterogeneous film undergoes a rapid change in energy, the adhesive interface which is connected to the beam suffers fluctuations in their energy states. When the accumulated bending strain energy in the strip is released, part of the released energy is transferred to the adhesive interface. When the absorbed energy at the interface exceeds its capacity, the excess energy is dissipated and results in crack extension. This reduces the cohesive energy. In addition, a part of the released energy is transferred to the loading point. During displacement-controlled loading an extra bending moment is produced at the loading point to absorb this energy at first before releasing it. To this end energy balance is ensured.

### A.5.3 Impact of Cohesive Parameters

For a bilinear cohesive zone model that considers failure in the mode-I direction four essential cohesive parameters are required; fracture energy  $G$ , slope at linear stage  $K_1$ , maximum traction  $\sigma_{max}$  and the critical separation at failure  $\delta_f$ . The first two parameters are obtained from experiments. Of the remaining two, one is picked arbitrarily and the other is derived using fracture energy. In this paper the maximum traction  $\sigma_{max}$  is chosen as a variable to study the impact of cohesive parameters on peel test simulations. Figure A.15(a) shows us the peel force-displacement response curves based on different  $\sigma_{max}$ . Figure A.15 (b) and (c) exhibit the variation of strain energy and cohesive energy, respectively. Variation of  $\sigma_{max}$  has little influence on the force-displacement response curve and the strain energy of the film. However, the cohesive energy curve changes with  $\sigma_{max}$  as expected. As discussed earlier, the magnitude of bending strain energy is usually much larger than the cohesive energy for the chosen adhesive film. It is the primary term that dominates fracture toughness of the film under peel. Therefore, even with a large variation in  $\sigma_{max}$  and change in cohesive energy at the interface, the peel performance does not change as much. Now, if fracture energy (area under the traction-separation law) is changed the influence

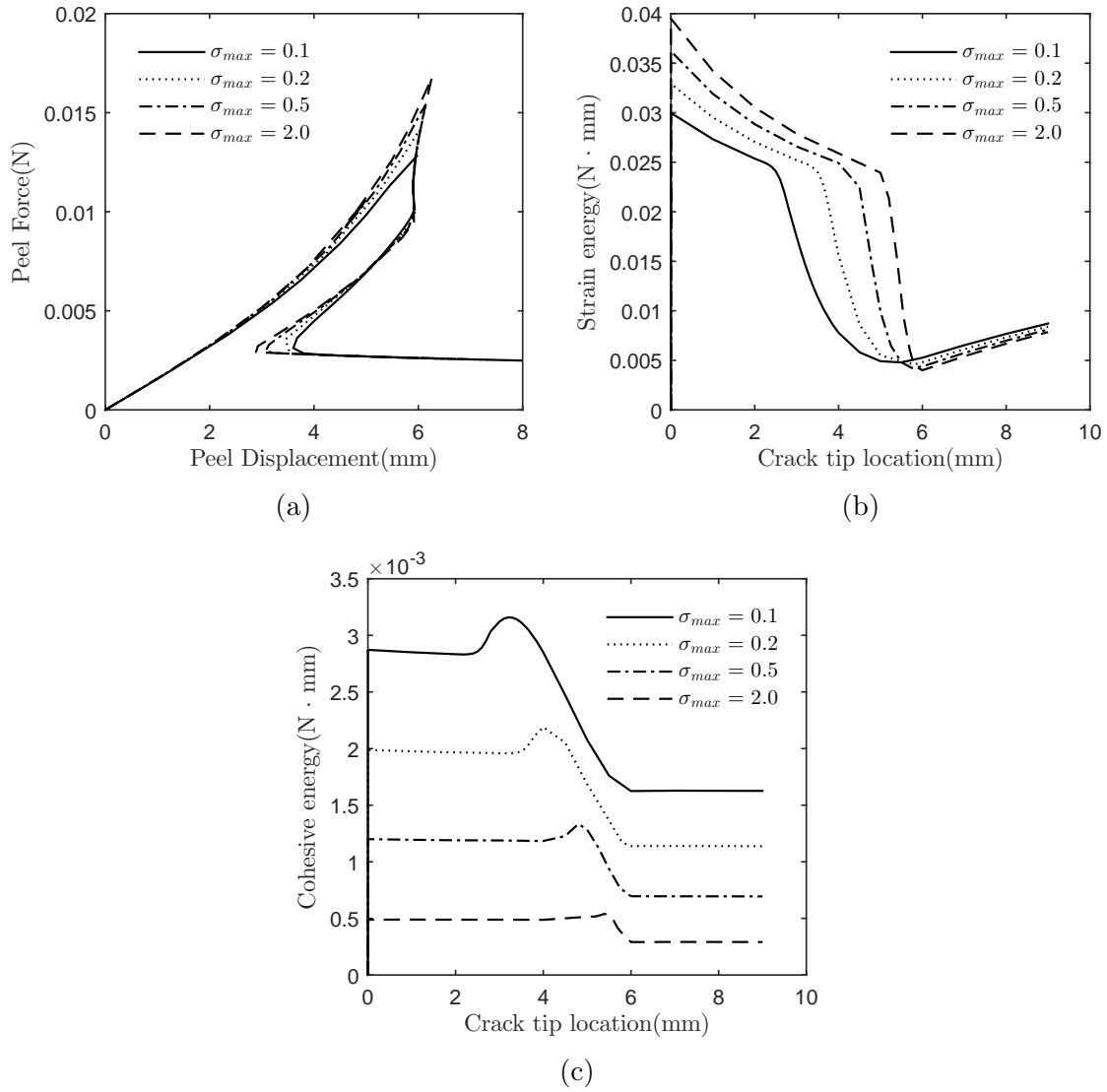


Figure A.15. The effect of cohesive parameter ( $\sigma_{max}$ ) on peeling performance of heterogeneous strip (a) Peel force changing with peel displacement. (b) Strain energy changing with crack tip location (c) Cohesive energy changing with crack tip location.

on peel performance is significant. This paper uses the values reported by Xia et al. [131] and no changes are made to the reported fracture toughness.

Although  $\sigma_{max}$  does not have a significant influence on the peaks in Figure A.15 (a) and (b), we observe from Figure A.15(b) and Fig.15(c) a delay in the release of energy. The release of energy after the delay is also much faster for larger  $\sigma_{max}$ . In addition, the fluctuation (the bump shown in the cohesive energy curve) before the unstable crack propagation is smaller. This implies that a higher  $\sigma_{max}$  will not be influenced by the strain energy in the bending beam as much. Figure A.15(c) shows another interesting phenomena. With increase in  $\sigma_{max}$ , the cohesive energy decreases similar in nature to the fracture process zone size. It signifies that the higher  $\sigma_{max}$  leads to a smaller fracture process zone size. A higher adhesive strength  $\sigma_{max}$  has a stronger local constraint on the adherent and therefore its fracture process zone is smaller. To summarize, we know that both a larger bending rigidity and a lower adhesive strength cause an increase in the fracture process zone size. A larger bending rigidity results in the increase of fracture toughness in peeling test but a lower adhesive strength reduces the fracture toughness. Although the fracture process zone is larger with a lower adhesive strength the fracture toughness is lower (damage zone is larger), so there is a tradeoff in choosing an appropriate adhesive strength.

## A.6 Summary

In this study, a semi-analytical method based on CZM was proposed to study the peeling failure of a heterogeneous film in a large deflection framework. Two loading scenarios, displacement-controlled and force-controlled loading are analyzed. It is worth noting that the semi-analytical solution provides an approach to study instability in heterogeneous adhesives during unstable crack propagation. Understanding the instability phenomena opens up another mechanism for designers to improve fracture toughness of the film without modifying the interface. This semi-analytical

method was validated with finite element simulations and the experimental results from literature. The main conclusions from this paper are summarized as follows.

1. The proposed semi-analytical method provides greater insight that cannot be obtained through existing simulation or experimental techniques. These additional pieces of information include the instantaneous process of load variation during unstable crack propagation, the fluctuation of fracture process zone size before debond, and the energy transfer during crack propagation.
2. The energy absorbed in the process of bending the composite beam is the reason for the improvement of fracture toughness. The transfer of energy depends on the rigidity of beam and the cohesive properties of adhesion interface. For the heterogeneous adhesive film, most of the external work is converted to elastic strain energy, and the rest into the cohesive energy at adhesive interface. If the rigidity of beam is larger, the fracture process zone size is larger due to a more rigid constraint at the adhesive interface. For the same cohesive law, a larger fracture process zone size signifies that more energy is absorbed at the cohesive interface. It also implies that the stress concentration around crack tip is not as significant in this case.
3. Unstable crack propagation occurs when the crack is extends through material interface from a stiff to a compliant segment in the composite film. Due to the difference in ability to store elastic strain energy between the two segments excess energy is released when the crack extends through the stiff segment. This excess release of energy causes the unstable crack propagation.
4. FEM simulation of both the thickness-enhanced and the material-enhanced heterogeneous films show that their peel performance is similar when they have equivalent bending stiffness. The only exception occurs at the interface going from a thick segment to thin segment and vice versa for the case of the thickness enhanced film. The force peak is different because a part of the edge has no constraints when compared to the material-enhanced film.



5. The choice of different cohesive parameters (e.g., the maximum cohesive strength, or the critical failure separation) for the same cohesive energy in CZM influences the peel performance. A smaller adhesive strength results in a larger fracture process zone size but, the relation is not necessarily linear. Therefore, the increase of fracture process zone size does not result in a larger energy absorption in the film. It follows that the lower cohesive strength will result in lower fracture toughness of heterogeneous adhesive film.

VITA

## VITA

Yuvraj was born and raised in Delhi, India. He joined Purdue in fall of 2007 to pursue an undergraduate degree in mechanical engineering. During his sophomore year, he joined Prof. Subbarayan's group as an undergraduate researcher through the SURF (Summer Undergraduate Research Fellowship) program. After completion of his undergraduate degree, he continued to work with Prof. Subbarayan's group as a graduate student. He received his masters degree in mechanical engineering in spring 2014 from Purdue. His work during his masters degree was related to lead-free solder characterization and thermal interface material characterization. He started his Ph.D. in the same group with his research focus on thin film characterization. After receiving his masters degree, Yuvraj spent six months on an internship with Freescale Semiconductor (now NXP) in Austin, Texas. He also interned with Intel Corporation during his Ph.D. He will be joining as a fulltime with the same group at Intel post completion of Ph.D requirements. His research interests are on packaging reliability for microelectronics with a focus on development of novel characterization techniques. His interests outside of work include following soccer, cooking and hiking.